Fracture and crack growth

A fracture mechanics approach

Olsen, David Holkmann

Publication date:
1997

Document Version
Publisher's PDF, also known as Version of record

racture
Growth
Mechanics Approach
© by David Holkmann Olsen
-tryk
Tekniske Universitet

740-237-5
-2167

Preface

The present thesis ***Concrete Fracture and Crack Growth - A Fracture Mechanics Approach*** is prepared as a partial fulfilment of the requirements for obtaining the Ph.D. degree.

The present work has been carried out at the Department of Structural Engineering, Technical University of Denmark under the supervision of Professor Dr. techn. M. P. Nielsen.

The work has partly been financed by a special grant from the Danish Technical Research Council (STVF), Knud Højgaards Fond and by the materials research program "High Performance Concretes in the 90'ies".

I wish to express my sincere thanks to Professor M. P. Nielsen for his guidance and encouragement during my study and to persons at the Department, who contributed to the completion of the Ph.D. study and this thesis.

Abstract

In this thesis concrete fracture and crack growth is investigated. The theoretical investigations are based on fracture mechanics and are mainly concentrated on the behaviour of the tensile fracture of concrete.

In the first part emphasis is put on evaluating theoretical values of stress intensity factors. The method is based on a rather unknown, highly simplified way of calculating stress intensity factors. It is shown, that very simple statically admissible stress fields may be used when determining actual values without considering the stress concentration at the crack tip.

In chapter 4 a newly developed crack growth model based on an energy criterion is presented. The model is able to predict crack propagation, loading and deformation in mode I.

The crack propagation formula is a first order differential equation. The stress intensity factors entering in the equation are determined on the basis of simple linear elastic finite element solutions. The non linearity is taken into account using a crack length correction. The basic principle of determining the crack growth, loading and deformation by the formula is presented briefly in the thesis.

A parametric study of the crack propagation formula has been carried out, to evaluate the consistency of the theory. It is shown, that the theory is able to predict size effects, and that the model is able to predict crack propagation in ductile as well as brittle materials.

In order to investigate the capability of the model a comparison between theory and experimental results is carried out with three point bending tests on plain concrete.

Full load-deflection curves for three point bending tests, where material properties of concrete such as compressive strength and maximum aggregate size together with beam dimensions are varied, are compared with theoretical results.

The crack propagation formula presented is able to predict the peak value and part of the descending branch of the load-deflection curve for different strength levels, variation of notch height ratios and different maximum aggregate sizes.

Chapter 5 contains the results and descriptions of a number of test series carried out in order to evaluate the physical properties and fracture of plain concrete.

The primary aim is to isolate and accurately estimate essential fracture mechanical parameters.

In this investigation a total of 232 test beams together with 714 cylinders are presented rendering values of the fracture energy G_F and flexural strength of concrete for different compressive strength levels, curing conditions, air-content and maximum aggregate size. An investigation of the size effect of beams are performed for normal and high strength concrete.

Furthermore the full load-deflection curve obtained by a displacement controlled testing machine are given for every beam test carried out.

Resumé

I denne afhandling er der foretaget undersøgelser af betons brudegenskaber og revnevækst. De teoretiske overvejelser er baseret på brudmekanik og omhandler primært trækbrudstyrken af beton.

I den første del af afhandlingen er der udført en analyse af teoretiske værdier for spændingsintensitetsfaktorer. Metoden, der er næsten ukendt, baserer sig på en meget simplificeret måde at beregne spændingsintensitetsfaktorer på. Der introduceres en metode, hvor simple statisk tilladelig spændingsfordelinger kan anvendes ved beregning af værdier for disse faktorer uden hensyntagen til spændingskoncentrationer ved revnespidsen.

En nyudviklet revnevækstteori baseret på energibetragtninger præsenteres i kapitel 4. Teorien er i stand til at forudsige revnevækst, brudlast og deformation for konstruktioner i mode I (trækbrud).

Revnevækstformlen er en 1. ordens differentialligning. De spændingsintensitetsfaktorer, der indgår i ligningen, bestemmes v.h.a. simple lineær-elastiske finite element beregninger, mens ulineariteten tages i regning ved hjælp af en revnelængdekorrektion. Beregningsprincipperne til bestemmelse af revnevækst, last og deformation gennemgås summarisk i afhandlingen.

Indledningsvis er der foretaget et parameterstudium af revnevækstformlen, der munder ud i en konsistensvurdering af modellen. Det eftervises, at teorien er i stånd til at forudsige størrelseseffekter, samt at modellen kan forudsige revnevækst i plastiske såvel som i skøre materialer.

De teoretiske resultater er sammenlignet med forsøgsresultater fra uarmerede betonbjælker påvirket til bøjning.

Last-deformations kurver for betonbjælkerne er angivet for forskellige betontrykstyrker, kærvlængder samt maximal stenstørrelse, og disse er sammenlignet med den teoretiske model.

Revnevækstteorien viser sig at kunne forudsige den opadgående del af last-deformation kurven samt brudlasten. Derudover er modellen i stand til at beskrive en del af den nedadgående del af arbejdskurven.

Kapitel 5 indeholder resultater og beskrivelser af en række forsøgsserier udført med det formål at vurdere de fysiske brudegenskaber for betonbjælker.

Det primære formål er at isolere og præcist estimere brudmekaniske egenskaber for beton.

I denne undersøgelse er ialt 232 betonbjælker og 714 betoncylindre afprøvet, og værdier for brudenergien G_F og bøjningstrækstyrken er præsenteret for forskellige betontrykstyrker, lagringsforhold, luftindhold i betonen og maksimal stenstørrelse i betonen. En undersøgelse af størrelseseffekten for bjælker af normal- og højstyrkebeton er ligeledes foretaget.

Derudover indeholder afhandlingen den totale last-deformationskurve målt v.h.a. en deformationsstyret forsøgsmaskine for samtlige bjælker i forsøgsprogrammet.

Contents

Page

Page

List of Figures

Page

Figures in Chapter 4:

Page

Figures in Chapter 5:

Page

List of Tables

Page

Notation

Symbols and notations used in this thesis have been chosen in conformity with the corresponding main literature references and with common practice. Below the most commonly used symbols are listed. Special symbols may occur and are explained in the text when they first emanate.

A	Fracture area.
a	Crack depth and notch height.
a_{eff}	Effective crack length.
a_p	Length of process zone.
a_y	Length of plastic zone.
a_0	Initial crack length.
B	Brittleness number.
b	Width of beam.
CMOD	Crack mouth opening displacement.
$CMOD_e$	Elastic crack mouth opening displacement.
CTOD	Crack tip opening displacement.
$CTOD_c$	Critical crack tip opening displacement.
c	Constant and support length.
D	Free surface energy.
d_{max}	Maximum aggregate size.
E	Modulus of elasticity (Youngs modulus).
E_c	Youngs modulus for concrete.
E_p	Potential energy.
f_c	Uniaxial cylinder compressive strength of concrete.

f_f	Flexural strength for concrete beam.
f_{sp}	Splitting strength of concrete.
f_t	Tensile strength of concrete.
f_y	Yield strength.
G	Energy release rate or shear modulus.
G_F	Fracture energy.
h	Height of beam.
K	Stress intensity factor.
K_c	The critical stress intensity factor.
k	Stiffness of testing machine.
L	Span of beam.
LEFM	Linear elastic fracture mechanics.
m_t	Weight of testing equipment.
m_g	Weight of test beam.
P	Load, force.
P_{max}	Maximum value of concentrated load.
P_{peak}	Peak value of concentrated load.
p,q	Uniformly distributed load.
r	Radius and distance from a crack.
U	Energy.
U_{beam}	Energy needed to deflect a beam.
U_m	Energy absorbed by testing machine.
U_p	Energy of the applied load P.
U_s	Total energy of a system.
u	Central deflection of test beam.
u_m	Deflection of testing machine.
u_0	Value of u when P has descended to 0 and final rupture occurs.
W	Elastic energy.
W_e	Area of experimentally determined load-deflection curve.
W_0	Strain energy of a non cracked beam.
W'	Strain energy per unit volume.
w	Crack opening displacement.
w_c	Critical crack opening displacement.
x,y,z	Cartesian coordinates.

δ	Deflection.
δ_0	Value of δ when P has descended to 0 and final rupture occurs.
ϵ	Strain.
θ,r	Polar coordinates.
ν	Poisson ratio.
σ	Stress.
σ_c	Compressive stress.
σ_t	Tensile stress.
τ	Shear stress.

Chapter 1

Introduction

1.1 General

Fracture mechanics has become popular as a research area in recent years in the concrete world. The background is of course the tremendous success of fracture mechanics when used for metals to explain fatigue failures and to calculate fatigue life.

Before fracture mechanics entered the scene of concrete, the basic tests to investigate the failure of concrete were the compression test on a cylinder, prism or cube together with the bending and splitting tests. These tests were the only means for receiving failure stresses which immediately could be put into further analysis of structures. Nowadays, many researchers are becoming aware of the fact that these tests are not sufficient to fully cover the failure properties of concrete, and that assumptions, which are made with respect to stress distributions in specimens, are seriously violated because of the inhomogeneity and the nonlinearity of concrete.

In concrete the main emphasis on fracture mechanics has been on the tensile behaviour. This is a little strange, because concrete is primarily utilized in com-

pression. The reason is of course the hope, that when understanding the tensile behaviour, i.e. crack growth in mode I, it is possible also to model the compressive failure.

The author does not share this hope. In his opinion compressive failures in concrete is essentially a failure by yielding in the cement paste. It is true, that also in compression, crack growth in mode I takes place mainly in the direction of the largest compressive stress. This is, however, a secondary phenomenon.

Nevertheless the behaviour of concrete in tension is worth studying. Although the tensile strength is not used directly when determining load carrying capacities, it is a very important structural property. First of all, knowledge of tensile behaviour is important when studying crack width theories, but it is also inherent in many strength calculations like the shear strength of non shear reinforced beams, bond strength between reinforcement bars and concrete, punching failures etc.

1.2 The Scope of the Thesis

In this thesis some aspects of fracture mechanics of concrete has been studied. In the first part emphasis is put on evaluating a rather unknown, highly simplified way of calculating stress intensity factors. It is shown that very simple statically admissible stress fields may be used, i.e. stress fields completely disregarding the stress concentration at the crack tip.

In the second part a newly developed crack growth formula is evaluated by studying crack growth in three point bending tests. The new theory seems to be able to describe the crack growth under these conditions, and it is also possible to calculate load-deflection curves including part of the descending branch.

In the third part a large number of tests carried out by the author is presented. The purpose of these tests is to determine fracture mechanics properties of concrete under a variety of circumstances.

Chapter 2

General Fracture Mechanics

2.1 Introduction

This section serves as an introduction to and a general description of the discipline "fracture mechanics".

When examining the strength of materials the structural component is normally considered as an ideal material free of defects and cracks. The theory of fracture mechanics starts by analyzing components with cracks either real or hypothetical. Since a crack is a discontinuity in the material, stresses and strains will in this area deviate from a smooth pattern. Criteria, other than an average stress compared to strength, have to be found in order to evaluate these important local effects. In the theory of linear elastic fracture mechanics two criteria are mostly used; the energy criterion developed by ***Griffith*** and the stress intensity criterion developed by ***Irwin***.

2.2 Stress Analysis for Members With Cracks

In order to analyze a cracked member it is important to investigate the manner in which a crack changes the stress and displacement fields in an ideal elastic solid. The solution to any such problem involves searching for a suitable "stress function", which satisfies the linear elastic theory including the boundary conditions. The components of stress and displacement are then directly determined from the stress function.

Using modifications of analytical methods described by ***Westergaard*** **[39.1]**, ***Irwin*** **[57.3]** published solutions for crack tip stress distributions associated with the three major modes of loading shown in Figure 2.2 - 2.4. Note that these modes involve different crack surface displacements. Each of these modes of deformation corresponds to a basic type of stress field in the vicinity of crack tips, see Figure 2.1 where the stress components and the coordinates r and θ are shown.

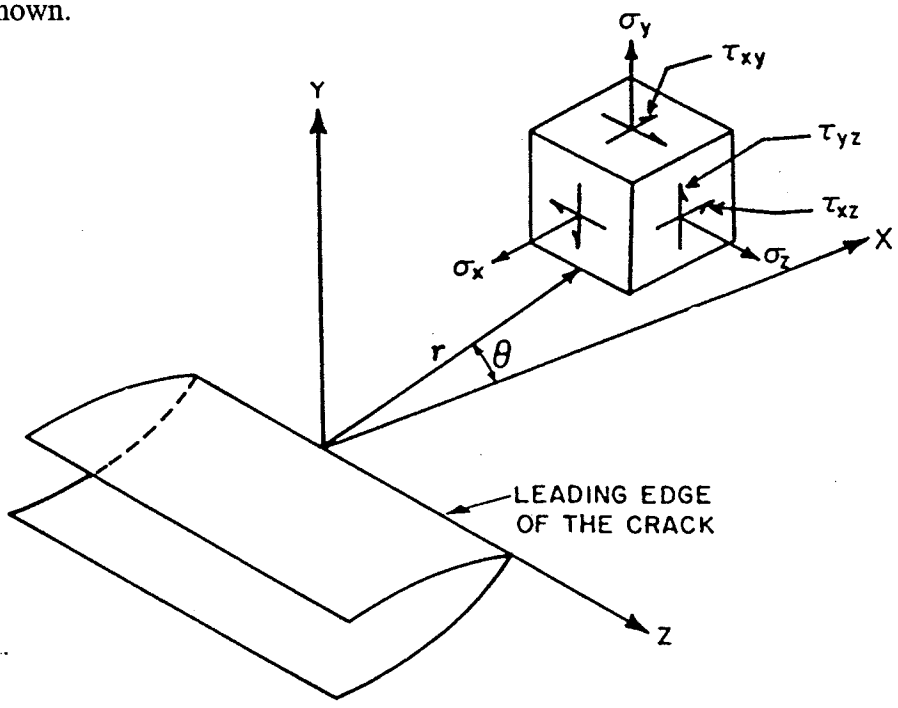

Figure 2.1 Stresses in vicinity of a crack tip.

Mode I, see Figure 2.2, is an opening mode, where the crack surface separate perpendicular to the maximum tensile stress i.e. the crack surfaces move directly apart. Mode I loading is encountered in an overwhelming majority of actual engineering situations involving cracked elements. Consequently, considerable attention has been given to both analytical and experimental methods designed to quantify Mode I stress-crack length relationship.

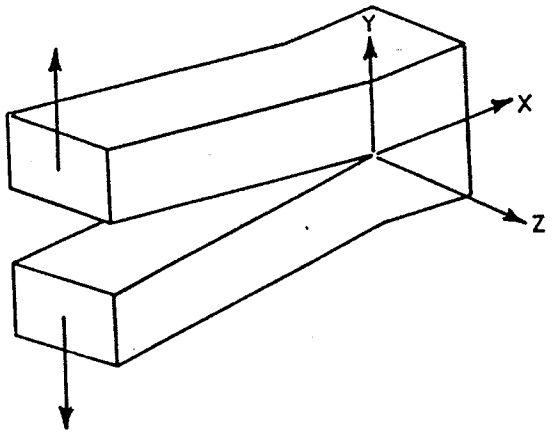

Figure 2.2 The Mode I loading.

For the notation shown in Figure 2.2, the crack tip stresses and displacements are found to be

$$\sigma_x = \frac{K_I}{\sqrt{2\pi r}} \cos\frac{\theta}{2}\left[1 - \sin\frac{\theta}{2} \sin\frac{3\theta}{2} \right] \tag{2.1}$$

$$\sigma_y = \frac{K_I}{\sqrt{2\pi r}} \cos\frac{\theta}{2}\left[1 + \sin\frac{\theta}{2} \sin\frac{3\theta}{2} \right] \tag{2.2}$$

$$\tau_{xy} = \frac{K_I}{\sqrt{2\pi r}} \sin\frac{\theta}{2} \cos\frac{\theta}{2} \cos\frac{3\theta}{2} \tag{2.3}$$

$$\tau_{xy} = \tau_{yz} = 0 \tag{2.4}$$

The constant K_I is the stress intensity factor for mode I.

Mode II, see Figure 2.3, is a sliding or in-plane shear mode, where the crack surfaces slide over one another in a direction perpendicular to the leading edge of the crack.

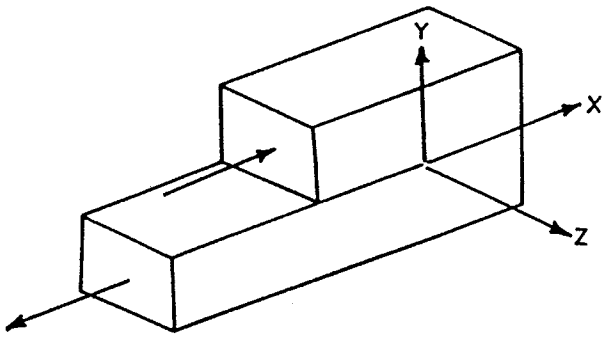

Figure 2.3 The Mode II loading.

The formulas for Mode II are

$$\sigma_x = -\frac{K_{II}}{\sqrt{2\pi r}} \sin\frac{\theta}{2}\left[2 + \cos\frac{\theta}{2}\cos\frac{3\theta}{2}\right] \tag{2.11}$$

$$\sigma_y = \frac{K_{II}}{\sqrt{2\pi r}} \sin\frac{\theta}{2}\cos\frac{\theta}{2}\cos\frac{3\theta}{2} \tag{2.12}$$

$$\tau_{xy} = \frac{K_{II}}{\sqrt{2\pi r}} \cos\frac{\theta}{2}\left[1 - \sin\frac{\theta}{2}\sin\frac{3\theta}{2}\right] \tag{2.13}$$

$$\tau_{xy} = \tau_{yz} = 0 \tag{2.14}$$

The constant K_{II} is the stress intensity factor for mode II.

Equations (2.1) - (2.4) are valid for Mode I loading in general. In the case of plane stress $\sigma_z = 0$ and the displacements are

$$u_x = \frac{K_I}{2E}(1+\nu)\left(\frac{r}{2\pi}\right)^{1/2}\left[\left(\frac{2(3-\nu)}{(1+\nu)} - 1\right)\cos\frac{\theta}{2} - \cos\frac{3\theta}{2}\right] \tag{2.5}$$

$$u_y = \frac{K_I}{2E}(1+\nu)\left(\frac{r}{2\pi}\right)^{1/2}\left[\left(\frac{2(3-\nu)}{(1+\nu)} + 1\right)\sin\frac{\theta}{2} - \sin\frac{3\theta}{2}\right] \tag{2.6}$$

$$u_z = -\left(\frac{\nu z}{E}\right)(\sigma_x + \sigma_y) \tag{2.7}$$

In the case of plane strain $u_z = 0$, the stress in the z-direction and the displacements in x- and y-direction are given by

$$\sigma_z = \nu\,(\sigma_x + \sigma_y) \tag{2.8}$$

$$u_x = \frac{K_I}{2E}(1+\nu)\left(\frac{r}{2\pi}\right)^{1/2}\left[(5-8\nu)\cos\frac{\theta}{2} - \cos\frac{3\theta}{2}\right] \tag{2.9}$$

$$u_y = \frac{K_I}{2E}(1+\nu)\left(\frac{r}{2\pi}\right)^{1/2}\left[(7-8\nu)\sin\frac{\theta}{2} - \sin\frac{3\theta}{2}\right] \tag{2.10}$$

In plane stress $\sigma_z = 0$, and the displacements u_x, u_y and u_z are given by

$$u_x = \frac{K_{II}}{2E}(1+\nu)\left(\frac{r}{2\pi}\right)^{1/2}\left[\left(\frac{2(3-\nu)}{(1+\nu)} + 3\right)\sin\frac{\theta}{2} + \sin\frac{3\theta}{2}\right] \tag{2.15}$$

$$u_y = -\frac{K_{II}}{2E}(1+\nu)\left(\frac{r}{2\pi}\right)^{1/2}\left[\left(\frac{2(3-\nu)}{(1+\nu)} - 3\right)\cos\frac{\theta}{2} + \cos\frac{3\theta}{2}\right] \tag{2.16}$$

$$u_z = -\left(\frac{\nu z}{E}\right)(\sigma_x + \sigma_y) \tag{2.17}$$

In plane strain $u_z = 0$ and σ_z is equal to

$$\sigma_z = \nu\,(\sigma_x + \sigma_y) \tag{2.18}$$

together with the displacements

$$u_x = \frac{K_{II}}{2E}(1+\nu)\left(\frac{r}{2\pi}\right)^{1/2}\left[(9-8\nu)\sin\frac{\theta}{2} + \sin\frac{3\theta}{2}\right] \tag{2.19}$$

$$u_y = -\frac{K_{II}}{2E}(1+\nu)\left(\frac{r}{2\pi}\right)^{1/2}\left[(3-8\nu)\cos\frac{\theta}{2} - \cos\frac{3\theta}{2}\right] \tag{2.20}$$

Mode III, see Figure 2.4, is the tearing or antiplane shear mode, where the crack surfaces move relative to one another and parallel to the leading edge of the crack. Mode III may be regarded as a pure shear problem, such as that involved in torsion problems.

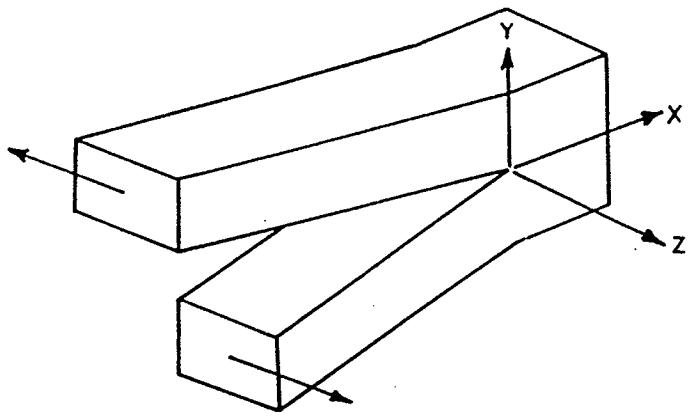

Figure 2.4 The Mode III loading.

The formulas may be expressed as in (2.21) - (2.25) when the notation in Figure 2.4 are used

$$\tau_{xy} = -\frac{K_{III}}{\sqrt{2\pi r}} \sin\frac{\theta}{2} \tag{2.21}$$

$$\tau_{xz} = \frac{K_{III}}{\sqrt{2\pi r}} \cos\frac{\theta}{2} \tag{2.22}$$

$$\sigma_x = \sigma_y = \sigma_z = \tau_{xy} = \tau_{yz} = 0 \tag{2.23}$$

The constant K_{III} is the stress intensity factor for mode III.

In Mode III only the displacement in the z-direction is non-zero yielding

$$u_x = u_y = 0 \tag{2.24}$$

$$u_z = \frac{K_{III}}{2E}\left(\frac{r}{2\pi}\right)^{1/2}\left[2(1+\nu)\sin\frac{\theta}{2}\right] \tag{2.25}$$

An important aspect of the formulas given for the different modes of fracture is that the stress and displacement distribution around any crack in a structure is similar and depends only on the parameters r and θ, i.e. we can in a simple form present the expressions for the stresses as

$$\sigma_{ij} = \frac{K}{\sqrt{2\pi r}} f_{ij}(\theta) \tag{2.26}$$

and the displacement as

$$u_i = \frac{K}{2E}\left(\frac{r}{2\pi}\right)^{1/2} f_i(\theta) \tag{2.27}$$

The difference between one cracked component and another lies in the magnitude of the stress field parameter also called the ***stress-intensity factor*** K. This factor serves as a scale factor to define the magnitude of the crack tip stress field. The stress intensity factor depends only on the applied loading and crack geometry and consequently determines the "intensity" of the local field. Many functions for K have been determined for various specimen geometries, see **[65.1]**, **[73.1]** and **[73.2]**.

The other parts of equations (2.26) - (2.27) (and of course (2.1) - (2.25)) are only parameters, which determine the distribution of the field; the radial component r and angular component θ.

However, one should be aware of the fact, that the above solutions for crack tip stresses and displacements are given by neglecting higher order terms of r in the derivations resulting in a restriction of the value of r. The terms given in (2.1) - (2.27) can be used in an area, where r is comparatively small in relation

2.3 The Griffith Criterion

Although fracture mechanics has been developed mainly since 1955, one of the basic equations was established already i 1921 by ***Griffith*** **[21.1]**.

Consider a linear elastic body with a small initial crack as shown in Figure 2.5.

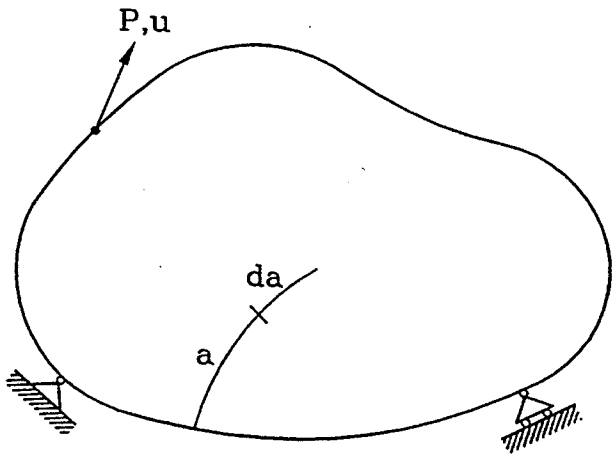

Figure 2.5 Cracked elastic body.

Griffith considered the energy necessary for creating one unit of new crack surface. When we consider a deformation controlled system, the decrease in elastic energy W of the loaded body shown in Figure 2.5 is equal to the energy necessary to create a corresponding crack surface, crack propagation initiates.

The most commonly used equation for formulating ***Griffith's*** theory is

$$G = -\frac{1}{b}\frac{\partial W}{\partial a} \tag{2.29}$$

where G is called the driving force or the energy release rate. b is the width of the cracked body considered and a the crack length.

When G takes the value G_F, the crack may start to propagate, i.e. the criterion for initiation of crack growth becomes

$$G = G_F \tag{2.30}$$

G_F can be considered as a crack resisting parameter and a material parameter and has normally been designated the "**Fracture Energy**" in the literature.

Griffith derived his theory for glass, which is a very brittle material. He therefore assumed, that the fracture energy G_F consisted of surface energy only. For other materials aside from ideally brittle materials, the fracture energy will consists of both surface energy and plastic energy due to the fact, that loading of a cracked body is accompanied by inelastic deformations in the neighbourhood of the crack tip. In ductile materials, such as metals, plastic deformation occurs at the crack tip resulting in energy dissipation for producing a plastic zone at the tip of an advancing crack. For ductile materials the plastic energy dissipation is the most important contribution to G_F. The surface energy may in fact be neglected.

In chapter 4 a more detailed description of the Griffith theory will be given, and in chapter 5 an experimental program is presented concerning the determination of the fracture energy G_F.

2.4 Relationship Between K and G

If a linear elastic crack tip field is considered, see Figure 2.6, we may find a relationship between the stress intensity factor K and the energy release rate G by calculating the energy release, when a crack of length a is extended to a length (a+∂a).

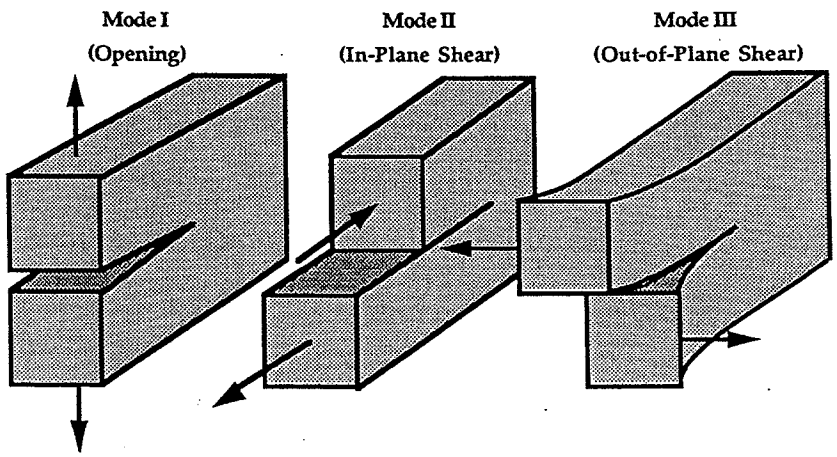

Figure 2.6 Member subjected to Mode I, II and III loading.

If we assume, that the body in Figure 2.6 is subjected to a tensile stress σ_{xx} (Mode I), a shear stress σ_{xy} (Mode II) and an antiplane shear stress σ_{xz} (Mode III), then the work done could be expressed as

$$G = \lim_{\partial a \to 0} \frac{1}{\partial a} \int_0^{\partial a} \left(\sigma_{xx} u_{xx} + \sigma_{xy} u_{xy} + \sigma_{xz} u_{xz} \right) \qquad (2.31)$$

where u_{xx}, u_{xy} and u_{xz} are deflecions in the direction of the respective modes.

Using the ***Westergaard*** solution for stresses and displacement and making the substitution $r=\partial a \sin^2(r')$, see ***Knott*** **[79.2]**, the equations (2.26) - (2.27) yields for plane stress

$$G = \frac{K_I^2}{E} + \frac{K_{II}^2}{E} + \frac{(1+\nu)\, K_{III}^2}{E} \tag{2.32}$$

and for plane strain

$$G = \frac{(1-\nu)\, K_I^2}{E} + \frac{(1-\nu)\, K_{II}^2}{E} + \frac{(1+\nu)\, K_{III}^2}{E} \tag{2.33}$$

We see, that the strain-energy release rate G and the stress intensity factors K have a very simple relationship in the linear elastic case, and that the energy release rates for different modes are additive.

2.5 Fracture Mechanics and Concrete

2.5.1 Introduction

In the preceding sections a short introduction to fracture mechanics has been given. The most important assumptions has been that only linear elastic materials have been considered.

Many researchers have studied the application of linear elastic fracture mechanics (LEFM) to concrete.

From the introduction of fracture mechanics by researchers like ***Irwin*** and ***Griffith*** in 1920, the first to use the theory of LEFM on concrete was ***Kaplan*** **[61.1]**. He performed three and four point bending experiments on notched beams with different dimensions.

Since then a large amount of written material has been published concerning crack stability and fracture mechanical test methods for concrete.

It turned out that great difficulties are encountered when using linear elastic fracture mechanics without modifications to concrete. That is the reason for the creation of a number of alternative theories described in the following.

This section will briefly present and describe some of the most important fracture mechanical models developed during the years, which are considered applicable to concrete.

2.5.2 The Fictitious Crack Model

A model for determining the creation and development of cracks in concrete was proposed by ***Hillerborg et. al.*** **[76.1]** in the years from 1976 to 1980. The model, which is based on an energy approach, introduces a *fictitious crack* for describing the development of a fracture zone at the tip of a crack. The main characteristics of the ***Fictitious Crack Model*** are shown in Figure 2.7, which illustrates the stress-deformation behaviour of concrete in a deformation controlled tension test.

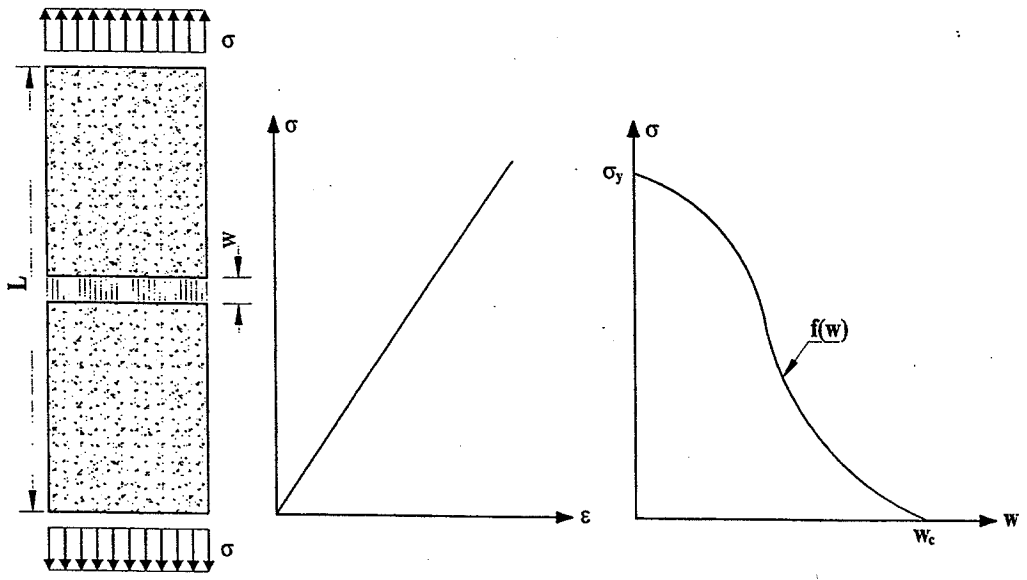

Figure 2.7 The fictitious crack model. Deformation behaviour in tension.

As the deformation is increased in a tensile test, the stress first increases and reaches a peak value and then decreases. The decrease in stress under increasing deformation is termed the strain softening. This softening was assumed to take place in a narrow zone in the specimen, called the fracture process zone or damage zone. The remaining part of the specimen simultaneously contracts elastically due to the decreasing stress.

A general description of the stress-deformation properties of the concrete can be given by introducing two curves, one stress-strain (σ-ϵ) curve up to the peak

value and one stress-deformation (σ-w) curve for the descending branch, see Figure 2.7. When the tensile strength of the concrete, σ_y, is reached, the damage zone (crack) is assumed to develop. The damage zone is similar to the cohesive zone introduced by ***Barenblatt*** **[60.2]**, where a microcracked zone ahead of the crack tip, a *fictitious crack*, was introduced. The width of the damage zone corresponding to the distance between the two uncracked parts is also termed the crack opening displacement w. As the crack opening displacement increases, the stress will gradually fall, until the ultimate crack width w_c is reached. At this point a real crack will develop, and a transfer of stresses between the two parts of the specimen will terminate.

The total amount of energy absorbed in a tensile test until failure is represented by the area below the load-deformation curve for the specimen. This energy can be divided into two parts, corresponding to the two curves in Figure 2.7. The area enclosed by the (σ-ϵ)-curve represents an energy per unit volume absorbed in the whole specimen. The area below the (σ-w)-curve represents the energy absorbed within the damage zone, denoted G_F, and can be written as

$$G_F = \int_0^{w_c} f(w)\,dw \qquad (2.34)$$

G_F is fracture energy per unit area of the fracture surface (projected area on a plane perpendicular to the stress direction). As f(w) is assumed a material function, the area under the function is a material parameter.

Numerical analyses based on the fictitious crack model are suitably performed by means of finite element methods making possible a theoretical analysis of the development of the damage zone and of the complete behaviour of a structure. The general principles of the finite element implementation of the fictitious crack model are described in detail in ***Petersson*** **[81.1]**.

2.5.3 The Crack Band Model

As was the case in the fictitious crack model, ***Bažant et. al.*** **[83.3]** and **[86.2]** found, that cracking in concrete was to be associated with the extent of micro-cracks in front of a crack tip. The *Crack Band Model* introduced by ***Bažant et. al.*** **[83.3]** is similar to the *Fictitious Crack Model*. The characteristic of this model is the introduction of a blunt crack band with a softening stress-strain relationship instead of using a softening stress-deformation relationship, as was the case in the *Fictitious Crack Model*. The crack band zone has a width of h_c, which is assumed to be a material parameter.

In Figure 2.8 the stress-strain relationship is given for a concrete bar subjected to pure tensile stresses in the axial direction.

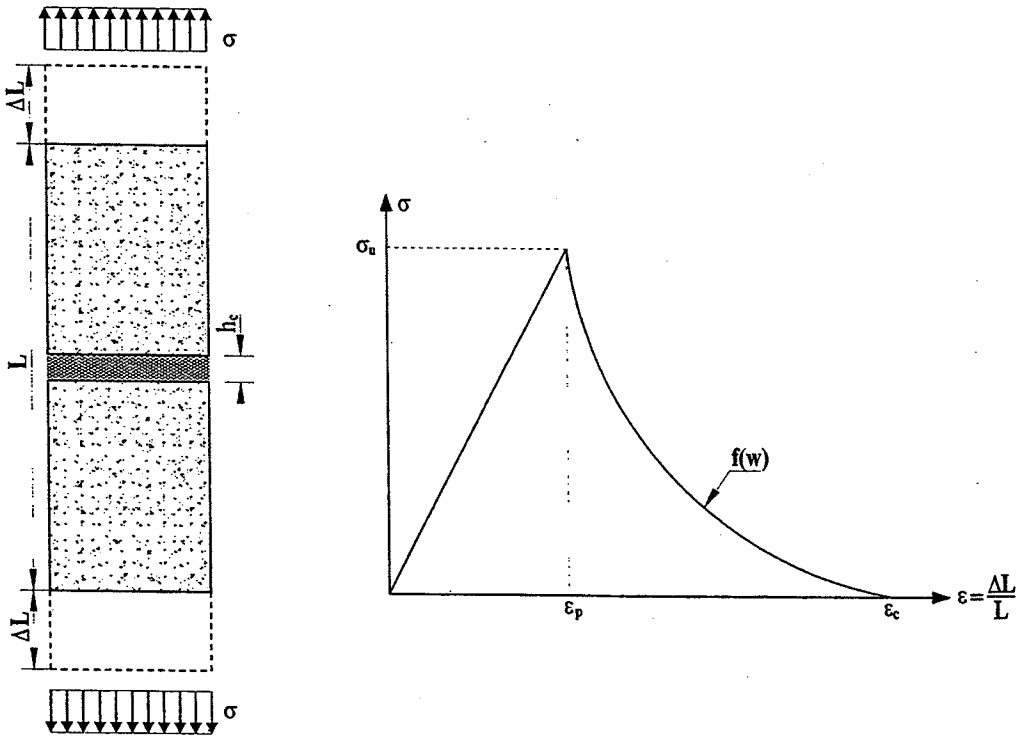

Figure 2.8 The crack band model. Stress-strain behaviour in tension.

The area below the (σ-ϵ)-curve represents the energy absorbed within the crack band, denoted G_F, and can be written as

$$G_F = \int_0^{h_c} \int_0^{\epsilon_c} f(\epsilon)\, d\epsilon\, dx \tag{2.35}$$

G_F is fracture energy per unit area of the fracture surface (projected area on a plane perpendicular to the stress direction). As $f(\epsilon)$ is assumed a material function, the area under the function is a material parameter.

The model is well suited for finite element calculations, when the stress-strain relationship has been established. As for the *Fictitious Crack Model* the material parameters of the concrete has to be known, and the *Crack Band Model* introduces an additional parameter, h_c, which has to be found by experiments. Investigations performed by ***Bažant*** seems to yield $h_c = 3d_{max}$, where d_{max} is the maximum aggregate size.

2.5.4 The Two Parameter Model

The *Fictitious Crack Model* and the *Crack Band Model* represents the fracture process zone with a damage band or a band of crack closing force, which can be determined from the post peak stress-strain relationship of the uniaxial tensile test. Due to the difficulties met in conducting the direct tension test, these relationships are often assumed linear or bilinear for simplification. The accuracy of the two models relies significantly on the selected post-peak stress-strain relationship and are primarily dependent on using numerical finite element methods. With this in mind, ***Jenq and Shah*** **[85.7]** proposed the *Two Parameter Model*. This model does not require the post-peak constitutive relation and is based on linear elastic fracture mechanics concepts. It is assumed, that the peak load is reached, when the stress intensity factor of an effective crack a_{eff} and the crack tip opening displacement (CTOD) at the initial crack tip a_0 reaches two critical values, K_{Ic}^{s} and $CTOD_c$, see Figure 2.9.

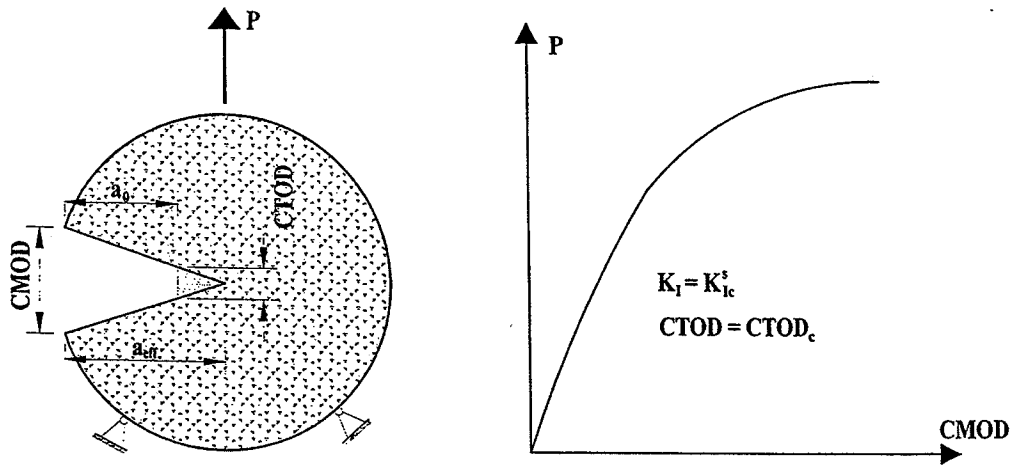

Figure 2.9 The two parameter model.

The two parameters K_I^s and CTOD are calculated according to LEFM. It is, however, not possible to measure the CTOD during an experiment, and instead the crack mouth opening displacement, CMOD, is measured. By using the CMOD at peak load the effective crack length can be found, and by using this crack length, K_{Ic}^s and $CTOD_c$ can be obtained.

The critical stress intensity factor K_{Ic}^s is calculated at the tip of the effective crack determined in such a way, that the measured elastic CMOD equals to the one calculated using LEFM. By either assuming the crack profile or directly using the LEFM formula the elastic critical crack tip opening displacement ($CTOD_c$) can be obtained. Since both fracture parameters are directly determined from LEFM formulae, crack tip singularity is automatically incorporated in the model. Figure 2.9 shows the typical load-CMOD response with the two critical fracture parameters.

Based on three point bending tests on different beam sizes and mix-proportions, they concluded, that both K_{Ic}^s and $CTOD_c$ are size independent. Several investigations have been made in order to check the applicability of the two parameter model. The findings in these investigations draw questionable conclusion on the size independence of the proposed *Two Parameter Model*.

Chapter 3

The Energy Approach

3.1 Introduction

The strict application of linear elastic theory for the determination of stress intensity factors are often cumbersome.

In this chapter a rather unknown method based on energy considerations is described. It is shown, that the energy may be determined using fairly simple statically admissible stress fields completely disregarding the stress singularities at the crack tip.

3.2 Determination of Stress-Intensity Factors Using Energy Methods

First we consider a linear elastic body, see Figure 3.1, with all six components of stresses, σ_x, σ_y, σ_z, τ_{xy}, τ_{yz}, τ_{xz}, present.

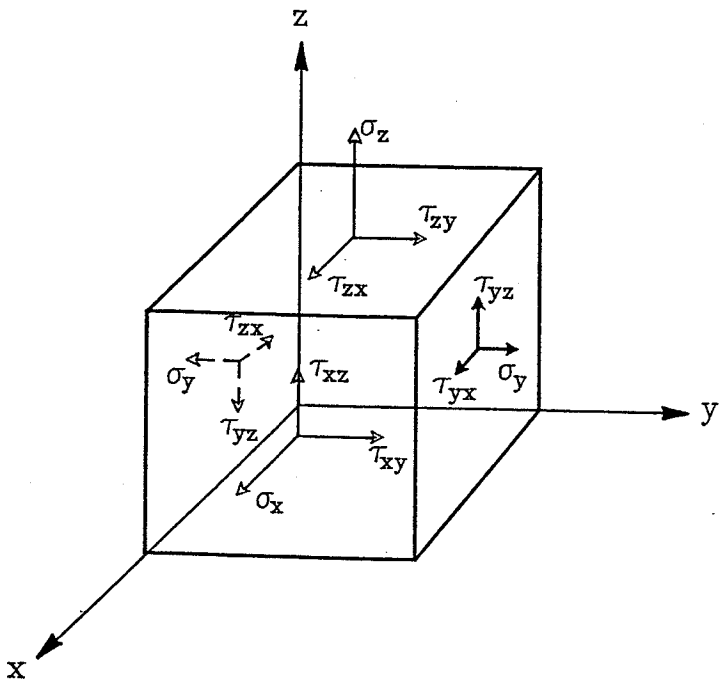

Figure 3.1 Linear elastic body.

The energy or the work to be performed, when the forces and thereby the stresses increase, is well known and given by

$$dW = W' dx\,dy\,dz \tag{3.1}$$

where

$$W' = \frac{1}{2}(\sigma_x \epsilon_x + \sigma_y \epsilon_y + \sigma_z \epsilon_z + \tau_{xy}\varphi_{xy} + \tau_{yz}\varphi_{yz} + \tau_{zx}\varphi_{zx}) \qquad (3.2)$$

The quantities σ_x, ϵ_x etc. are to be considered the final values of the stresses and strains.

Thus W' is the amount of work per unit volume or strain energy per unit volume. It is assumed that the body remains elastic, and that no kinetic energy is developed.

The total strain energy or elastic energy of a deformed elastic body is obtained from the strain energy per unit volume W' by integration:

$$W = \iiint W' dx dy dz \qquad (3.3)$$

Introducing Hooke's law, which has of course already been used when developing (3.2), we can express W' as a function of the stress components only. Then (3.2) becomes

$$W' = \frac{1}{2E}(\sigma_x^2 + \sigma_y^2 + \sigma_z^2) - \frac{\nu}{E}(\sigma_x\sigma_y + \sigma_y\sigma_z + \sigma_z\sigma_x) + \frac{1}{2G}(\tau_{xy}^2 + \tau_{yz}^2 + \tau_{xz}^2) \qquad (3.4)$$

where ν is the Poisson ratio, E the Youngs modulus and G is the shear modulus.

In the case of plane stress, in which $\sigma_z = \tau_{yz} = \tau_{xz} = 0$, we have from (3.4)

$$W' = \frac{1}{2E}(\sigma_x^2 + \sigma_y^2) - \frac{\nu}{E}\sigma_x\sigma_y + \frac{1}{2G}\tau_{xy}^2 \qquad (3.5)$$

If the well known relation from elastic theory

$$G = \frac{E}{2(1+\nu)} \tag{3.6}$$

is introduced in (3.5) the energy expression becomes

$$W' = \frac{1}{2E}\left(\sigma_x^2 + \sigma_y^2 - \nu\sigma_x\sigma_y + 2(1+\nu)\tau_{xy}^2 \right) \tag{3.7}$$

This is the elastic energy per unit volume for an element in plane stress, and the total elastic energy is easily obtained through (3.3) by integration with respect to x and y and by multiplying by the thickness of the member considered. By introducing this well known expression into fracture mechanics, i.e. into the Griffith equation for a cracked element, and calculating the derivative of the energy with respect to a well defined crack length a, we are in a position to numerically determine stress-intensity factors K for different geometries.

This determination of K is commonly done by finite element methods. A procedure, which is often employed, is the computation of the energy W for a series of crack sizes. If δa corresponds to a crack size increment and if δW is the increase of W for that increment, K can be obtained through, (by combining formula (2.29) and (2.32))

$$K = \sqrt{GE} = \sqrt{\frac{\partial W}{\partial a}E} \tag{3.8}$$

If we assume, that the energy can be written as $W = \frac{1}{2}\sum P_i u_i$ corresponding to a compliance calibration, where the force P_i is held constant, and u_i is the displacement parallel to P_i of the local region of load application, the above formula can be expressed as

$$K = \sqrt{\frac{\partial W}{\partial a}E} = \sqrt{\frac{1}{2}\sum P_i E \frac{\partial u_i}{\partial a}} \tag{3.9}$$

The advantage of the procedure is, that the refinement of the finite element mesh toward very small element sizes near the crack tip has little influence on the displacement increment, δu_i, remote from the crack, and is therefore not required. The procedure will be shown in the next section in form of an example.

3.3 Example of Calculated Stress-Intensity Factors

Consider an infinite cracked plate of unit thickness with a central transverse crack of length 2a, see Figure 3.2. The plate is at infinity loaded by a tensile stress p.

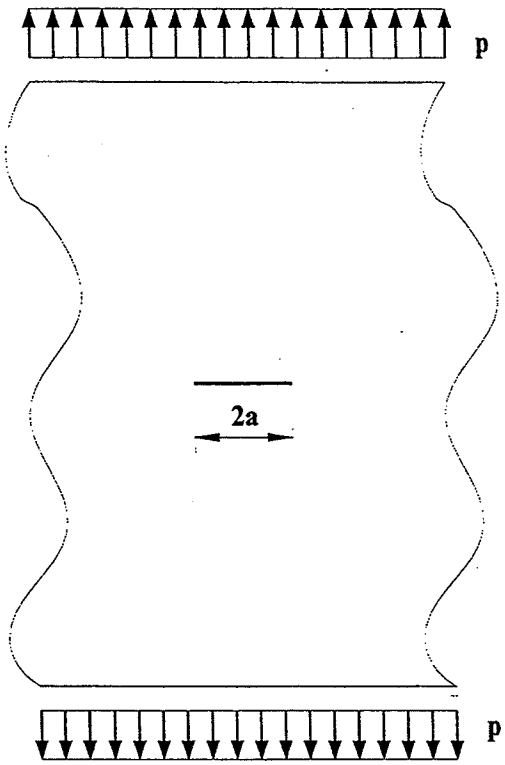

Figure 3.2 Infinite plate containing a through-thickness crack of length 2a.

We consider for a moment the body to be in a load controlled situation.

The important features of the energy balance are illustrated in Figure 3.3, where the load-deflection diagram is given.

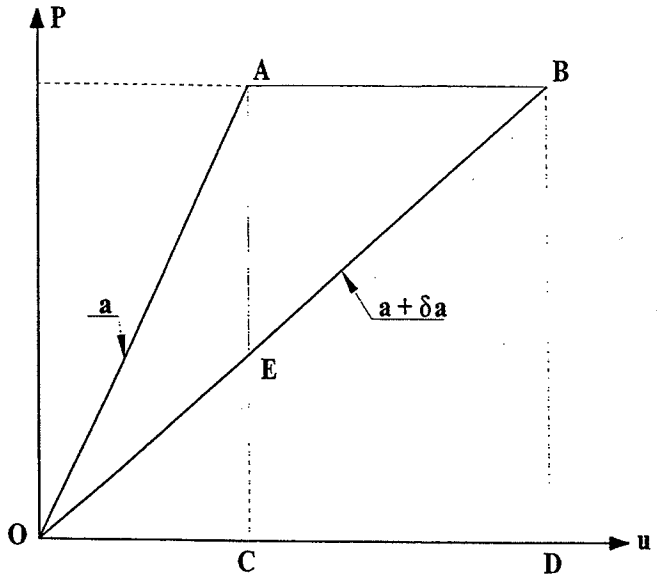

Figure 3.3 Elastic loading curves for crack lengths a and (a+δa).

For a given crack length a the load-deflection curve may be the straight line OA. The elastic energy is represented by the triangle OAC. If the crack length of the body is increased to a+δa, the stiffness will decrease. The load-deflection curve is now OB, and the elastic energy is represented by the area of the triangle OBD, which is larger than OAC. If in a load controlled experiment the body is loaded, when the crack length is a, the load-deflection curve will follow OA. If the crack at the load P is increased to a+δa, while the force is kept constant, the load-deflection curve will follow the line AB, which is parallel to the deflection axis u. The external work performed, is represented by the area of the rectangle ABDC. This work is partly used to increase the strain energy (area of triangle OBD minus area of triangle OAC) and partly to produce a crack extension δa.

By simple geometry it may be shown, that half the external work is used for increasing the strain energy and half the external work is used for crack extension.

If the body is unloaded from B it will follow the line BO. The area of the triangle OAB is the work used for crack extension. This work is dissipated, i.e. used for producing surface energy and heat.

If the body, after being taken from O to A, is kept under a constant deflection equal to that obtained in point A (deformation controlled experiment), and the

crack is extended from a to δa, the load will decrease. In the load-deflection curve this is represented by the vertical line AE. The strain energy is decreased, this time represented by the area OAC minus the area OEC. This strain energy is used for crack extension, and the area OAE represents the dissipated energy.

In both cases, a load controlled experiment and a deformation controlled experiment, the condition for crack growth are practically the same.

For a load controlled experiment we have

$$-\frac{\partial W}{\partial a} + G_F b = 0 \tag{3.10}$$

In this case $\partial W/\partial a$ is positive.

For a deformation controlled experiment the condition is governed by

$$\frac{\partial W}{\partial a} + G_F b = 0 \tag{3.11}$$

Here $\partial W/\partial a$ will be negative.

We return to these conditions in chapter 4.

Griffith sought to confirm his theory, formula (3.10-11), by applying it to the above described model for a crack. For this he took advantage of the ***Inglis*** **[13.1]** analysis of the plate with a narrow elliptical crack. From the ***Inglis*** solution of the stress and strain fields the elastic energy is readily computed for each volume element outside the crack. Integrating over the volume then gives for unit thickness and for plane stress:

$$W = \frac{\pi p^2 a^2}{E} \tag{3.12}$$

In this case W means the **increase** in strain energy because of the presence of the crack.

It is well known from classical continuum mechanics, that if the elastic energy W is calculated on the basis of a statically admissible stress field, the elastic energy will be higher or possibly equal to the true value. If the stress field is represented by some functions containing several parameters, the best value of the strain energy is obtained by minimizing the strain energy with respect to the parameters.

It will now be investigated, whether an extremely simple statically admissible stress field, completely disregarding the singularities at the crack tip, may be used, when finding the elastic energy for different crack sizes a.

We will go to the extreme by using stress fields from the plastic theory, see *Nielsen* **[84.1]**.

The plate considered, see Figure 3.4, is assumed loaded at infinity by a constant uniaxial stress p.

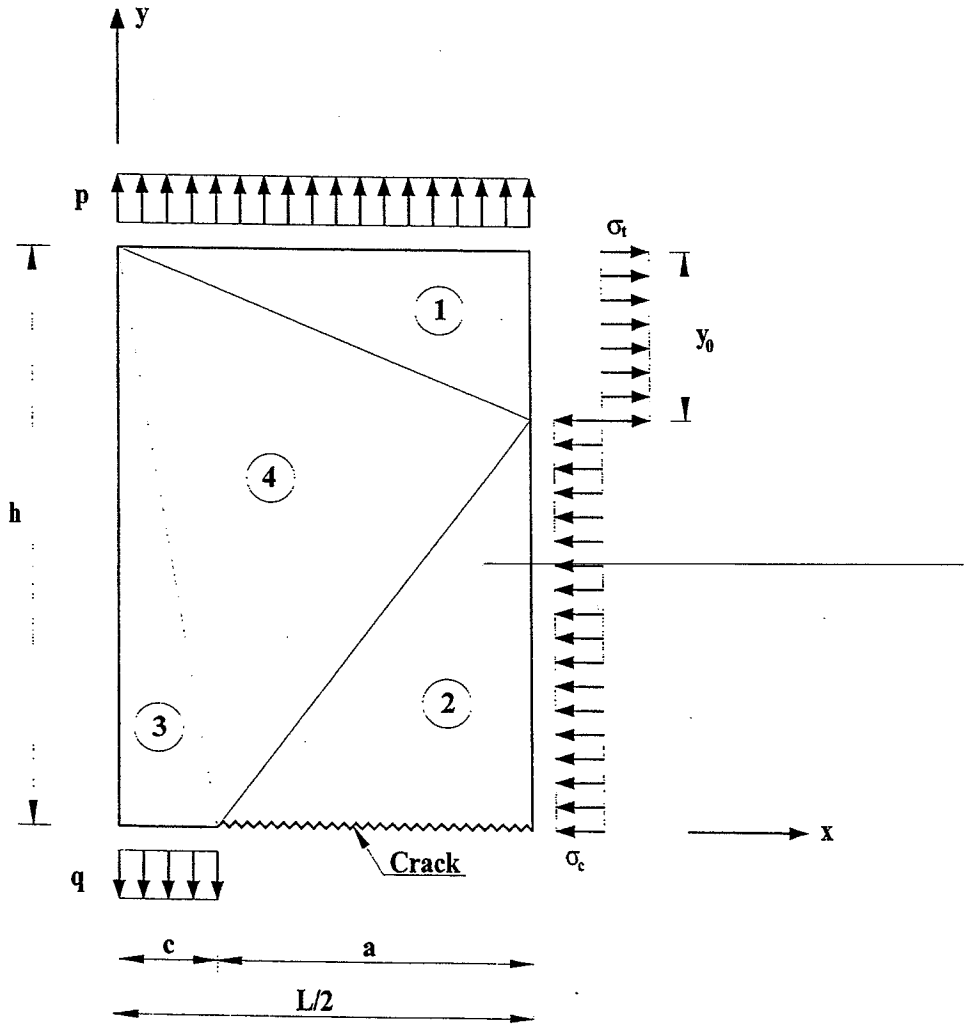

Figure 3.4 Discontinuous stress field in a plate.

The **increase** in strain energy due to the presence of the crack may be found by determining the elastic energy in the area (a+c)h reduced by the elastic energy in the same area for an uncracked specimen. The total increase will then be four times this energy difference.

Denoting the elastic energy in the area (a+c)h for a cracked plate U_{tot} we have

$$W = 4\left(U_{tot} - \frac{1}{2}\frac{p^2(a+c)h}{E}\right) \tag{3.13}$$

The best solution is obtained by an optimization of the energy with respect to the geometrical parameters h, c and y_0, see Figure 3.4. Thus we want to find

$$W = \min\left(4U_{tot} - \frac{2p^2(a+c)h}{E}\right) \tag{3.14}$$

As the energy W in this case is a function of several parameters a minimization of the function W is performed numerically.

Optimization of the function W (objective function) was performed by applying the chain rule of derivative calculus and thereby finding a stationary point of W. The numerical analysis was carried out by using a standard numerical algorithm which was able to perform nonlinear global optimization for functions with multiple variables. The results given in the following are *strong global minima* as the Hessian matrix, the symmetric matrix of second order derivatives is positive definite.

The computation of the energy U_{tot} will be given in the following.

The plate shown in Figure 3.4, is sub-divided into 4 parts each containing a homogeneous stress field separated by lines of discontinuity. In order to fulfill equilibrium conditions the bottom side of part 3 is assumed to act as a support with the stress (force pr. area) q. The bottom side of part 2 has the length a and is assumed stress free, ie. $\sigma_y = 0$.

For $x = 0.5L$ the moment is at a maximum, and the stress distribution is assumed to be rectangular corresponding to a normal compressive stress equal to σ_c and a normal tensile stress equal to σ_t.

External force equilibrium in the vertical direction gives directly

$$q = \frac{pL}{2c} \tag{3.15}$$

where c is the support length.

External moment equilibrium yields

$$\frac{1}{2}\sigma_c y_o th - \frac{1}{2}qct(L-c) + \frac{1}{8}ptL^2 = 0 \tag{3.16}$$

Inserting (3.15) results in the following expression for σ_t

$$\sigma_t = \frac{pL}{2hy_o}\left(\frac{1}{2}L-c\right) = \frac{pL}{2hy_o}a \tag{3.17}$$

where a is the crack length.

External force equilibrium in the horizontal direction gives

$$\sigma_c(h-y_o)t = \sigma_t y_o t \tag{3.18}$$

which means that

$$\sigma_c = \frac{pL}{2h(h-y_o}\left(\frac{1}{2}L-c\right) = \frac{pL}{2h(h-y_o)}a \tag{3.19}$$

Stresses in Part 1

The stress field in part 1, see Figure 3.5, is given as

$$\left.\begin{aligned} \sigma_x^1 &= \sigma_t = \frac{pL}{2hy_o}a \\ \sigma_y^1 &= p \\ \tau_{xy}^1 &= 0 \end{aligned}\right\} \qquad (3.20)$$

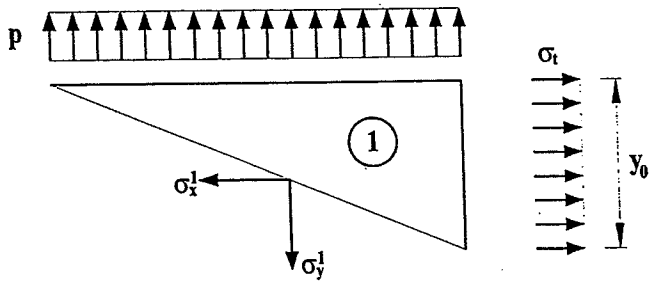

Figure 3.5 Force diagram for part 1.

Stresses in Part 2

The stress field in part 2, see Figure 3.6, is homogeneous, as it must be uniaxial, as one side is stress free. Therefore the stresses are directly given as

$$\left.\begin{aligned} \sigma_x^2 &= \sigma_c = -\frac{pL}{2h(h-y_o)}a \\ \sigma_y^2 &= 0 \\ \tau_{xy}^2 &= 0 \end{aligned}\right\} \qquad (3.21)$$

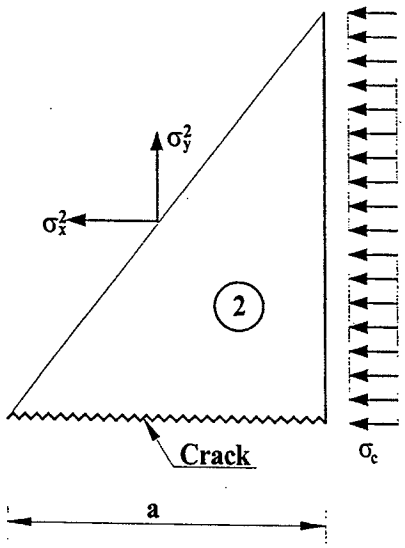

Figure 3.6 Force diagram for part 2.

Stresses in Part 3

In part 3 which is the triangle that contains the support on the bottom side and is stress free on the vertical side, see Figure 3.7, the three stress components are

$$\left.\begin{aligned} \sigma_x^3 &= 0 \\ \sigma_y^3 &= q = \frac{pL}{2c} \\ \tau_{xy}^3 &= 0 \end{aligned}\right\} \qquad (3.22)$$

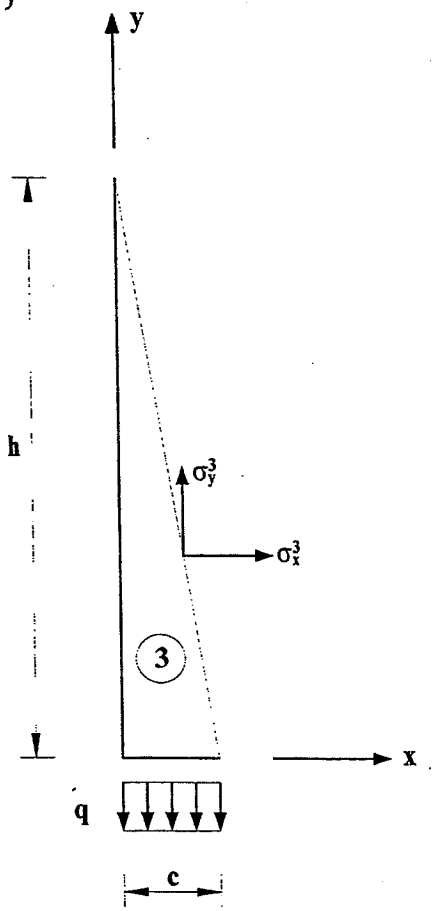

Figure 3.7 Force diagram for part 3.

Stresses in Part 4

In part 4 the stresses are determined by considering the stresses along a vertical line (σ_x, τ_{xy}) and a horizontal line (σ_y, τ_{yx}), see Figure 3.8.

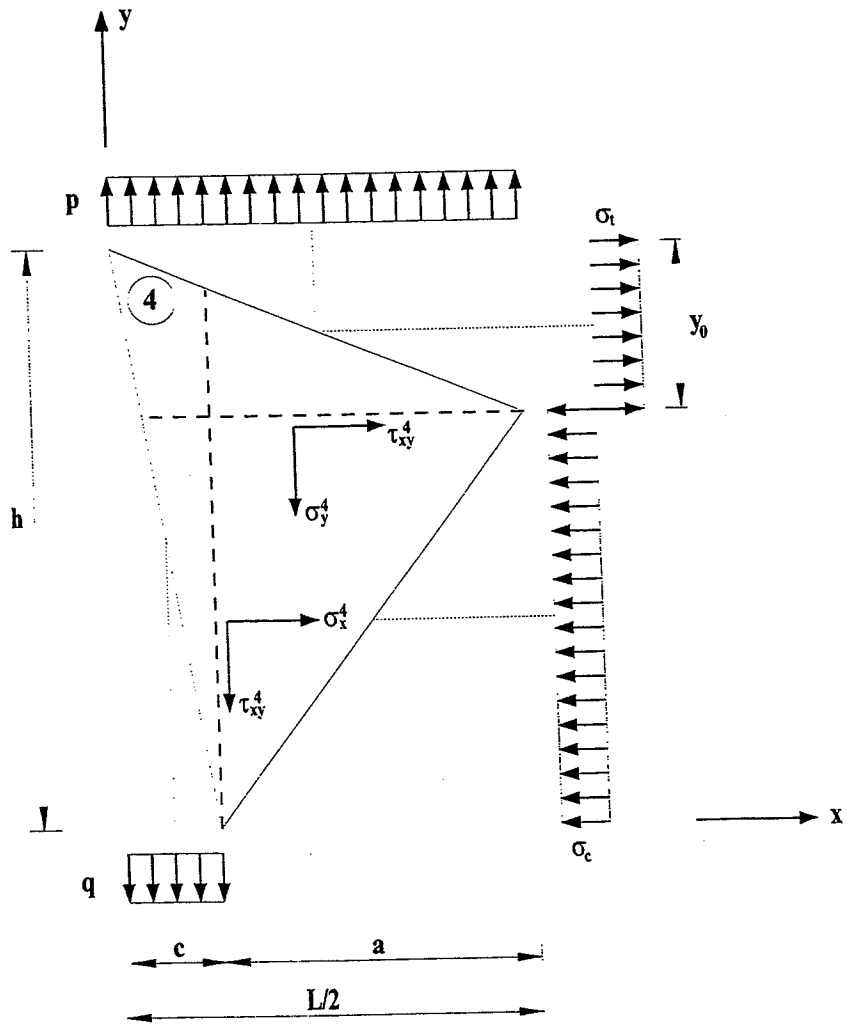

Figure 3.8 Force diagram for part 4.

In Figure 3.8 σ_x is determined by projecting on horizontal which yields

$$\sigma_x^4 = \frac{2\sigma_t y_o tc}{L} \tag{3.23}$$

Using (3.17) we find

$$\sigma_x^4 = -\frac{pLca}{h(hL-2y_oc)} \tag{3.24}$$

and

$$\tau_{xy}^4 = \frac{pLa}{hL-2y_oc} \tag{3.25}$$

In Figure 3.8 σ_y is determined by projecting on vertical which yields

$$\sigma_y^4 = \frac{pL(h-y_o)}{hL-2y_oc} \tag{3.26}$$

and

$$\tau_{xy}^4 = \frac{pLa}{hL-2y_oc} \tag{3.27}$$

Using the above given stresses for the different parts of the plate a calculation of the elastic energy for the cracked plate can be made by optimizing the parameters h, y_0 and c to render minimum energy according to (3.14).

A comparison of this result with the solution given by ***Inglis*** **[13.1]**, formula (3.12), i.e.

$$W = \frac{\pi p^2 a^2}{E} \tag{3.28}$$

can then be made.

The result of minimizing the energy of the solution with homogeneous stress fields is

$$W = \frac{7.7p^2a^2}{E} \tag{3.29}$$

This is more than twice the result of the exact solution given by (3.28).

It seems that it is too rough a method for an infinite plate to use only a local stress field around the crack. The problem has been studied in more detail in [98.1].

The conclusion is that for an infinite plate it is necessary to model the stress field in such a way that stresses can be carried further away from the crack and, what is more important, it is not required to model the singularity of the crack tip accurately. This means that an ordinary linear elastic finite element solution can be used.

3.4 Discussion

The result obtained in section 3.3 is extremely important from a practical point of view. The elastic energy may be calculated with an accuracy, which in many situations will be sufficient, by using statically admissible stress fields which completely disregards the stress singularities at the crack tip.

This means that ordinary finite element calculations may be used without taking specific notice of the mesh size near the crack tips. This method will be utilized in the following chapter, when determining stress intensity factors. It must of course be noted, that since stress intensity factors are the derivatives of the elastic energy, they may be less accurate than the energy itself.

Chapter 4

Crack Growth in Concrete

4.1 Introduction

4.1.1 General

The fracture and cracking of hardened cement paste and concrete has been studied at least since ***Richart et. al.*** **[28.1]** in 1928 investigated the development of cracks in concrete under compressive loading. Since then a great deal of work has been carried out concerning the development of crack patterns in concrete under applied load or from thermal and shrinkage stresses.

The energy balance concept of fracture was proposed by ***Griffith*** **[21.1]** in 1921. After World War II a great deal of work was done for metal structures starting with the work of ***Irwin*** **[60.1]**. But it took almost forty years, before the concept of fracture mechanics was applied to cementitious materials like concrete, and there is still some controversy as to the applicability of fracture mechanics to these materials.

The work presented in this thesis was inspired by the initial research performed by ***M. P. Nielsen*** on the behaviour of crack growth in monotonic and cyclic

loading, see **[90.1]**.

The main purpose of this chapter is to describe some of the potentialities of this work when applied to concrete.

In order to investigate crack growth in plain concrete, a fracture mechanical model, see **[90.1]**, based on an energy balance criterion is presented and compared with test results.

Three point bending tests on plain concrete beams have been performed at the Department of Structural Engineering, Technical University of Denmark, see chapter 5 and ***Olsen*** **[94.1]**. As a result the experimental values of load-deflection curves have been established, and they will be compared with the results from the theoretical model in this thesis.

Three separate investigations will be reported.

First a comparison between experimental and theoretical values of load-deflection curves for different compressive strength levels will be described. Four different compressive strength levels are tested, 30 MPa, 50 MPa, 70 MPa and 100 MPa.

Secondly a comparison will be made regarding the capability of the model to predict load-deflection curves when varying the notch-depth ratio (a/h) of the beams used. The notch sensitivity is tested using three different notch - depth ratios, namely 0.1, 0.25 and 0.5 .

In an attempt to show the correspondence between theory and experimental values, a third comparison is made, where test beams with different aggregate sizes are used. Two compressive strength levels are examined; 30 MPa and 100 MPa. For each strength level the maximum aggregate size d_{max} takes the values 0 mm (cement paste), 4 mm, 8 mm and 16 mm.

4.2 The Energy Balance Crack Growth Formula

4.2.1 Introduction

Application of fracture mechanics to concrete can be traced back to ***Kaplan*** **[61.1]**. Classic fracture mechanics, which has been developed mainly for analyzing crack propagation in metals, yields quite disputable results, when applied to concrete.
In this thesis a fracture mechanical model based on an energy balance criterion is presented. The model has been used to predict crack growth in metals subjected to dynamic loading, see **[94.3]**, and will in this thesis be compared with three point bending tests on plain concrete beams. As fracture mechanics studies indicate that structural behaviour depends not only on strength, but also on fracture resistance and dimensions as well, the model will be compared with test beams where several parameters such as beam dimensions, compressive strength of concrete and aggregate size are varied.
The fracture mechanical model introduced has been developed by ***M. P. Nielsen***, see **[90.1]** and is based on energy balance.
In this section a short description of the energy criterion proposed by ***Griffith*** will be given together with a review of the *Energy Balance Crack Propagation Formula*.

4.2.2 The Energy Criterion

A. A. Griffith is credited for contributing much of the theoretical foundations for the study of fracture in cracked solids. ***Griffith's*** two pioneering papers **[21.1]** and **[24.1]**, published some 70 years ago, contained his proposed explanation of fracture phenomena in terms of the energy required for crack propagation. His basic assumption was that unstable crack propagation takes place, if an increment of crack growth results in more stored energy being released, than is absorbed by the development of a new crack surface.

As an initial stage we consider, as did ***Griffith***, a system containing an elastic body with an internal crack of length a, see Figure 4.1. The body is subjected to loads applied at the boundary of the element.

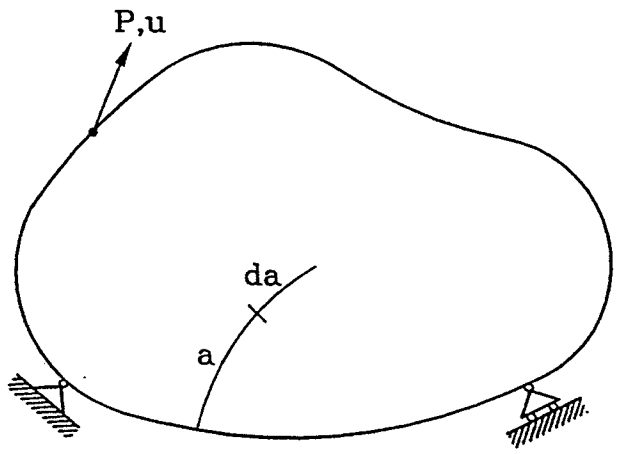

Figure 4.1 Cracked elastic body.

Griffith **[21.1]** sought the configuration which minimized the total energy of the system, thus resulting the system to be in a state of equilibrium and the crack on the verge of extension.

The change of the total energy of the system denoted U_s can be written in differential form as:

$$\delta U_s = \delta(-U_P + W) + \delta D \tag{4.1}$$

As seen from the above equation the total energy change contains three different energy terms, which changes as a result of a crack formation. U_P is the work done by the applied loads, when the cracked body undergoes a change in

displacement. An increase in this term would for a conservative system be equal to a corresponding decrease in potential energy. W is the elastic energy of the body, also called the strain energy, which is highly dependent on the geometry (crack extension).

These two terms in combination is the amount of energy, that can be used for crack extension. The formation of new crack surface creates a free surface energy D. In other words, the energy balance equation (4.1) may be considered as being comprised of two parts, one part $\delta(-U_P + W)$ is the mechanical energy which favours crack extension, while the second part δD opposes it.

This is the energy balance concept presented by ***Griffith***, and the equilibrium requirement

$$\frac{\partial U_s}{\partial a} = 0 \tag{4.2}$$

governs the condition for crack growth, which then becomes

$$-\frac{\partial(-U_P + W)}{\partial a} = \frac{\partial D}{\partial a} \tag{4.3}$$

It is assumed, that all stored energy is used for creating crack extension. Normally the surface energy is only a small part of energy required to form a crack. In materials capable of yielding, the plastic work is the major part. The total energy necessary for creating a new unit area crack surface is denoted G_F, G_F is termed the fracture energy. If the thickness of the body is b, the right hand side of (4.3) may be written

$$\frac{\partial D}{\partial a} = G_F b \tag{4.4}$$

Equation (4.3) may thus be expressed as

$$-\frac{\partial(-U_P + W)}{\partial a} = G_F b \tag{4.5}$$

The first term $-U_P + W$ is the potential energy, E_P, of the system, with the crack length considered. Therefore (4.5) may be written

$$\frac{\partial E_P}{\partial a} + G_F b = 0 \tag{4.6}$$

This is the energy balance equation for crack growth as stipulated in ***Griffith*** **[21.1]** and **[24.1]**.

For a load controlled system with only one force P, the potential energy in an equilibrium configuration is $E_P = -\frac{1}{2}Pu = -W$. Formula (4.6) reads in this case

$$-\frac{\partial W}{\partial a} + G_F b = 0 \tag{4.7}$$

For a load controlled system the strain energy W is increasing for increasing crack length a.

For a displacement controlled system with only one displacement parameter the potential energy in an equilibrium configuration is $E_P = W$. In this case (4.6) reads

$$\frac{\partial W}{\partial a} + G_F b = 0 \tag{4.8}$$

Here W is decreasing when the crack length a is increasing.

4.2.3 Irwins Crack Length Correction

As is well known from linear elastic fracture mechanics, the normal stress σ_y along the axis of a sharp crack is determined by the term:

$$\sigma_y = \frac{K_I}{\sqrt{2\pi r}} \tag{4.9}$$

Here K_I is the stress intensity factor, and r is the distance from the crack.
If at some distance $r=a_y$ from the crack tip the stress σ_y equals the yield stress f_y, we have according to (4.9):

$$a_y = \frac{1}{2\pi}\frac{K_I^2}{f_y^2} \tag{4.10}$$

The stress resultant of the σ_y-stresses per unit thickness along the distance a_y is

$$\int_0^{a_y} \frac{K_I}{\sqrt{2\pi r}}\,dr = \sqrt{\frac{2}{\pi}}\,K_I\sqrt{a_y} = \frac{1}{\pi}\frac{K_I^2}{f_y} \tag{4.11}$$

This is twice the value of the resultant of the constant stress f_y along a_y.
This led ***Irwin*** **[60.1]** to suggest, that if there is a plastic zone in the crack tip, it must have a length of $2a_y$. Half this length he considered as an additional crack length, which must be added to the real crack length a.
The additional term:

$$l_e = a_y = \frac{1}{2\pi}\frac{K_I^2}{f_y^2} \tag{4.12}$$

is called the effective crack length term wich is shown in Figure 4.2. The effective crack length is:

$$a_{eff} = a + l_e \tag{4.13}$$

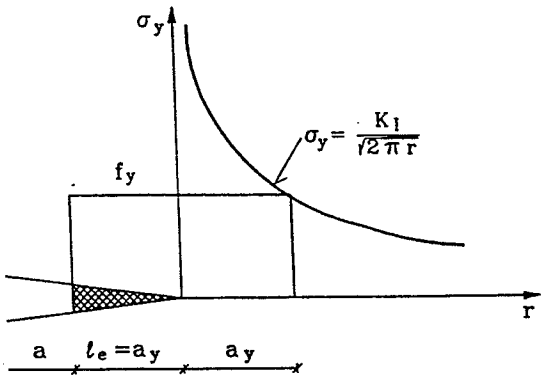

Figure 4.2 Effective crack length at a crack tip with plastic yielding.

In **[90.1]** l_e has been determined in an alternative way by some approximate energy considerations.
For a material with yield strength f_y and tensile strength f_t it was shown, that l_e may be put equal to:

$$l_e = a_p' = \frac{1}{2\pi}\frac{K_I^2}{f_y f_t} \tag{4.14}$$

where a_p' is the length of the fracture zone, see Figure 4.3. The length of the plastic zone, a_y, may be calculated by formula (4.10).

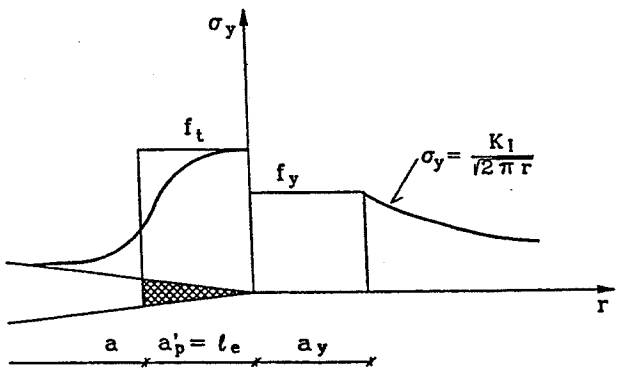

Figure 4.3 Approximate stress field around the crack tip of an elastic-quasi plastic material.

For an elastic-brittle material like concrete it was shown in **[90.1]**, that l_e may be put equal to:

$$l_e = 0.4\, a_p' = 0.4 \frac{K_I^2}{\pi f_t^2} \qquad (4.15)$$

The stresses at the crack tip in an elastic-brittle material is illustrated in Figure 4.4.

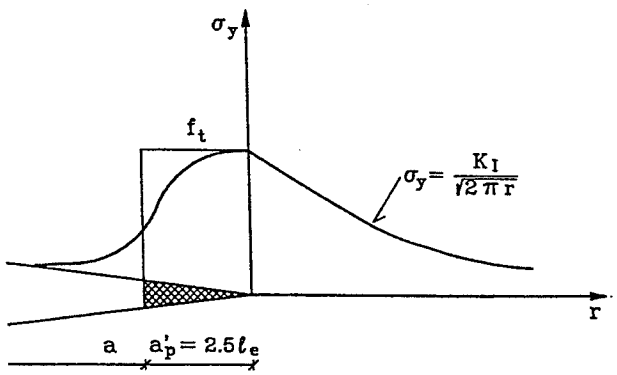

Figure 4.4 Approximate stress field around the crack tip of an elastic-brittle material.

4.2.4 Crack Growth Determined by Energy Balance

Consider first a load controlled system. Taking into account the effective crack length l_e in the energy balance equation formula (4.5) becomes

$$\frac{\partial W}{\partial a}da + \frac{\partial W}{\partial a}dl_e - P\frac{\partial u}{\partial a}da - P\frac{\partial u}{\partial a}dl_e + G_F b da = 0 \qquad (4.16)$$

having put $\partial U_P/\partial a = P\partial u/\partial a$. Rearranging the terms gives us

$$\left(\frac{\partial W}{\partial a} - P\frac{\partial u}{\partial a}\right)da + \left(\frac{\partial W}{\partial a} - P\frac{\partial u}{\partial a}\right)dl_e + G_F b da = 0 \qquad (4.17)$$

Solving for da yields

$$da = \frac{-\frac{\partial(W - Pu)}{\partial a}dl_e}{G_F b + \frac{\partial(W - Pu)}{\partial a}} \qquad (4.18)$$

In the case of a load controlled problem we have $\partial(W\text{-}Pu)/\partial a$ equals $-\partial W/\partial a$, see section 4.2.2, leading to

$$da = \frac{\frac{\partial W}{\partial a}dl_e}{G_F b - \frac{\partial W}{\partial a}} \qquad (4.19)$$

If crack growth has to be possible, dl_e must be positive. When P is the leading parameter, l_e is a function of both load P and crack length a, i.e.

$$dl_e = \frac{\partial l_e}{\partial P}dP + \frac{\partial l_e}{\partial a}da \qquad (4.20)$$

Inserting formula (4.20) into (4.19) gives us

$$da = \frac{\frac{\partial W}{\partial a}\left(\frac{\partial l_e}{\partial P}dP + \frac{\partial l_e}{\partial a}da\right)}{G_F b - \frac{\partial W}{\partial a}} \tag{4.21}$$

After some alterations the *Energy Balance Crack Propagation Formula* in a load controlled system is given by

$$\frac{da}{dP} = \frac{\frac{\partial W}{\partial a}\frac{\partial l_e}{\partial P}}{G_F b - \frac{\partial W}{\partial a}\left(1 + \frac{\partial l_e}{\partial a}\right)} \tag{4.22}$$

The derivative $\partial W/\partial a$ should be taken at $a+l_e$, while $\partial l_e/\partial u$ and $\partial l_e/\partial a$ may be taken at a.

For a displacement controlled test the crack length a and the deformation u are independent variables. By using the same procedure as for the loading controlled system and by taking into account the correction l_e of the crack length a, we get the *Energy Balance Crack Propagation Formula* for a displacement controlled system.

$$\frac{da}{du} = \frac{-\frac{\partial W}{\partial a}\frac{\partial l_e}{\partial u}}{G_F b + \frac{\partial W}{\partial a}\left(1 + \frac{\partial l_e}{\partial a}\right)} \tag{4.23}$$

The derivative $\partial W/\partial a$ should be taken at $a+l_e$, while $\partial l_e/\partial u$ and $\partial l_e/\partial a$ may be taken at a.

4.3 Numerical Determination of Crack Growth

4.3.1 Introduction

In this section the use of the crack propagation formula will be described. The theory depends upon the change of elastic strain energy $\partial W/\partial a$ with the crack length a, which can be determined on the basis of finite element methods (FEM). The method will be described in section 4.3.2.

The advantage of the new theory compared to the majority of other theories of fracture mechanics in concrete, is that the FEM calculation is based on simple linear elastic calculations, which demand very little computation time. The non-linear behaviour is taken into account in the crack propagation formula.

The crack propagation formula is a first order differential equation. In section 4.3.3 a numerical method to solve the differential equation will be presented. In section 4.3.4 the basic principles of predicting crack propagation using the new theory will be described, and a few relevant examples will be shown. The parameters in the formula will be discussed and their influence in general will be illustrated by numerical examples.

4.3.2 The Finite Element Method for the Determination of Energy Change

As mentioned earlier the crack propagation formula is based on an energy balance criterion. Therefore, it is necessary to determine the elastic energy in the actual cracked model (beam, disk etc.) for any loading condition.

The elastic strain energy W can be determined by means of a finite element method and thereby be expressed as a function of the force P or the displacement u and the crack length a.

In the case where one wishes to determine the load-deflection curve of a concrete beam, it will be convenient to express the energy W by the displacement u, because the numerical solution of the crack growth formula becomes more convenient, if the controlling parameter is the displacement.

Therefore we have:

$$W = W(u,a) \tag{4.24}$$

It is important to be aware of the fact, that the crack propagation formula takes into account the plastic behavior near the crack tip, although it is based on elastic energy W, as described in section 4.3.3.

It is common knowledge, that the elastic strain energy is proportional to the square of the displacement. Therefore, if we can determine W for a constant displacement at any crack length, we may express the energy as:

$$W(u,a) = \left(\frac{u}{u_0}\right)^2 W_{const\,u}(a) \tag{4.25}$$

where u_0 is the value of the displacement, for which $W_{const\,u}$ has been determined.

It is also known, that the elastic strain energy is proportional to the Youngs modulus E, i.e.

$$W(u,a) = \left(\frac{u}{u_0}\right)^2 \left(\frac{E}{E_0}\right) W_{const\,E,u}(a) \tag{4.26}$$

The problem is now reduced to determining the elastic energy as a function of the crack length - everything depending only on the model geometry.

Very simple finite element models can be used to determine this function, see chapter 3. The problem may be solved for instance by taking twenty beams with the same geometry, except for the length of the crack, and subject all the beams to a constant displacement and determine the force P in each case.

The elastic strain energy in cases with only one load is given by $W = \frac{1}{2}Pu$, P being the load and u the deflection in the direction of the load. Therefore in the case of three point bending (see Figure 4.5) the elastic strain energy is given by:

$$W = \frac{1}{2}Pu \tag{4.27}$$

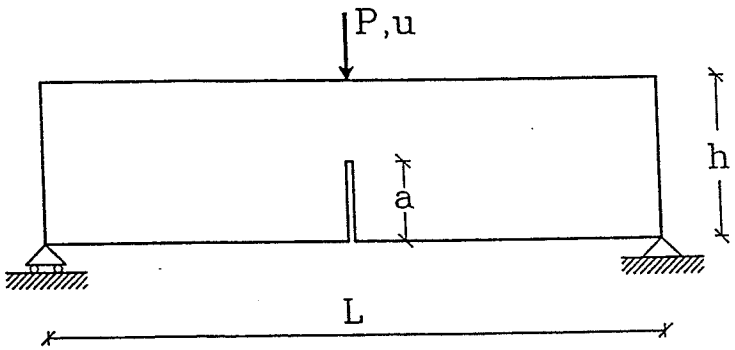

Figure 4.5 Notched beam in three point bending.

When the elastic strain energy is determined for each crack length, a simple polynomial fit can be made, which can be used to determine the elastic strain energy analytically for constant displacement at any crack length. For increasing crack length, the energy curve (for constant displacement) decreases as shown in Figure 4.6.

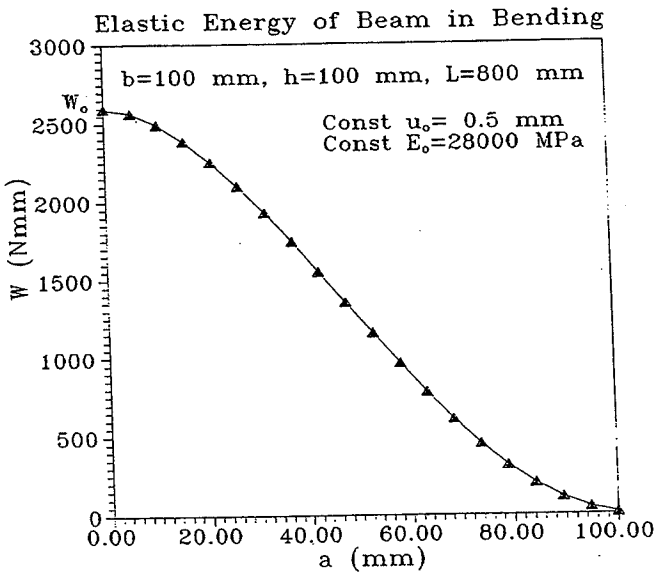

Figure 4.6 Elastic strain energy for three point bending under constant displacement.

In Figure 4.6 W_0 is the strain energy related to a non-cracked beam.

When one is dealing with finite element methods, it is customary to use a relatively fine mesh, especially near the crack tip, because of large stress gradients in this area. This is partly in contradiction to the findings in chapter 3. It has been found, that when the number of elements shown in Figure 4.7 was doubled, the change in W was negligible in accordance with the results given in chapter 3.

The element mesh shown in Figure 4.7 was used.

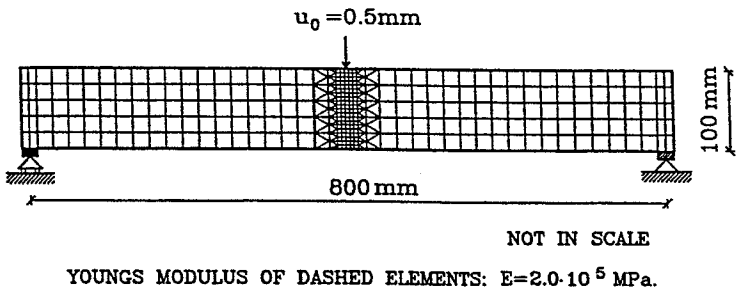

Figure 4.7 FEM model used in the calculation.

4.3.3 Runge Kutta method

The crack growth formula is a first order differential equation, which is difficult or impossible to solve analytically. Therefore, a numerical method to solve the equation will be introduced in this section.

Mathematically the problem is to solve an equation of the form:

$$\frac{dy}{dx} = f(x,y) \tag{4.28}$$

A simple way perform this numerically if the initial conditions are given in the form $y=y_o$ for $x=x_o$, is to choose a small step length h, calculate dy/dx at $(x,y)=(x_o,y_o)$ by (4.28) and then put the increment Δy at $x=x_o$ equal to $f(x_o,y_o)h$. Then $x=x_o+h$ is treated the same way and so on. This is called Euler's method:

$$y_{n+1} = y_n + hf(x_n,y_n) \tag{4.29}$$

The principle is illustrated in Figure 4.8.

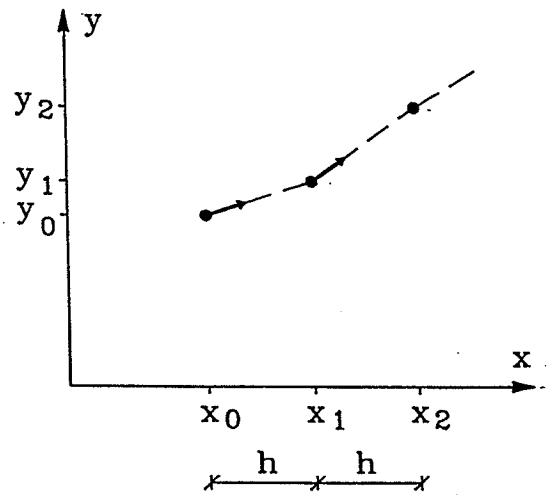

Figure 4.8 Euler's method.

The method, however, can easily be improved by using one or more derivatives, for instance the derivative at the midpoint of the interval as well as at the starting point to determine the next function value y_{n+1}. In Runge Kuttas second order method, also called the midpoint method, one uses the derivatives in the midpoint to calculate the function value by the following procedure:

$$\begin{aligned} k_1 &= f(x_n, y_n) \\ k_2 &= f\left(x_n + \frac{h}{2}, y_n + \frac{h}{2}k_1\right) \\ y_{n+1} &= y_n + hk_2 \end{aligned} \tag{4.30}$$

The principle is illustrated in Figure 4.9.

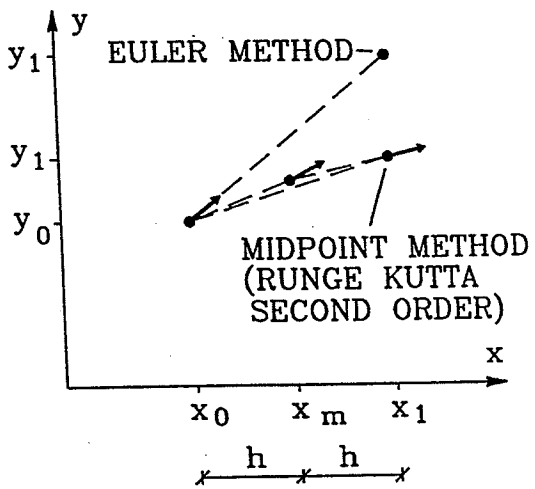

Figure 4.9 Runge Kutta second order method.

This will increase the accuracy of the method relatively to the step length h compared to Eulers method.

The number of derivatives to be included in the method is a balance between the number of terms in the method, and the accuracy obtained relatively to the step length h.

The most often used method is the "fourth order Runge Kutta method". It gives a high accuracy, though the step length h may be taken relatively large, and a higher number of terms does not lead to significant improvements.

In the fourth order Runge Kutta method the function value y_{n+1} is determined on the basis of four derivatives:

$$y_{n+1} = y_n + \frac{h}{6}(k_1 + 2k_2 + 2k_3 + k_4) \tag{4.31}$$

where:

$$\begin{aligned} k_1 &= f(x_n, y_n) \\ k_2 &= f(x_n + \frac{h}{2}, y_n + \frac{h}{2}k_1) \\ k_3 &= f(x_n + \frac{h}{2}, y_n + \frac{h}{2}k_2) \\ k_4 &= f(x_n + h, y_n + hk_3) \end{aligned} \tag{4.32}$$

In our case the problem is to solve the differential equation:

$$\frac{da}{du} = f(u,a) \tag{4.33}$$

where a is the crack length, and u is the displacement. f(u,a) is the right hand side of the crack propagation formula (see formula (4.23) and note that $\partial W/\partial a$ is a function of u and a).
The start values will be:

$$\mathbf{u_0 = u_{min}}$$
$$\mathbf{a_0 = a(u_0) = \text{start notch length}}$$

and the step length is:

$$\mathbf{h = du = (u_{max} - u_{min})/\ \text{number of steps}}$$

The following Pascal routine solves the crack propagation formula by means of the Runge Kutta fourth order method.

```
procedure rungekutta;
begin
    k[1]:=1;
    j:=1;
      for i:=1 to 4 do
      begin
            m:=(trunc(i/2))/2; (* calculate 0,½,½,1 when i=1 to 4 *)
            ru:=u+m*du;
            ra:=a+m*du*k[j];
            crackformula;  (* procedure which calculate da/du=f(ru,ra) *)
            k[i]:=dadu;
            j:=i;
       end;
     anew:=a+(du/6)*(k[1]+2*k[2]+2*k[3]+k[4]);
     da:=anew-a;
     a:=anew;
end;
```

This procedure can be used to solve any kind of a 1st order differential equation, if there is a convergent solution. It is of course necessary to provide the procedure with a 'write to file' command so that the calculated data are saved.

The procedure to calculate da/du is given below:

```
procedure crackformula;
begin
   le:=l(ru,ra,b,w,fy,ft);            (* function call *)
   dledu:=dle(ru,ra,b,w,fy,ft);       (* function call *)
   dleda:=dla(ru,ra,b,w,fy,ft);       (* function call *)
   dwda:=dwda(ru,ra+le,b,w);          (* function call *)
   dadu:= (dwda*dledu) / (gf*b-(dwda+(dwda*dleda)));
end;
```

The crack length correction l_e may be calculated by the formulas given in section 4.2.3. All the other parameters are calculated on the basis of the elastic strain energy of the cracked body, see section 4.3.2

4.3.4 Crack Growth Determined by the Energy Balance Crack Propagation Formula.

Before comparing the test results with theory, it would be appropriate briefly to describe the load-deflection curve. As usual the load-deflection curve is given by the force P as a function of the displacement u. In Figure 4.10 two typical load-deflection curves are presented:

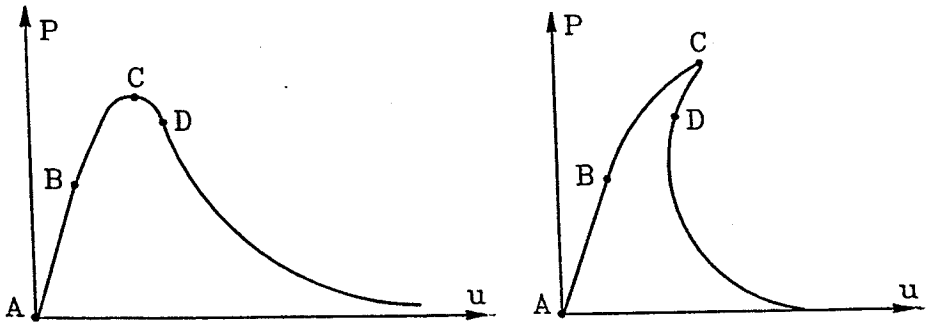

Figure 4.10 Typical load-deflection curves.

The curve to the left is the most common load-deflection curve. The curve to the right shows the phenomenon called snap back.

In the range from A to B the curves are linear elastic. In this range no crack has developed. From B to C micro cracks are developed, and a so-called process zone appears. Therefore the curve is bending off, and the stiffness of the system is slightly decreasing. With further loading micro crack formation will be progressing. The initial slope depends on Youngs modulus E and the start notch length a_0. Point C, the peak value, represents the load carrying capacity, which depends on the tensile strength f_t and the start notch length. After point D the specimen shows visible cracks. The descending branch depends on several parameters.

When the process zone reaches the top of the beam, the assumptions of the crack growth formula ceases to be valid. Therefore, only a part of the descending tail can be calculated by the formula.

To calculate the load-deflection curve using the crack propagation formula, several parameters have to be known. The advantage of the formula is, that these parameters are well known geometrical and mechanical parameters, which can be determined by simple statical tests.

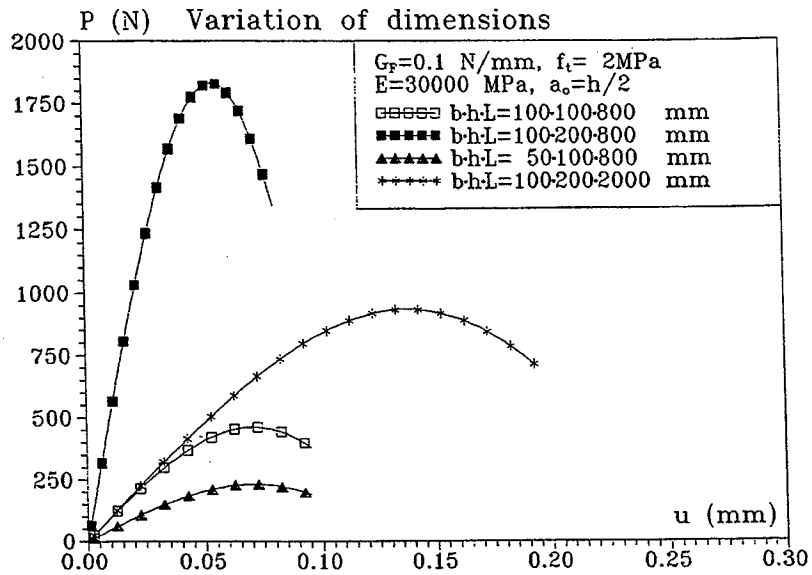

Figure 4.12 Load-deflection curve for various dimensions.

If instead we change the mechanical parameters E, f_t, G_F and the start notch length a_0, the calculated load-deflection curve will change as shown in Figure 4.13.

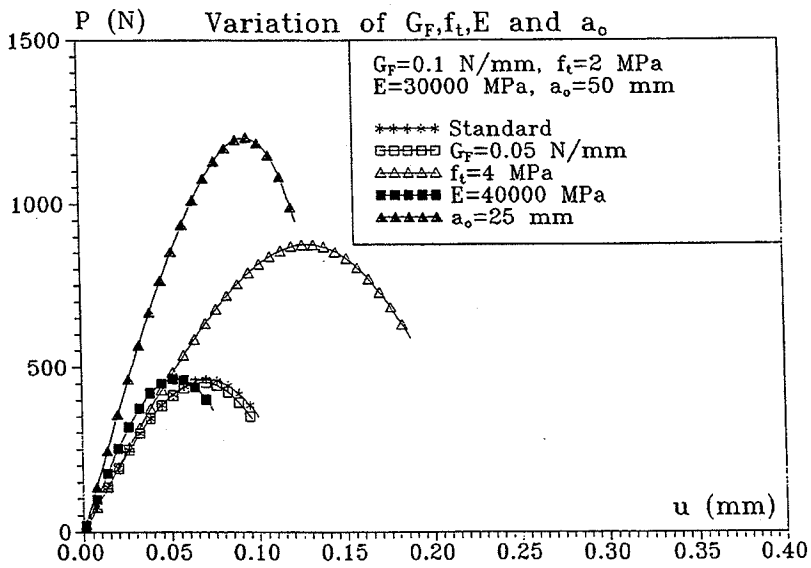

Figure 4.13 Load-deflection curves for different mechanical parameters.

One of the curves is the reference curve, and in the four others one of the parameters have been changed. In the case where the start notch length has been changed we see a large effect on the peak value, which is quite natural because a decrease in the start notch length will increase the fracture area of the beam and thereby increase the strength.

In the tests the start notch length as well as the dimensions of the beam were fixed parameters, and therefore can not be used to manipulate the load-deflection curve to fit the test results. This can only be done by changing the three mechanical parameters E, f_t and G_F

The Youngs modulus changes the slope from start point to peak, but the influence on the peak value is negligible. The tensile strength, on the contrary, changes the value at the peak, but does not change the slope.

The fracture energy G_F may be defined by:

$$G_F = \frac{\text{external energy supplied}}{\text{area of cracked surface}}$$
$$\Downarrow \qquad (4.34)$$
$$G_F = \frac{\Delta A}{b \cdot \Delta a}$$

Here ΔA represents the area shown in Figure 4.15. In Figure 4.14 Δa is the fully developed part of the crack, i.e. the total crack length minus the crack correction length l_e:

$$\Delta a = a_{eff} - l_e - a_o \qquad (4.35)$$

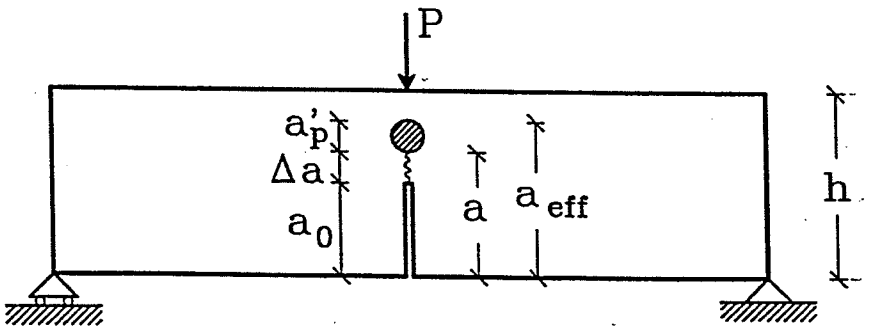

Figure 4.14 Beam with propagating crack.

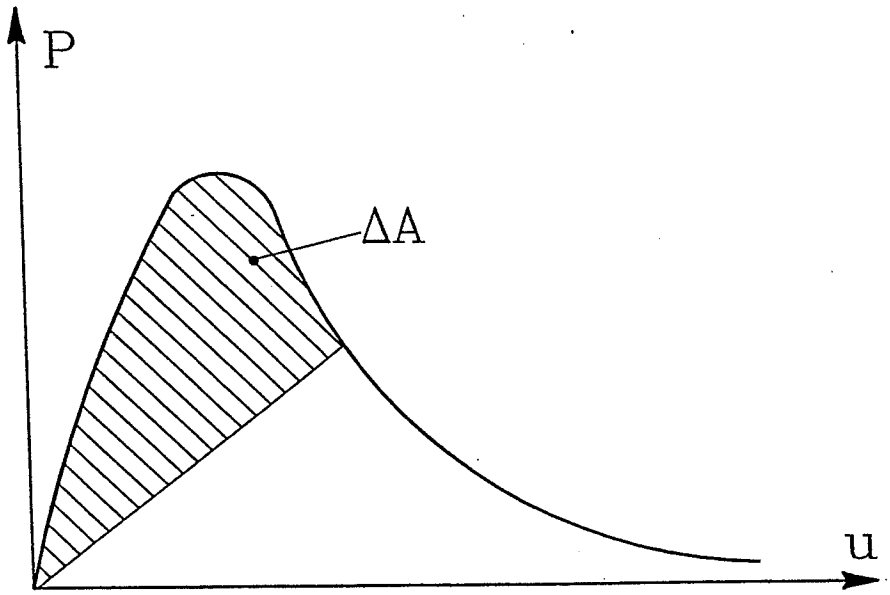

Figure 4.15 Definition of the area ΔA from the load-deflection curve.

As shown in section 4.2.3 the crack length correction l_e may be calculated by formula (4.15): $l_e = 0.4a_p' = 0.4K_I^2/\pi f_t^2$.

The process zone is approximately $a_p' \approx 2.5l_e$. If the process zone is large, a change in G_F will not affect the peak value of the load-deflection curve significantly. If the process zone, on the contrary, is small compared to the crack length, a change in G_F will have a noticeable effect on the peak value. This may be traced back to the fact, that G_F influences the ratio between the length of the process zone and the crack length a at peak. If in a calculation G_F is set to a small value, then a/l_e is large, i.e. the beam behaves in a brittle manner. If G_F is increased, l_e (and a_p' respectively) will increase until a certain point determined by the beam depth. This has the effect on the load-deflection curve, that if G_F is increased, the peak value approaches asymptotically an upper limit as shown in Figure 4.16. The material behaves more ductile, and the load carrying capacity approaches an upper plastic limit, as will be discussed later in this section.

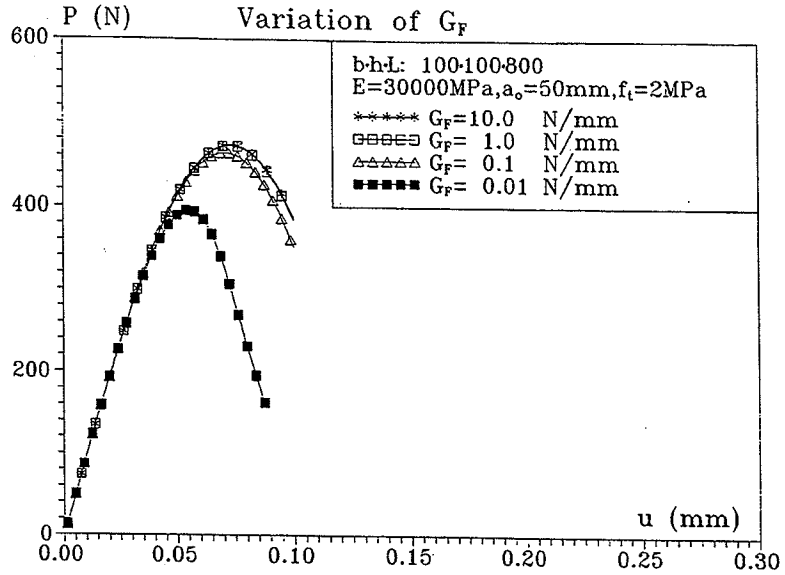

Figure 4.16 Increasing G_F gives asymptotical upper limit of the load carrying capacity.

In some special cases the phenomenon called snap back arises. To accomplish this effect, one has to change the mechanical parameters in the following way:

- the tensile strength f_t is increased
- E, G_F or a_0 is decreased.

Snap back arises after the peak value has been reached. If snap back is near the peak, the numerical calculations may not reach the peak value. This can be avoided by decreasing the step length in the numerical calculation.

When snap back arises the calculation terminates, because the denominator in the crack propagation formula approaches zero. It is, however, possible to continue the calculations by using the inverse crack propagation formula, after the snap back point is reached, see formula (4.36).

$$\frac{du}{da} = \frac{G_F b + \frac{\partial W}{\partial a}\left(1 + \frac{\partial l_e}{\partial a}\right)}{-\frac{\partial W}{\partial a}\frac{\partial l_e}{\partial u}} \tag{4.36}$$

In Figure 4.17 a typical snap back calculation of the load-deflection curve is shown.

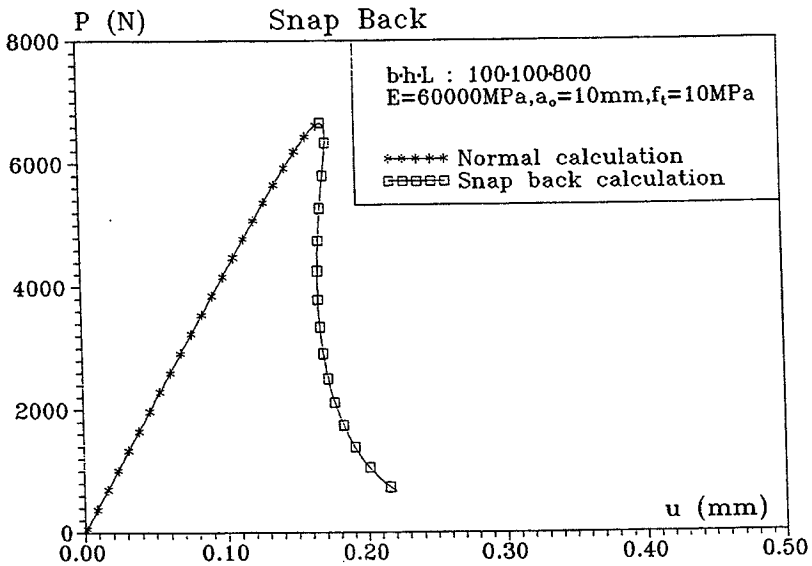

Figure 4.17 Calculated snap back behaviour.

When a load-deflection curve has been calculated, it is possible to check the energy balance by calculating the area ΔA in Figure 4.15.

Consider as an example the following standard values of the parameters: E=30000 MPa, f_t=2 MPa, a_0=50 mm, b·h·L=100·100·800 mm^3. Let us separately vary the values of G_F, f_t, E and a_0. The results are shown in Table 4.1. ΔA is determined using a numerical integration formula. Δa is found by solving numerically the energy crack propagation formula. It is observed, that the results show good agreement except for a small numerical error, which can be eliminated by decreasing the increment step.

	ΔA (Nmm)	Δa (mm)	$G_F=\Delta A/b\cdot\Delta a$	G_F (theory)
Standard	16.30	1.64	0.0993	0.1
G_F=0.05N/mm	17.69	3.58	0.0494	0.05
f_t=4 MPa	76.50	7.71	0.0992	0.1
E=40000 MPa	12.78	1.29	0.0989	0.1
a_o=25 mm	57.91	5.86	0.0989	0.1

Table 4.1 Verification of energy balance.

Since the theory determines the load carrying capacity of any structure under the conditions described, it will be able to predict size effects, i.e. it will be able to give the load carrying capacity as a function of the absolute value of any geometrical parameter D characterizing the size of the structure. As a measure of brittleness we take the common value:

$$B = \frac{f_t^2 D}{G_F E} \tag{4.37}$$

In our case we put D = h. Formula (4.37) reflects the fact, that the larger the strength f_t and the size D the more brittle the structure. The smaller the value of G_F or E the more brittle the structure. Large values of B belong to perfectly brittle structures.

For a perfectly brittle structure the load carrying capacity may be determined by Linear Elastic Fracture Mechanics (LEFM), i.e. by setting:

$$K_I = K_{IC} = \sqrt{G_F E} \tag{4.38}$$

where K_{IC} is the critical value of the stress intensity factor, the fracture toughness. If we solve the crack propagation formula for increasing values of B by decreasing G_F, the load carrying capacity P_{peak} will be decreasing. The value of K_I^2/E at the peak should, according to (4.38), approach the G_F value assumed in the calculation, if the results approach the load carrying capacity of LEFM.

The results of such a calculation are shown in Table 4.3, where the standard values used in the calculations are given in Table 4.2. We observe, that the value of K_I^2/E approaches the value of G_F for increasing brittleness.

The load carrying capacity has been given in dimensionless form as the Navier stress σ_o along the depth $h-a_o$ divided by f_t, i.e:

$$\frac{\sigma_o}{f_t} = \frac{3}{2}\frac{P_{peak}L}{b(h-a_0)^2}\frac{1}{f_t} \tag{4.39}$$

G_F (N/mm)	E (MPa)	f_t (MPa)	a_o (mm)	b·h·L (mm)
Varies	30000	2	50	100·100·800

Table 4.2 Standard values used in formula (4.39).

No	G_F (N/mm)	B	P_{peak} (N)	σ_o/f_t	K_I^2/E	l_e (mm)
g1	10000	1.33E-6	529.7	1.27	4.3E-3	11
g2	100	1.33E-4	529.7	1.27	4.3E-3	11
g3	1	1.33E-2	528.3	1.26	4.2E-3	11
g4	0.5	0.0267	526.9	1.26	4.2E-3	11
g5	0.2	0.0667	522.8	1.25	4.1E-3	10
g6	0.1	0.1333	516.1	1.24	4.0E-3	9
g7	50.0E-3	0.2667	503.4	1.21	3.8E-3	9
g8	10.0E-3	1.333	426.0	1.02	2.8E-3	6
g9	10.0E-4	13.33	209.9	0.50	6.7E-4	1
g10	10.0E-5	133.3	73.55	0.18	8.0E-5	0.1

Table 4.3 Load carrying capacity as a function of G_F.

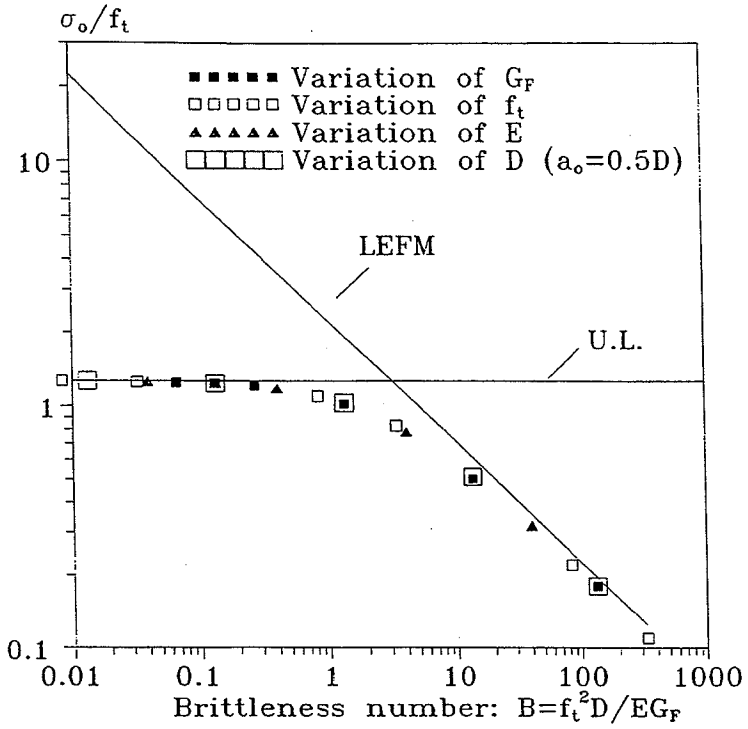

Figure 4.18 Failure load versus brittleness number.

The results are also depicted in Figure 4.18 (points marked "variation of G_F"). It appears that when increasing the brittleness number B, the load carrying capacity approaches the results given by LEFM, i.e. the results for a perfectly brittle structure. For small values of B, the result is expected to approach the load carrying capacity of an almost perfectly plastic structure. For an unnotched perfectly plastic beam with rectangular section in bending with the tensile strength f_t and an infinite compressive strength f_c the theoretical upper limit (U.L.) equals $\sigma_o/f_t=3$. Having a finite compressive stress f_c and if the ratio between f_t and f_c is put to $\alpha=f_t/f_c=0.1$, we get the theoretical upper limit $\sigma_o/f_t=2.73$, see **[94.4]**.

For decreasing start notch length the results of the theory will approach a limiting value close to this upper plastic solution as shown in Table 4.4. With a start notch depth being half the full depth h, the limiting value is reduced. As we observed in Table 4.3, the value is found to be $\sigma_o/f_t=1.27$ in this case.

G_F=0.1N/mm, f_t=2MPa, E=30000MPa, B=0.133			
a_0 (mm)	P_{peak} (N)	σ_o/f_t	l_e (mm)
50	516.4	1.24	10
25	1327	1.42	14
10	2302	1.71	15
5	2905	1.93	13
1	3806	2.33	7
0.001	4306	2.58	6
0.00001	4307	2.58	6

Table 4.4 The relative stress approaches the upper plastic limit for an unnotched beam when the notch length is decreased.

In Figure 4.18 also results found by varying the other parameters determining the brittleness number B have been shown. It appears, that the results are lying on the same curve as before, as they should.

The theory takes the size effects into account by the variation of the crack length correction l_e with K_I. If l_e is large (relative to the beam height), the material behaves ductile in agreement with what we observed in Table 4.3, where l_e is large for small values of the brittleness number.

The LEFM limit has been determined on basis of the formula $G_F=K_{IC}^2/E$, where $K_I=K_{IC}$ is determined at P_{peak}, using the procedure:

1) $K_I = K_{IC} = \sqrt{EG_F}$, G_F is varied
2) $P = f(K_I)$
3) $\sigma_o = \dfrac{3}{2}\dfrac{P_{peak}L}{b(h-a_o)^2} \rightarrow \dfrac{\sigma_o}{f_t}$ (4.40)
4) $B = \dfrac{f_t^2 D}{EG_F}$

When examining the effect of varying the dimensions, it should be noticed that the similarity requirements only deal with the depth and the length to get the same failure mode. The thickness b do not influence the result.

The relative sizes used in this investigation are shown in Figure 4.19.

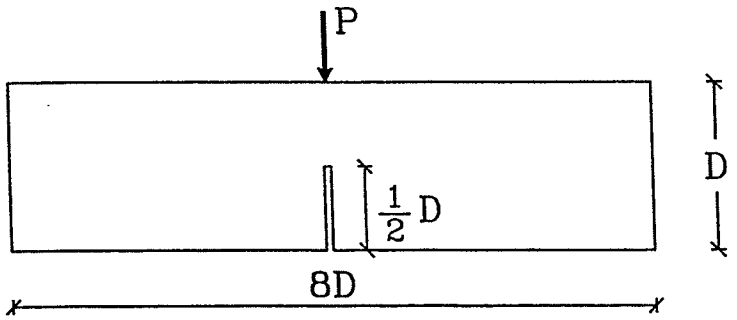

Figure 4.19 Relative beam dimensions.

In section 4.4 test results will be compared with the calculations.

4.4 Comparison with Experimental Results

4.4.1 Introduction

In the preceding sections of chapter 4 a model for determining crack growth and crack propagation applied to plain concrete has been presented.

In order to verify the crack growth formula and it's application to concrete, this chapter presents a comparison of the theoretical model with experiments performed at the Department of Structural Engineering, Technical University of Denmark in 1991-92. The experimental results are presented in chapter 5 and in **[94.1]** and **[94.2]**.

This chapter will compare the theoretical load - deflection curves obtained from the crack growth formula with the experimental values for a number of three point bending tests on notched beams described in chapter 5.

The prediction of load-deflection relationships for concrete using the crack propagation formula is dependent on the accurate estimation of essential material properties of plain concrete. These material properties have been established in **[94.1]** and are given in chapter 5.

For the purpose of presenting the potentialities of the crack propagation formula three separate series of comparisons will be introduced in the following. The basis for all three investigations is that only three point bending tests on notched beams will be utilized. The essential parameters used in the theory such as the compressive strength f_c, the tensile strength of concrete f_t and the modulus of elasticity E_c will be taken directly from the published test results in chapter 5 and **[94.1]** for the selected test beams used in the comparison.

In order to examine the capability of the theoretical model to predict the bending strength of concrete and the load-deflection relationship for a three point bending test, test beams with four different compressive strength levels are used. Two test beams with normal strength concrete (30 MPa and 50 MPa) and two with high strength concrete (70 MPa and 100 MPa) have been chosen to represent the complete range of strength levels.

Secondly, the capability of the model to predict load - deflection relationships for different notch-depth ratios (a/h) of the test beams will be given. The variation

of a/h are: 0.1, 0.25 and 0.5 .

The last comparison made in this paper concerns three point bending results for beams with different maximum aggregate size. Two compressive strength levels are examined; 30 MPa and 100 MPa. For each strength level the maximum aggregate size d_{max} takes the values 4 mm - 8 mm - 16 mm.

Determination of the fracture parameters used in the crack growth formula is carried out according to the test program presented in chapter 5. Basic strength parameters of concrete such as compressive strength, tensile strength and modulus of elasticity are determined by standard methods, that are in accordance with standard procedures throughout the world.

The values used for determining the fracture energy of concrete are based on experimental results carried out on three point bending tests on notched beams.

Experimentally one might conclude, that a determination of G_F is most effectively and efficiently obtained through a stable uniaxial tensile test. A performance of this kind of test immediately produces important information about both the tensile strength f_t, the modulus of elasticity E_c and the fracture energy G_F.

It is, however, difficult in practice to perform stable tensile tests. What is required is a sophisticated servo-controlled system making possible a deformation controlled uniaxial tensile test on realistic specimen sizes. Even with advanced testing equipment difficulties can be encountered in load application and with establishing a uniform deformation distribution over the fracture zone during the test.

For the above reasons it seems clear, that performing uniaxial tensile tests, although very favorable from a theoretical point of view, is difficult and has been discarded in this paper in favour of the more simple testing procedure involving a three point bending test on notched beams in accordance with the ***RILEM Technical Committee 50-FMC*** **[85.1]**. In this method the measured load-deflection curve does not give the total amount of energy consumed due to the fact, that the energy is not only supplied from the applied force, but also from the netweight of the beam, which has to be taken into account when determining G_F. This is done using the method suggested by ***Hillerborg*** **[85.1]**, by putting the total energy equal to the area under the measured load-deflection curve plus the secondary part from the netweight. G_F used in the theoretical calculations will be determined for a concentrated load only, disregarding the netweight of the beam. The comparisons made will thus take place for measured load-deflection curves, the load meaning the applied concentrated load and the deflection meaning the

deflection measured in the test, having zero value when the beam is acted upon only by its own weight.

The splitting strength f_{sp} was determined for each concrete mix using standard procedures, see chapter 5. The tensile strength used in the theory is put equal to $f_f=1.25f_{sp}$. This value is close to the flexural modulus.

The modulus of elasticity E_c was determined for all the concrete mixes by separate cylinder tests using standard procedures, see chapter 5.

4.4.2 The Bending Strength of Concrete

The primary aim of this section is to determine the capability of the theoretical model to predict the bending strength and load-deflection relationship for concrete for different strength levels.

Test results from reference **[94.1]** and **[94.2]**, see chapter 5, are used in the comparison between the theory and the tests. The experimental values of the fracture energy G_F has here been reduced by a value corresponding to the energy supplied by the weight of the beam. The test program includes test specimens with different concrete compressive strength levels, which enable the evaluation of the theory to take place both for normal and high strength concrete.

The basic fracture parameters, that will be used in the crack growth formula are tabulated in Table 4.5.

Beam No	f_c	f_{sp}	E_c	G_F	$f_f = 1.25*f_{sp}$
	MPa	MPa	MPa	N/m	MPa
A-B30.3N	25.8	2.90	25160	81.1	3.63
A-B50.3N	48.0	3.76	32950	64.0	4.70
A-B70.3	72.6	4.82	35300	85.8	6.03
A-B100.3	99.0	5.49	42210	95.7	6.86

Table 4.5 Fracture parameters for analyzing the bending strength of concrete.

Table 4.5 presents the fracture parameters taken as mean values of the experimental results. The results of experimentally determined load-deflection curves will in this section be compared to the theoretical ones obtained through calculations. The beams used for the comparison will have geometrical properties as given in Figure 4.20.

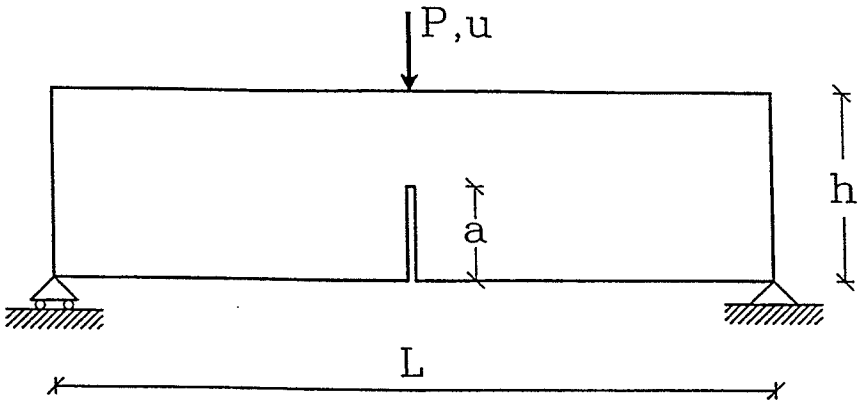

Figure 4.20 Geometrical properties of beams used in bending strength analysis.

The compressive strength of the beams will be varied according to Table 4.5 i.e. four different compressive strength levels of the beams are examined, 30 MPa, 50 MPa, 70 MPa and 100 MPa. The notch-depth ratio (a/h) of the beams will be held constant on the value 0.5.

In Figure 4.21 - 4.24 the experimental values obtained through test results reported in chapter 5 are shown and compared with the values obtained by using the crack propagation formula. Only one beam test for each compressive strength level is shown.

In the figures the fully drawn line represents the experimental value and the dotted line the theoretical value according to the crack propagation formula. In Figure 4.25 the load deflection curves for all beam tests together with the theoretical values are given.

From the figures it can be seen, that the crack propagation theory presented in this paper is able to predict both the ascending part of the load deflection curve and the peak value for all compressive strength levels.

The theory is unfortunately only able to predict a part of the descending branch of the load deflection curve due to the fact, as explained in section 4.3, that when the process zone reaches the top of the beam, the assumptions, that are used in the theory, are no longer valid.

From the curves it can be seen, that the maximum load increases with increasing compressive strength, and that the deformation at maximum load is independent of concrete strength, which is also in agreement with the theoretical results.

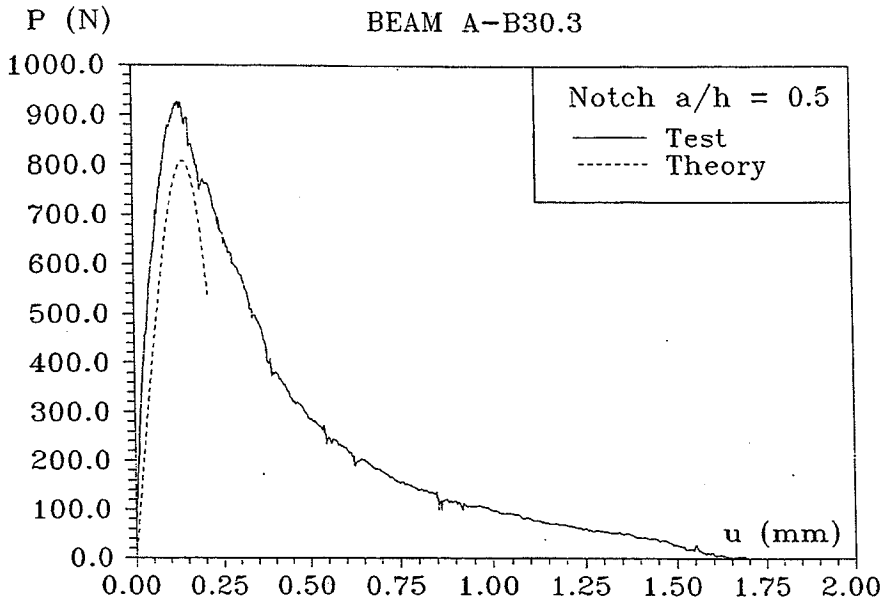

Figure 4.21 Theoretical and experimental results for beam A-B30.3.

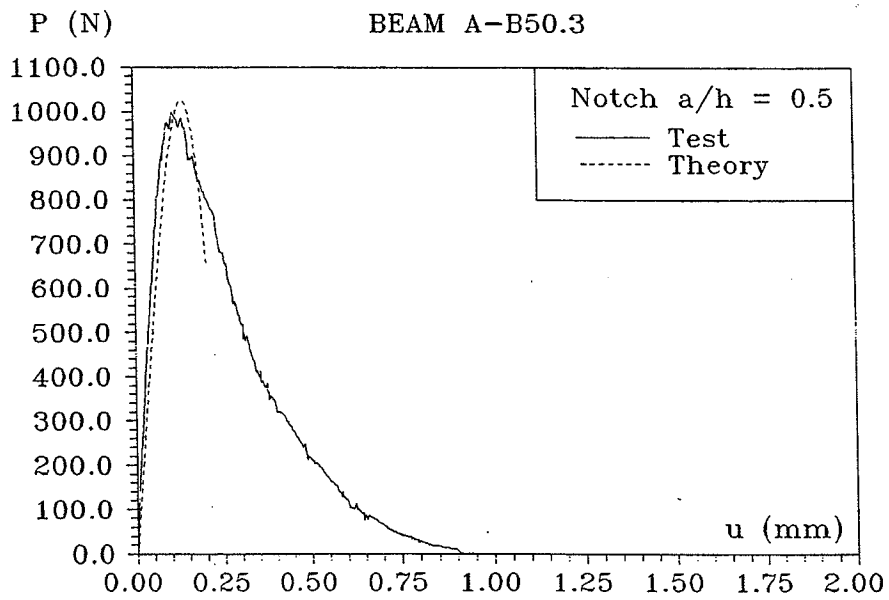

Figure 4.22 Theoretical and experimental results for beam A-B50.3.

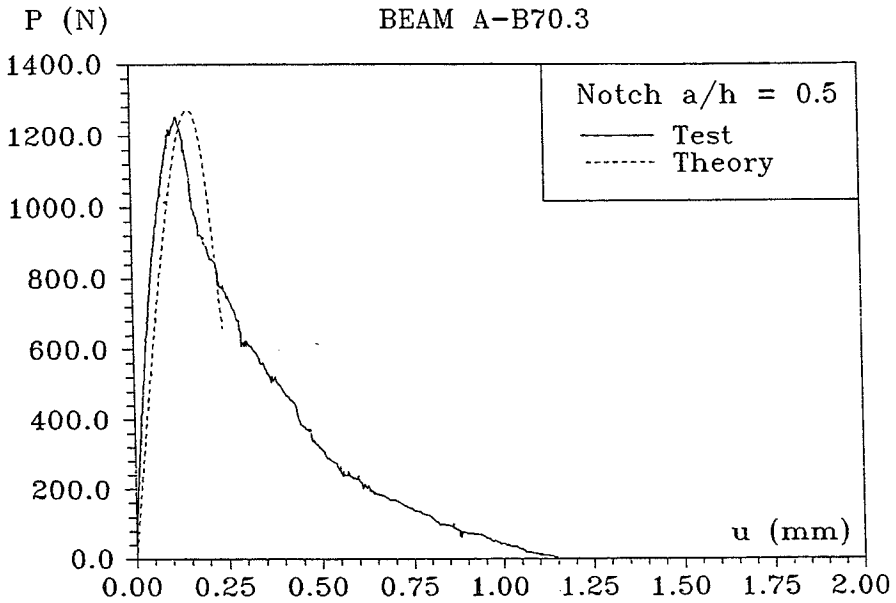

Figure 4.23 Theoretical and experimental results for beam A-B70.3.

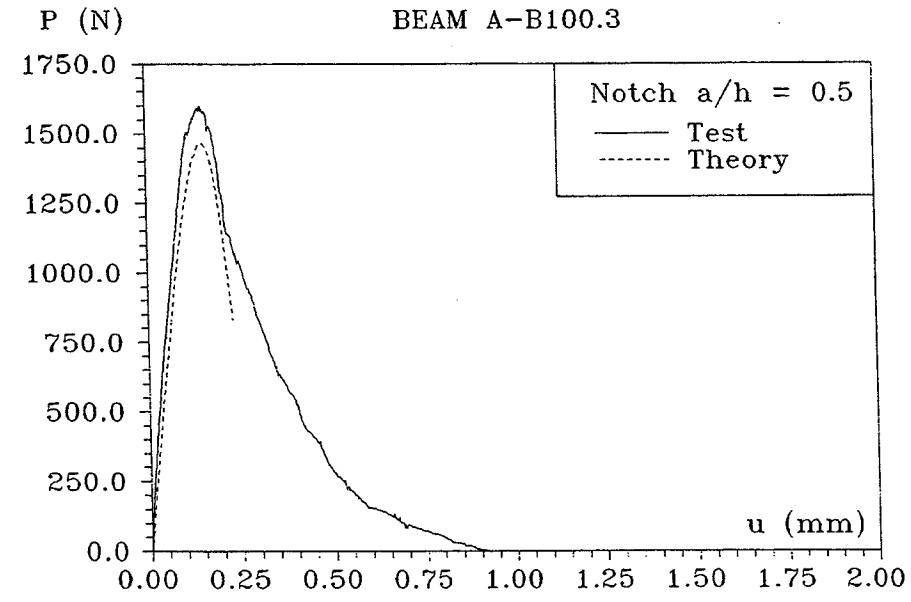

Figure 4.24 Theoretical and experimental results for beam A-B100.3.

4.4.3 Notch Sensitivity

The primary aim of this section is to describe the relationship between theoretical and experimental values for bending strength and load-deflection curves for concrete beams. The beam specimens used for this purpose has the dimensions suggested by ***RILEM*** **[85.1]** (i.e. bxhxL = 100x100x800 mm^3).

Four compressive strength levels are chosen, 30 MPa, 50 MPa, 70 MPa and 100 MPa. Within each strength level the notch-depth ratio (a/h) is taken to 0.1 - 0.25 - 0.5 respectively.

The basic fracture parameters, that will be used in the crack growth formula are tabulated in Table 4.6 and represents the experimentally determined values from **[94.1]** and **[94.2]**, see also chapter 5. The experimental values of the fracture energy G_F has been reduced by a value corresponding to the energy supplied by the weight of the beam.

Beam No	a	f_c	f_{sp}	E_c	G_F	$f_f = 1.25*f_{sp}$
	mm	MPa	MPa	MPa	N/m	MPa
A-B30.1	10	28.1	2.32	26110	105.0	2.90
A-B30.2N	25	31.8	2.84	27330	117.6	3.55
A-B30.3N	50	25.8	2.90	25160	81.1	3.63
A-B50.1	10	51.0	3.87	33640	113.2	4.84
A-B50.2	25	55.5	3.72	32490	106.2	4.65
A-B50.3N	50	48.0	3.76	32950	64.0	4.70
A-B70.1	10	78.0	5.38	37330	124.2	6.73
A-B70.2	25	68.1	4.52	33800	102.3	5.65
A-B70.3	50	72.6	4.82	35300	85.8	6.03
A-B100.1	10	99.4	5.66	42070	161.9	7.08
A-B100.2	25	100.1	5.78	42240	118.8	7.23
A-B100.3	50	99.0	5.49	42210	95.7	6.86

Table 4.6 Fracture parameters for analyzing notch sensitivity.

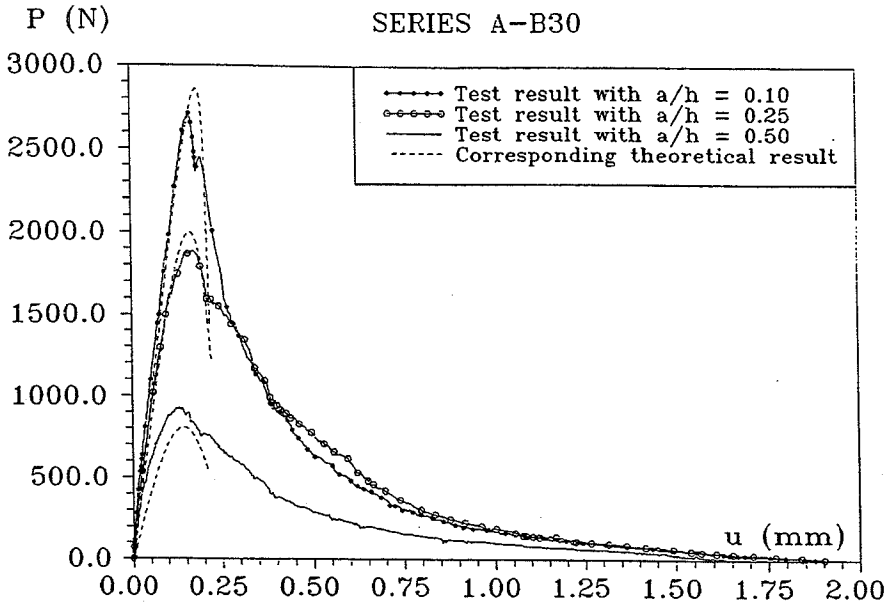

Figure 4.26 Theoretical and experimental results for beams A-B30.

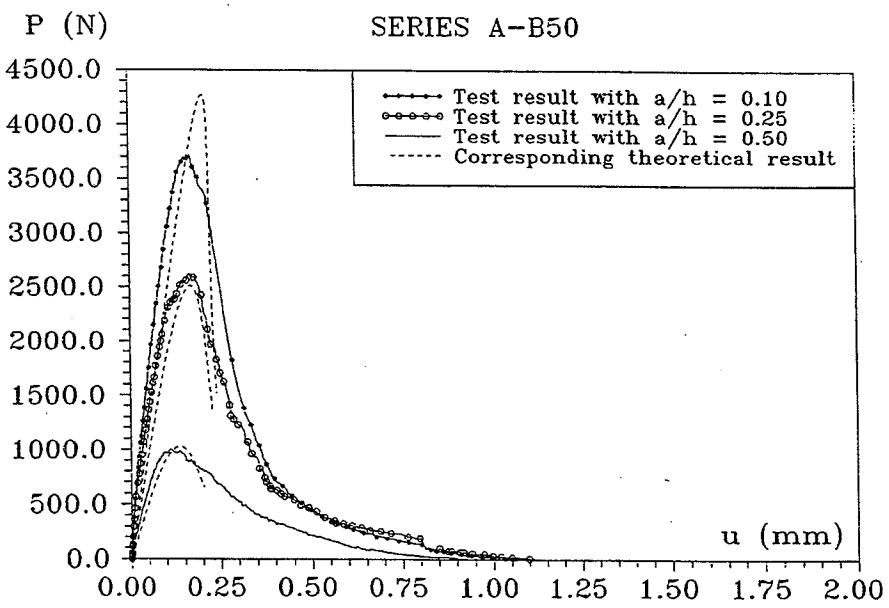

Figure 4.27 Theoretical and experimental results for beams A-B50.

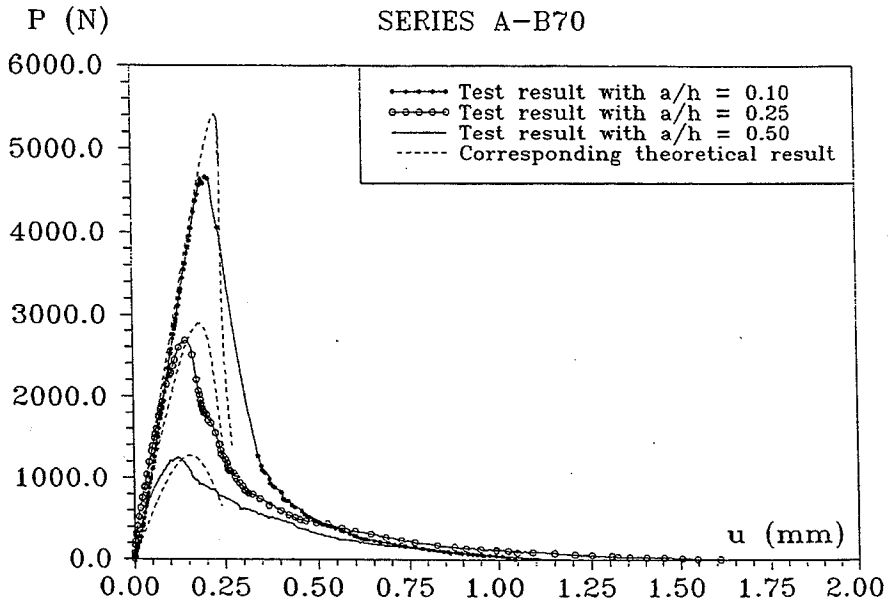

Figure 4.28 Theoretical and experimental results for beams A-B70.

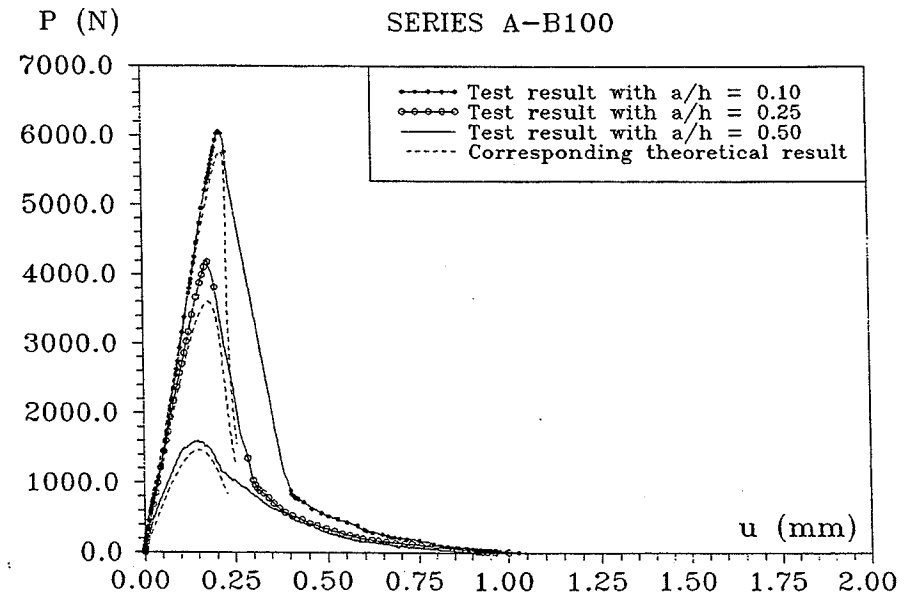

Figure 4.29 Theoretical and experimental results for beam A-B100.

In Figure 4.26 - 4.29 the load deflection curves are given for different concrete strengths and a/h-ratios. Each experimental curve in Figure 4.26 - 4.29 is an average curve from a batch of 6 beam tests made. In **[94.2]** and chapter 5 all test results are given together with beam data and the observed value of maximum load and deflection.

The load deflection curves are compared with the values obtained by the crack propagation formula, which are represented by a dotted line in the figures.

From the figures it can be seen, that the crack propagation theory is able to predict both the ascending part of the load deflection curve and the peak value for all compressive strength levels and notch - height ratios.

As was the case in section 4.4.2, the theory is only able to predict a part of the descending branch of the load deflection curve.

4.4.4 The Influence of Maximum Aggregate Size

In this section a comparison between theoretical and experimental results for concretes, where aggregate sizes and grading curves are varied, is carried out. Results of bending strength and load-deflection curves for beams, where volume concentration of coarse aggregate is varied will be presented.

The bond strength between the cement matrix and aggregate will be investigated for two compressive strength levels; 30 MPa and 100 MPa, which enables the evaluation of the theory to take place both for normal and high strength concrete. For each strength level the maximum aggregate size d_{max} takes the values 0 mm (cement paste), 4 mm, 8 mm and 16 mm.

The basic fracture parameters, that are used in the comparison are given in Table 4.7.

Beam No	d_{max}	f_c	f_{sp}	E_c	G_F	$f_f = 1.25*f_{sp}$
	mm	MPa	MPa	MPa	N/m	MPa
C-B30.1	0	26.9	2.00*	10450	3.7	2.50
C-B30.2	4	24.4	2.27	22120	18.0	2.84
C-B30.3	8	23.3	2.51	27460	32.7	3.14
A-B30.3N	16	25.8	2.90	25160	81.1	3.63
C-B100.1	0	98.9	4.79	26370	13.5	5.99
C-B100.2	4	72.5	4.78	37230	40.3	5.98
C-B100.3	8	94.8	5.55	41470	73.6	6.94
A-B100.3	16	99.0	5.49	42210	95.7	6.86

* The splitting strength for this test series was not measured, the value is an estimate based on the other splitting strengths.

Table 4.7 Fracture parameters for analyzing the influence of maximum aggregate size.

Test results from reference **[94.1]** and **[94.2]**, see chapter 5, are used in the comparison between theory and tests. The experimental values of the fracture energy G_F has been reduced with a value corresponding to the energy supplied by the weight of the beam.

As was the case in section 4.4.2 and 4.4.3 only the smallest beam size recommended by ***RILEM*** **[85.1]** will be used in the comparison. The notch depth a is held constant and equal to 50 mm. (a/h = 0.5)

In Figure 4.30 - 4.33 typical load-deflection curves from chapter 5 are compared with the theoretical values obtained by the crack propagation formula. In these figures a variation of the maximum aggregate size for a normal strength concrete has been performed. Furthermore a comparison between theory and experiments for a high strength concrete can be seen in Figure 4.34 - 4.37.

Similar for the two investigations is the fact, that the crack propagation formula is able to predict the load- deflection curves in most cases with good agreement with the measured value.

A decrease in aggregate size results in a decrease in steepness of the ascending part of the load-deflection curve. It can be seen from the figures, that the theory represented by the dotted line is in good agreement both with regard to the steepness of the ascending part, the peak value and also the first part of the descending branch.

There can be no doubt, that a post-peak behavior is present even for high strength cement paste, but the post peak behavior measured might be the result of snap back, which could not be followed by the present testing equipment. See Figure 4.34.

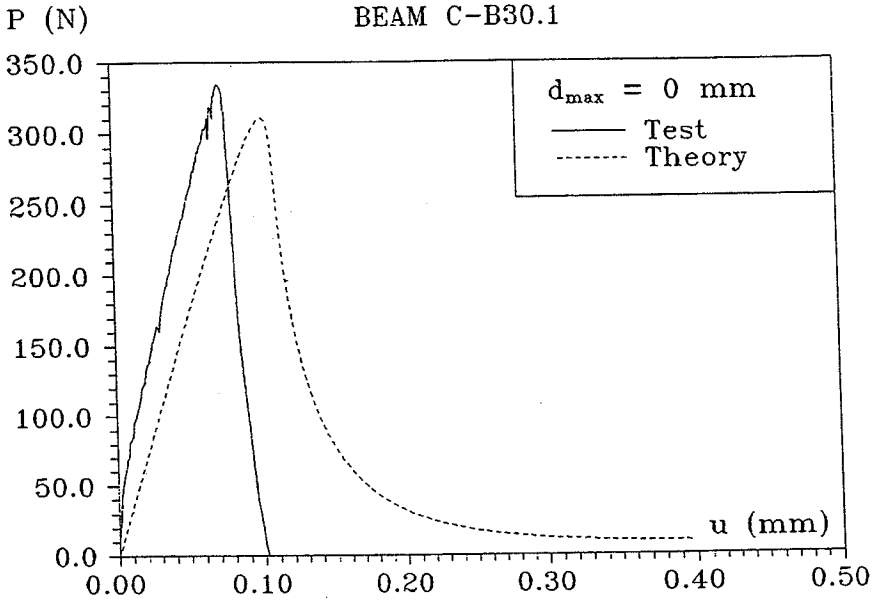

Figure 4.30 Theoretical and experimental results for d_{max} = 0 mm, $f_c \approx 30$ MPa (cementpaste).

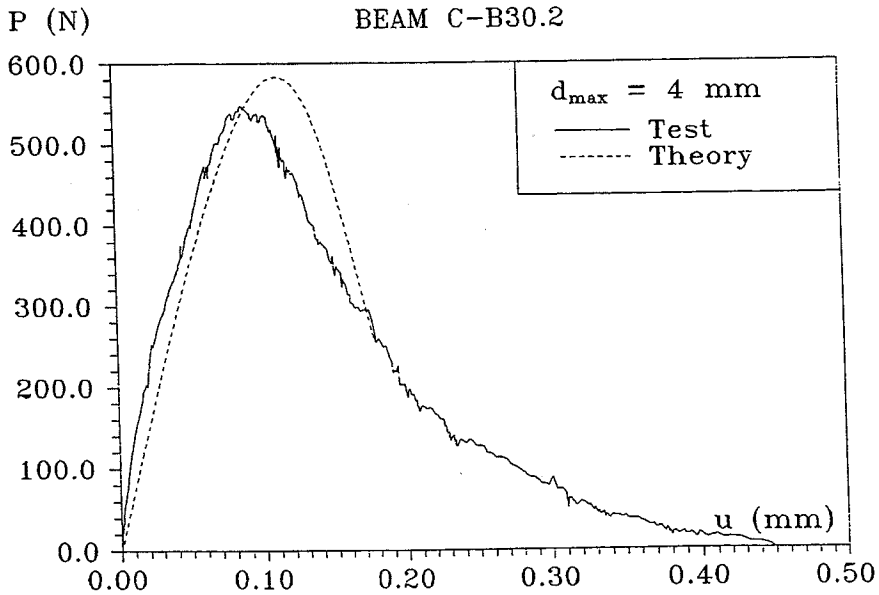

Figure 4.31 Theoretical and experimental results for d_{max} = 4 mm, $f_c \approx 30$ MPa.

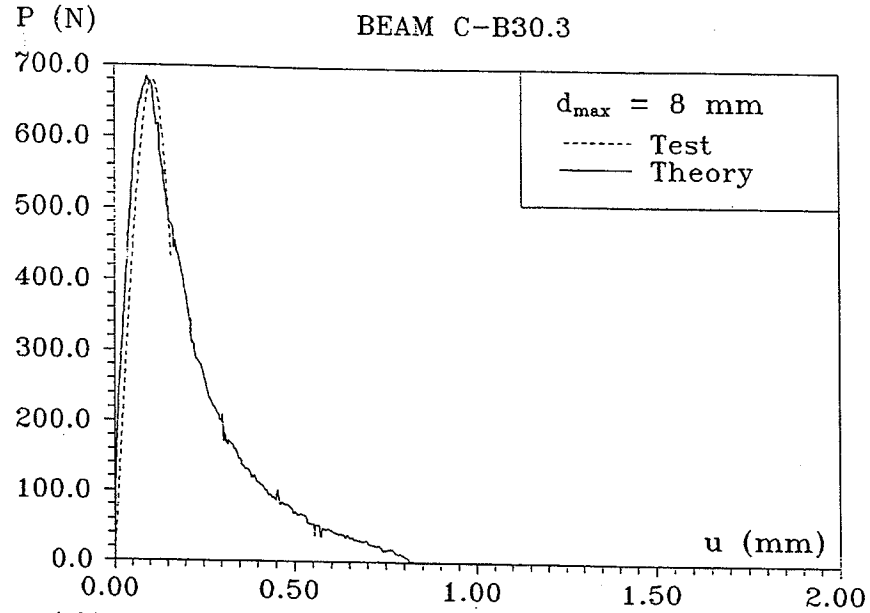

MPa

Figure 4.32 Theoretical and experimental results for d_{max} = 8 mm, $f_c \approx 30$ MPa.

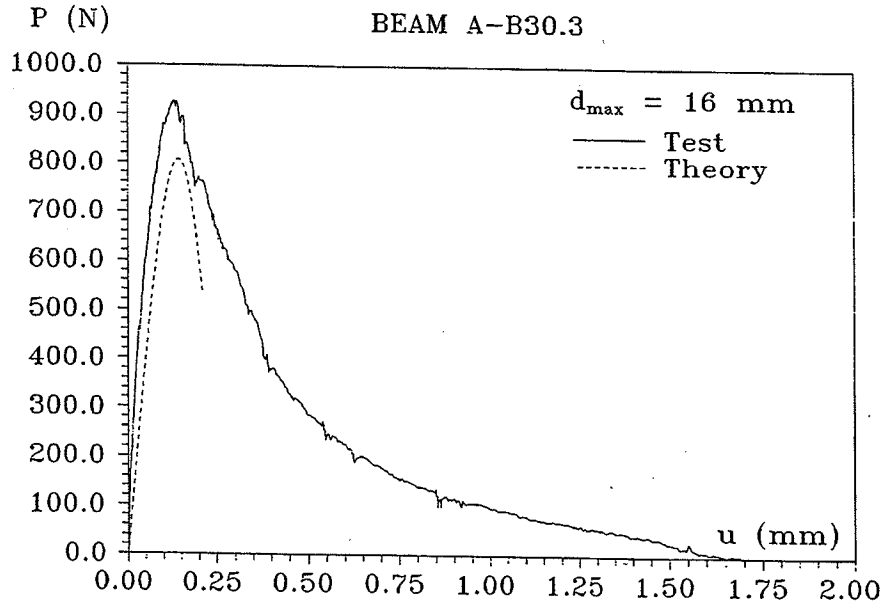

Figure 4.33 Theoretical and experimental results for d_{max}=16 mm, $f_c \approx 30$ MPa.

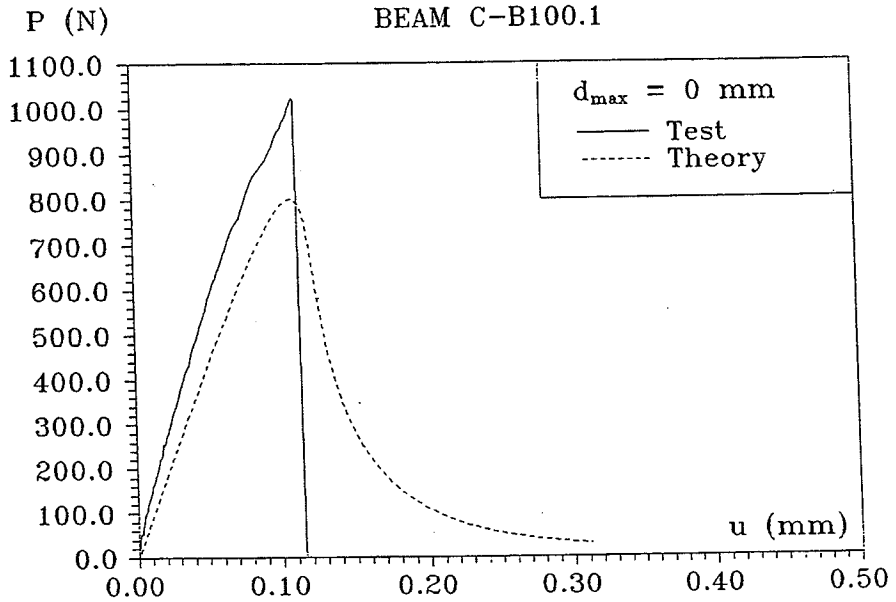

Figure 4.34 Theoretical and experimental results for d_{max}=0 mm, $f_c \approx 100$ MPa (cementpaste).

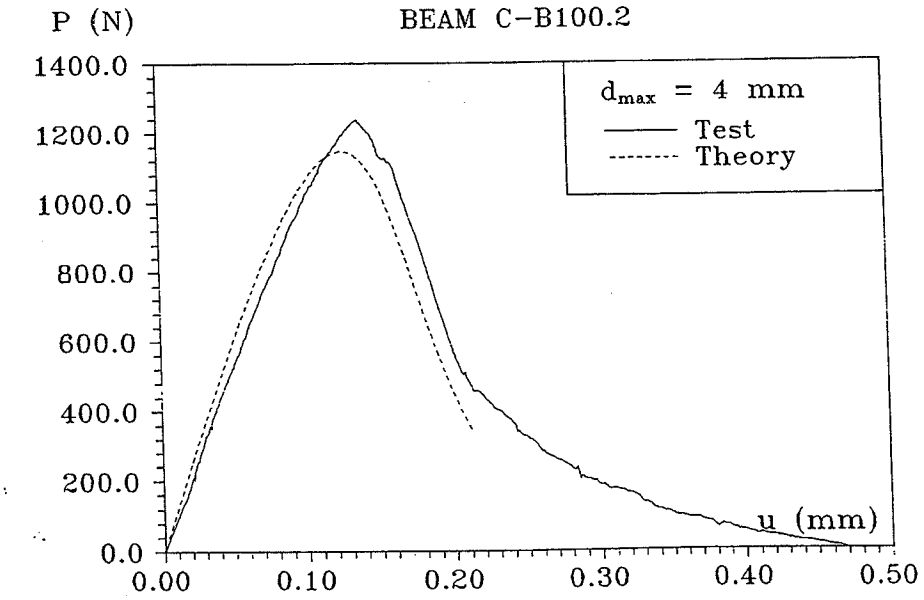

Figure 4.35 Theoretical and experimental results for d_{max}=4 mm, $f_c \approx 100$ MPa.

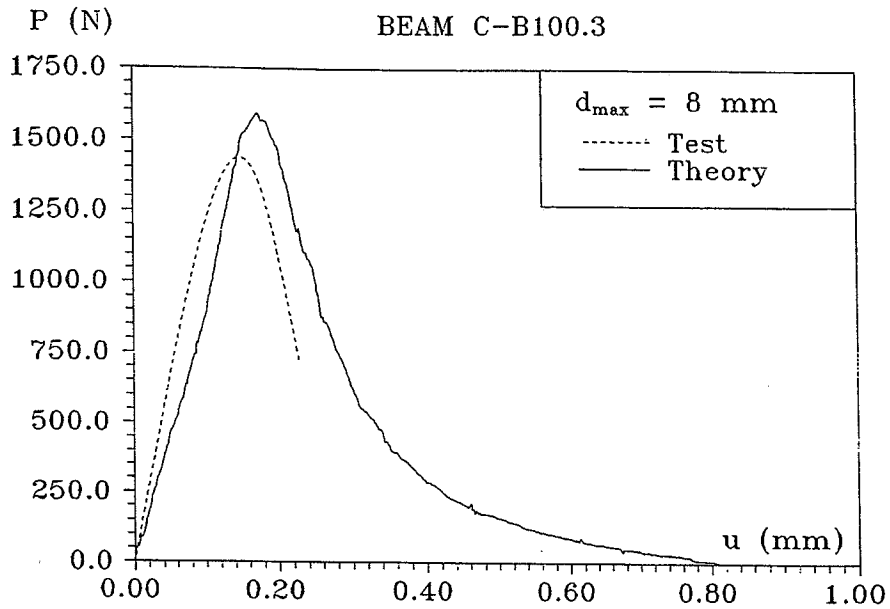

Figure 4.36 Theoretical and experimental results for d_{max}=8 mm, $f_c \approx 100$ MPa.

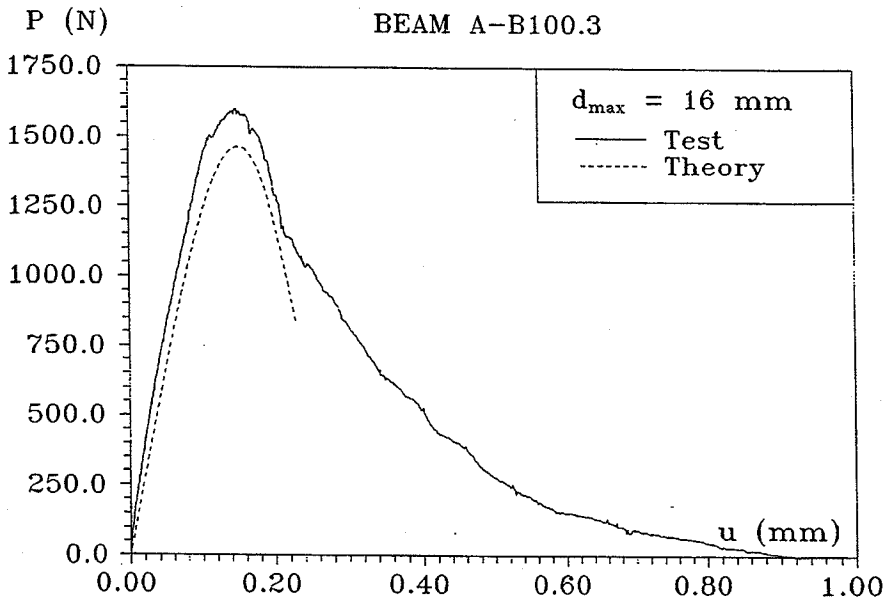

Figure 4.37 Theoretical and experimental results for d_{max}=16 mm, $f_c \approx 100$ MPa.

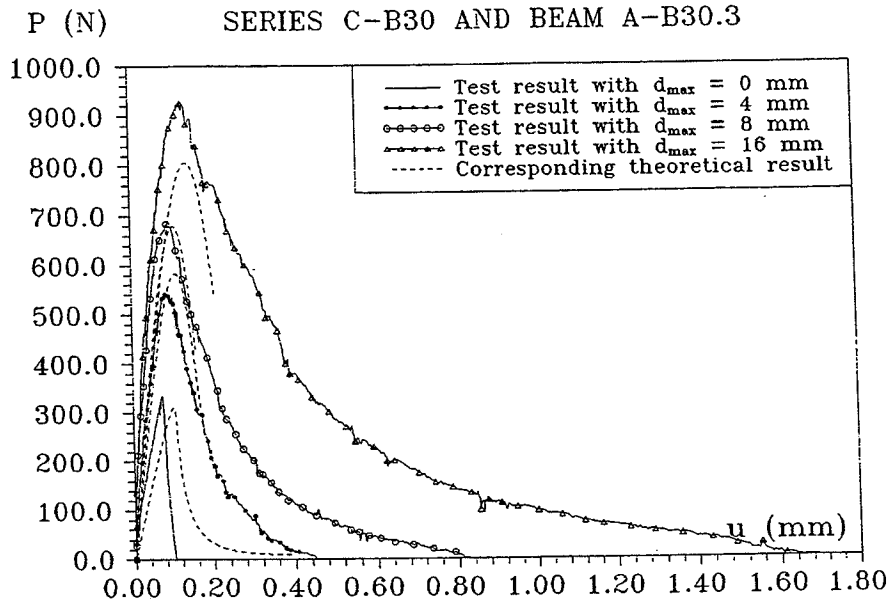

Figure 4.38 Theoretical and experimental results for different maximum aggregate sizes, $f_c \approx 30$ MPa.

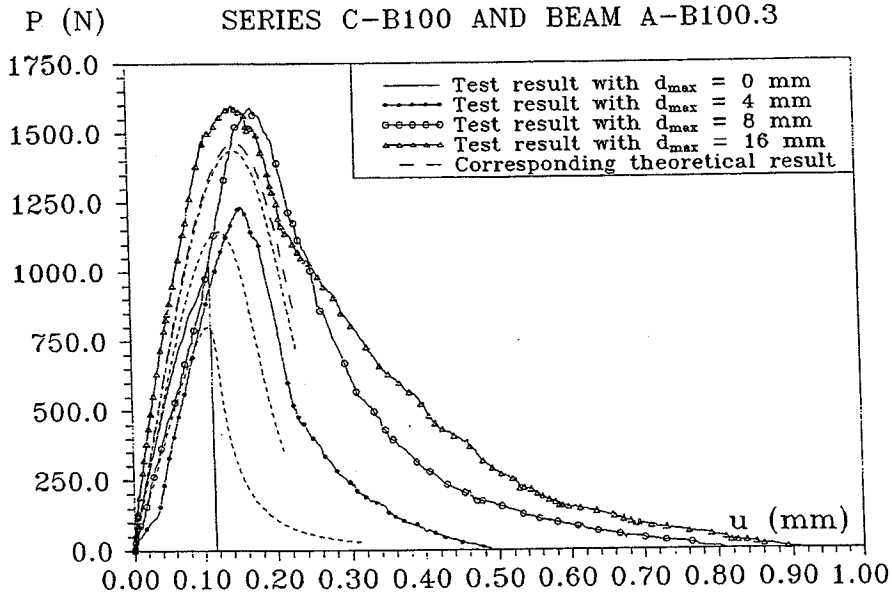

Figure 4.39 Theoretical and experimental results for different maximum aggregate sizes, $f_c \approx 100$ MPa.

4.5 Conclusion

The purpose of this section has been to make an investigation of the potentialities of a new crack propagation formula based on an energy criterion when applied to concrete. An investigation of crack propagation under static loading and the capability of the model to predict size effects have been performed. It has been shown, that the model is able to predict crack propagation in both ductile and brittle materials.

The model has been compared with experimental results of three point bending tests of plain concrete beams. The main conclusions are, that the theory presented is able to predict the peak value and part of the descending branch of the load - deflection curve for different strength levels, variation of notch depth ratios and maximum aggregate sizes. The results presented indicate, that the new crack propagation formula is applicable to a brittle material like concrete.

The model has not yet been able to predict the major part of the descending branch of the load deflection curve due to the fact, that the process zone is determined on the basis of the stress concentration factor in the first term. This assumption is only valid for small values of the process zone compared to the crack length.

It may however be concluded, that by using the new crack propagation formula, it is possible to predict crack growth, load carrying capacity and deflection for a number of structural elements subjected to statical loading.

Chapter 5

Fracture of Concrete. A Test Series

5.1 Introduction

5.1.1 General

This chapter is divided into subsections each representing a presentation and description of the testing results for different concrete beams. For every test series A through F the parameters involved are given individually together with the specific testing procedure.

5.1.2 The Purpose of the Investigation

There is a growing international interest concerning the application of fracture mechanics to concrete structures, which has given new ways of understanding and model phenomena, which earlier only could be treated empirically. Where other theoretical approaches has been discarded, fracture mechanics calculations have already proven useful in situations, which otherwise would have remained unsolved.

Even though the tensile strength of concrete is not taken into account in many design calculations, the importance of the tensile fracture is well understood nowadays. This is mainly due to the fact, that fracture mechanics entered the field of concrete design in combination with an increasing importance of finite element calculations.

Fracture mechanic properties, however, must be examined thoroughly both theoretically and experimentally to gather experience for practical use.

This chapter deals with the micro fracture of plain concrete. The physical properties and fracture of a large number of notched specimens are presented.

The experiments described in this chapter are carried out in order to verify the theoretical work presented in chapter 4. The calculation model for crack growth in concrete are dependent on the accurate estimation of essential material parameters for a number of properties of plain concrete.

5.1.3 The Test program

In this chapter the experimental results of 234 test beams together with cylinder data will be presented.

Results from measured load-deflection curves, maximum load and deflection, fracture energy and flexural strength will be compared to specific parameters, that are varied for each series.

Only summaries of the test results will be given here in order to evaluate the effect of the different parameters, that are altered. Individual results for each cylinder and beam tests are presented in the attached appendix.

In the following sections each batch will be designated a letter A-E followed by a number representing a strength level 30, 50, 70 or 100. Furthermore a number will be added to represent the variation of a specific parameter. For example the number E-B30.2 corresponds to a beam (B) in batch (E) with an expected compressive strength level of (30) MPa, and the beam has a length of 1200mm (2).

The total test program comprises of 5 series (Series A - E) each having the specific purpose of isolating an essential fracture mechanical parameter and investigating it's influence.

In Series A the main purpose is to investigate the influence of notch sensitivity and compressive strength on the fracture energy. Four different compressive strength levels are tested, 30 MPa, 50 MPa, 70 MPa and 100 MPa to investigate the difference between normal and high strength concrete with respect to the fracture energy.

Furthermore, the notch sensitivity is tested using three different notch - height (a/h) ratios namely 0.1, 0.25 and 0.5 .

In Series B investigation of curing conditions are analyzed to determine the influence of shrinkage and creep on fracture mechanical parameters.

In Series C the aim is to reveal the influence of maximum aggregate size and type of aggregate on fracture mechanics parameters. Two compressive strength levels are examined; 30 MPa and 100 MPa. For each strength level the maximum aggregate size d_{max} takes the values 4 mm - 8 mm - 16 mm - 32 mm making a total of 24 test beams for each strength level. The aggregates used in this series was granite.

In Series D the air-content in the concrete is varied to examine the influence of this parameter on the fracture of concrete.

In Series E investigation of size-effect is performed in order to obtain knowledge of the size dependance on the fracture energy and the flexural strength for normal and high strength concrete, when carrying out small size variations. The beam length is varied from 550 mm to 2000 mm, keeping the height-width ratio of the beam constant throughout the series at a value equal to 1.

5.2 The Fracture Energy G_F of Concrete

5.2.1 Introduction

In accordance with the RILEM specifications given in ***RILEM*** **[85.1]** an experimental determination of the fracture energy G_F will be made and presented in this section.

5.2.2 The Theoretical Basis for G_F

The fracture energy G_F is defined as the total amount of energy necessary to create one unit area of crack. G_F was according to ***Hillerborg*** **[76.1]** (the fictitious crack model) defined by means of a uniaxial stable tensile test, where the total stress deformation curve was obtained. The stress deformation curve can be divided into two parts, the elastic deformation (σ-ϵ) and the strain softening (σ-w) curve, see Figure 5.1.

The area of the (σ-ϵ) curve represents the elastic energy per unit volume absorbed in the whole specimen. The (σ-w) curve represents the energy per unit area absorbed within the damage zone. The area below the (σ-w) curve defines according to ***Hillerborg*** **[76.1]** the fracture energy pr. unit area of the fracture surface (projected area of a plane perpendicular to the stress direction) G_F.

Experimentally one might conclude, that a determination of G_F is most effectively and efficiently obtained through a stable uniaxial tensile test. A performance of this kind of test immediately produces important information about both the tensile strength f_t, the modulus of elasticity E_c and the fracture energy G_F.

It is, however, difficult in practice to perform stable tensile tests. What is required is a sophisticated servo-controlled system making possible a deformation controlled uniaxial tensile test on realistic specimen sizes. Even with advanced testing equipment difficulties can be encountered in load application and in establishing a uniform deformation distribution over the fracture zone during the test.

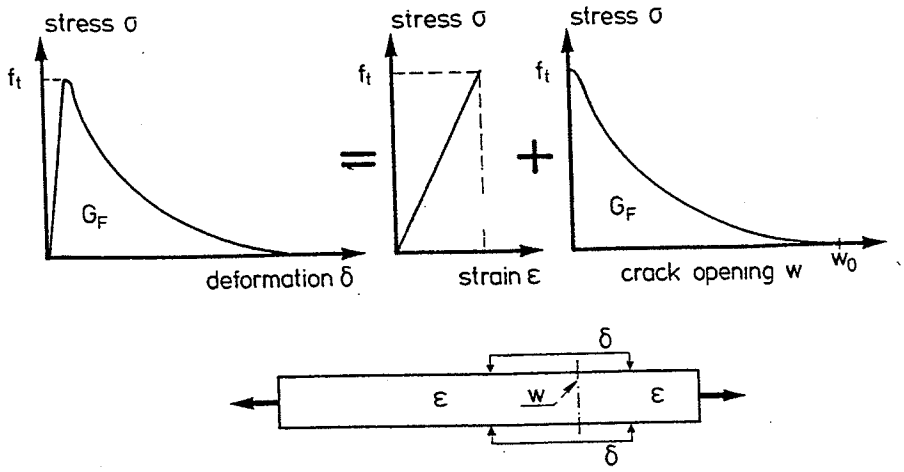

Figure 5.1 Stress-deformation curves for tensile behaviour according to *Hillerborg* **[76.1]**.

For the above reasons it seems clear, that performing uniaxial tensile tests, although very favorable from a theoretical point of view, are difficult and have been discarded in this thesis in favor of the more simple testing procedure involving a three point bending test on notched beams in accordance with the ***RILEM Technical Committee 50-FMC*** **[85.1]**.

An experimentally determined value of G_F, obtained through a stable three point bending test on a notched beam, will now be discussed in detail. This type of test is basically a measurement of the total amount of energy required to break a beam in two halves and thereby measurering the total amount of energy consumption from the start of crack initiation, until the crack has propagated right through the beam. It is essential, that all energy supplied by the load equals the amount of energy consumed by crack propagation, and that secondary effects are minimized. In order to fulfill this requirement, fracture must be stable, resulting in a rather strict stiffness criteria for the testing machine. (See section 5.3)

Consider a horizontal, simply supported notched beam centrally loaded by a force $P(\delta)$. See Figure 5.2.

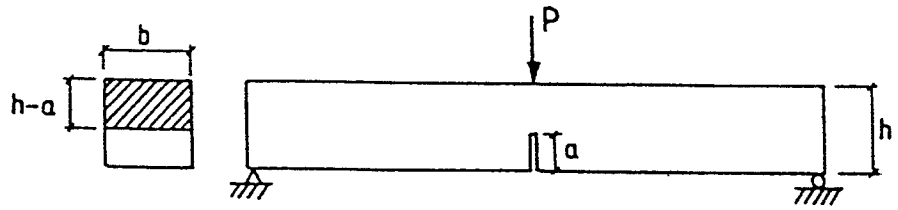

Figure 5.2 Test beam for G_F tests.

In an idealized situation this will result in a load-deflection curve as depicted in Figure 5.3.

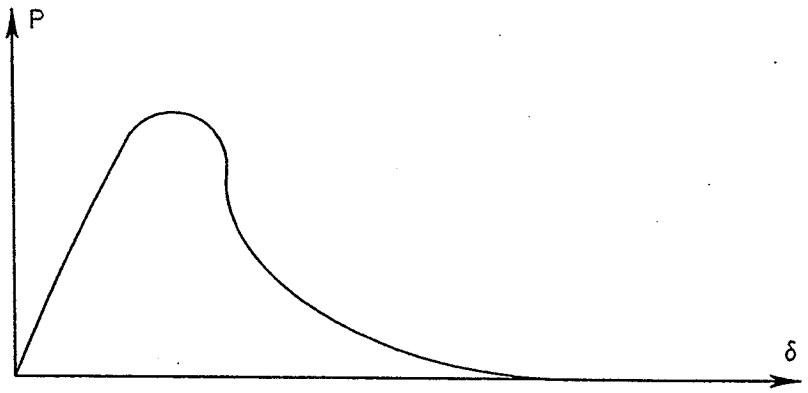

Figure 5.3 Load-deflection curve from a G_F test.

The above curve shows the result when carrying out a stable three point bending test. Energy, however, is not only supplied by the force, but also by the weight of the beam and part of the testing equipment. Consequently the measured load-deflection curve during the experiment does not give the total amount of energy,

and a correction, that takes account of the secondary effects must be made as shown in Figure 5.4.

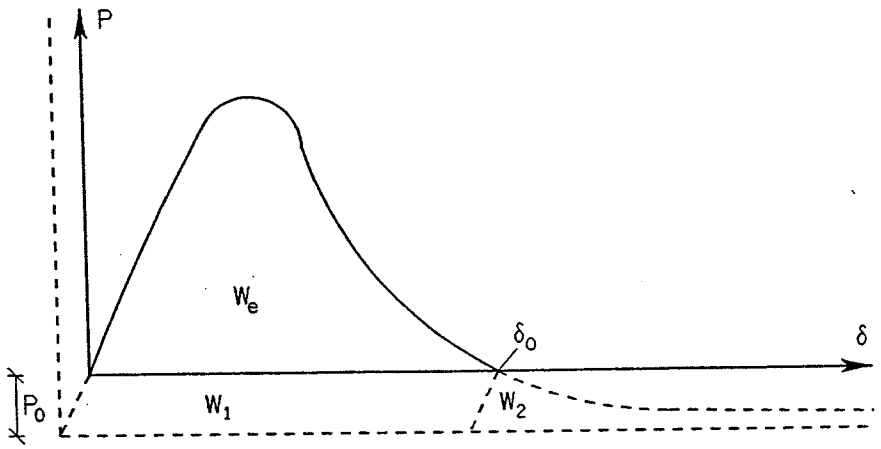

Figure 5.4 Load-deflection curve from a G_F test and the corresponding complete curve when the weight of the beam and testing equipment are taken into account.

Figure 5.4 shows the full load-deflection history for the beam, where the full line represents the actually measured values of force and deflection during the experiment, and the dotted lines represent a hypothetical curve for the complete load-deflection history. The total amount of absorbed energy of the beam can be expressed as

$$W = W_e + W_1 + W_2 \tag{5.1}$$

where W_e is the area of the experimentally determined load-deflection curve, and W_1 can be expressed as

$$W_1 = P_0 \delta_0 \tag{5.2}$$

where δ_0 is the deformation when P=0 and the beam breaks. P_0 is the central force, that results in the same amount of work as the weight of the beam m_g and the testing equipment m_t.

Assuming triangular deflection curve, the concentrated force P_0 equivalent to the weight of the beam (uniform) and the weight of the testing equipment (concentrated) may be determined by

$$P_0 \delta = \left(2 \frac{m_g}{2} \frac{\delta}{2} + m_t \delta \right) g \tag{5.3}$$

or

$$P_0 = \left(\frac{m_g}{2} + m_t \right) g \tag{5.4}$$

where g is the acceleration due to gravity.

The value of W_2 may give rise to some problems. Theoretically the load deflection curve for a weightless beam will be infinitely long (the dotted curve in Figure 5.4). ***Petersson*** **[81.1]** suggests a relationship between the force and deflection on the descending branch of the curve given by

$$P(\delta) = \frac{c}{\delta^2} \tag{5.5}$$

where c is a constant.

Using (5.5) the area in Figure 5.4 can now be calculated as

$$W_2 = \int_{\delta_0}^{\infty} P(\delta)\,d\delta = \int_{\delta_0}^{\infty} \frac{c}{\delta^2}\,d\delta = \frac{c}{\delta_0} \tag{5.6}$$

and consequently inserting (5.5) into (5.6) results in

$$W_2 = P(\delta)\,\delta_0 = P_0\delta_0 \tag{5.7}$$

This means that the value of W_2 equals W_1 and an expression for the total amount of absorbed energy can be taken as

$$W = W_e + 2P_0\delta_0 \tag{5.8}$$

or

$$W = W_e + (m_g + 2m_t)g\,\delta_0 \tag{5.9}$$

The fracture energy G_F may now be determined as the total energy consumption of the beam W divided by the projected fracture area b(h-a), where b is the width of the beam, h the height of the beam and a the notch length, see Figure 5.2.

$$G_F = \frac{W}{b(h-a)} = \frac{W_e + (m_g + 2m_t)g\,\delta_0}{b(h-a)} \tag{5.10}$$

Notice that the area of the crack is not the real area of the fracture surface but a representative area making a realistic G_F-value only valid through an average of many test beams.

5.3 The Test Rig

5.3.1 Introduction

For determining the fracture energy of concrete G_F a detailed knowledge of the full load, P, - deflection, u, curve is needed. The fact that concrete is a brittle material presents a problem in determining the descending branch of the curve. A test rig must be designed that enables the obtainability of a stable fracture of the test beam using a displacement controlled testing machine. A load controlled machine will always produce an unstable fracture after maximum load has been reached. Investigation into this problem has been made for the last 10 years by researchers like ***Hillerborg*** **[77.2]**, ***Modéer*** **[79.5]** and ***Cooper*** **[77.4]**.

5.3.2 Stability and Stiffness Condition for Bending Tests

With a normal load deflection curve for unreinforced concrete, see Figure 5.5, a stable crack propagation may be obtained when the stiffness of the testing machine is large enough.

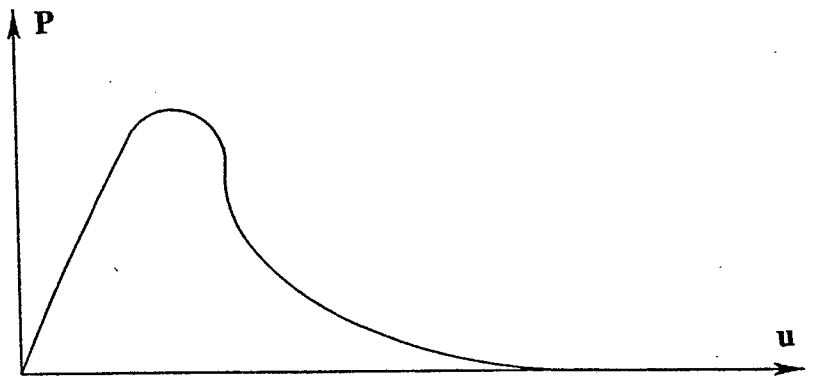

Figure 5.5 Load-deflection curve for a three point bending test.

Using an energy calculation we can determine the stiffness k necessary to obtain a stable fracture for a three-point bend test on a notched beam.
The work necessary to deflect a beam u_1 can be calculated directly from the load-deflection curve as

$$U_{beam} = \int_0^{u_1} P(u)\,du \tag{5.11}$$

If the stiffness of the testing machine is denoted k, it can be expressed as

$$k = \frac{P(u)}{u_m} \tag{5.12}$$

Introducing energy terms the total energy absorbed by the testing machine when deflecting a distance u_m is

$$U_m = \frac{1}{2}P(u)u_m = \frac{P(u)^2}{2k} \tag{5.13}$$

Using equations (5.12) and (5.13) the total energy consumption of the system can be given in differential terms as

$$\frac{\partial(U_{beam} + U_m)}{\partial u} = P(u) + \frac{P(u)}{k}\frac{\partial P(u)}{\partial u} \tag{5.14}$$

The requirement for a stable fracture must be, that the above derivative at all times is greater than zero making the total energy change of the system positive. This can in terms of stiffness requirements for the testing machine be expressed as

$$k > -\frac{\partial P(u)}{\partial u} \tag{5.15}$$

The condition for a stable fracture as given in (5.15) requires, that the testing machine always has a positive and steeper load-deformation curve than the concrete.

5.3.3 The Test Set-Up

In the present section a description of a testing machine which satisfy the established requirements in 5.3.2 will be presented.

The fact that no electro-hydraulic servo control system, with a maximum load greater than 10 kN, at the time of the tests was available at the Department of Structural Engineering motivated the building of a testing machine capable of obtaining the descending branch of the load deflection curve by manual control. Such a result can only be achieved, when tricking a conventional one way hydraulic oil pressure jack by inserting steel bars in parallel to the deformation of the jack and specimen deflection.

The effect of loading these stiffening bars in parallel on the total load-deformation diagram can be seen in Figure 5.6.

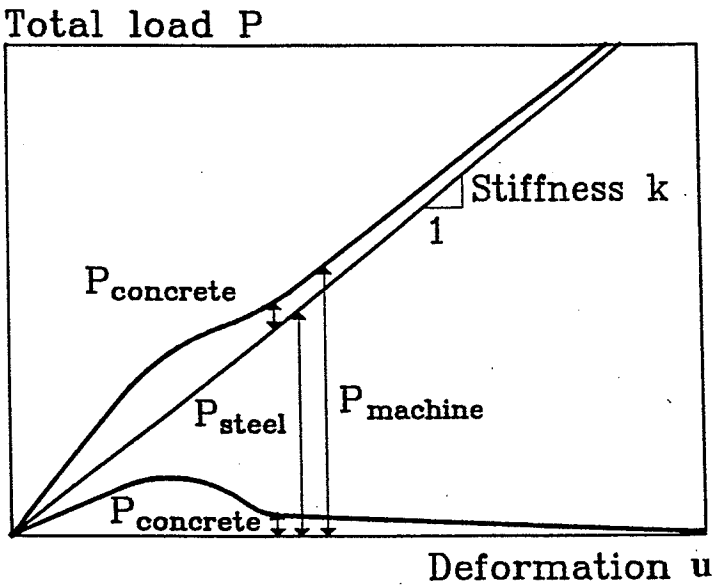

Figure 5.6 The effect of introducing steel bars on the load-deflection curve for a three point bend test.

Due to the stiffening bars, the descending branch of the concrete can be obtained in a stable manner, when the total load from the jack increases continuously for an increasing deformation. In practice this means, for the tests in question, that a testing machine has to be designed so that the stiffness has to be greater than the steepest slope of the descending part of the load-deformation curve for the concrete.

The principle of the test set-up is shown in Figure 5.7.

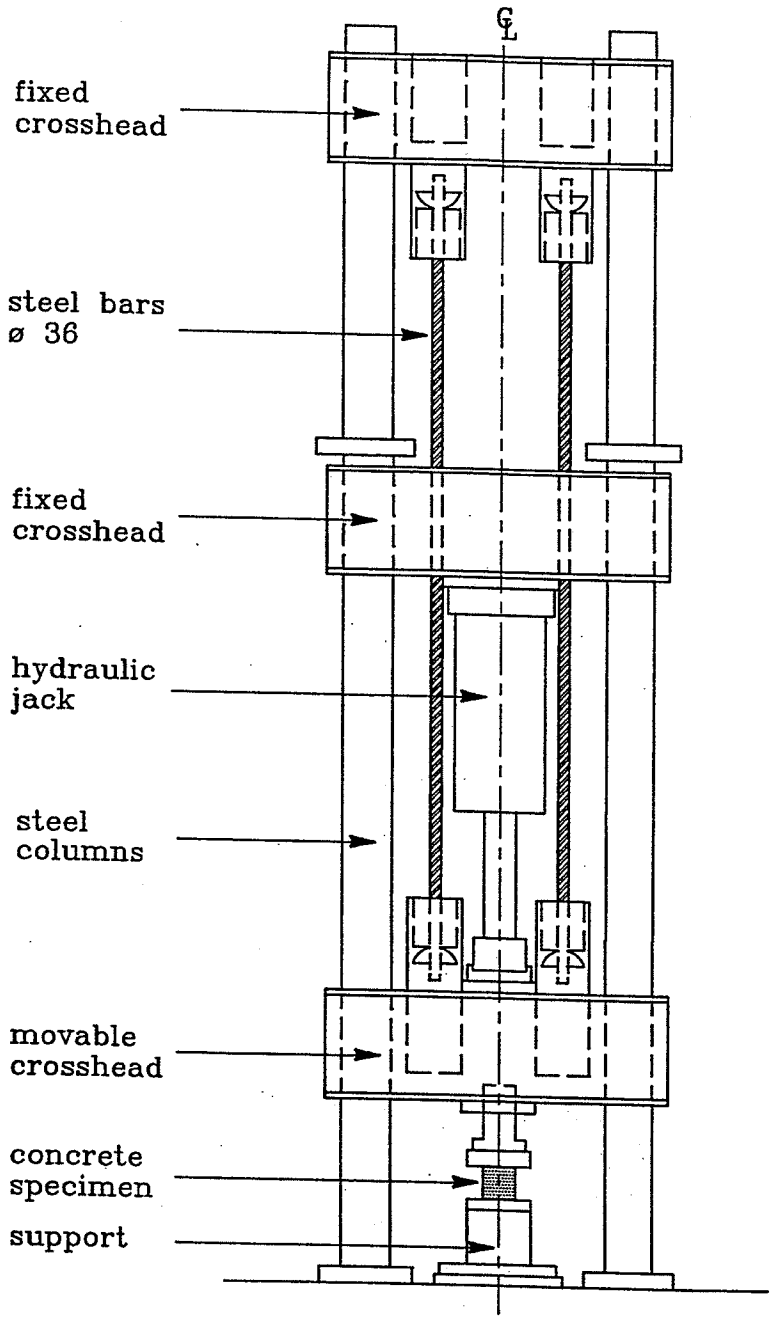

Figure 5.7 The principle of the test set-up.

The vertical load P from the pressure jack is transferred to a horizontally placed stiff yoke, which in return is held up by two stiffening steel bars. As the load is increased a vertical linear elastic deformation of the bars is initiated resulting in a controlled vertical movement of the yoke. The deformation of the yoke is transferred through a dynamometer to the concrete specimen and thereby introducing the deformation as control parameter rather than the load.

Photos of the test set-up together with pictures of the support arrangements and devices used for measurering deflections are shown in Figure 5.8 and 5.9.

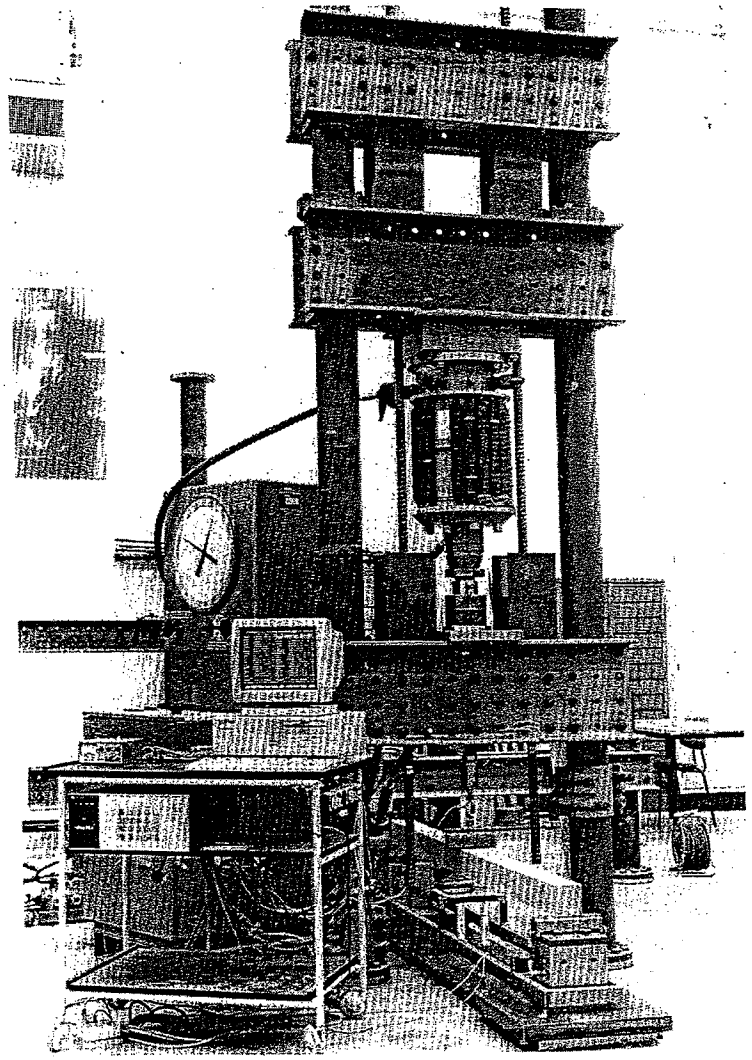

Figure 5.8 The test set-up for fracture energy tests.

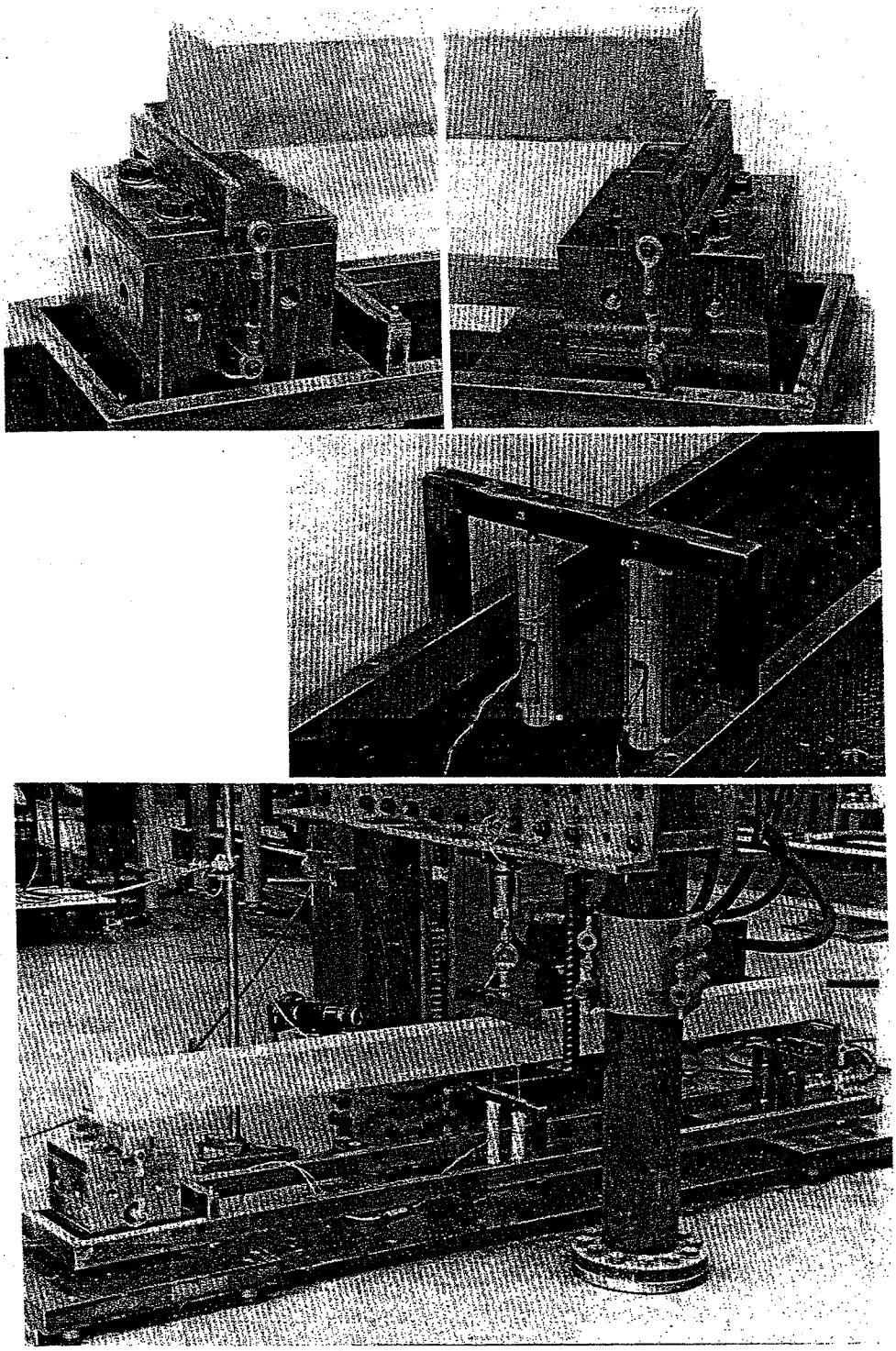

Figure 5.9 The test set-up for fracture energy tests.

5.4 Experimental Program

5.4.1 Introduction

The properties and general constituents of the concrete used in the tests will be described in this section. Furthermore a description of the mixing and casting procedure together with general procedure during handling of the concrete will be furnished on account of the specific parameters, that are varied in the tests.

5.4.2 The Test Program

The total test program comprises of 5 series (Series A - E) each representing a specific purpose and variation of specific parameters.

In Series A the main purpose is to investigate the influence of notch sensitivity and compressive strength on the fracture energy. Four different compressive strength levels are tested 30 MPa, 50 MPa, 70 MPa and 100 MPa to investigate the difference between normal and high strength concrete on the fracture energy.

Furthermore the notch sensitivity is tested using three different a/h - ratios namely 0.1, 0.25 and 0.5 .

In Series B investigation of curing conditions are analyzed to determine the influence of shrinkage and damage ratio on fracture mechanics parameters. Two different compressive strength levels are examined, a normal strength concrete (30 MPa) and a high strength concrete (100 MPa).

In Series C the aim is to reveal the influence of maximum aggregate size and type of aggregate on fracture mechanics parameters. Two compressive strength levels are examined; 30 MPa and 100 MPa. For each strength level the maximum aggregate size d_{max} is varied from 4 mm over 8 mm to 16 mm making a total of 24 test beams for each strength level. Also pure cement paste was considered (d_{max} = 0 mm). The aggregates used in this series was sand (0-4 mm) and natural gravel (4-8 mm) from Danish marine deposits and crushed granite (8-16 mm).

In Series D the air-content is varied to examine the influence of this parameter on the fracture of concrete.

In Series E a small investigation of size effects is carried out where the length of the beams are varied from 550 mm to 2000 mm.

5.4.3 Properties of the Concrete

Cement : During the whole test series the Danish Rapid Hardening Portland Cement, ASTM Type III, supplied by AAlborg Portland, Denmark is used. The Danish classification is PC (R/IS/MA/G).
This specific cement is used in the tests primarily because of its rapid strength development. The fact that this type of cement develops a higher rate of heat is assumed of minor consequence for the test results. Approximately 5 % fly ash is admixed to the cement. The cement has a fineness of 430 m^2/kg according to the Blaine method. The specific gravity is 3100 kg/m^3.

Fly Ash : Fly Ash or pulverized-fuel ash from the combustion of coal used in power stations is added to some of the mixes in order to improve workability of the concrete due to the lubricating effect of the spherical particles.
Fly ash was supplied by Amagerværket, Copenhagen. Specific gravity was assumed to be 2200 kg/m^3.

Silica Fume Slurry: Special micro silica fume in liquid state (slurry) was used from Elkem Materials Ltd., Norway. Certified by Dantest and applied with the certification 104 MSK/S. The use of silica fume as replacement of a part of the cement gives a considerable strength gain and is an essential factor for producing concrete with a compressive strength level that exceeds 80 MPa. The micro silica slurry used contained a dry-matter percentage of 51.6, and has a density of 1391 kg/m^3.

Fine Aggregate : Sand (0 - 4 mm) from Danish marine deposits. Specific gravity was 2567 kg/m^3.

Coarse Aggregate : Natural gravel called gravelit (4 - 8 mm) from Danish marine deposits. Specific gravity was 2627 kg/m^3.
Crushed granite (8 - 16 mm) from Kalundborg. Specific gravity was 2735 kg/m^3.

Admixtures : Plasticizer CONPLAST 212 which fulfill the requirements in BS 5075 part 1, 1982 and ASTM C 494 type A. CONPLAST 212 is a Lignosulphonate based plasticizer and has a density of 1170 kg/m^3, and a dry-matter percentage of 36.

Superplasticizer PERAMIN F is a Melamine based superplasticizer and has a density of 1210 kg/m^3 and a dry-matter percentage of 34. Plasticizers and superplasticizers are essential for producing a workable high strength concrete.

Water : Tap water from the city's network was used.

5.4.4 Mixing Proportion for Series A, B and E

In this experimental program a set of concrete recipes was established for the four compressive strength levels investigated. These sets of recipes are based more or less on conventional mixing technologies, and contains constituents that are normally used in concrete production. In the following these recipes will be characterized as a set of standard recipes.

For the test series A, B and E the standard recipes are shown in Table 5.1. Four different mixing proportions were applied to create the necessary strength levels.

Expected Compressive Strength	30 MPa	50 MPa	70 MPa	100 MPa
Materials	kg/m^3	kg/m^3	kg/m^3	kg/m^3
Portland Rapid Cement	188	260	305	390
Fly Ash	80	40	-	-
Mikrosilica Fume-Slurry	-	36	60	80
Sand 0 - 4 mm	640	600	558	521
Natural Gravel 4 - 8 mm	272	257	273	247
Crushed Gravel 4 - 16 mm	1089	1026	1093	989
Water	175	162	127	61
Plasticizer	-	1.33	-	2.40
Superplasticizer	-		5.81	18.04
Water-Cement Ratio	0.84	0.54	0.39	0.21

Table 5.1 Mixing proportions for the concrete in Series A, B and E.

5.4.5 Mixing Proportion for Series C

In Series C concrete with different maximum aggregate size were investigated. The standard recipes given in Table 5.1 are modified to fulfill the demand of producing concrete with a maximum aggregate size varying from 0 mm (paste) over 4 mm (mortar) and lastly to 8 mm. A normal strength admixture 30 MPa and a high strength 100 MPa were investigated. See Table 5.2.

Aggregate size d_{max}	0 mm		4 mm		8 mm	
Compressive Strength	30 MPa	100 MPa	30 MPa	100 MPa	30 MPa	100 MPa
Materials	kg/m^3	kg/m^3	kg/m^3	kg/m^3	kg/m^3	kg/m^3
Rapid Cement	188	390	354	390	206	390
Fly Ash	80	-	80	-	80	-
MSF-Slurry	-	80	-	80	-	80
Sand 0-4 mm	-	-	2001	1757	640	521
Gravel 4-8 mm	-	-	-	-	1361	1236
Water	175	61	313	61	190	61
Plasticizer	-	2.00	-	2.40	-	2.40
Superplasticizer	-	15.40	-	60.00	-	18.04
w/c	0.84	0.21	0.84	0.21	0.84	0.21

Table 5.2 Mixing proportions for the concrete in series C.

5.4.6 Mixing Proportion for Series D

The second modification of the standard recipes were applied in order to investigate the influence of air in the concrete. In Table 5.3 each constituent and their amount are shown. As air-entraining agent CONPLAST 316 AEA was used. CONPLAST 316 AEA fulfills the requirements in BS 5075 part 2 and ASTM C 260-74 and has a density of 1020 kg/m^3 and a dry-matter percentage of 11.

Two different intended air content of 5% and 10% was investigated for a normal and high strength concrete.

Expected Air Content	5 %		10 %	
Expected Compressive Strength	30 MPa	100 MPa	30 MPa	100 MPa
Materials	kg/m^3	kg/m^3	kg/m^3	kg/m^3
Portland Rapid Cement	197	415	265	420
Fly Ash	80	-	40	-
Mikrosilica Fume-Slurry	-	80	36	80
Sand 0 - 4 mm	540	474	508	474
Gravel 4 - 8 mm	297	259	280	259
Gravel 4 - 16 mm	1164	1024	1095	1024
Water	165	61	162	61
Plasticizer	-	2.40	1.33	2.40
Superplasticizer	-	18.04	-	18.04
Air-Entraining Agent	0.393	0.643	0.643	0.993
Water-Cement Ratio	0.76	0.20	0.53	0.20

Table 5.3 Mixing proportions for the concrete in series D.

5.4.7 Mixing of Test Specimens

During mixing of each batch of concrete a 0.3 m^3 capacity paddle mixer was used. Sand and coarse aggregate were mixed in dry condition for approximately 3-4 minutes after which the cement and if necessary fly ash were added. After a period of 4 minutes with continuing mixing, the remaining constituents i.e. water, micro silica slurry, air entraining agent, plasticizer and super plasticizer were blended together and slowly added to the mix. Further mixing continued for approximately 2 minutes while superplastisizer was added to the mix until adequate workability was obtained.

Prior to casting the slump and air content of the fresh mix was measured according to *DS 423.12*, **[84.4]** and *DS 423.15*, **[84.5]** respectively.

Only one mix was required to produce the necessary amount of test beams and cylinders of every batch.

5.4.8 Casting and Curing of Test Specimens

The specimens in one series, consisting of 6 beams, were cast together with 12 cylinders from one batch of concrete simultaneously. The specimens were cast in plywood moulds. Two different types of moulds were used. The first mould was used for specimens having the required geometrical standards used by ***RILEM*** **[85.1]** and a second mould was used for varying the specimen length. See section 5.9.

6 cylinders, ø 100x200 mm^2 from each batch were cast in polyethylene moulds and 6 cylinders ø 150x300 mm^2 were cast in steel moulds. The cylinders were used for measurering the compressive strength and the splitting strength respectively.

Before assembling the moulds, its mating surfaces was covered with mineral oil and a thin layer of similar oil was applied to the inside surfaces of the moulds in order to reduce the development of bond between the moulds and the concrete.

The specimens and cylinders were all vibrated on a vibrating table.

After casting, the specimens were covered by plastic. After approximately 24 hours the formwork was removed and the specimens were, with the exception of Series B, all cured in lime saturated water for 28 days after which testing began.

5.4.9 Procedure for Cylinder Tests

In order to obtain a detailed knowledge of the test beams used, cylinders used for measurering the compressive strength f_c, the splitting strength f_{sp} and the modulus of elasticity E_c were cast and tested together with the test beams.

For each batch 6 cylinders ø 100x200 mm^2 were tested in order to determine the compressive strength. To overcome the ill-effects of an uneven end surface of the specimens a cardboard is applied to both ends of the cylinder. The compressive tests were performed with a rate of 0.4 MPa/sec and accomplished in accordance with *DS 423.23*, **[84.6]**. Three of the cylinders were applied with extensiometers making it possible to measure the secant modulus of the concrete

prior to failure. Each test used to determine the elastic modulus were done according to *DS 423.25*, **[84.7]**. The results yield a value for the modulus as a secant value of a stress-strain diagram.

Furthermore 6 ø 150x300 mm^2 cylinders were tested in order to determine the splitting strength according to *DS 423.24*, **[84.8]**. A line load was introduced by a narrow strip of plywood interposed between the load platen and the cylinder. The testing rate for the splitting experiments were 0.04 MPa/sec.

All cylinder tests were carried out using a 200 MP MFL (Prüff und Mess MFL Systeme) compressive test machine. The machine was servo controlled by a Walter und Bai SRG 5000.

5.4.10 Procedure for Specimen Tests

24 hours before testing the beams were removed from the curing basin and placed in a small transportable plastic receptacle able to contain 6 beams, 6 compressive cylinders and 6 splitting cylinders.

The beams are then sawn under wet conditions. With the exception of Series A, a notch of 3 mm width and half the beam height was cut with a diamond saw in the middle of the specimen.

Prior to testing of the beams, the weight and dimensions of each specimen were determined.

Before placing the beam in the test rig a preloading of the steel bars to 150 kN were initiated in order to obtain the maximum stiffness and stability conditions during the test.

When placed in the test rig, the instrumentation (i.e. load cell and transducers) were adjusted and a preloading of the beam to approximately 1/10 of the maximum load was done in order to detect any discrepancies in the signals and the loading arrangement. After this, an unloading took place and the actual test could commence.

The test was performed with a constant rate of deformation of 0.1 mm/min.

5.5 Experimental Results for Series A

5.5.1 Introduction

The primary aim in this series is to determine any relationship between the compressive strength and the notch length on the fracture energy of concrete. The beam specimens used for this purpose has the dimensions suggested by ***RILEM*** **[85.1]** (i.e. b x h x L = 100 x 100 x 800 mm^3).

Three compressive strength levels are chosen, 30 MPa, 50 MPa, 70 MPa and 100 MPa. Within each strength level the notch-height, a/h, ratio is varied from 0.1 - 0.25 - 0.5.

5.5.2 Results of Cylinder Tests

In Table 5.4 the results of the compressive strength, splitting strength and modulus of elasticity are given for each batch. The compressive and splitting tests are a mean value of 6 cylinders, while the mean value of 3 cylinders were used for determining the modulus of elasticity. Figure 5.10 shows a comparison between the compressive and splitting strength of concrete together with the proposed relationship given by the Danish code of practice, ***DS 411***, **[84.3]**.

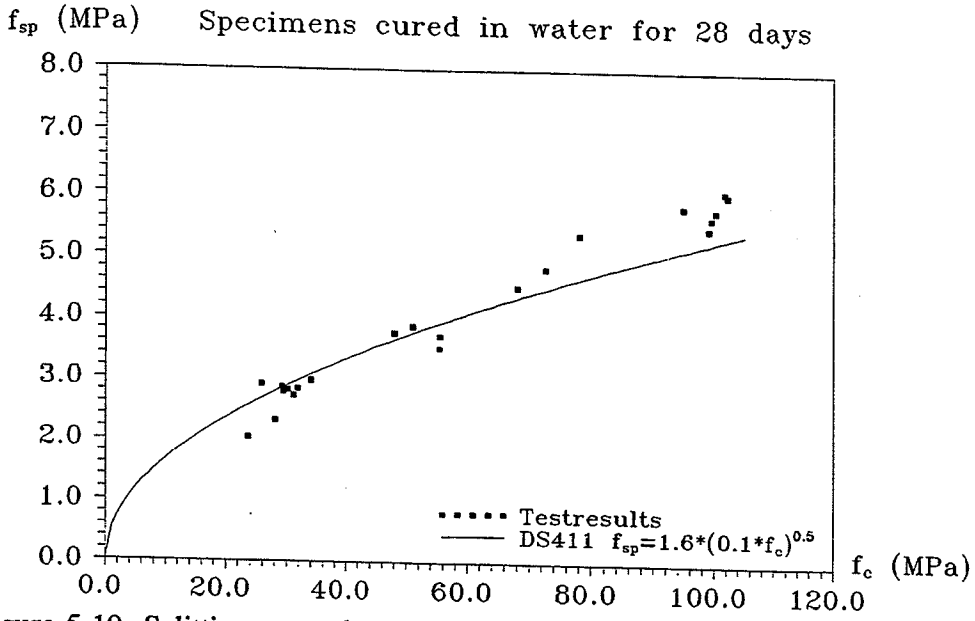

Figure 5.10 Splitting strength as a function of the compressive strength.

In Figure 5.10 the test results are compared with the formula from the Danish code given by

$$f_{sp} = 1.6\sqrt{0.1 f_c} \tag{5.16}$$

For normal strength concrete the relationship must be considered good. For high strength concrete, however, the formula tends to underestimate the splitting strength.

Batch No	Compressive Tests f_c (MPa)		Splitting Tests f_{sp} (MPa)		Modulus of Elasticity E_c (MPa)	
	Mean Value	Standard Deviation	Mean Value	Standard Deviation	Mean Value	Standard Deviation
A-B30.1	28.1	1.0	2.32	0.07	26110	467
A-B30.2	29.2	1.4	2.87	0.11	27220	147
A-B30.2N	31.8	2.9	2.84	0.15	27330	354
A-B30.3	29.5	1.1	2.79	0.10	25600	606
A-B30.3N	25.8	1.5	2.90	0.44	25160	319
A-B50.1	51.0	1.5	3.87	0.22	33640	824
A-B50.2	55.5	1.6	3.72	0.35	32490	1322
A-B50.3	55.4	1.9	3.52	0.40	-	-
A-B50.3N	48.0	0.5	3.76	0.21	32950	209
A-B70.1	78.0	1.6	5.38	0.34	37330	1058
A-B70.2	68.1	2.8	4.52	0.20	33800	231
A-B70.3	72.6	0.9	4.82	0.14	35300	1344
A-B100.1	99.4	2.8	5.66	0.24	42070	2620
A-B100.2	100.1	3.6	5.78	0.27	42240	1280
A-B100.3	99.0	2.6	5.49	0.35	42210	1167

Table 5.4 Cylinder values for the concrete in series A.

In order to check the suitability of the standard mixes the rate of gain in the strength of the concrete was considered. See Table 5.5 and Figure 5.11. These tests were performed under the same curing conditions, as the cylinders used for reference. They were all cured in lime saturated water and tested at the age of 7, 14, 21 and 28 days.

	Compressive Strength in MPa.			
Batch No	7 Days	14 Days	21 Days	28 Days
A-B30.4	14.7	19.6	22.2	23.7
A-B50.3N	30.8	40.9	44.6	48.0
A-B70.2	47.6	58.8	64.0	68.1
A-B100.3	71.4	84.6	95.2	99.0

Table 5.5 Compressive strength development for cylinders in Series A.

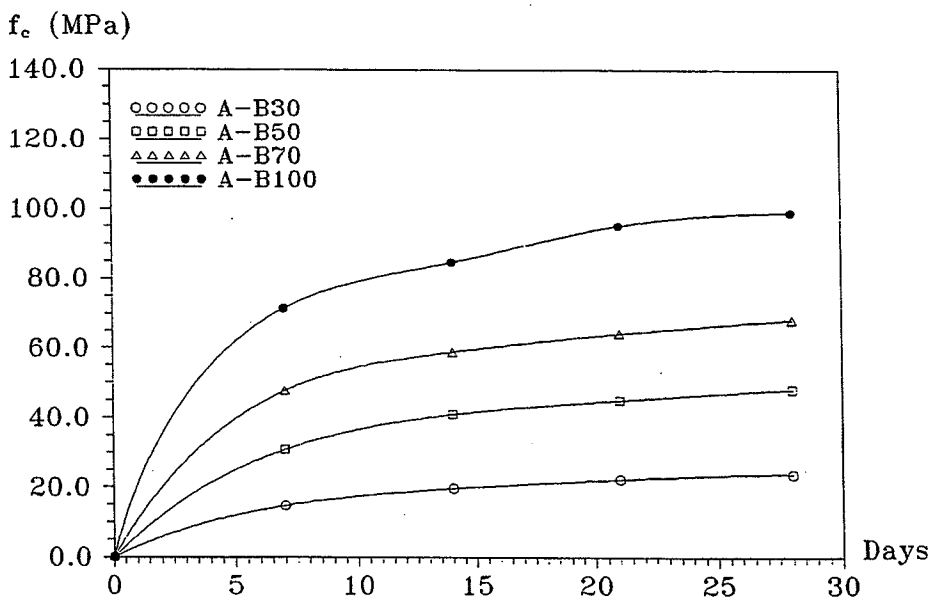

Figure 5.11 Compressive strength development for cylinders in Series A.

The results are evident, shoving that the use of Rapid Portland Cement results in a rapid gain in strength, so that 60% of the compressive strength is reached within 7 days of curing.

5.5.3 Results of Beam Tests

In order to determine the fracture energy of concrete according to ***RILEM*** **[85.1]** the full load deflection curve has to be established.

In Figure 5.12 and Figure 5.13 the load deflection curves are given for different concrete strengths and a/h-ratios. From the curves it can be seen, that the maximum load increases with increasing compressive strength and that the deformation at maximum load is independent of concrete strength and notch height. The value is approximately equal to 0.2 mm. As the strength increases the ultimate deformation (deflection at rupture) decreases. Furthermore the descending branch of the load deflection curve is steeper for high strength concrete than for normal strength concrete. It is interesting to note, that by increasing the notch height the descending branch decreases in steepness. This is more clearly illustrated in Figure 5.14 and Figure 5.15 where load deflection curves for different a/h-ratios are given.

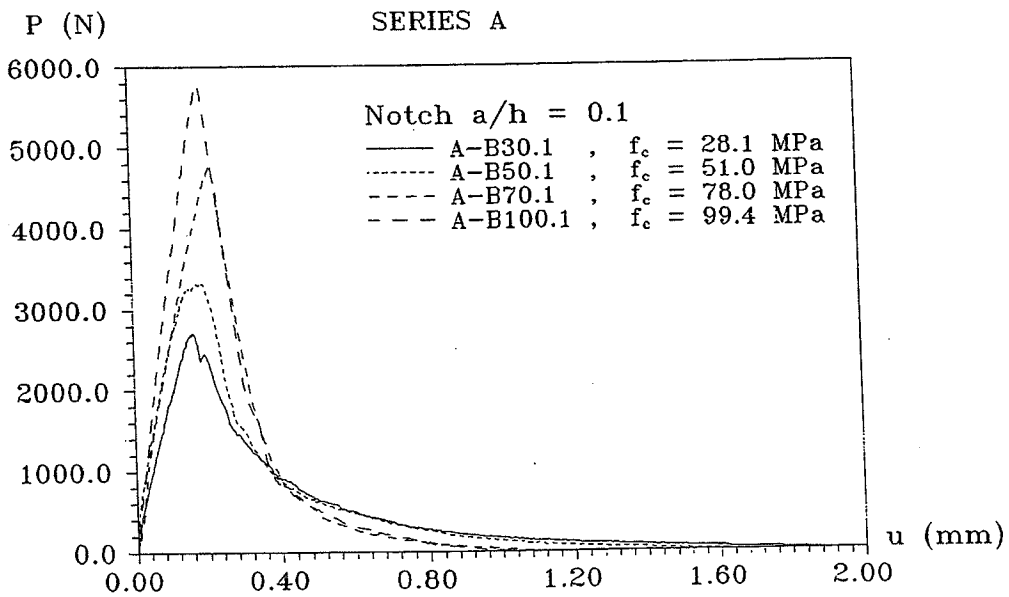

Figure 5.12 Load-deflection curves for different compressive strength levels.

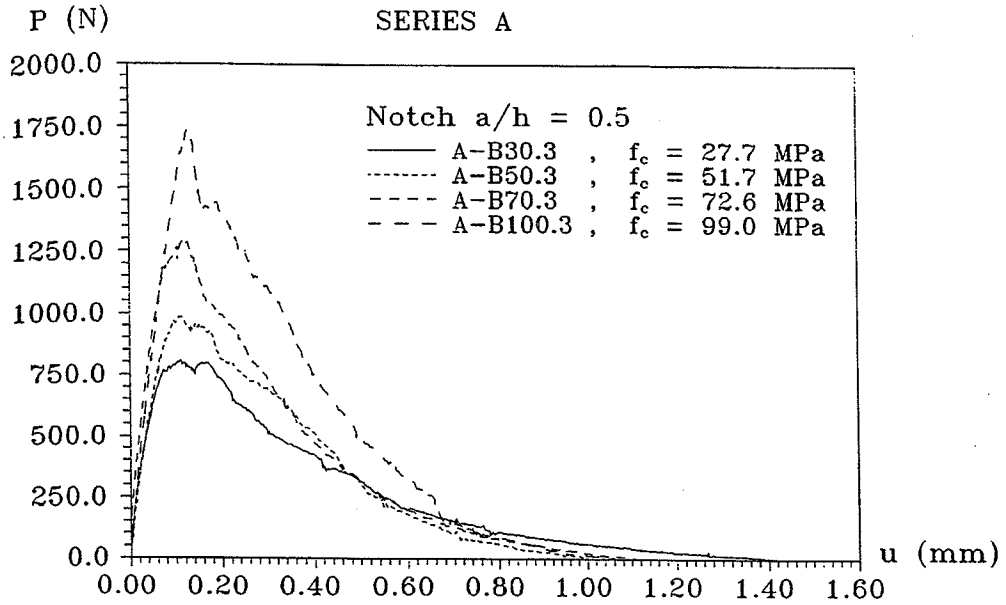

Figure 5.13 Load-deflection curves for different compressive strength levels.

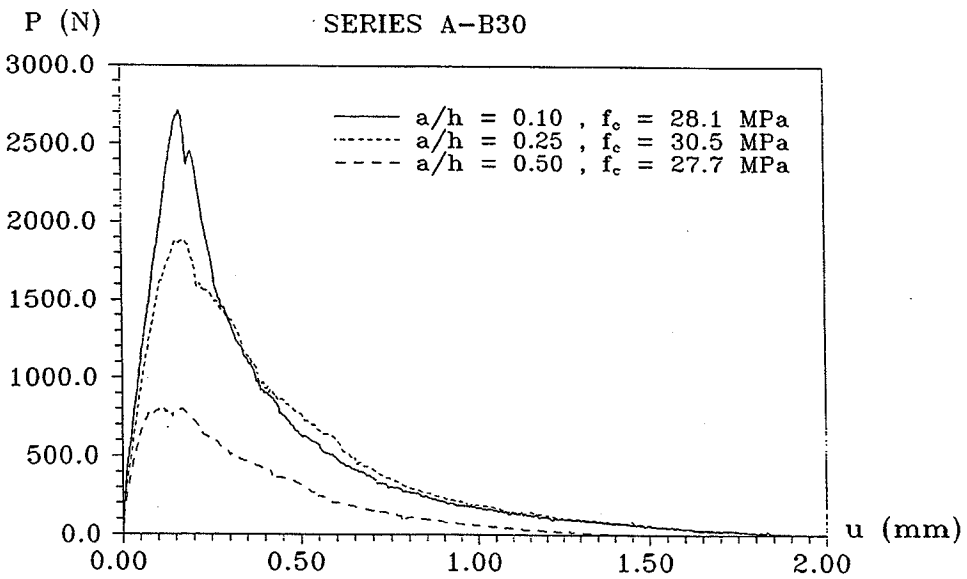

Figure 5.14 Load-deflection curves for different a/h- ratios, $f_c \approx 30$ MPa.

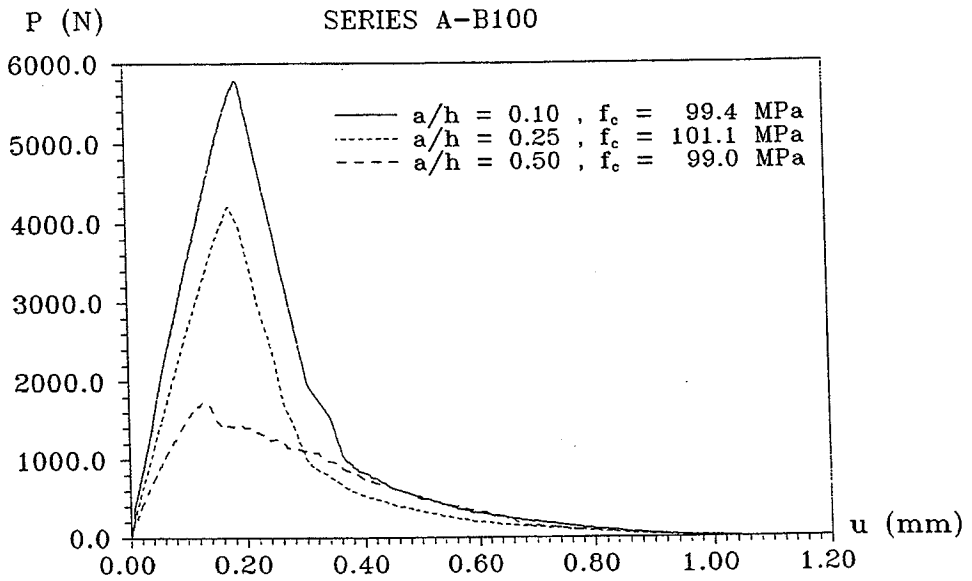

Figure 5.15 Load-deflection curves for different a/h-ratios, $f_c \approx 100$ MPa.

Each curve in Figure 5.12 - 5.15 is an average curve from a batch of 6 beam tests made. In Appendix I all test results are given together with beam data and the observed value of maximum load and deflection.

In Table 5.6 the results of the calculated fracture energies and flexural strengths from the measured load-deflection curves are listed. Each batch no. refers to a mean value of at least 6 beams. The data are in Figure 5.16 and Figure 5.17 depicted in a (f_c,G_F) and (a/h,G_F) diagram. It is clear from these figures, that an increase in the compressive strength (and tensile strength) has a tendency to cause a rise in the G_F-value.

A variation with regard to the notch depth is almost negligible. Figure 5.17 shows the variation of G_F with a/h and a small decrease in the fracture energy with increasing a/h-ratio can be observed. It can, however, not be excluded that the decrease is a result of a general high scatter in the calculated values for G_F. The decrease in G_F is only 8 - 12%, when increasing the a/h-ratio from 0.1 to 0.5.

	a/h -	f_c (MPa)	G_F (N/m)		f_f (MPa)	
Batch No		Mean Value	Mean Value	Standard Deviation	Mean Value	Standard Deviation
A-B30.1	0.10	28.1	132.5	36.8	3.89	0.35
A-B30.2*	0.25	30.5	139.8	58.2	4.15	0.41
A-B30.3*	0.5	27.7	122.8	27.3	4.18	0.53
A-B50.1	0.10	51.0	144.5	20.2	5.49	0.34
A-B50.2	0.25	55.5	138.8	18.9	5.71	0.45
A-B50.3*	0.50	51.7	117.6	28.6	5.72	0.56
A-B70.1	0.10	78.0	158.1	13.0	6.99	0.24
A-B70.2	0.25	68.1	136.1	19.3	6.18	0.26
A-B70.3	0.50	72.6	125.0	14.8	6.54	0.24
A-B100.1	0.10	99.4	166.3	15.3	8.92	0.43
A-B100.2	0.25	100.1	151.0	13.1	9.07	0.35
A-B100.3	0.50	99.0	152.2	25.5	8.80	1.03

* 12 beams were tested.

Table 5.6 Summary of test results for Series A.

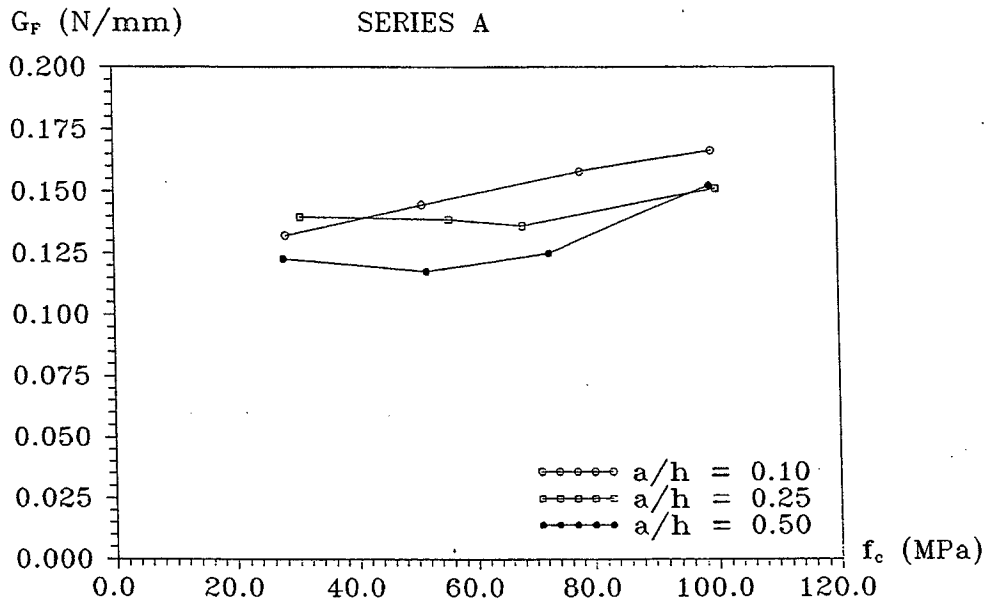

Figure 5.16 Fracture energy as a function of the compressive strength in Series A.

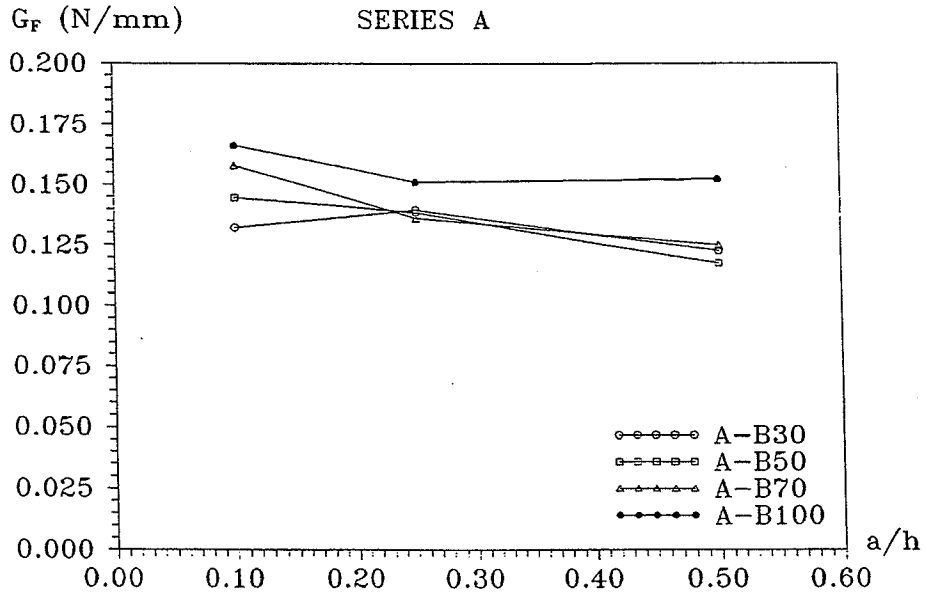

Figure 5.17 Fracture energy as a function of a/h in Series A.

In the first draft of the ***CEB-FIB Model Code 1990*** **[90.2]**, a relationship between the compressive strength and the fracture energy is given. It is proposed, that "in absence of experimental data" G_F may be estimated by

$$G_F = \alpha_F f_c^{0.7} \tag{5.17}$$

In the above formula f_{ck} is the compressive characteristic strength and α_F is a coefficient depending on the maximum aggregate size d_{max}. For d_{max} equal to 16 mm α_F takes the value 6.

The test results from Series A have in Figure 5.18 been been depicted together with the calculated values obtained by using equation (5.17). The tendency for G_F to increase with increasing compressive strength coincides well with the experimental results.

The calculated values recomended by the ***CEB Model Code 1990*** are, however, on the conservative side for concrete with a strength level below approximately 80 MPa.

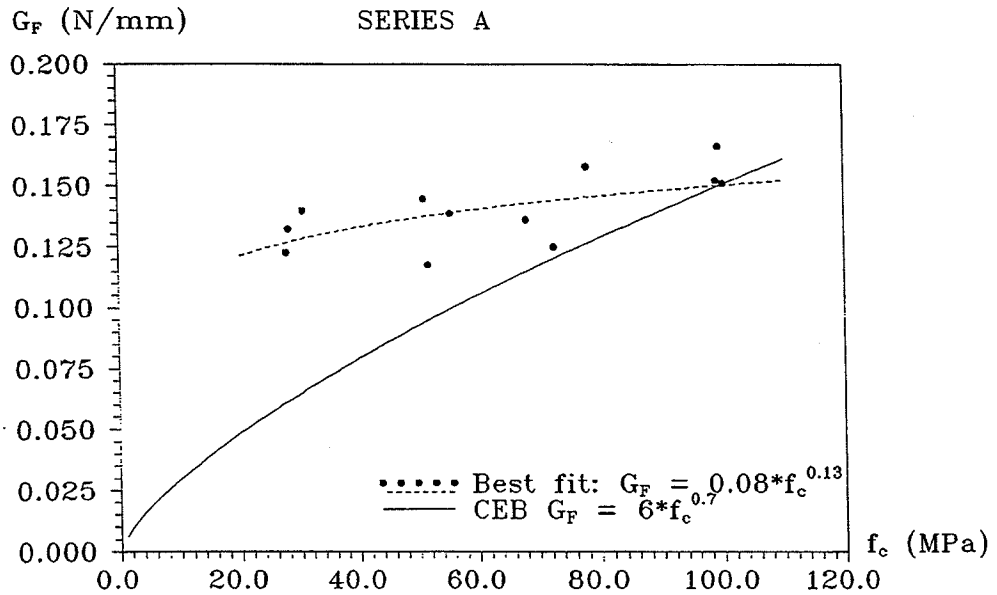

Figure 5.18 Fracture energy tests compared to ***CEB Model Code 1990*** **[90.2]**.

5.6 Experimental Results for Series B

5.6.1 Introduction

In connection with establishing test results for concrete members curing conditions must always be kept as identical as possible. Differences in curing conditions can make comparisons of test results from different laboratories difficult.

According to the specification given in ***RILEM*** **[85.1]**, test beams for determining the fracture energy should be kept in lime saturated water during the whole curing period (approximately 28 days). Four different curing conditions, that deviates from the ***RILEM*** specification, are investigated in this section. Two different compressive strength levels are used, 30 MPa and 100 MPa.

The first batch (B-B30.1 and B-B100.1) was placed outside after casting during the whole curing period. The temperature varied between 10 °C and 20 °C with the relative humidity RH being approximately 75 %.

The second batch (B-B30.2 and B-B100.2) was prior to casting placed in a heating chamber during the whole curing period. The temperature was kept constant at 40 °C and RH was 34 %.

In order to detect any effects of changing the curing conditions during the 28 days before the elements were tested, the third batch (B-B30.3 and B-B100.3) were cured in water for 14 days (20 °C) and in a heating chamber for 14 days at 40 °C and RH at 34 %.

The last batch (B-B30.4 and B-B100.4) were cured in water for 28 days (20 °C) and in a heating chamber for 161 days at 40 °C and RH at 34 %.

General test procedures are explained in section 5.4. The beam specimens used were identical to the beams tested in Series A (i.e. b x h x L = 100 x 100 x 800 mm^3) with a notch-hight (a/h) ratio of 0.5.

5.6.2 Results of Cylinder Test

In Table 5.7 and 5.8 the results of the obtained cylinder data are given. As can be seen from Table 5.8 the results reflects, that a moderate rise in temperature (Curing condition 1 and 3) beneficially affects the early strength of concrete without any ill-effects on the later strength. See also Table 5.5 where the compressive strength development for Series A are given. A higher temperature during placing and setting (Curing condition 2), however, adversely affects the strength from about 7 days onwards. This is more pronounced for normal strength concrete, than for high strength concrete.

	Cur*	Compressive Tests f_c (MPa)		Splitting Tests f_{sp} (MPa)		Modulus of Elasticity E_c (MPa)	
Batch No		Mean Value	Standard Deviation	Mean Value	Standard Deviation	Mean Value	Standard Deviation
B-B30.1	1	26.7	1.8	1.95	0.12	24380	834
B-B30.2	2	15.8	0.6	2.02	0.13	15320	1310
B-B30.3	3	34.4	1.4	3.86	0.07	28480	1075
B-B30.4	4	32.4	1.4	3.10	0.12	-	-
B-B100.1	1	83.7	2.6	6.27	0.59	36210	1315
B-B100.2	2	90.6	1.9	4.93	0.51	36900	2066
B-B100.3	3	106.9	5.4	6.47	0.45	41440	203
B-B100.4	4	104.7	3.6	5.86	0.32	-	-

* 1. Specimens were cured outdoor for 28 days at about 20 °C and 75 % RH.
2. Specimens were cured in a heating chamber for 28 days at 40 °C and 34 % RH.
3. Specimens were cured in water for 14 days (20 °C) and in a heating chamber for 14 days at 40 °C and 34 % RH.
4. Specimens were cured in water for 28 days (20 °C) and in a heating chamber for 161 days at 40 °C and 34 % RH.

Table 5.7 Cylinder data for the concrete in Series B.

	Compressive Strength in MPa.				
Batch No	7 Days	14 Days	16 Days	21 Days	28 Days
B-B30.1	16.2	20.4	-	23.8	26.7
B-B30.2	14.6	16.4	-	16.6	15.8
B-B30.3	17.4	20.9	24.1	32.3	34.4
B-B100.1	65.4	76.8	-	83.2	83.7
B-B100.2	92.5	93.7	-	91.1	90.6
B-B100.3	75.0	81.3	99.3	103.4	106.9

Table 5.8 Compressive strength development for cylinders in Series B.

5.6.3 Results of Beam Tests

The influence on the load-deflection curves, when varying the curing conditions for the beams, can be seen in Figure 5.19 for normal strength concrete and in Figure 5.20 for high strength concrete. In the figures the results of beams tested with a curing condition corresponding to an environment of lime saturated water for 28 days from Series A (A-B30.3 and A-B100.3) are added.

Although nothing conclusive can be drawn from the results, it is evident, that the maximum load and deflection at rupture is significantly higher for beams cured in water for 28 days followed by an exposure to heat for 161 days (curing condition 4).

As was the case for Series A, the maximum load increases with increasing compressive strength, and the deformation at maximum load is fairly independent of concrete strength and curing condition.

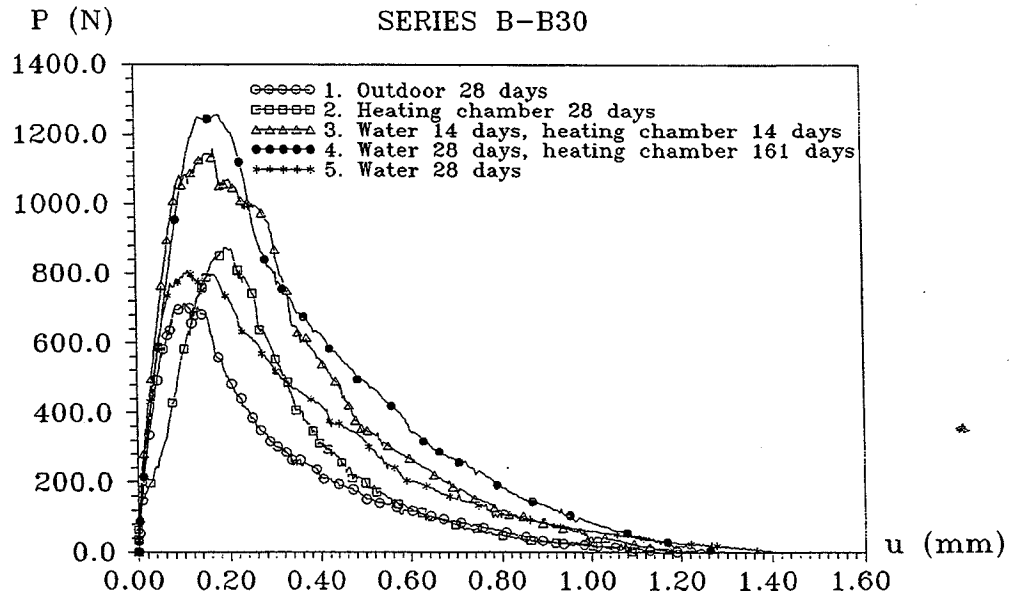

Figure 5.19 Load-deflection curves for Series B-B30.

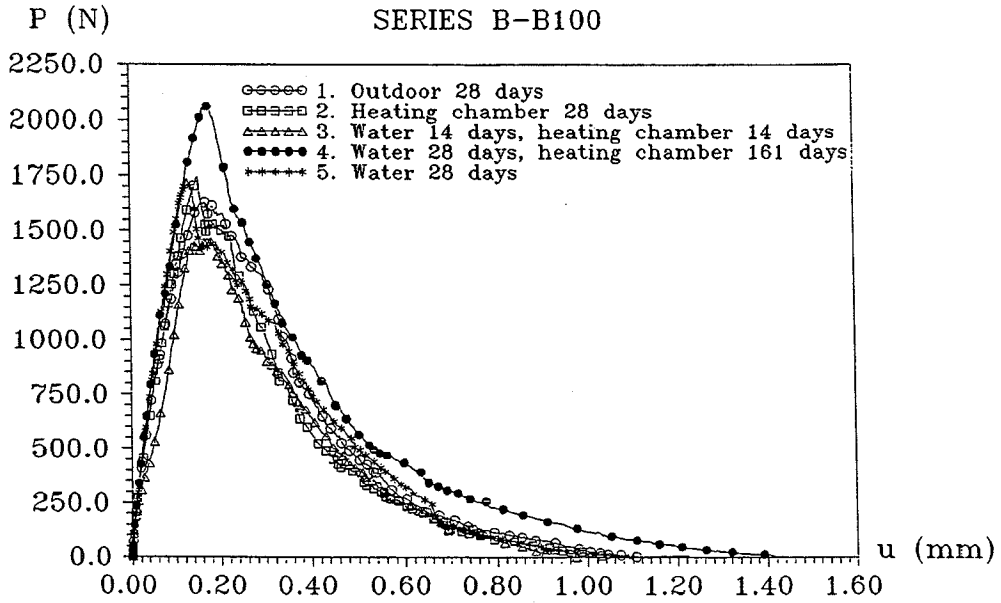

Figure 5.20 Load-deflection curves for Series B-B100.

The main results of tests on beam specimens in Series B are summarized in Table 5.9. Results of the fracture energy G_F and flexural strength f_f are given as a mean value of 6 beams for each curing condition. Individual results are presented in the attached appendix.

In Figure 5.21 and 5.22 the calculated values of the fracture energy are depicted as a function of the different curing conditions. The values are supplied with data from Series A (beam no. A-B30.3 and A-B100.3), where the compressive strength and notch-hight ratio is comparable.

For a constant curing condition it can be seen, that the fracture energy increases with increasing compressive strength. The result show, that for the different curing conditions used in this test series, none or almost no effect on the fracture energy and flexural strength can be seen.

Batch No	Curing cond.*	f_c (MPa)	G_F (N/m)		f_f (MPa)	
		Mean Value	Mean Value	Standard Deviation	Mean Value	Standard Deviation
B-B30.1	1	26.7	103.4	16.3	3.75	0.23
B-B30.2	2	15.8	101.8	15.1	4.63	0.25
B-B30.3	3	34.4	131.1	21.0	5.91	0.18
B-B30.4	4	32.4	173.0	11.9	6.41	0.26
B-B100.1	1	83.7	157.3	20.2	7.72	0.26
B-B100.2	2	90.6	171.3	11.8	8.69	0.33
B-B100.3	3	106.9	143.6	19.3	7.69	0.57
B-B100.4	4	104.7	197.0	12.5	9.99	0.61

* 1. Specimens were cured outdoor for 28 days at about 20 °C and 75 % RH.
2. Specimens were cured in a heating chamber for 28 days at 40 °C and 34 % RH.
3. Specimens were cured in water for 14 days (20 °C) and in a heating chamber for 14 days at 40 °C and 34 % RH.
4. Specimens were cured in water for 28 days (20 °C) and in a heating chamber for 161 days at 40 °C and 34 % RH.

Table 5.9 Three point bending test results for Series B.

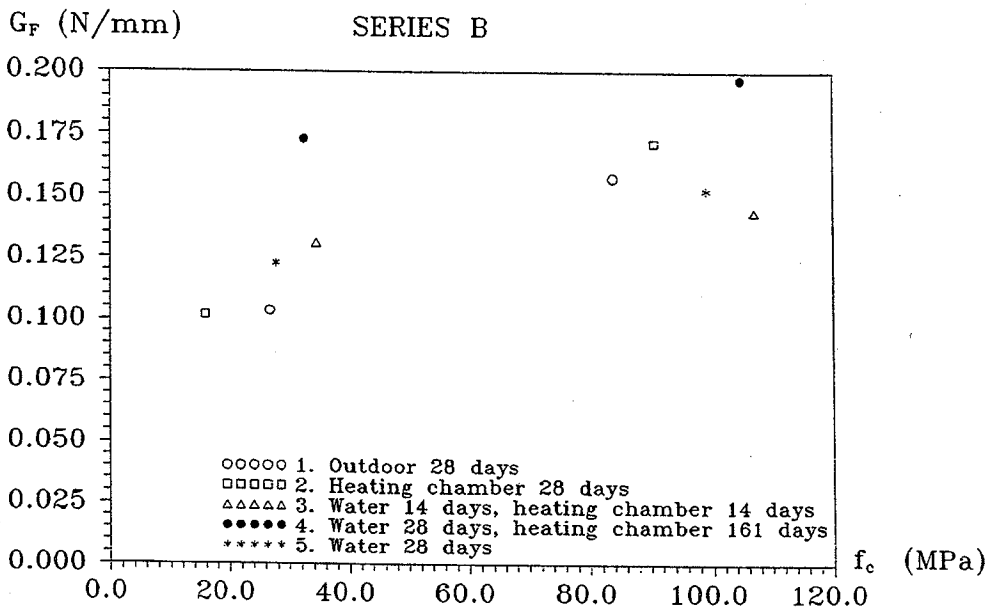

Figure 5.21 Fracture energy for concrete when changing the curing conditions.

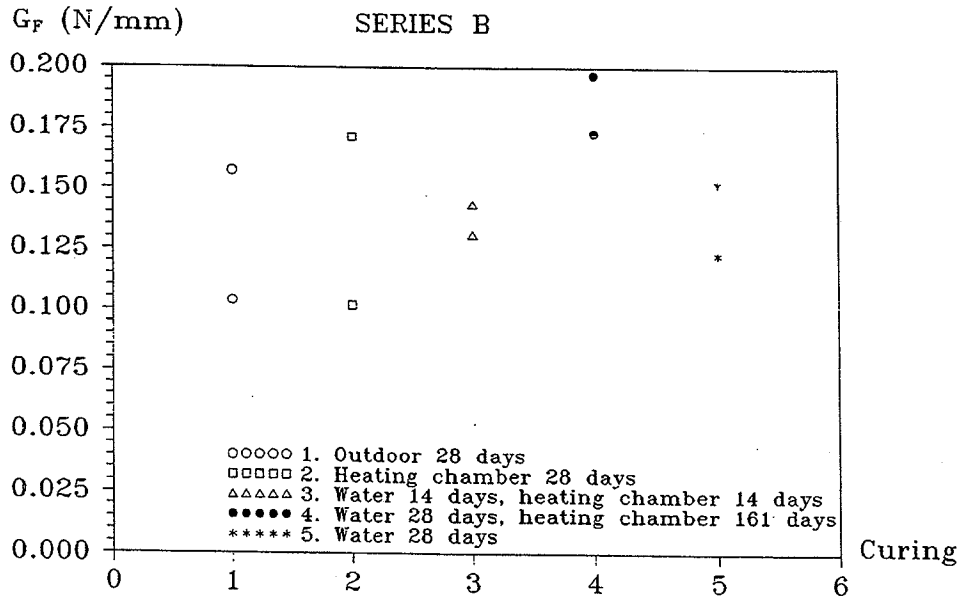

Figure 5.22 Fracture energy for concrete when changing the curing conditions.

5.7 Experimental Results for Series C

5.7.1 Introduction

In order to gain experimental results on fracture mechanics properties, an investigation, where aggregate size and grading curve are varied, is carried out. In this section results will be presented, that describes the influence, when volume concentration of coarse aggregate is varied. Further, the bond strength between the cement matrix and aggregate will be investigated for two compressive strength levels. General test procedures are explained in Section 5.4. As was the case in Series B, only the smallest beam size recommended by ***RILEM*** **[85.1]** will be used. The notch height is constant and equal to 50 mm. (a/h = 0.5)

Every test element was cured for 28 days at 20 °C in water with an admixture of lime. All test elements were tested wet as explained in Section 4.8.

It is a well known fact, that aggregates restrain the amount of shrinkage. This will result in cracking in the cement paste. All specimens in this series were kept wet during the whole curing time, which means, that possible differences in micro cracking for different aggregate sizes are left out of this investigation.

5.7.2 Results of Cylinder Tests

In Table 5.10 the results of the obtained cylinder data are given. In this series the batch number is C-Bx.y, where x represents the intended strength level and y a number 1-3. The number 1 indicates cement paste, 2 mortar and 3 concrete with d_{max} = 8 mm.

The results reflects well, what is evident from previous investigations. The modulus of elasticity increases with the concrete strength and with the maximum aggregate size.

The main purpose was to keep the compressive strength constant at a level of either 30 MPa or 100 MPa. As can be seen from Table 5.10 only batch number C-B100.2 (high strength mortar) deviates from this intent, and this must be taken into account, when comparing the fracture parameters.

Batch No	d_{max} (mm)	Compressive Tests f_c (MPa)		Splitting Tests f_{sp} (MPa)		Modulus of Elasticity E_c (MPa)	
		Mean Value	Standard Deviation	Mean Value	Standard Deviation	Mean Value	Standard Deviation
C-B30.1	0	26.9	1.3	-	-	10450	214
C-B30.2	4	24.4	0.7	2.27	0.28	22120	870
C-B30.3	8	23.3	0.4	2.51	0.21	27460	390
C-B100.1	0	98.9	6.8	4.79	0.54	26370	53
C-B100.2	4	72.5	3.0	4.78	0.29	37230	325
C-B100.3	8	94.8	4.9	5.55	0.16	41470	586

Table 5.10 Cylinder data for the concrete in Series C.

5.7.3 Results of Beam Tests

The influence of maximum aggregate size is shown in Figures 5.23 and 5.24.

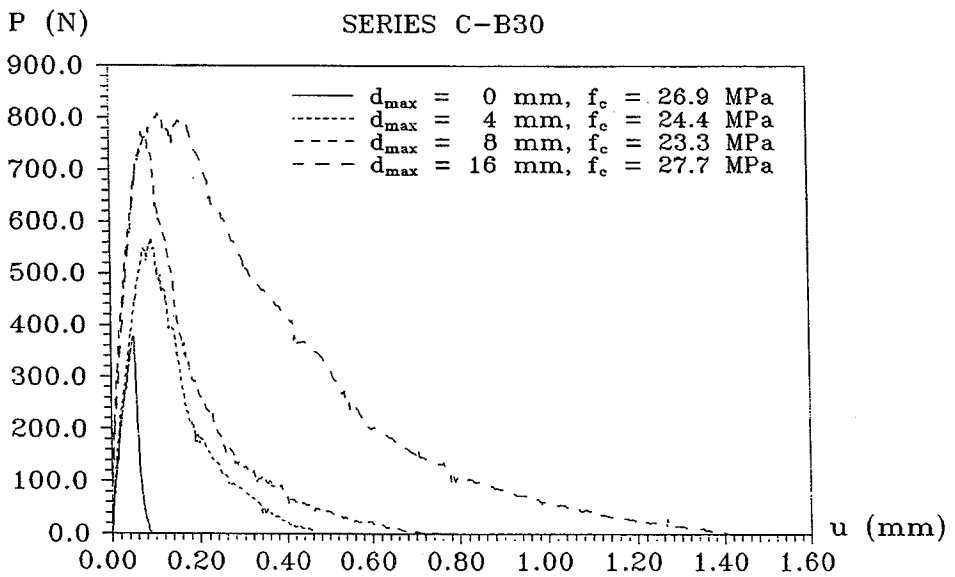

Figure 5.23 Load-deflection curves for normal strength beams with different d_{max}.

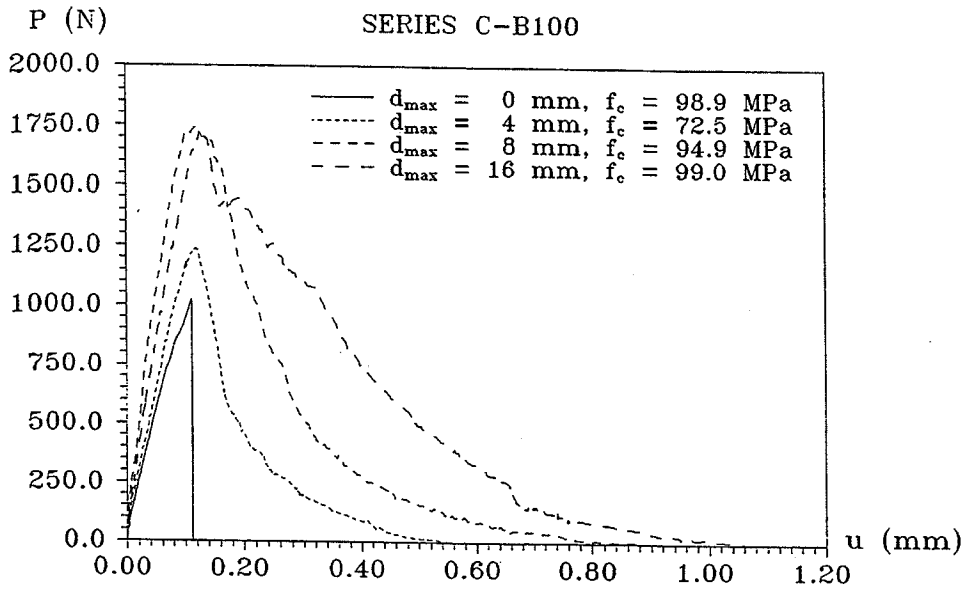

Figure 5.24 Load-deflection curves for high strength beams for different d_{max}.

The above figures are typical load-deflection curves from Series C. Figure 5.23 represents the load-deflection curves for normal strength concrete and Figure 5.24 for a high strength concrete. Similar for the two investigations are the fact, that a decrease in aggregate size results in an increase in steepness of the post-peak behaviour. There can be no doubt, that a post-peak behaviour is present even for high strength cement paste, but the post peak behaviour measured might be the result of snap back, which could not be followed by the present testing equipment. Regarding the maximum load (flexural strength) an increase can be seen from cement paste to mortar and further on to concrete. This increase, however, is not so pronounced, when increasing the aggregate from 8 mm to 16 mm. The reader must bear in mind, that these observations are not drawn from individual tests but from a mean value of at least 6 tests. Individual results are presented in the attached appendix.

The main results of tests on specimens in Series C are summarized in Table 5.11. Results of the fracture energy G_F and flexural strength f_f are given for different concrete mixes, where the aggregate size has been varied.

	d_{max} mm	f_c (MPa)	G_F (N/m)		f_f (MPa)	
Batch No		Mean Value	Mean Value	Standard Deviation	Mean Value	Standard Deviation
C-B30.1	0	26.9	6.7	1.3		
C-B30.2	4	24.4	34.9	3.0	3.23	0.24
C-B30.3	8	23.3	57.4	5.2	3.94	0.14
C-B100.1	0	98.9	20.2	6.0		
C-B100.2	4	72.5	57.8	4.1	6.03	0.34
C-B100.3	8	94.9	118.5	19.2	8.41	0.93

Table 5.11 Summary of test results for Series C.

In Figure 5.25 and Figure 5.26 the fracture energy G_F is plotted against the maximum aggregate size and compressive strength respectively.

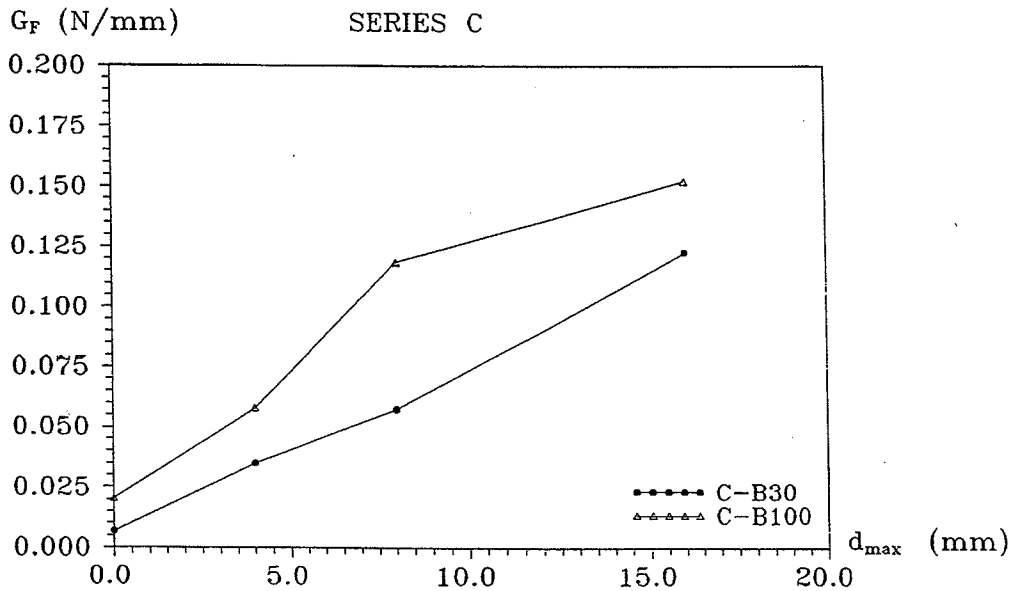

Figure 5.25 Fracture energy for concrete with different d_{max}.

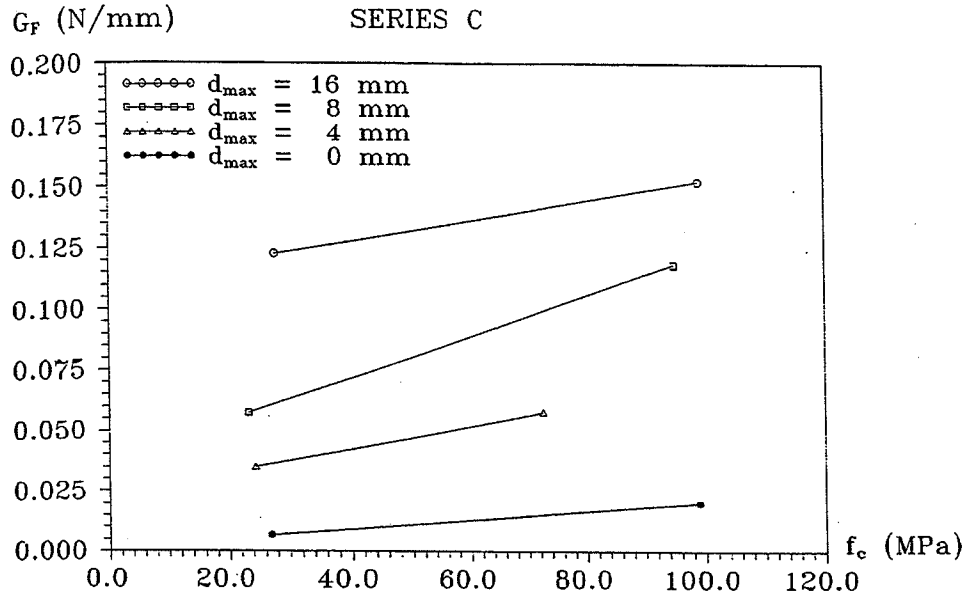

Figure 5.26 Fracture energy for concrete with different d_{max}.

A distinctive dependence between the fracture energy and maximum aggregate size is discernable. When the maximum aggregate size d_{max} and volume concentration of coarse aggregate are increased, the fracture energy increases. In the figures the experimental data from Series A (A-B30.3 and A-B100.3) are added. For normal strength concrete this increase can be explained by the development of a more tortuous crack path, when testing concrete with larger grains. In this case the cement paste is comparably weaker than the grains i.e. the crack runs through the paste and at the interfaces between the grains and the paste. In Figure 5.27 photos of the fracture areas for normal strength concrete are given. When the grain size exceeds 4 mm, a clear illustration of a more tortuous crack path can be observed. The grains are seen to be pulled out of the cement matrix transferring friction forces over the crack. When the cement paste reaches the strength of the aggregate either due to the increased strength of the paste in the case of high strength concrete or due to a relative weak aggregate, the crack will split most of the grains in the concrete. In Figure 5.28 pictures of the fracture areas for a high strength concrete are illustrated for different maximum aggregate sizes. The load carrying capacity for greater crack width decreases rapidly, which is the reason for the more brittle behaviour of high strength concrete.

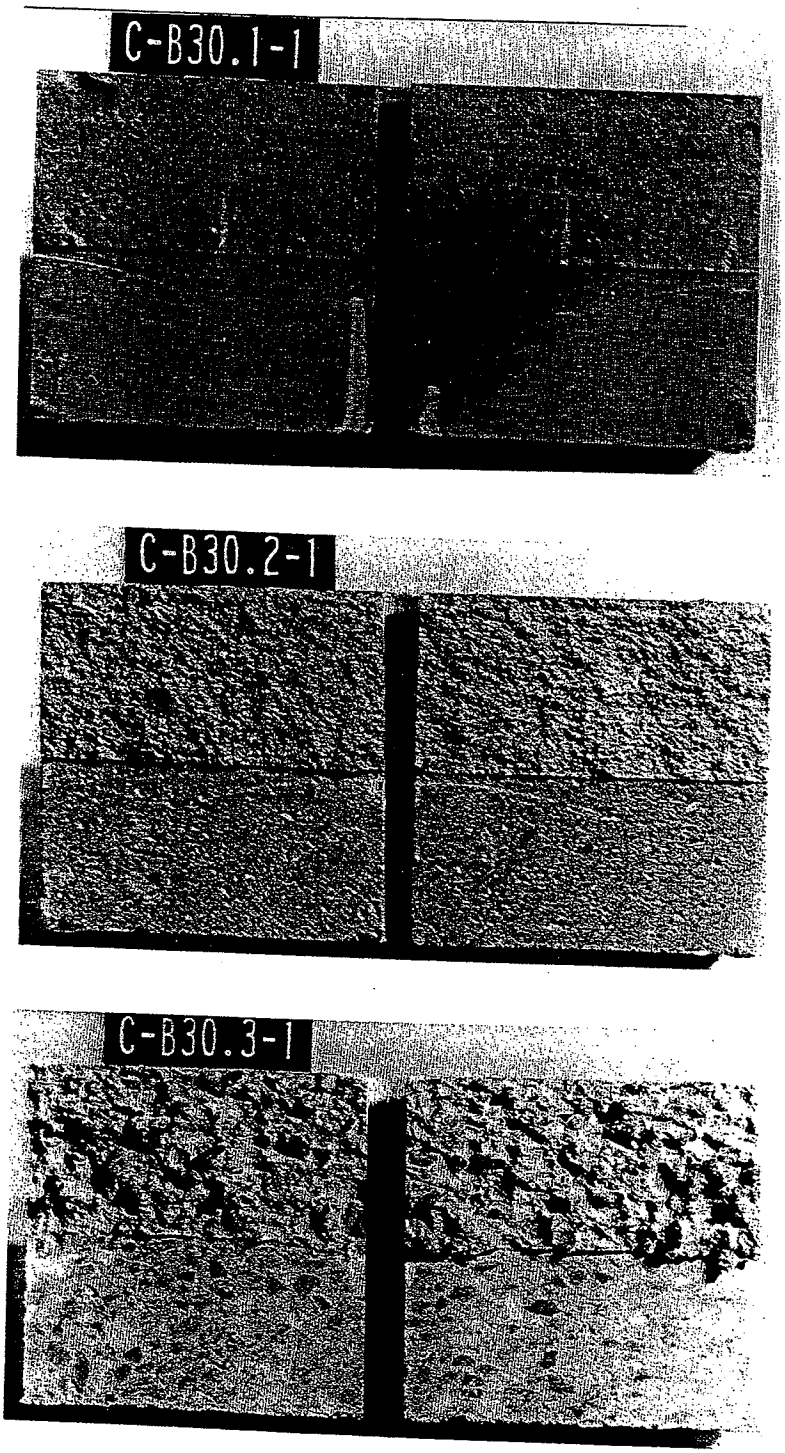

Figure 5.27 Fracture area for beams in Series C-B30.

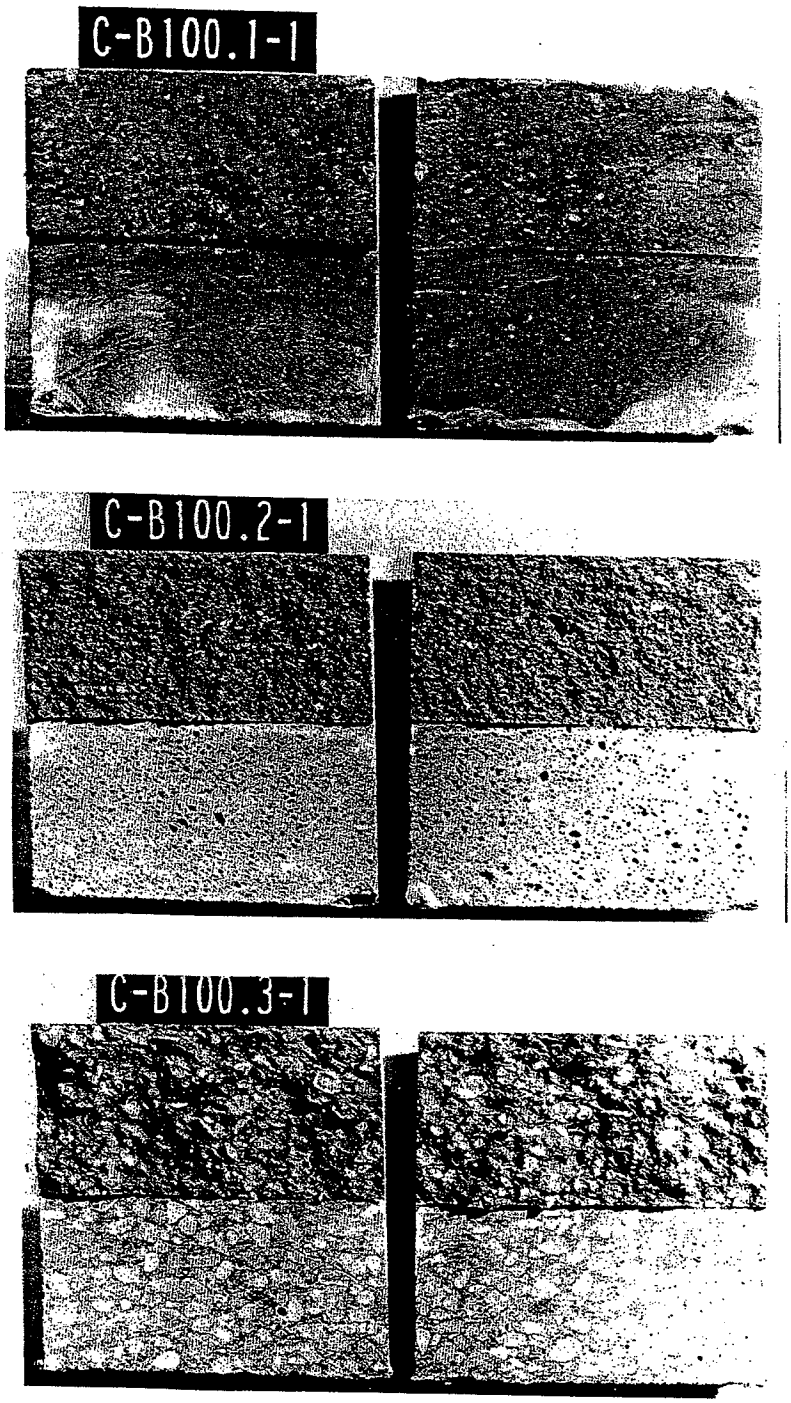

Figure 5.28 Fracture area for beams in Series C-B100.

5.8.3 Results of Beam Tests

In Figure 5.29 and Figure 5.30 results of typical load-deflection curves are given for beams with different air content. The maximum load does not seem to be influenced by the amount of air in the concrete. Only the test results obtained for beam D-B30.3 with 10% air has a lower peak value, which can be explained by a lower compressive strength level for this particular batch. The post-peak behaviour, however, is very much different in the way, that an increase in air voids results in a remarkable decrease in the ultimate deflection. This result is independent of the strength level, as a high strength concrete shows the same effect, see Figure 5.30.

In general the peak value increases with increasing concrete strength, and the deformation at rupture decreases with increasing concrete strength. The deformation at maximum load is not influenced by the concrete strength.

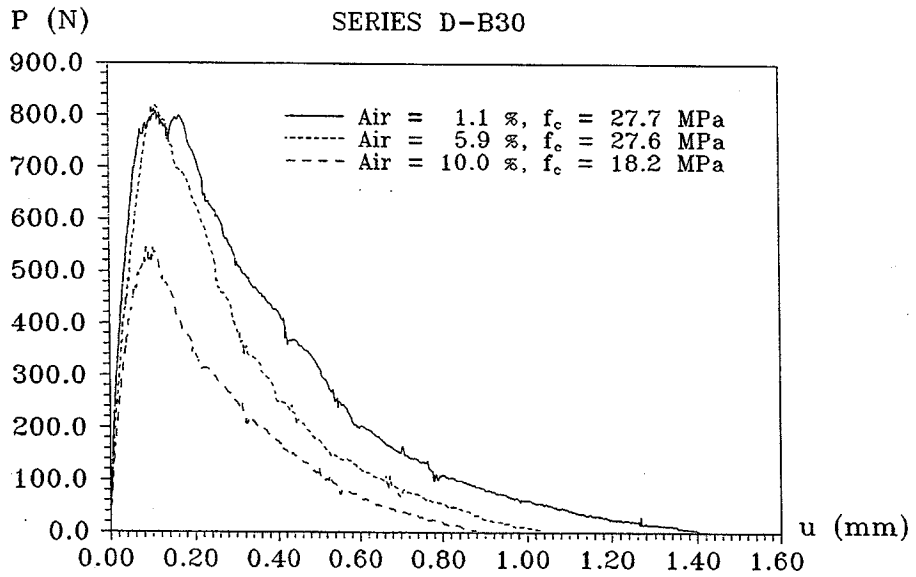

Figure 5.29 Load-deflection curves for normal strength concrete beams with different air contents.

5.8 Experimental Results for Series D

5.8.1 Introduction

In order to elucidate the effects of increasing the void content in the concrete by an air-entraining agent, 24 test beams were cast. The concrete mixes are given in section 5.4.6. The beams had dimensions identical with Series A, B and C with a/h = 0.5. Two amounts of intended air content were chosen to 5% (1) and 10% (2) together with two compressive strength levels, 30 MPa and 100 MPa.

5.8.2 Results of Cylinder Tests

In Table 5.12 the results of the cylinder tests are given.

	Air %	Compressive Tests f_c (MPa)		Splitting Tests f_{sp} (MPa)		Modulus of Elasticity E_c (MPa)	
Batch No		Mean Value	Standard Deviation	Mean Value	Standard Deviation	Mean Value	Standard Deviation
D-B30.1	5.9	27.6	2.1	2.57	0.14	24100	866
D-B30.2	10.0	18.2	0.7	1.86	0.15	14690	93
D-B100.1	3.8	99.3	5.3	6.09	0.12	37870	1407
D-B100.2	9.0	86.6	1.1	5.48	0.10	35390	913

Table 5.12 Cylinder data for the concrete in Series D.

If the strength of air-entrained concrete is to be the same as that of a non-air-entrained mix, it is necessary to base the initial mix design on a strength higher than the actually desired. The loss of compressive strength due to voids is, according to *Neville* **[81.2]**, about 5.5% for each percent of entrained air. As can be seen from Table 5.12 reaching the desired strength level was not successful for batch no. D-B30.2 and to some extent for D-B100.2. This of course has to be taken into account, when evaluating the fracture parameters.

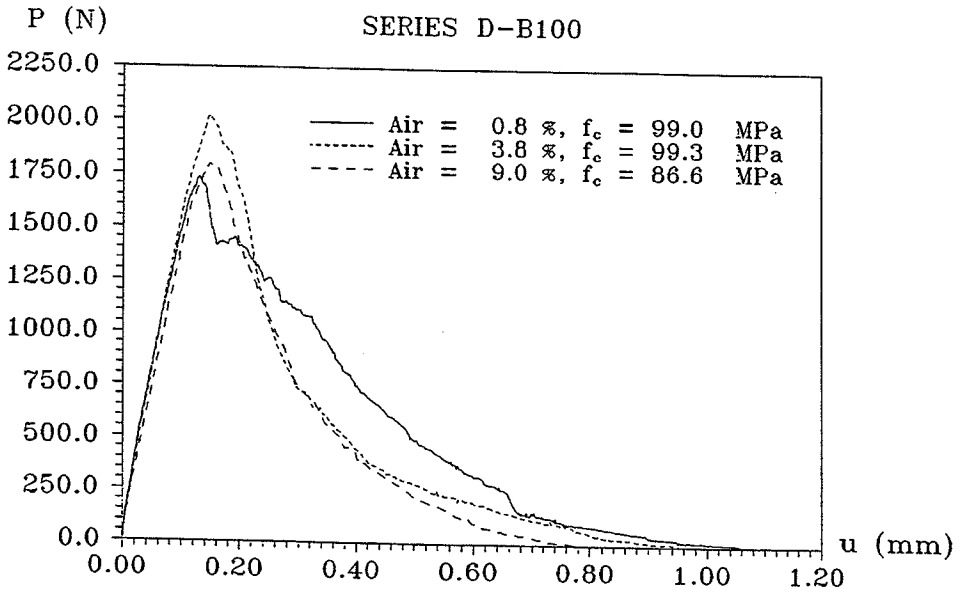

Figure 5.30 Load-deflection curves for high strength concrete beams with different air contents.

In Table 5.13 the main results of calculated values for G_F and flexural strength are given. In Figure 5.31 and Figure 5.32 the values for the fracture energy are depicted against the measured content of air and the measured compressive strength respectively.

	Air %	f_c (MPa)	G_F (N/m)		f_f (MPa)	
Batch No		Mean Value	Mean Value	Standard Deviation	Mean Value	Standard Deviation
D-B30.1	5.9	27.6	91.5	14.8	4.23	0.28
D-B30.2	10.0	18.2	64.5	10.6	3.06	0.23
D-B100.1	3.8	99.3	144.0	16.3	9.64	0.57
D-B100.2	9.0	86.6	126.9	21.1	8.63	0.40

Table 5.13 Summary of test results for Series D.

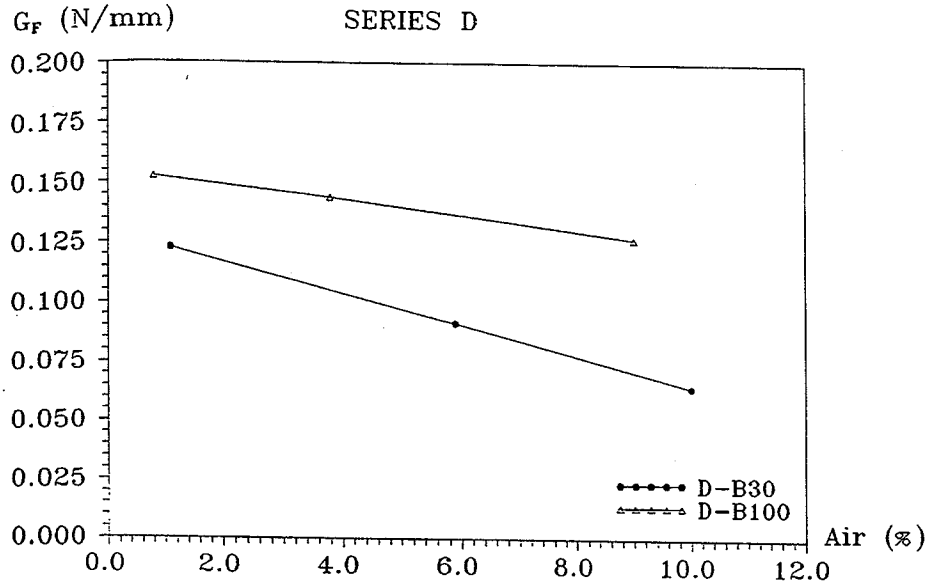

Figure 5.31 Fracture energy for concrete with different air contents.

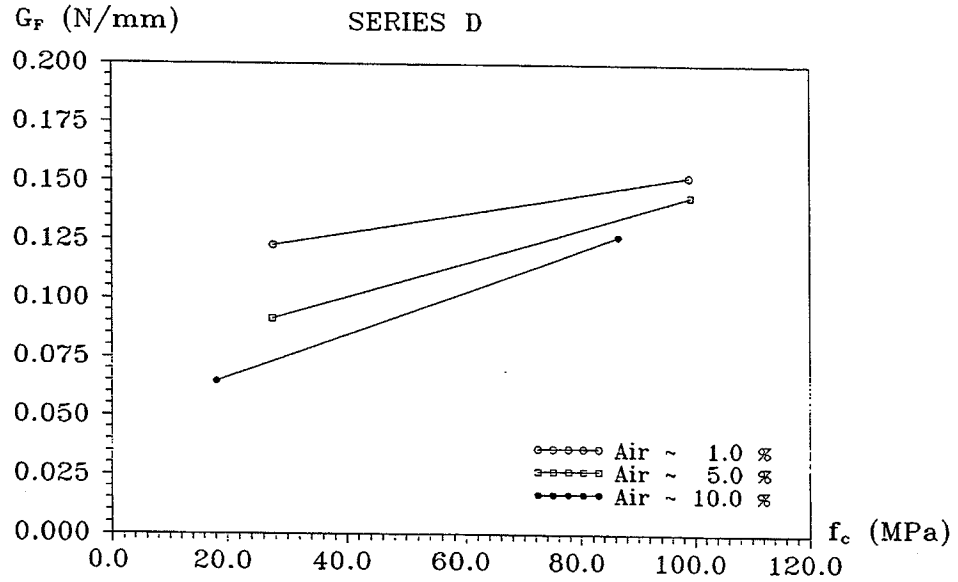

Figure 5.32 Fracture energy for concrete with different air contents.

The values depicted in Figure 5.31 and Figure 5.32 are supplied with data from Series A, where the concrete constituents and compressive strength were comparable. The measured air content in Series A was approximately 1%.

The effect of the air-entraining agents on the G_F value is pronounced. An increase in air content results in a drop in the value for G_F.

5.9 Experimental Results for Series E

5.9.1 Introduction

The aim of this series is to obtain knowledge of the size dependence on the fracture energy and flexural strength for normal and high strength concrete when carrying out a small size variation.

The concrete used is identical with the mixes used in Series A and B. The cross sections are constant and equal to 100x100 mm^2 with a sawn notch of 50 mm in height and 3 mm wide. Two compressive strength levels, 30 MPa and 100 MPa, are examined. Beam lengths varied from 550 mm (1) over 1200 mm (2) to 2000 mm (3). Specimens and cylinders were cured in water for 28 days after which they were tested. See section 5.4.

5.9.2 Results of Cylinder Tests

In Table 5.14 the results of the cylinder tests made in Series E are presented. The results reflects the intended strength levels well. No investigation of the modulus of elasticity were performed, as the mixes used were identical to Series A in all respects.

	Compressive Tests f_c (MPa)		Splitting Tests f_{sp} (MPa)	
Batch No	Mean Value	Standard Deviation	Mean Value	Standard Deviation
E-B30.1	30.2	1.9	2.82	0.41
E-B30.2	34.0	2.7	2.98	0.21
E-B30.3	31.2	2.3	2.73	0.21
E-B100.1	94.8	2.3	5.83	0.17
E-B100.2	101.7	7.1	6.08	0.14
E-B100.3	102.1	4.0	6.03	0.28

Table 5.14 Cylinder data for the concrete in Series E.

5.9.3 Results of Beam Tests

The influence on the load-deflection curves, when varying the beam length L for normal and high strength concrete, are shown in Figure 5.33 and 5.34 respectively.

The figures are typical load-deflection curves from Series E supplied with beams A-B30.3 and A-B100.3 from Series A with a length of 800 mm.

Similar for the two compressive strength levels are the fact, that an increase in beam length results in a decrease in both the maximum load and the steepness of the descending branch of the curve. Furthermore, an increase in beam length also have an effect on the maximum deflection at rupture for normal strength concrete. For high strength concrete this effect was not detected as can be seen from Figure 5.34.

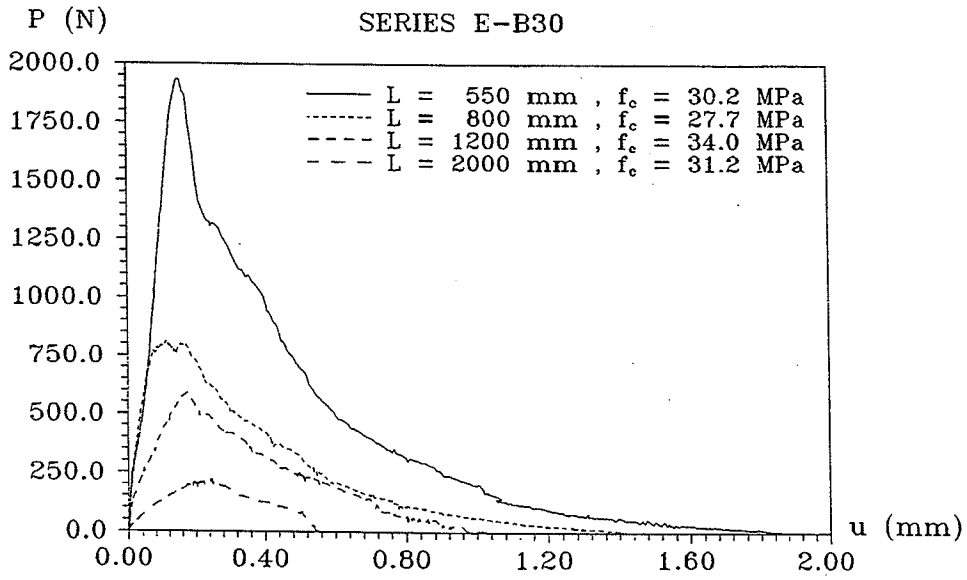

Figure 5.33 Load-deflection curves for a normal strength concrete with different specimen lengths.

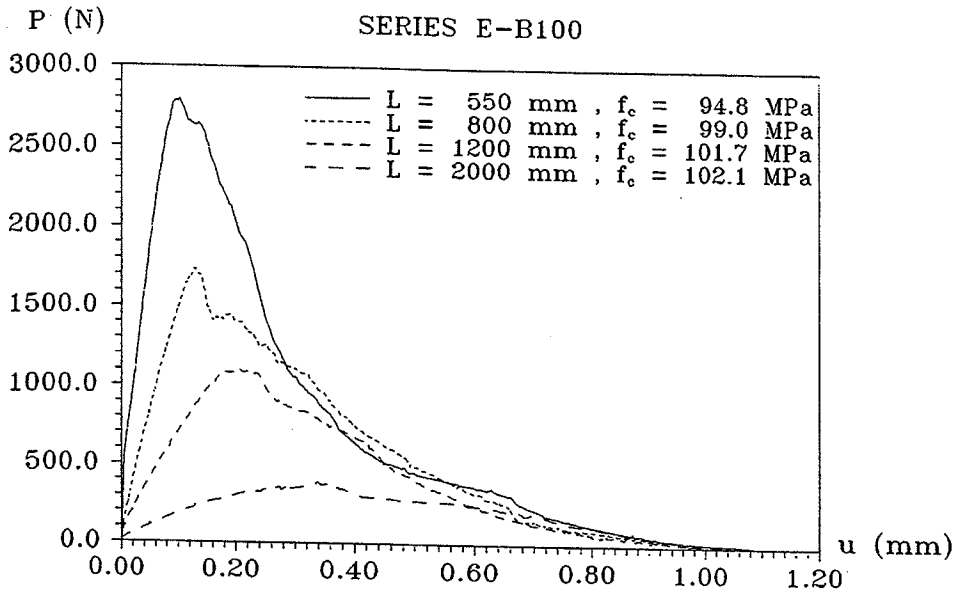

Figure 5.34 Load-deflection curves for a high strength concrete with different specimen lengths.

In Table 5.15 the main results of the fracture energy G_F and flexural strength of the beams investigated are given. In Figure 5.35 - 5.37 these results are presented graphically.

A distinctive dependence between the fracture energy and beam length are found. Both for normal and high strength concrete an increase in beam length results in a dramatic drop in the calculated value of G_F.

This of course can be explained as size effects, which was discussed in chapter 4 and will be dealt with in more detail in future works.

Batch No	L mm	f_c (MPa)	G_F (N/m)		f_f (MPa)	
		Mean Value	Mean Value	Standard Deviation	Mean Value	Standard Deviation
E-B30.1	550	30.2	191.7	28.0	6.23	0.58
E-B30.2	1200	34.0	110.7	8.8	5.03	0.19
E-B30.3	2000	31.2	78.9	22.0	4.93	0.59
E-B100.1	550	94.8	185.9	14.5	9.34	0.62
E-B100.2	1200	101.7	141.0	13.5	9.23	0.72
E-B100.3	2000	102.1	95.3	12.2	7.50	0.35

Table 5.15 Summary of test results for Series E.

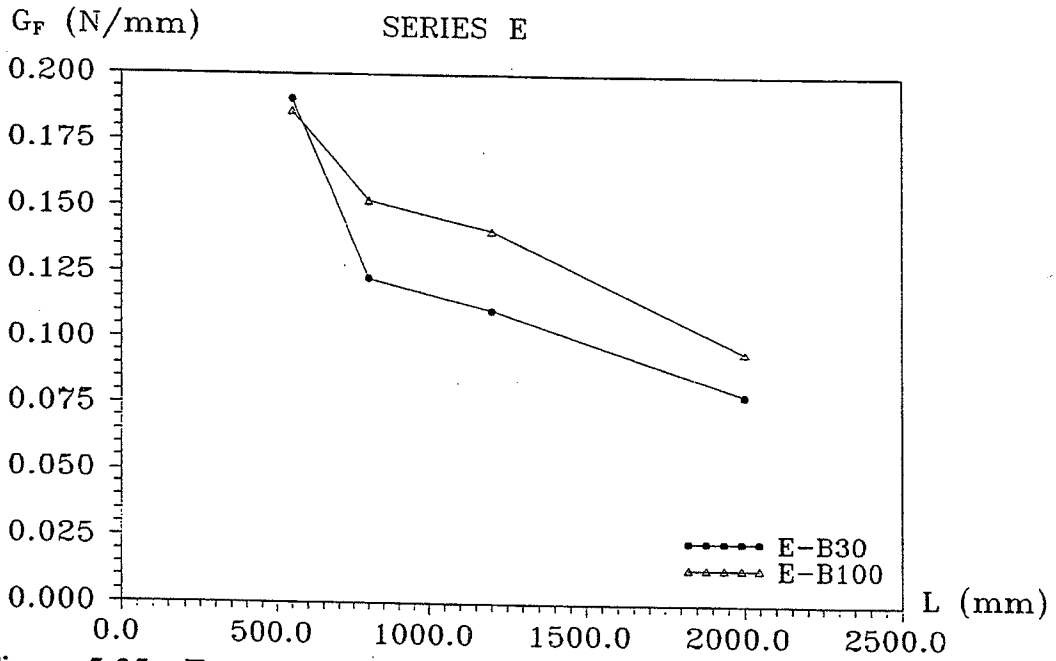

Figure 5.35 Fracture energy as a function of beam length.

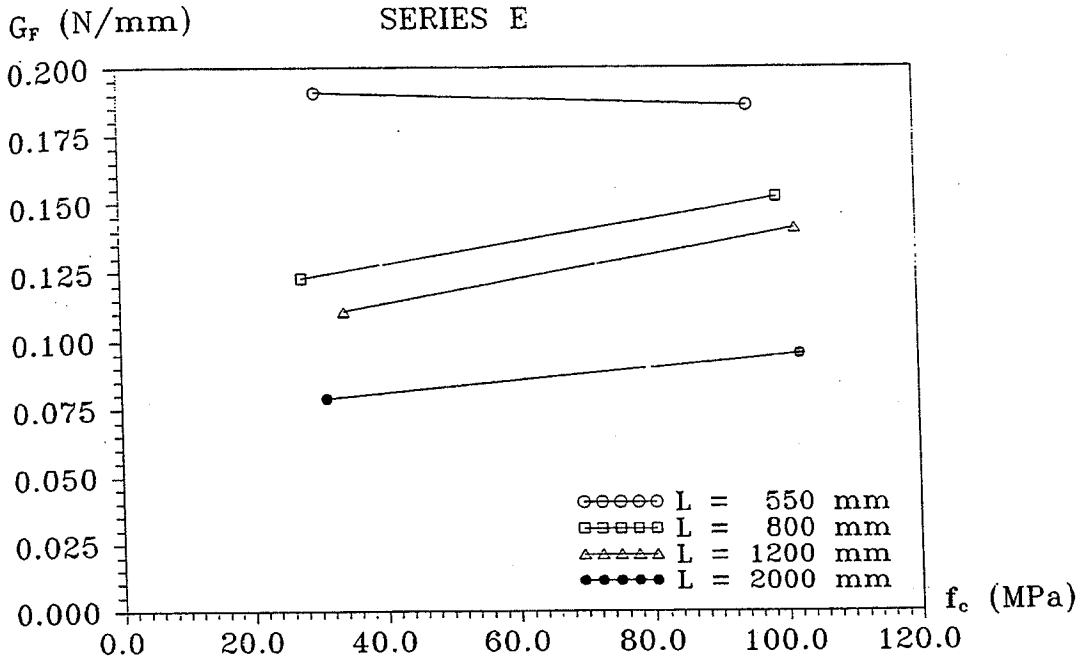

Figure 5.36 Fracture energy as a function of concrete strength for different beam lengths.

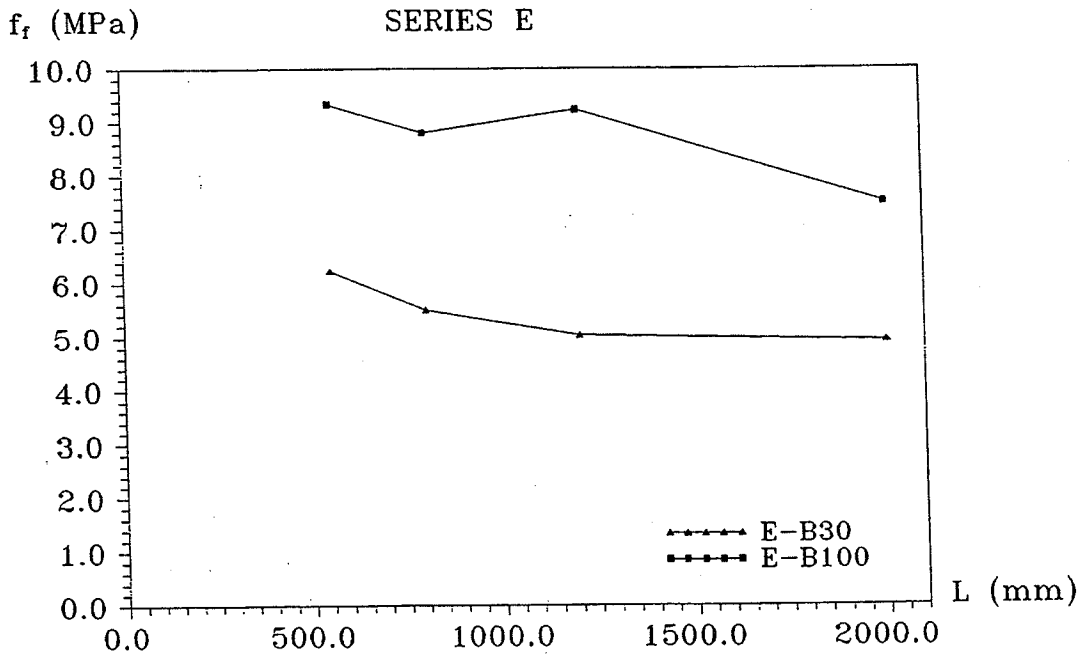

Figure 5.37 Flexural strength as a function of beam length.

5.10 Conclusion

In this section the results from a large experimental program have been reported. The scope of the experimental program was to investigate the fracture of concrete concentrating on the determination of fracture mechanical properties and flexural strength of concrete.

Only experimental values are presented and described. Comparison with results from other researchers and with theoretically established models for describing crack growth in normal and high strength concrete were given in chapter 4.

The concrete tests shows a considerable change in fracture energy when varying the compressive strength of concrete. The difference in fracture and behaviour is pronounced when increasing the compressive strength.

A distinctive dependency between the fracture energy and maximum aggregate size, air content in concrete and beam dimensions have also been demonstrated.

Chapter 6

Summarized Comments

Utilization of fracture mechanics when studying concrete fracture has become more and more popular. The results obtained for concrete structures by not including the tensile strength in the theoretical expressions are often satisfactory. In the case of determining crack width and when studying anchorage effects, tensile stresses in concrete must be taken into account, and this has shown to produce problems. Fracture mechanics serves in this case to clarify some of the parameters for a full understanding of tensile fracture in concrete.

In this thesis some aspects of fracture mechanics of concrete has been studied. In the first part emphasis is put on evaluating a rather unknown, highly simplified way of calculating stress intensity factors. It is shown, that very simple statically admissible stress fields may be used, i.e. stress fields completely disregarding the stress concentration at the crack tip. Comparison between the calculated and the theoretical values have shown to be promising. Further work in this field is of course necessary before any final conclusions can be drawn. Calculations performed on beams subjected to three point bending and to pure bending using the same procedure has also shown good agreement with the theoretical values given

in the literature. The results have unfortunately not been presented in this thesis due to time limitations.

Chapter 4 presents an investigation of the potentialities of the new crack propagation formula based on energy criterion when applied to concrete. An investigation of crack propagation under static loading and the capability of the model to predict size effects has been performed. It has been shown, that the model is able to predict crack propagation in both ductile and brittle materials.

The model has been compared with experimental results of three point bending tests of plain concrete beams. The main conclusions are, that the theory presented is able to predict the peak value and part of the descending branch of the load - deflection curve for different strength levels, variation of notch height ratios and maximum aggregate sizes. The results presented indicates, that the new crack propagation formula is applicable to a brittle material like concrete.

The model has not yet been able to predict the major part of the descending branch of the load-deflection curve due to the fact, that the process zone l_e is determined on the basis of the stress concentration factor in the first term. This assumption is only valid for small values of l_e compared to the crack length a.

It has presently been shown that by taking account of the linear second term of the stress concentration factor, l_e will decrease for large values of the crack length a and thus result in a larger part of the descending part of the load-deflection curve. These results have not been presented in this paper due to the fact, that more work is necessary to fully understand the theoretical behaviour of the crack correction length l_e.

It may, however, be concluded that by using the new crack propagation formula, it is possible to predict crack growth, load and deflection for a number of structural elements subjected to statical loading.

In chapter 5 the results from a large experimental program have been reported. The scope of the experimental program was to investigate the fracture of concrete concentrating on the determination of fracture mechanical properties and flexural strength of concrete.

The experiments were performed using a deformation controlled testing machine, which was constructed at the Department of Structural Engineering, Technical University of Denmark.

Only experimental values are presented and described. Comparison with results from other researchers and with theoretically established models for describing crack growth in normal and high strength concrete are given in chapter 4.

The concrete tests displays a considerable change in fracture energy when varying the compressive strength of concrete. The difference in fracture and behaviour is pronounced, when increasing the compressive strength.

A distinctive dependency between the fracture energy and maximum aggregate size, air content in concrete and beam dimensions have also been demonstrated.

Chapter 7

Bibliography

[13.1] Inglis, C. E.:
"Stresses in a Plate Due to the Presence of Cracks and Sharp Corners". Transactions of the Institute of Naval Architects, Royal Institute of Naval Architects, vol. 55, pp. 219 - 230, 1913.

[21.1] Griffith, A. A.:
"The Phenomena of Rupture and Flow in Solids". Philosophical Transactions, Royal Society of London, Series A, vol. 221, pp. 163 - 198, 1921.

[24.1] Griffith, A. A.:
"The Theory of Rupture". Proceedings of the 1st International Congress of Applied Mechanics, Delft, p. 55, 1924.

[28.1] Richart, F. E., Brandtzaeg, A. and Brown, R. L.:
"A Study of the Failure of Concrete under Combined Stresses". Bulletin No. 185, Engineering Experiment Station, University of Illinois, 1928.

[39.1] **Westergaard, H. M.:**
"Bearing Pressures and Cracks". Journal of Applied Mechanics, vol. 61, pp. 49 - 53, 1939.

[47.1] **Davidenkov, N., Shevandin, E. and Wittman, F.:**
"The Influence of Size on the Brittle Strength of Steel". Journal of Applied Mechanics, vol. 14, pp. A63 - A67, 1947.

[52.1] **Wright P. J. F. and Garwood, F.:**
"The Effect of the Method of Test on Flexural Strength of Concrete". Magazine of Concrete Research, vol. 4, no. 11, pp. 67 - 76, October 1952.

[54.1] **Nielsen, K. E. C.:**
"Effect of Various Factors on the Flexural Strength of Concrete Test Beams". Magazine of Concrete Research, vol. 5, no. 15, pp. 105 - 114, March 1954.

[57.1] **Williams, M. L.:**
"On the Stress Distribution at the Base of a Stationary Crack". Journal of Applied Mechanics, vol. 24, pp. 109 - 114, March 1957.

[57.2] **Irwin, G. R.:**
"Fracturing of Metals". ASM, Cleveland, Ohio, p. 147, 1957.

[57.3] **Irwin, G. R.:**
"Analysis of Stresses and Strains Near the End of a Crack Traversing a Plate ". Journal of Applied Mechanics, vol. 24, pp. 361 - 364, September 1957.

[58.1] **Irwin, G. R.:**
"Fracture". Handbuch der Physik VI, Flügge ed., Springer Verlag, pp. 551 - 590, 1958.

[60.1] Irwin, G. R.:
"Plastic Zone Near a Crack and Fracture Toughness". Proceedings, 7th Sagamore Conference, pp. IV-63, 1960.

[60.2] Barenblatt, G. I.:
"The Mathematical Theory of Equilibrium of Cracks in Brittle Fracture". Advances in Applied Mechanics, vol. 7, pp. 55 - 129, 1962. See also Prikl. Mat. Mech., vol. 24, no. 2, p.453, 1960.

[60.3] Dugdale, D. S.::
"Yielding of Steel Sheets Containing Slits". Journal of the Mechanics and Physics of Solids, vol. 8, pp. 100 - 108, 1960.

[61.1] Kaplan, M. F.:
"Crack Propagation and the Fracture of Concrete". Journal of the American Concrete Institute, vol. 58, pp. 591 - 609, 1961.

[63.1] Paris, P. C., and Erdogan, F.:
"A Critical Analysis of Crack Propagation Laws". Journal of Basic Engineering, Transactions of the American Society for Mechanical Engineering, Series D, vol. 85, no. 4, December 1963.

[65.1] Paris, P. C. and Sih, G. C. M.:
ASTM Special Technical Publication STP 381, 1965

[68.1] Rice J. R.:
"A Path Independent Integral and the Approximate Analysis of Strain Concentration by Notches and Cracks". Journal of Applied Mechanics, vol. 35, pp. 379 - 386, 1968.

[68.2] Evans, R. H. and Marathe, M. S.:
"Microcracking and Stress-Strain Curves for Concrete in Tension". Materiaux et Constructions, no. 1, pp. 61 - 64, 1968.

[68.3] **Johnston, C. D. and Sidwell, E. H.:**
"Testing Concrete in Tension and in Compression". Magazine of Concrete Research, vol. 20, pp. 221 - 228, 1968.

[68.4] **Bilby, B. A., Cottrell, A. H. and Swinden, K. H:**
"The Spread of Plastic Yield From a Notch". Proceedings of the Royal Society, A272, p. 304, London, 1968.

[69.1] **Welch, G. B. and Haisman, B.:**
"The Application of Fracture Mechanics to Concrete and the Measurement of Fracture Toughness ". Materiaux et Constructions, no. 2, pp. 171 - 177, 1969.

[70.1] **Andersson, H. and Bergkvist, H.:**
"Analysis of a Non-Linear Crack Model". Journal of the Mechanics and Physics of Solids, vol. 18, pp. 1 - 28, 1970.

[71.1] **Hansen, B.:**
"Brudmekanik". Svejsecentralen. Akadamiet for de Tekniske Videnskaber, København 1971.

[71.2] **Stanley P.:**
"Fracture Mechanics in Engineering Practice". Applied Science Publishers LTD, London 1971.

[71.3] **Fracture Toughness:**
Proceedings of the 1971 National Symposium on Fracture Mechanics PART II, University of Illinois. ASTM Special Technical Publication STP 514, Philadelphia, Pa. 1971.

[72.1] **Brown, J. H.:**
"Measuring the Fracture Toughness of Cement Paste and Mortar". Magazine of Concrete Research, vol. 24, pp. 185 - 196, 1972.

[72.2] **Walsh, P. F.:**
"Fracture of Plain Concrete". The Indian Concrete Journal, vol. 46, pp. 469 - 476, 1972.

[73.1] **Tada, H., Paris, P.C. and Irwin, G. R.:**
"The Stress Analysis of Cracks Handbook". Del. Research, Hellertown, Pa., 1973.

[73.2] **Sih, G. C. M.:**
"Handbook of Stress Intensity Factors". Lehigh University 1973.

[73.3] **Brown, J. H. and Pomeroy, C. D.:**
"Fracture Toughness of Cement Paste and Mortars". Cement and Concrete Research, vol. 3, pp. 475 - 480, 1973.

[73.4] **Cherepanov, G. P. and Halmanov, H.:**
"Fatigue Crack Propagation in Martensitic and Austenitic Steels". Metallurgical Trans., Vol. 4, pp. 1263-1273, May 1973.

[75.1] **Lawn, B. R. and Wilshaw, T. R.:**
"Fracture of Brittle Solids". Cambridge University Press. Cambridge 95, 1975.

[76.1] **Hillerborg, A., Modéer, M. and Petersson, P. E:**
"Analysis of Crack Formation and Crack Growth in Concrete by Means of Fracture Mechanics and Finite Elements". Magazine of Concrete Research, vol. 6, pp. 773 - 782, 1976.

[76.2] **Higgins, D. D. and Bailey, J. E.:**
"Fracture Measurements on Cement Paste". Journal of the Materials Science, vol. 11, pp. 1995 -2003, 1976.

[77.1] **Rolfe, S. T. and Barsom, J. M.:**
"Fracture and Fatigue Control in Structures. Applications of Fracture Mechanics". Prentice-Hall, Inc. Englewood Cliffs, New Jersey 1977.

[77.2] **Hillerborg, A.:**
"Materialbrott". Report TVBM-3004, Division of Building Materials, Lund Institute of Technology, Sweden 1977.

[77.3] **Gustafsson P. J.:**
"Brottmekaniska Studier; Lättbetong och Fiberarmerad Betong". Report TVBM-5001, Division of Building Materials, Lund Institute of Technology, Sweden 1977.

[77.4] **Cooper, G. A.:**
"Optimization of the Three-Point Bend Test for Fracture Energy Measurement". Journal of the Materials Science, vol. 12, pp. 277-289, 1977.

[77.5] **Gjørv, O. E., Sørensen, S. I. and Arnesen, A.:**
"Notch Sensitivity and Fracture Toughness of Concrete". Cement and Concrete Research, vol. 7, pp. 333 - 344, 1977.

[79.1] **Hutchinson, J. W.:**
"Nonlinear Fracture Mechanics". Department of Solid Mechanics, The Technical University of Denmark 1979.

[79.2] **Knott, J. F.:**
"Fundamentals of Fracture Mechanics". 3'rd edition, Butterworth, London 1979. (First edition published in 1973)

[79.3] **Sabnis, G. M. and Mirza, S. M:**
"Size Effects in Model Concrete". Journal of the Structural Division, Proceedings of the American Society of Civil Engineers, vol. 105, no. ST6 pp. 1007 - 1020, june 1979.

[79.4] **Mai, Y. W.:**
"Strength and Fracture Properties of Asbestos-Cement Mortar Composites". Journal of the Materials Science, vol. 14, pp. 2091 -2102, 1979.

[79.5] Modéer, M.:
"A Fracture Mechanics Approach to Failure Analysis of Concrete Materials". Report TVBM-1001, Division of Building Materials, Lund Institute of Technology, Sweden 1979.

[79.6] Hillerborg, A.:
"The Fictitious Crack Model and Its Use in Numerical Analyses". Fracture Mechanics in Engineering Application, Proceedings of the International Conference, Bangalore, 1979.

[80.1] Ziegeldorf, H. S., Müller, H. S. and Hilsdorf, H. K.:
"A Model Law for the Notch Sensitivity of Brittle Materials". Cement and Concrete Research, vol. 10, pp. 589 - 599, 1980.

[80.2] Petersson, P. E:
"Fracture Energy of Concrete: Method of Determination". Cement and Concrete Research, vol. 10, pp. 78 - 89, 1980.

[80.3] Petersson, P. E:
"Fracture Energy of Concrete: Practical Performance and Experimental Results". Cement and Concrete Research, vol. 10, pp. 91 - 101, 1980.

[80.4] Hillerborg, A.:
"Analysis of Fracture by Means of the Fictitious Crack Model, Particularly for Fibre Reinforced Concrete". International Journal of Cement Composites, vol. 2, pp. 177 - 184, 1980.

[81.1] Petersson, P. E.:
"Crack Growth and Development of Fracture Zones in Plain Concrete and Similar Materials". Report TVBM-1006, Division of Building Materials, Lund Institute of Technology, Sweden 1981.

[81.2] Neville, A. M.:
"Properties of Concrete". 3rd Edition, Longman Scientific & Technical, 1981.

[81.3] Hillerborg, A. and Petersson, P. E.:
"Fracture Mechanical Calculations, Test Methods and Results for Concrete and Similar Materials". Advances in Fracture Research. 5th International Conference on Fracture, Cannes 29 March - 2 April, 1981, pp. 1515 - 1522, Ed. D. Francois, Pergamon Press, 1981.

[83.1] Hertzberg, R. W.:
"Deformation and Fracture Mechanics of Engineering Materials". 2'nd edition, John Wiley & Sons, New York 1983.

[83.2] Gylltoft, K.:
"Fracture Mechanics Models for Fatigue in Concrete Structures". Doctoral Thesis, Division of Structural Engineering, Luleå University of Technology. 1983:25 D, 1983.

[83.3] Bažant, Z. P. and Oh, B. H.:
"Crack Band Theory for Fracture of Concrete". Materiaux et Constructions, Vol. 16, no. 93, pp. 155 - 177, 1983.

[84.1] Nielsen, M. P.:
"Limit Analysis and Concrete Plasticity". Prentice-Hall, Inc., Englewood Cliffs, New Jersey 1984.

[84.2] Carpinteri, A. and Ingraffea, A. R:
"Fracture Mechanics of Concrete". Matinus Nijhoff Publishers, The Hague, The Nederlands 1984.

[84.3] DS 411:
"Dansk Ingeniørforenings Norm for Betonkonstruktioner (Code of Practice for the Structural Use of Concrete)". Teknisk forlag, Normstyrelsens Publikationer, NP-169-N, 3. Ed., 1984.

[84.4] DS 423.12:
"Betonprøvning. Frisk beton. Sætmål. (Testing of Concrete. Consistency of Fresh Concrete. Slump Test)". Dansk Standard, DS 423.12, 2. udg., March 1984.

[84.5] DS 423.15:
"Betonprøvning. Frisk beton. Luftindhold. (Testing of Concrete. Determination of the Content of Airvoid in Fresh Concrete.)". Dansk Standard, DS 423.15, 1. udg., March 1984.

[84.6] DS 423.23:
"Betonprøvning. Hærdnet beton. Trykstyrke. (Testing of Concrete. Hardened Concrete. Compressive Strength.)". Dansk Standard, DS 423.23, 2. udg., March 1984.

[84.7] DS 423.25:
"Betonprøvning. Hærdnet beton. Elasticitetsmodul. (Testing of Concrete. Hardened Concrete. Modulus of Elasticity.)". Dansk Standard, DS 423.25, 2. udg., March 1984.

[84.8] DS 423.24:
"Betonprøvning. Hærdnet beton. Trækstyrke. (Testing of Concrete. Hardened Concrete. Tensile Strength.)". Dansk Standard, DS 423.24, 2. udg., March 1984.

[85.1] RILEM:
"Determination of the Fracture Energy of Mortar and Concrete by Means of Three-Point Bend Tests on Notched Beams". Materiaux et Constructions, Vol. 18, no. 106, pp. 285 - 290, 1985.

[85.2] Hillerborg, A.:
"The Theoretical Basis of a Method to Determine the Fracture Energy G_F of Concrete". Materiaux et Constructions, Vol. 18, no. 106, pp. 291 - 296, 1985.

[85.3] Hillerborg, A.:
"Results of three comparative test series to determine the fracture energy G_F of concrete". Materiaux et Constructions, Vol. 18, no. 107, pp. 407 - 413, 1985.

[85.4] **Gustafsson, P. J.:**
"Fracture Mechanics Studies of Non-Yielding Materials Like Concrete: Modelling of Tensile Fracture and Applied Strength Analysis". Report TVBM-1007, Division of Building Materials, Lund Institute of Technology, Sweden 1985.

[85.5] **Hillerborg, A. :**
"Influence of Beam Size on Concrete Fracture Energy Determined According to a Draft RILEM Recommendation". Report TVBM-3021, Division of Building Materials, Lund Institute of Technology, Sweden 1985.

[85.6] **Hillerborg, A.:**
"Numerical Methods to Simulate Softening and Fracture of Concrete". Fracture Mechanics of Concrete, G. C. Sih and A. Ditommaso editors, Martinus Nijhoff Publication, 1985.

[85.7] **Jenq, Y. S. and Shah, S. P.:**
"Two Parameter Fracture Model for Concrete". Journal of Engineering Mechanics, ASCE, Vol. 111, No. 10, pp. 1227-1241, October 1985.

[85.8] **Jenq, Y. S. and Shah, S. P.:**
"Nonlinear Fracture Parameters for Cement Based Composites: Theory and Experiments". Application of Fracture Mechanics to Cementitious Composites, Editor S. P. Shah, Martinus Nijhoff Publishers, pp. 319-359, 1985.

[85.9] **Jenq, Y. S. and Shah, S. P.:**
"A Fracture Toughness Criterion for Concrete". Engineering Fracture Mechanics, Vol. 21, No. 5, pp. 1055-1069, 1985

[86.1] **Broek, D.:**
"Elementary Engineering Fracture Mechanics". Fourth revised edition, Matinus Nijhoff Publishers, Dordrecht, The Nederlands 1986.

[86.2] Bažant, Z. P.:
"Mechanics of Distributed Cracking". Applied Mechanics Reviews, ASME, Vol. 39, No. 5, pp. 675-705, May 1986.

[87.1] Shah, S. P. and Swartz, S. E.:
"Fracture of Concrete and rock". SEM-RILEM International Conference, June 17-19, 1987, Houston, Texas, USA. Springer-Verlag, New York 1987.

[87.2] Proceedings of the International Symposium on Fracture Mechanics:
Canadian Institute of Mining and Metallurgy, 1987.

[87.3] Neville, A. M. and Brooks, J. J.:
"Concrete Technology". Longman Group UK limited, 1987.

[88.1] Nordberg, J.:
"Some Observations on a Fracture Mechanics Analysis of Concrete Structures". Publication 4/88, Department of Structural Engineering, Royal Institute of Technology, S-100 44 Stockholm, Sweden, 1988.

[89.1] Holmberg, Å.:
"The Strength Concept in Code Writing". Testimonials. Dipartimento Di Ingegneria Strutturale, Politecnico Di Torino 1989.

[89.2] Elfgren, L.:
"Fracture Mechanics of Concrete Structures. From Theory to applications". Report of the Technical Committee 90-FMA Fracture Mechanics to Concrete - Applications. RILEM, (The International Union of Testing and Research Laboratories for Materials and Structures). Chapman and Hall, London 1989.

[89.3] Meguid, S. A.:
"Engineering Fracture Mechanics". Elsevier Applied Science, London 1989.

[89.4] **Shah, S. P., Swartz, S. E. and Barr, B.:**
"Fracture of Concrete and Rock". Elsevier Science Publishers LTD, Crown House, Essex, England 1989.

[89.5] **Lagace, P. A.:**
"Composite Materials. Fatigue and Fracture". 2'nd volume, American Society for Testing and Materials (ASTM), STP 1012, Philadelphia 1989.

[89.6] **Hordijk, D. A.:**
"Deformation-Controlled Uniaxial Tensile Tests on Concrete". Report 25.5-89-15/VFA, Delft University of Technology, Dec. 1989.

[89.7] **Carpenteri, A.:**
"Constitutive Laws and Fracture Mechanics of Concrete in NPP Structures". Department of Structural Engineering, 10129 Torino, Italy, 1989.

[90.1] **Nielsen, M. P.:**
"An Energy Balance Crack Growth Formula". Bygningsstatiske Meddelelser, no. 3-4, pp. 71-125, 1990.

[90.2] **CEB Model Code 1990:**
Comite Euro-International Du Beton, Bulletin d'Information no. 196, 1990.

[94.1] **Olsen, D. H.:**
"Fracture of Concrete, A Test Series". Department of Structural Engineering, Technical University of Denmark, Series R, No. 312, 1994.

[94.2] **Olsen, D. H.:**
"Fracture of Concrete, Appendix I". Department of Structural Engineering, Technical University of Denmark, Series R, No. 313, 1994.

[94.3] **Hansen, T. C.:**
"Fatigue and Crack Propagation". Department of Structural Engineering, Technical University of Denmark, Series R, No. 316, 1994.

[94.4] Olsen, P. C.:
"Some Comments on the Bending Strength of Concrete Beams". Magazine of Concrete Research, vol. 46, no. 168, pp. 209-214, 1994.

[96.1] Hansen, T. C. and Olsen, D. H.:
"Fracture and Crack Growth in Concrete. A New Approach to Predict Crack Propagation Behaviour". Department of Structural Engineering and Materials, Technical University of Denmark, Series R, No. 11, 1996.

[98.1] Christiansen, M. B.:
"Crack Tip Stress Field Modelling". Department of Structural Engineering and Materials, Technical University of Denmark, 1998. (Public pending)

Appendix I

Experimental Results

Appendix I

Experimental Results

In the following appendix the test results of 232 beams together with 714 cylinder results are given.
The appendix contains the concrete recipes used in the test series, measurements of the compressive and splitting strength on cylindrical test specimens. Furthermore the value of the modulus of elasticity are given.
The load-deflection curve for each three point bending test are given together with measured values of maximum load and deflection, calculated value of fracture energy and flexural strength.
In addition, photos of the fracture area for three beams in every series are given.

SERIES A

Intended Compressive Strength	30 MPa	50 MPa	70 MPa	100 MPa
Materials	kg/m^3	kg/m^3	kg/m^3	kg/m^3
Portland Rapid Cement	188	260	305	390
Fly Ash	80	40	-	-
Mikrosilica Fume-Slurry	-	36	60	80
Sand 0 - 4 mm	640	600	558	521
Natural Gravel 4 - 8 mm	272	257	273	247
Crushed Gravel 4 - 16 mm	1089	1026	1093	989
Water	175	162	127	61
Plasticizer	-	1.33	-	2.40
Superplasticizer	-		5.81	18.04
Water-Cement Ratio	0.84	0.54	0.39	0.21

Table I.1 Mixing proportions for the concrete in Series A.

	Compressive Strength in MPa.			
Batch No	7 Days	14 Days	21 Days	28 Days
A-B30.4	14.7	19.6	22.2	23.7
A-B50.3N	30.8	40.9	44.6	48.0
A-B70.2	47.6	58.8	64.0	68.1
A-B100.3	71.4	84.6	95.2	99.0

Table I.2 Compressive strength developement for cylinders in Series A.

Batch No	Compressive Tests f_c (MPa)		Splitting Tests f_{sp} (MPa)		Modulus of Elastic E_c (MPa)	
	Mean Value	Standard Deviation	Mean Value	Standard Deviation	Mean Value	Standa Deviati
A-B30.1	28.1	1.0	2.32	0.07	26110	467
A-B30.2	29.2	1.4	2.87	0.11	27220	147
A-B30.2N	31.8	2.9	2.84	0.15	27330	354
A-B30.3	29.5	1.1	2.79	0.10	25600	606
A-B30.3N	25.8	1.5	2.90	0.44	25160	319
A-B50.1	51.0	1.5	3.87	0.22	33640	824
A-B50.2	55.5	1.6	3.72	0.35	32490	1322
A-B50.3	55.4	1.9	3.52	0.40	-	-
A-B50.3N	48.0	0.5	3.76	0.21	32950	209
A-B70.1	78.0	1.6	5.38	0.34	37330	1058
A-B70.2	68.1	2.8	4.52	0.20	33800	231
A-B70.3	72.6	0.9	4.82	0.14	35300	1344
A-B100.1	99.4	2.8	5.66	0.24	42070	2620
A-B100.2	100.1	3.6	5.78	0.27	42240	1280
A-B100.3	99.0	2.6	5.49	0.35	42210	1167

Table I.3 Cylinder values for the concrete in series A.

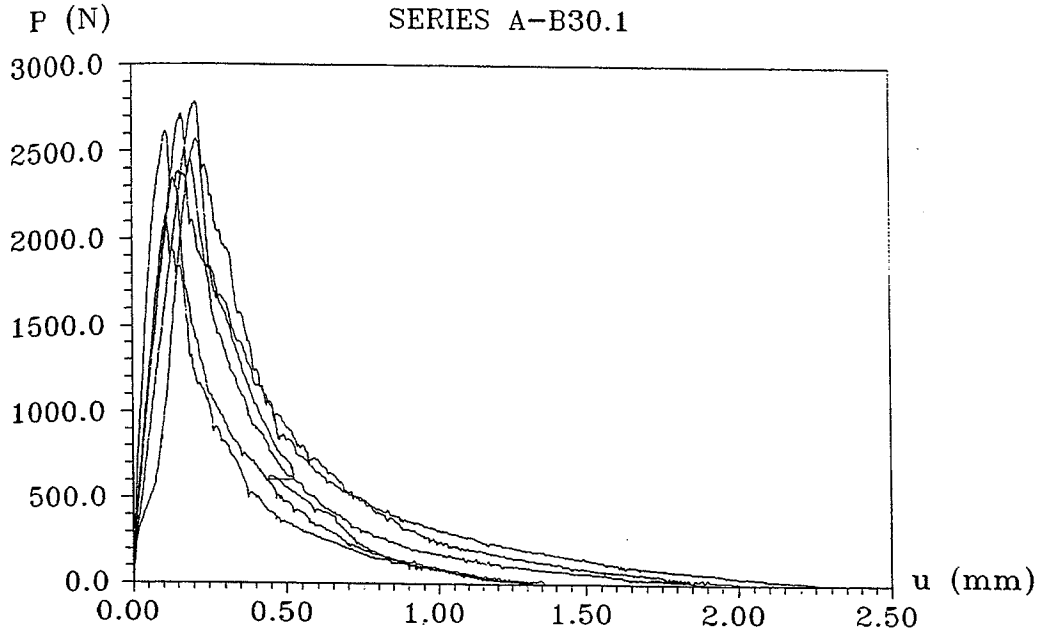

Figure I.1 Load-deflection curves for Series A-B30.1.

Beam no.	a/h	f_c (MPa)	f_{sp} (MPa)	u_0 (mm)	P_{max} (N)	W_e (Nmm)	G_F (N/m)	f_f (MPa)
A-B301-1	0.10	28.14	2.32	1.33	2614.1	748.4	110.8	4.01
A-B301-2				1.32	2135.3	605.7	94.7	3.30
A-B301-3				2.31	2782.7	1201.9	181.4	4.26
A-B301-4				2.03	2385.6	1109.4	165.4	3.67
A-B301-5				1.90	2716.1	949.1	144.8	4.16
A-B301-6				1.55	2571.9	583.7	97.0	3.95
Mean	-	-	-	1.74	2534.3	866.37	132.35	3.89

Table I.4 Three point bending test results for Series A-B30.1.

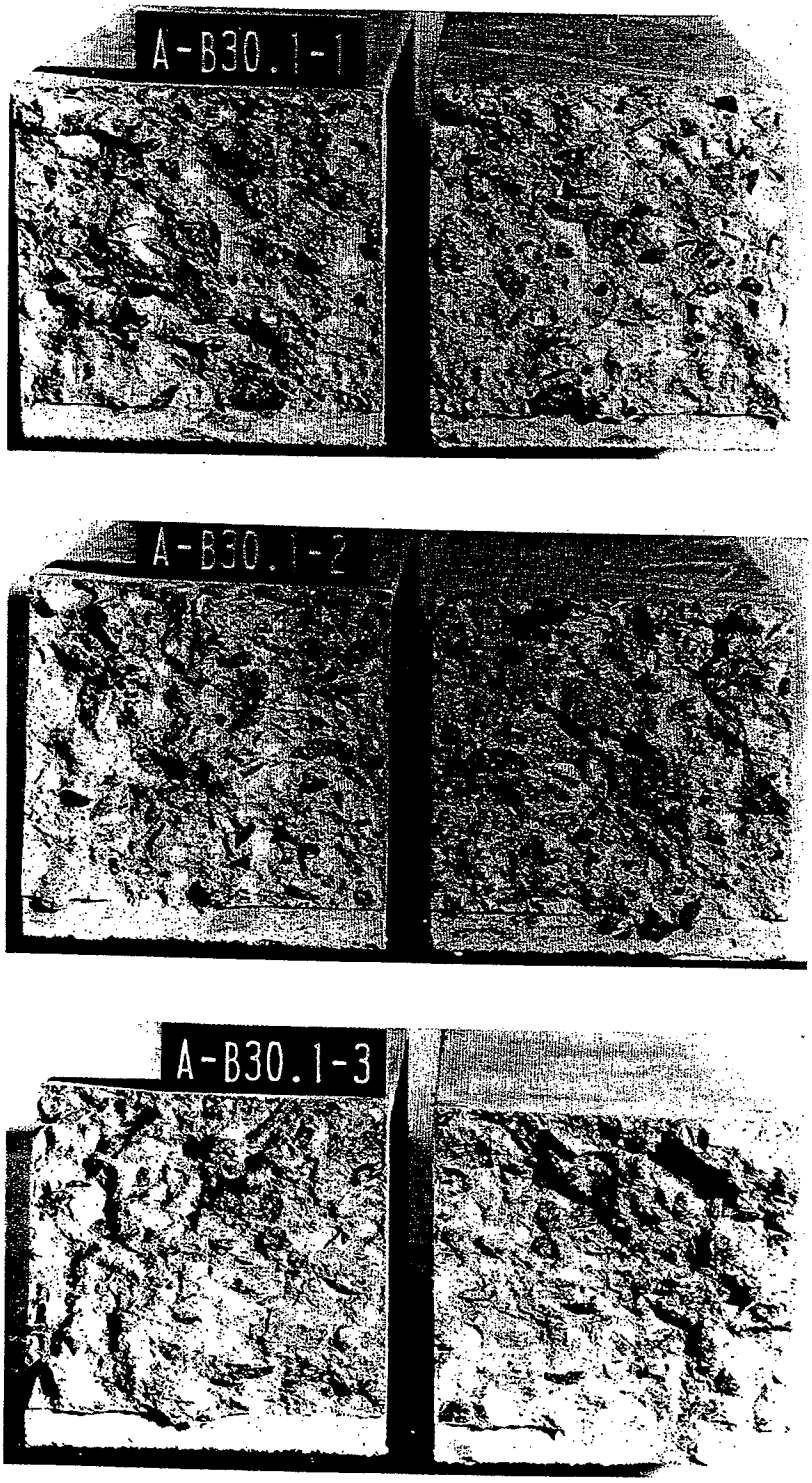

Figure I.2 Fracture area for beams in Series A-B30.1.

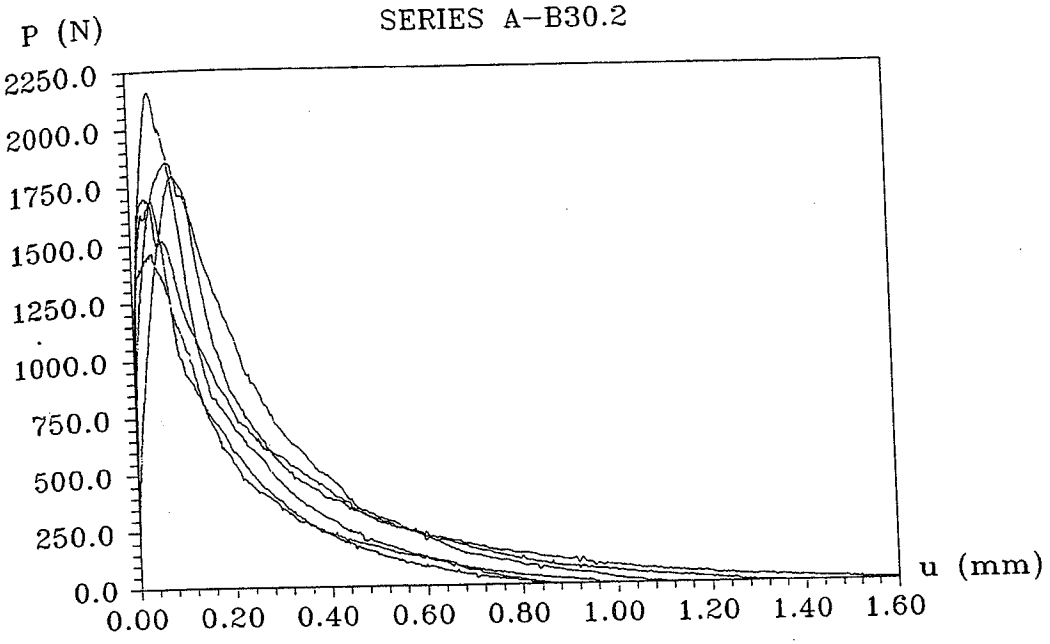

Figure I.3 Load-deflection curves for Series A-B30.2.

Beam no.	a/h	f_c (MPa)	f_{sp} (MPa)	u_0 (mm)	P_{max} (N)	W_e (Nmm)	G_F (N/m)	f_f (MPa)
A-B302-1	0.25	29.17	2.87	1.14	1794.0	475.6	92.0	4.03
A-B302-2				1.35	1701.4	485.9	98.4	3.83
A-B302-3				1.72	1851.1	592.7	121.9	4.15
A-B302-4				0.87	2162.5	433.0	79.3	4.81
A-B302-5				0.86	1632.1	337.6	66.4	3.68
A-B302-6				0.96	1462.1	338.4	69.0	3.32
Mean	-	-	-	1.15	1767.2	443.9	87.8	3.97

Table I.5 Three point bending test results for Series A-B30.2.

Figure I.4 Fracture area for beams in Series A-B30.2.

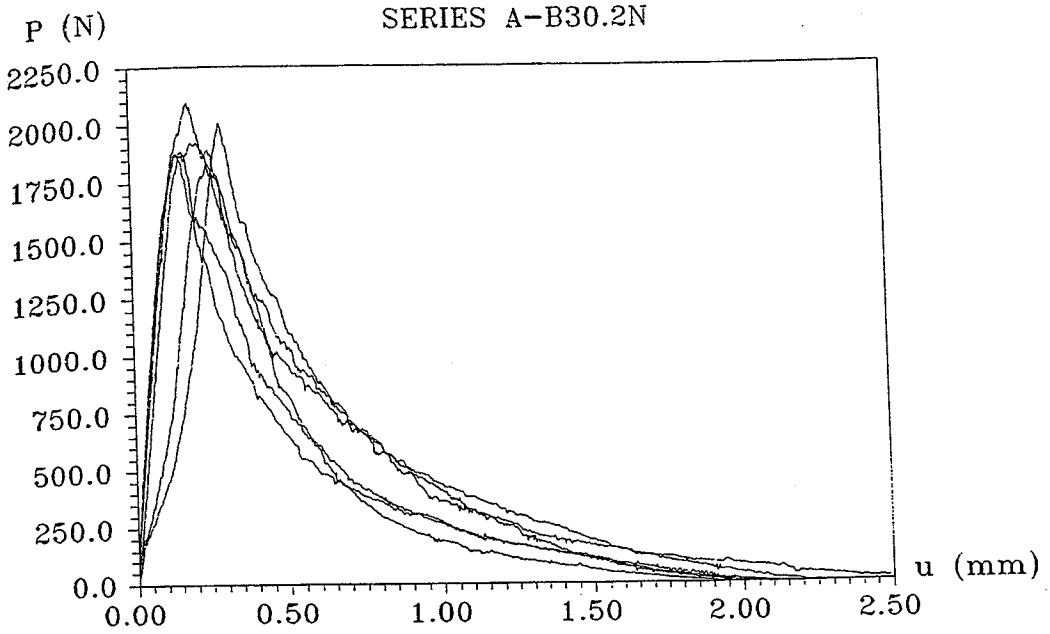

Figure I.5 Load-deflection curves for Series A-B30.2N.

Beam no.	a/h	f_c (MPa)	f_{sp} (MPa)	u_0 (mm)	P_{max} (N)	W_e (Nmm)	G_F (N/m)	f_f (MPa)
A-B302N-1	0.25	31.8	2.84	2.78	1920.4	1196.0	228.7	4.30
A-B302N-2				2.26	2004.8	1107.7	203.9	4.48
A-B302N-3				2.15	1836.1	1047.6	193.2	4.12
A-B302N-4				2.05	1868.8	885.3	168.9	4.19
A-B302N-5				2.02	2093.2	1040.2	188.9	4.66
A-B302N-6				1.96	1893.7	885.8	166.9	4.24
Mean	-	-	-	2.20	1936.2	1027.1	191.8	4.33

Table I.6 Three point bending test results for Series A-B30.2N.

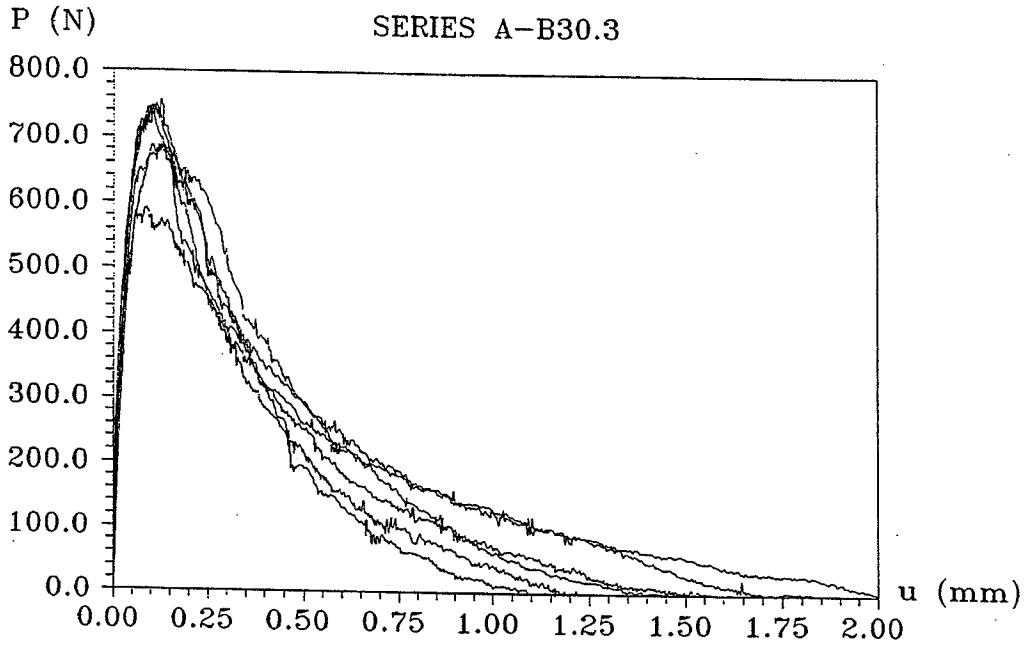

Figure I.6 Load-deflection curves for Series A-B30.3.

Beam no.	a/h	f_c (MPa)	f_{sp} (MPa)	u_0 (mm)	P_{max} (N)	W_e (Nmm)	G_F (N/m)	f_f (MPa)
A-B303-1	0.50	29.49	2.79	1.70	748.1	387.8	141.1	4.04
A-B303-2				1.09	745.3	265.8	93.9	4.02
A-B303-3				1.57	586.2	296.8	118.0	3.26
A-B303-4				1.16	682.8	285.7	100.4	3.72
A-B303-5				1.44	688.2	345.3	123.0	3.75
A-B303-6				2.00	735.8	383.1	151.1	3.98
Mean	-	-	-	1.49	697.7	327.4	121.3	3.80

Table I.7 Three point bending test results for Series A-B30.3.

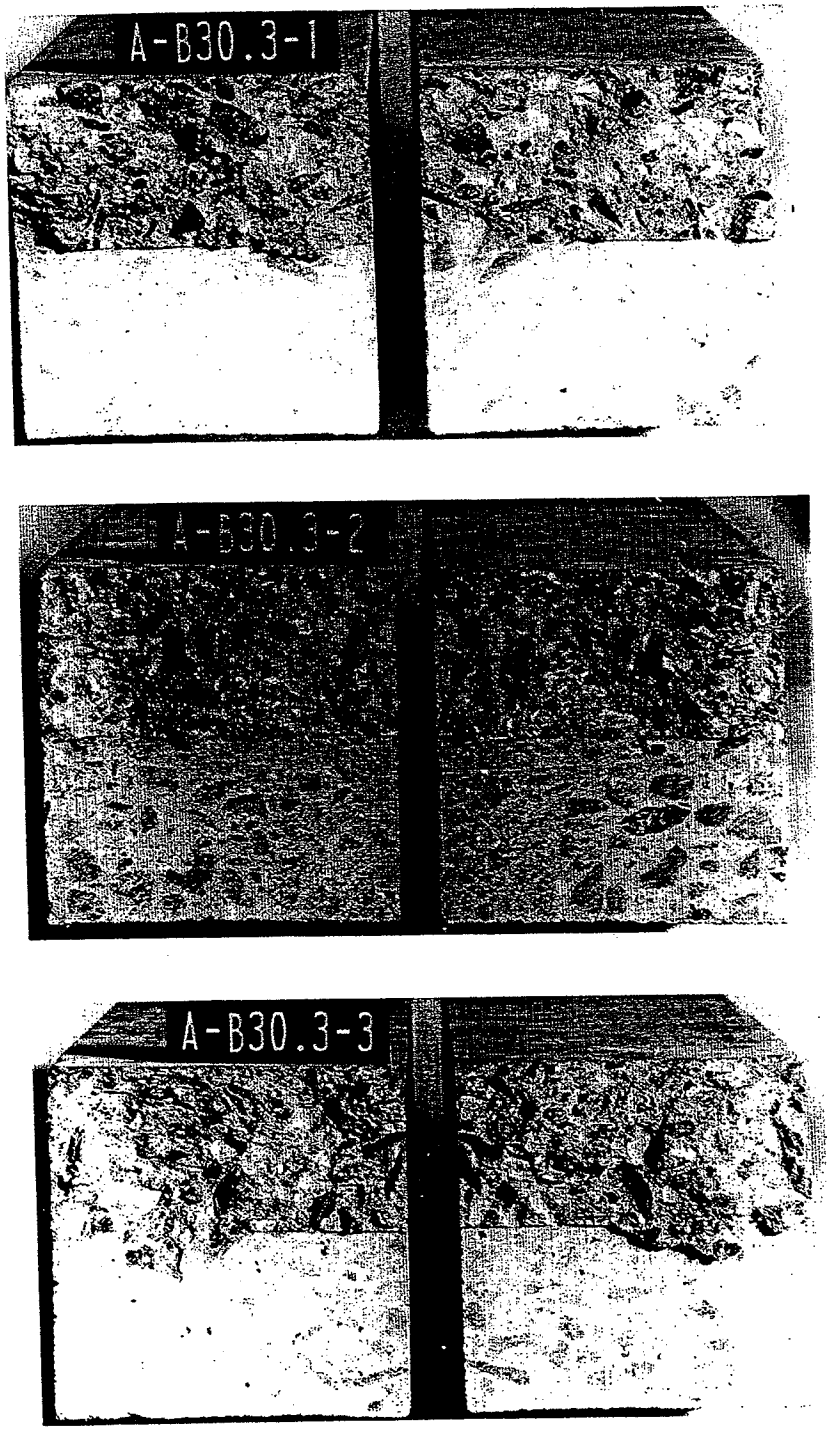

Figure I.7 Fracture area for beams in Series A-B30.3.

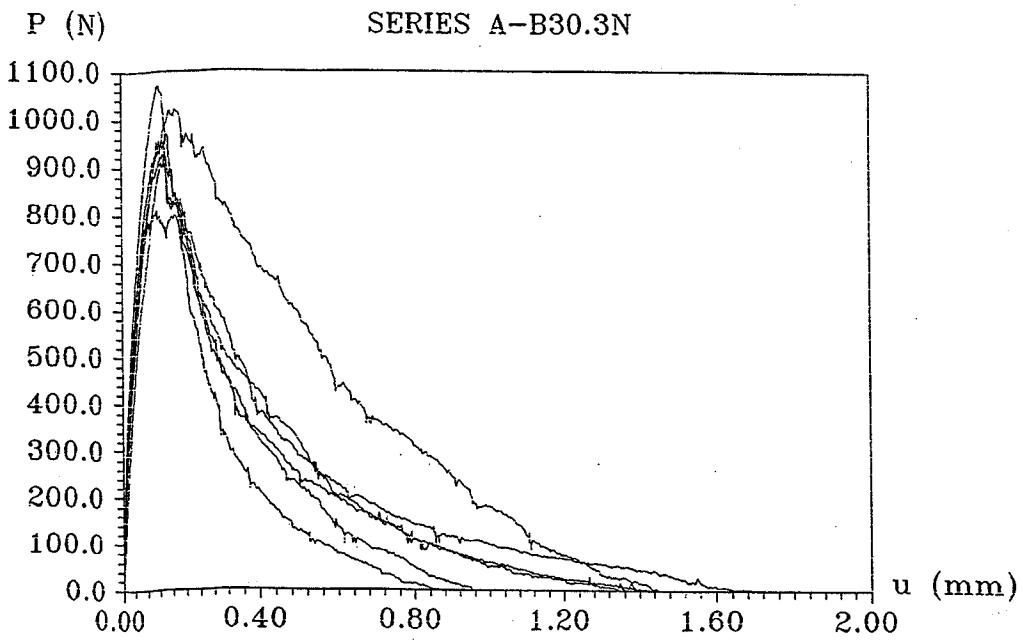

Figure I.8 Load-deflection curves for Series A-B30.3N.

Beam no.	a/h	f_c (MPa)	f_{sp} (MPa)	u_0 (mm)	P_{max} (N)	W_e (Nmm)	G_F (N/m)	f_f (MPa)
A-B303N-1	0.50	25.84	2.90	0.87	915.3	241.1	80.6	4.39
A-B303N-2				1.45	1021.4	589.2	172.0	4.90
A-B303N-3				1.42	954.8	352.0	123.3	4.58
A-B303N-4				1.41	809.3	362.2	125.1	3.88
A-B303N-5				1.69	926.2	407.8	144.6	4.45
A-B303N-6				0.95	1070.4	321.4	99.8	5.14
Mean	-	-	-	1.30	949.6	379.0	124.2	4.56

Table I.8 Three point bending test results for Series A-B30.3N.

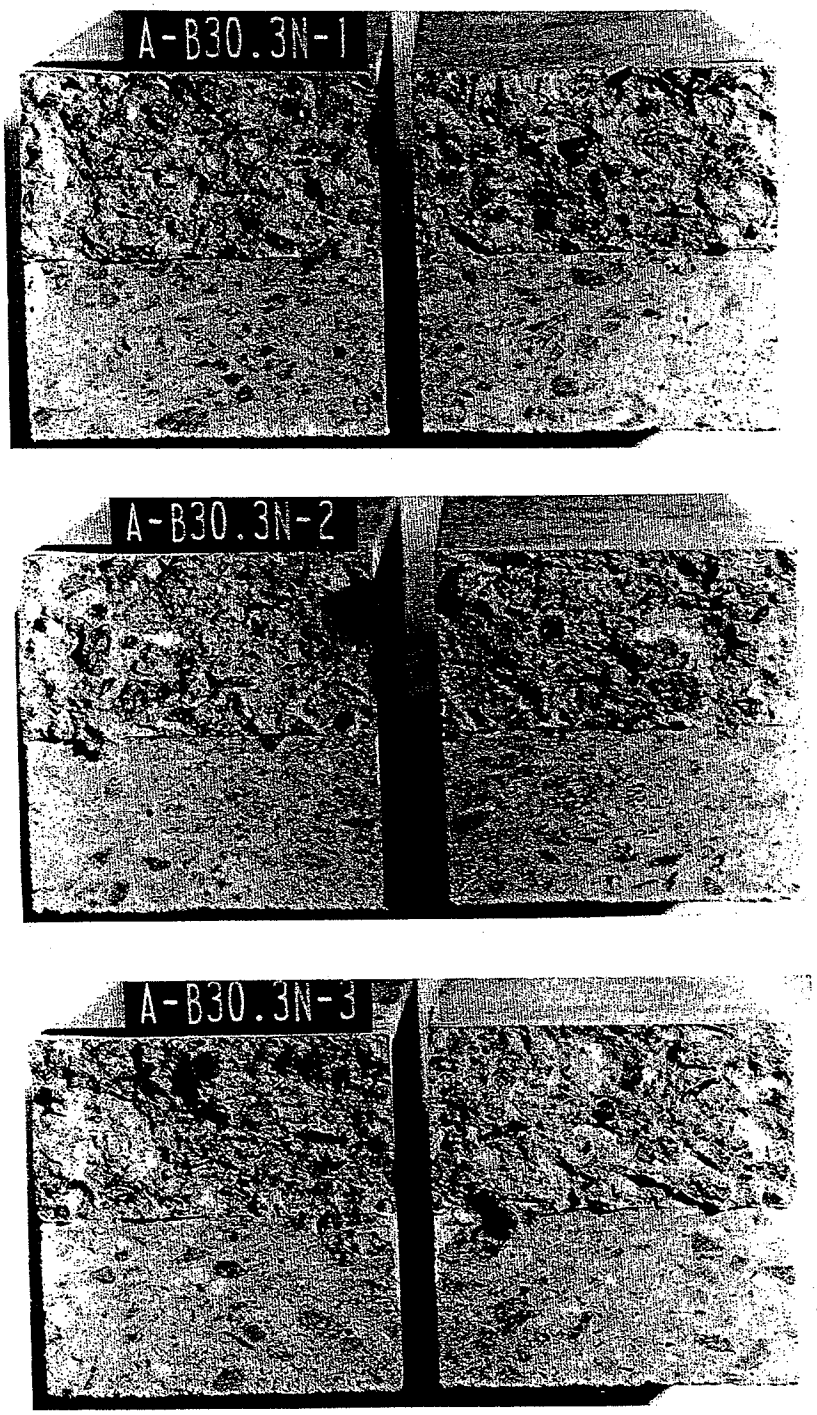

Figure I.9 Fracture area for beams in Series A-B30.3N.

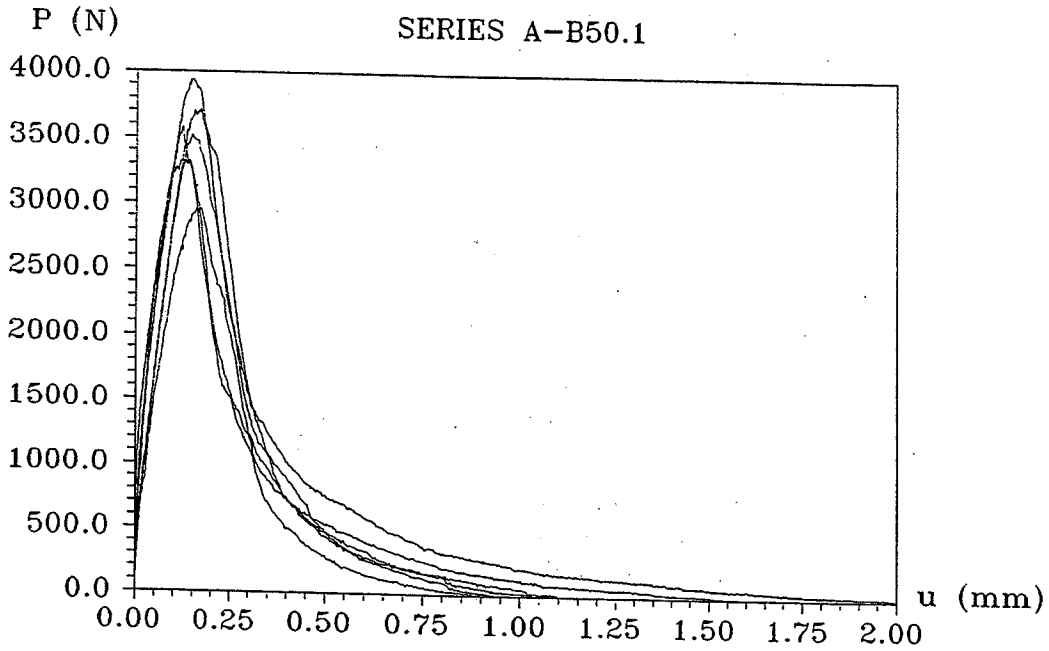

Figure I.10 Load-deflection curves for Series A-B50.1.

Beam no.	a/h	f_c (MPa)	f_{sp} (MPa)	u_0 (mm)	P_{max} (N)	W_e (Nmm)	G_F (N/m)	f_f (MPa)
A-B501-1	0.10	51.03	3.87	1.08	3699.4	1022.2	135.8	5.62
A-B501-2				1.13	3573.0	945.1	128.5	5.43
A-B501-3				0.94	3936.1	1051.7	136.4	5.97
A-B501-4				1.59	3324.1	984.3	142.4	5.06
A-B501-5				2.11	3522.6	1223.5	179.6	5.36
A-B501-6				-	-	-	-	-
Mean	-	-	-	1.37	3611.0	1045.4	144.5	5.49

Table I.9 Three point bending test results for Series A-B50.1.

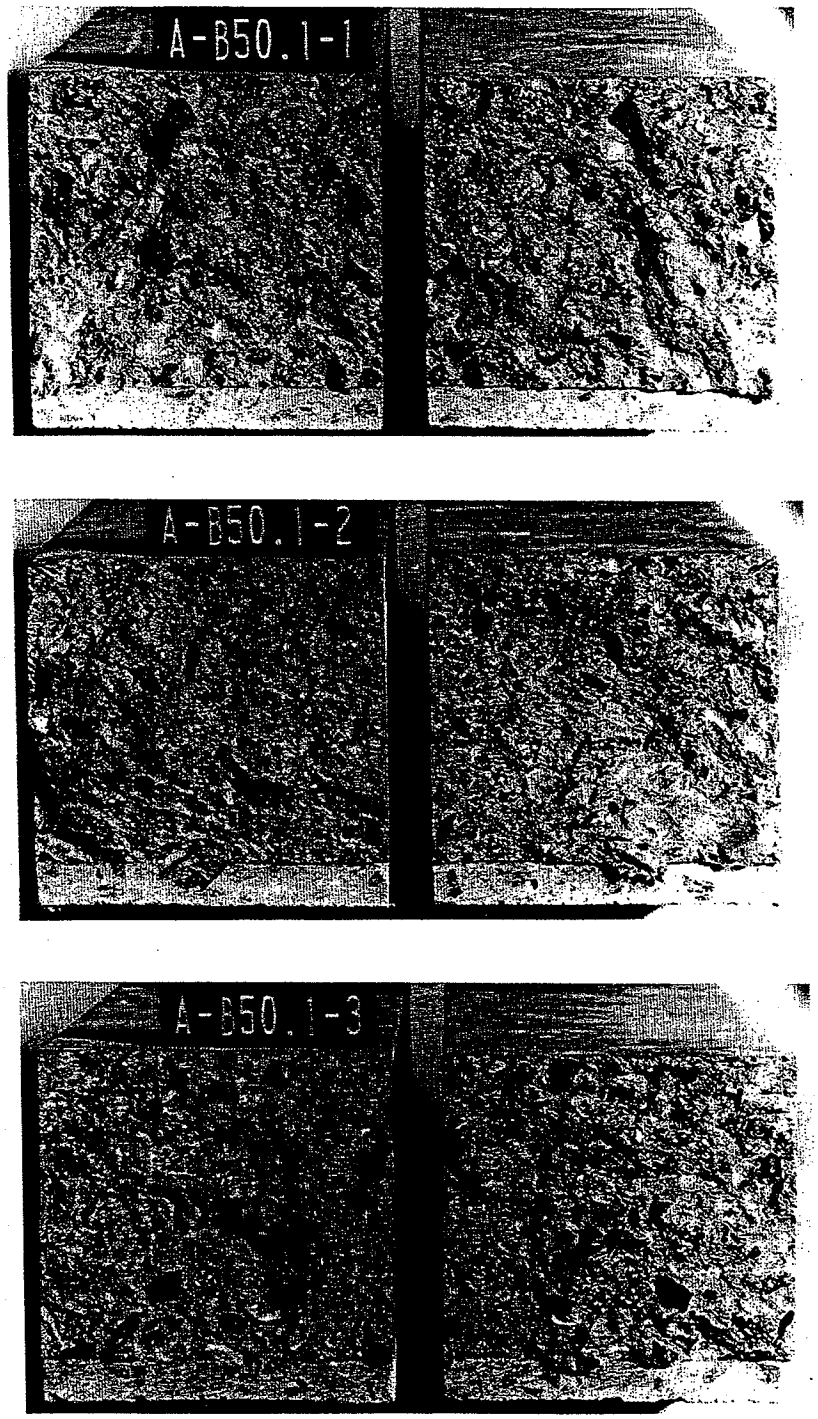

Figure I.11 Fracture area for beams in Series A-B50.1.

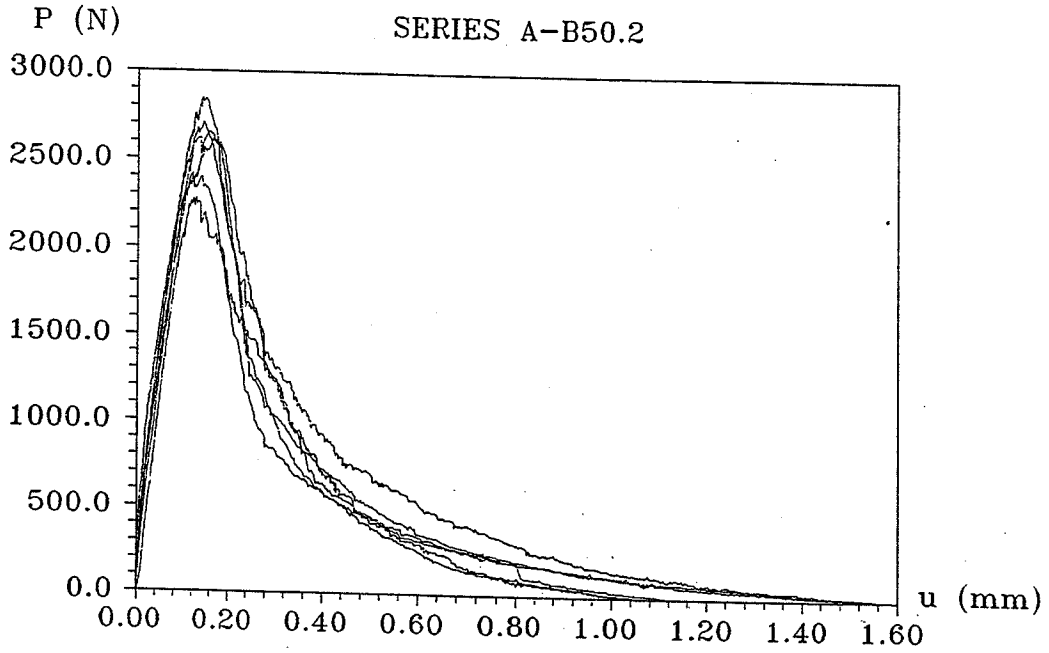

Figure I.12 Load-deflection curves for Series A-B50.2.

Beam no.	a/h	f_c (MPa)	f_{sp} (MPa)	u_0 (mm)	P_{max} (N)	W_e (Nmm)	G_F (N/m)	f_f (MPa)
A-B502-1	0.25	55.51	3.72	1.58	2395.1	736.0	137.5	5.31
A-B502-2				1.58	2653.5	853.2	153.0	5.86
A-B502-3				1.02	2712.0	714.0	120.7	5.98
A-B502-4				1.12	2615.5	797.5	134.2	5.78
A-B502-5				1.05	2271.4	697.5	119.2	5.04
A-B502-6				1.53	2839.9	974.6	168.0	6.26
Mean	-	-	-	1.31	2581.2	795.47	138.77	5.71

Table I.10 Three point bending test results for Series A-B50.2.

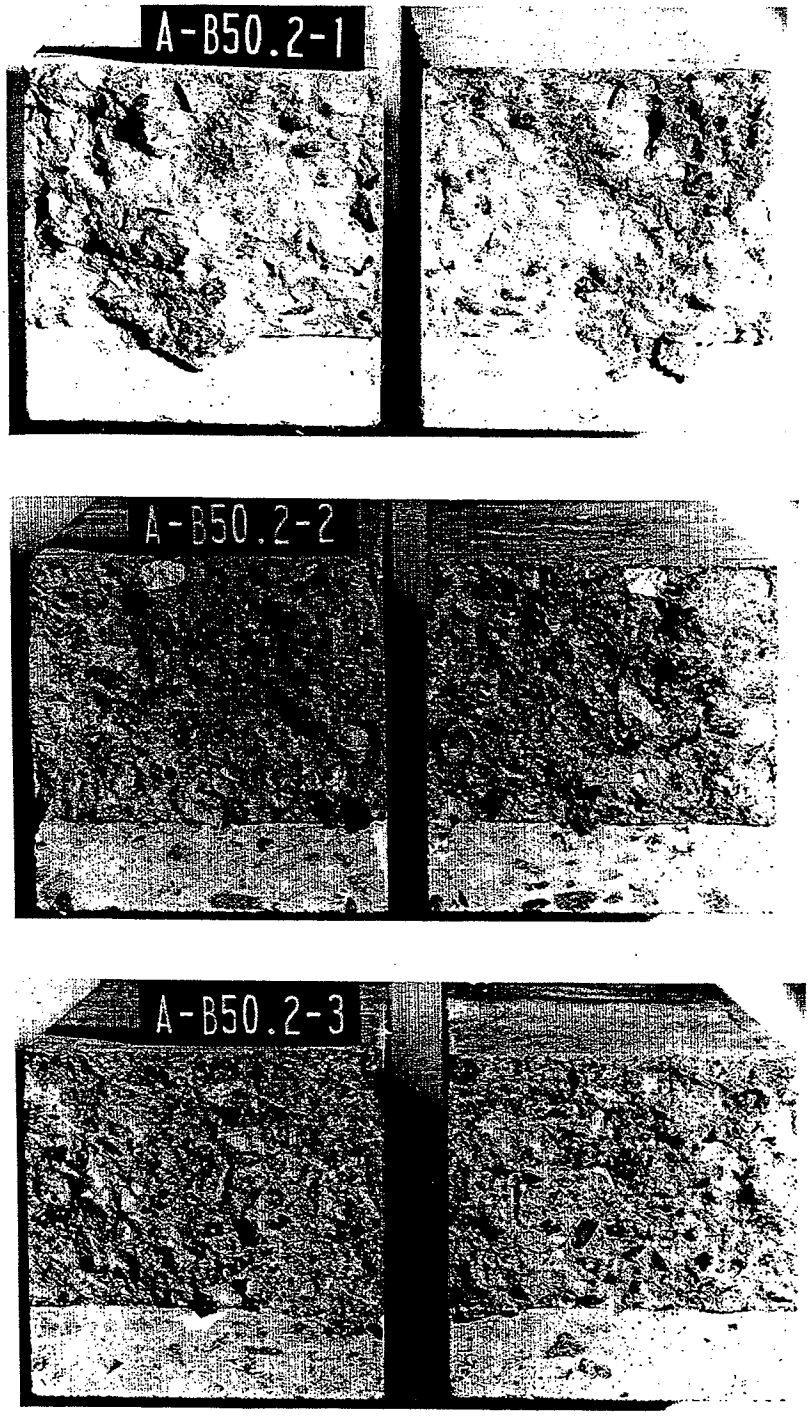

Figure I.13 Fracture area for beams in Series A-B50.2.

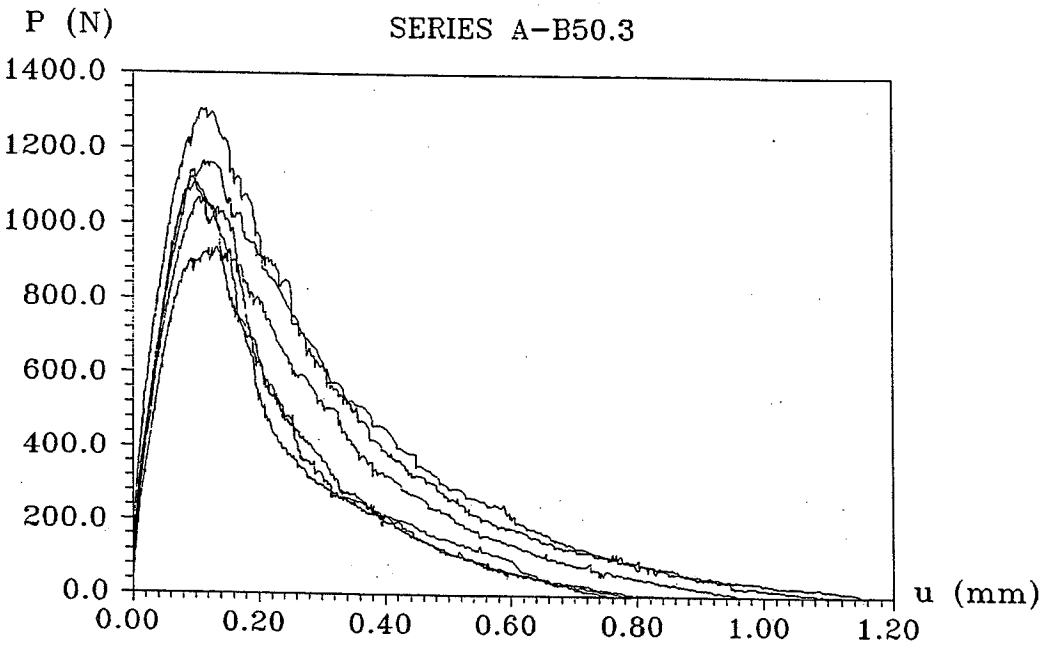

Figure I.14 Load-deflection curves for Series A-B50.3.

Beam no.	a/h	f_c (MPa)	f_{sp} (MPa)	u_0 (mm)	P_{max} (N)	W_e (Nmm)	G_F (N/m)	f_f (MPa)
A-B503-1	0.50	55.40	3.52	0.78	1067.7	265.9	82.6	5.57
A-B503-2				0.78	1123.4	261.1	81.2	5.84
A-B503-3				1.16	1304.3	437.3	130.7	6.71
A-B503-4				0.83	1138.4	261.2	83.5	5.91
A-B503-5				0.96	933.0	319.3	99.8	4.93
A-B503-6				1.12	1165.6	396.4	121.0	6.04
Mean	-	-	-	0.94	1122.1	323.5	99.8	5.83

Table I.11 Three point bending test results for Series A-B50.3.

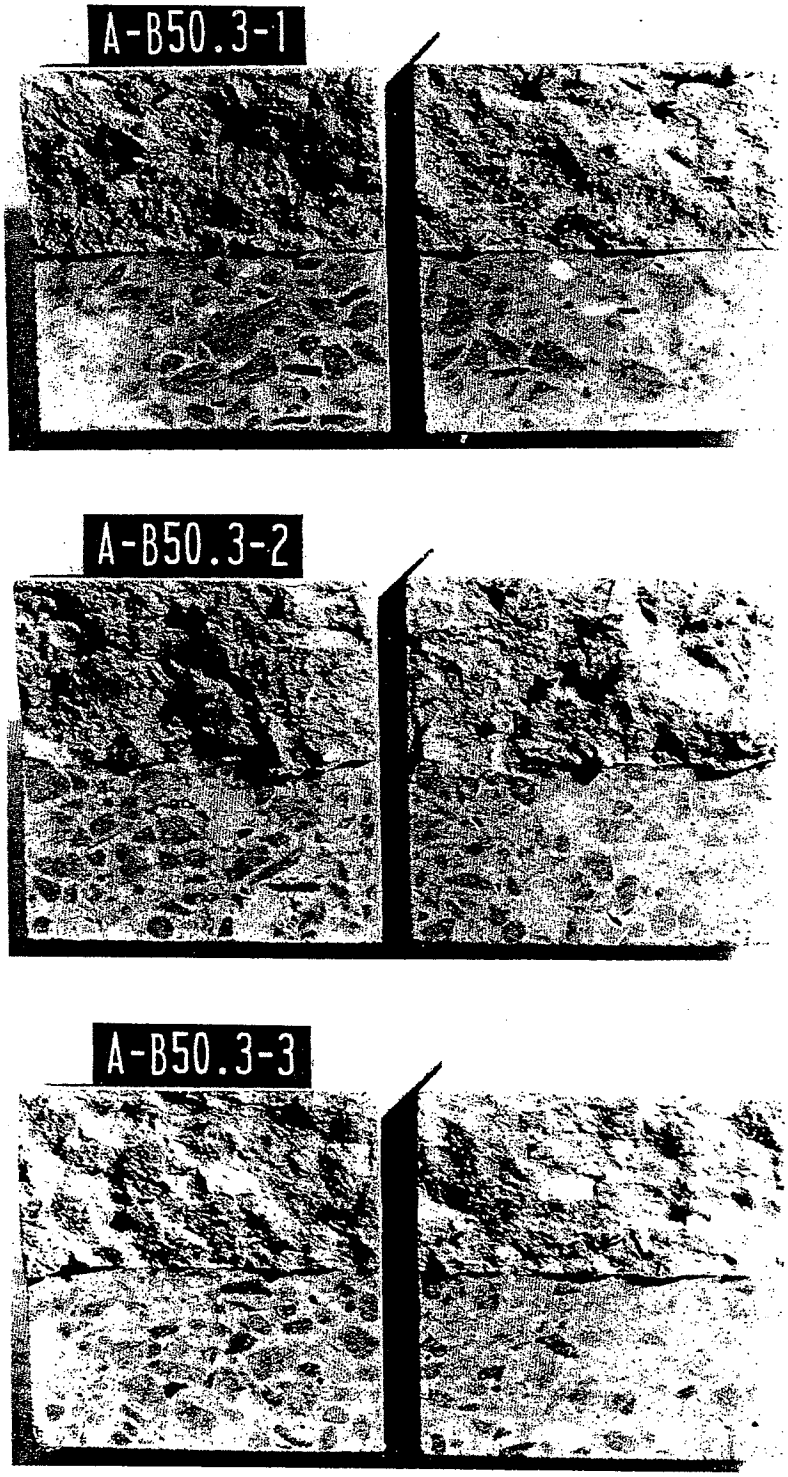

Figure I.15 Fracture area for beams in Series A-B50.3.

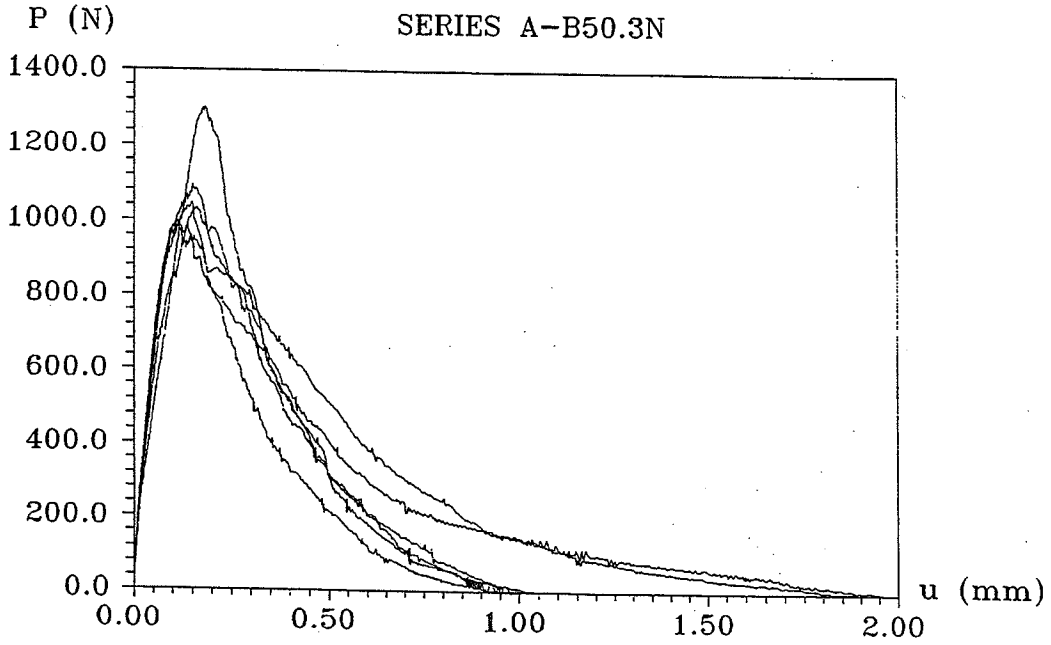

Figure I.16 Load-deflection curves for Series A-B50.3N.

Beam no.	a/h	f_c (MPa)	f_{sp} (MPa)	u_0 (mm)	P_{max} (N)	W_e (Nmm)	G_F (N/m)	f_f (MPa)
A-B503N-1	0.50	48.04	3.76	1.89	1047.3	556.7	181.7	5.47
A-B503N-2				0.94	999.7	320.7	99.4	5.25
A-B503N-3				1.00	984.7	380.1	113.4	5.17
A-B503N-4				1.96	1084.0	529.3	178.9	5.65
A-B503N-5				1.04	1300.2	430.5	124.8	6.69
A-B503N-6				0.98	1032.3	388.2	114.2	5.40
Mean	-	-	-	1.30	1074.7	434.3	135.4	5.61

Table I.12 Three point bending test results for Series A-B50.3N.

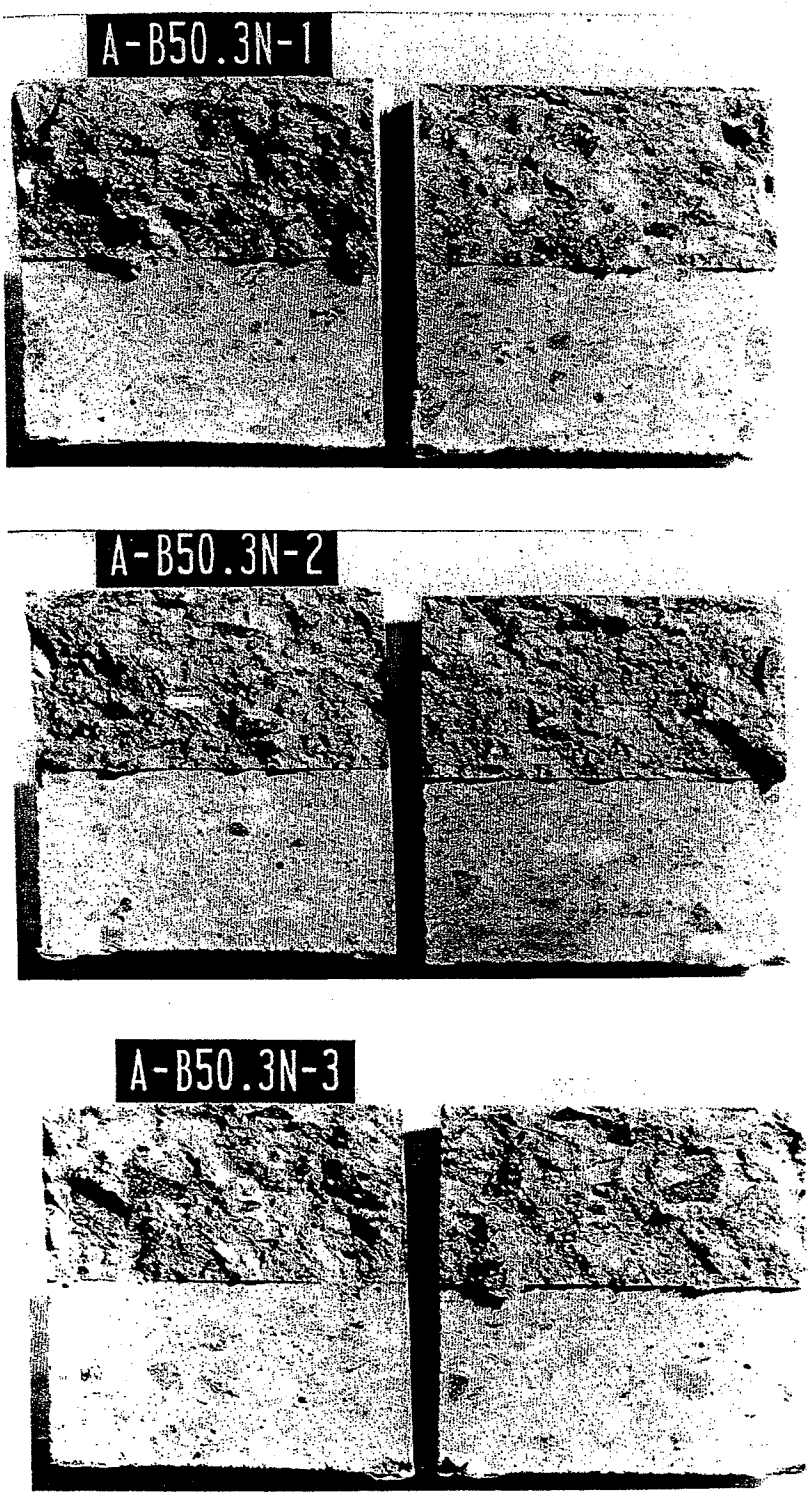

Figure I.17 Fracture area for beams in Series A-B50.3N.

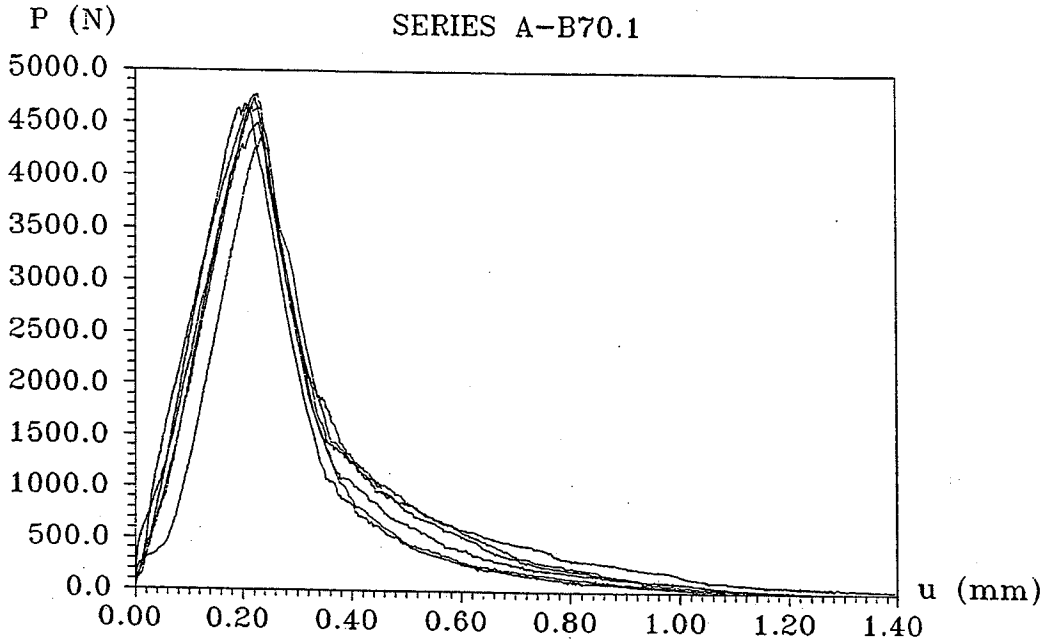

Figure I.18 Load-deflection curves for Series A-B70.1.

Beam no.	a/h	f_c (MPa)	f_{sp} (MPa)	u_0 (mm)	P_{max} (N)	W_e (Nmm)	G_F (N/m)	f_f (MPa)
A-B701-1	0.10	78.04	5.38	1.24	4370.0	1045.4	142.0	6.61
A-B701-2				1.05	4681.4	1117.3	146.0	7.07
A-B701-3				1.15	4501.9	1251.9	163.0	6.81
A-B701-4				1.19	4657.0	1293.4	168.4	7.04
A-B701-5				1.41	4776.6	1212.3	175.2	7.21
A-B701-6				1.11	4764.4	1175.4	153.8	7.20
Mean	-	-	-	1.19	4625.2	1182.6	158.1	6.99

Table I.13 Three point bending test results for Series A-B70.1.

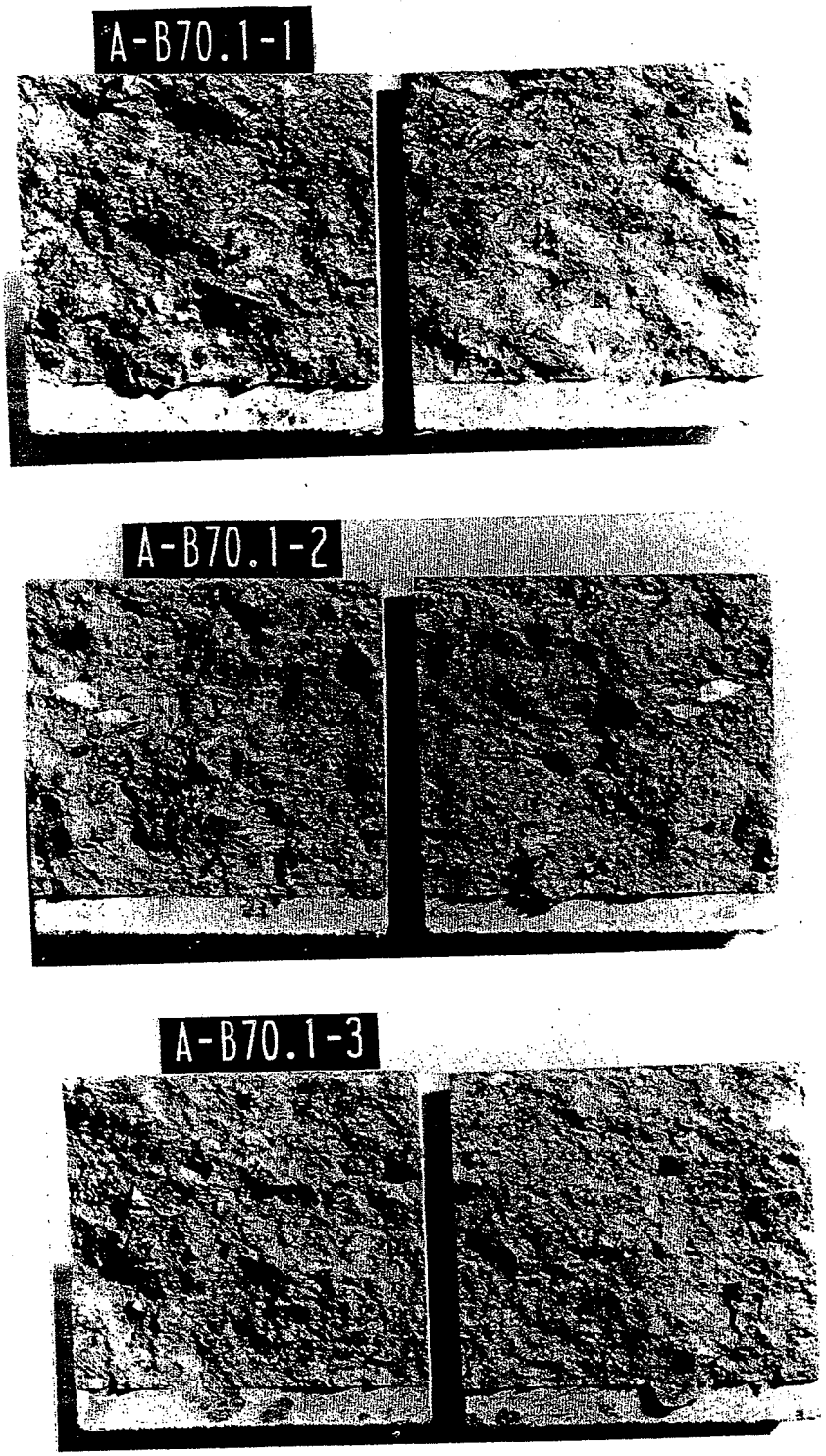

Figure I.19 Fracture area for beams in Series A-B70.1.

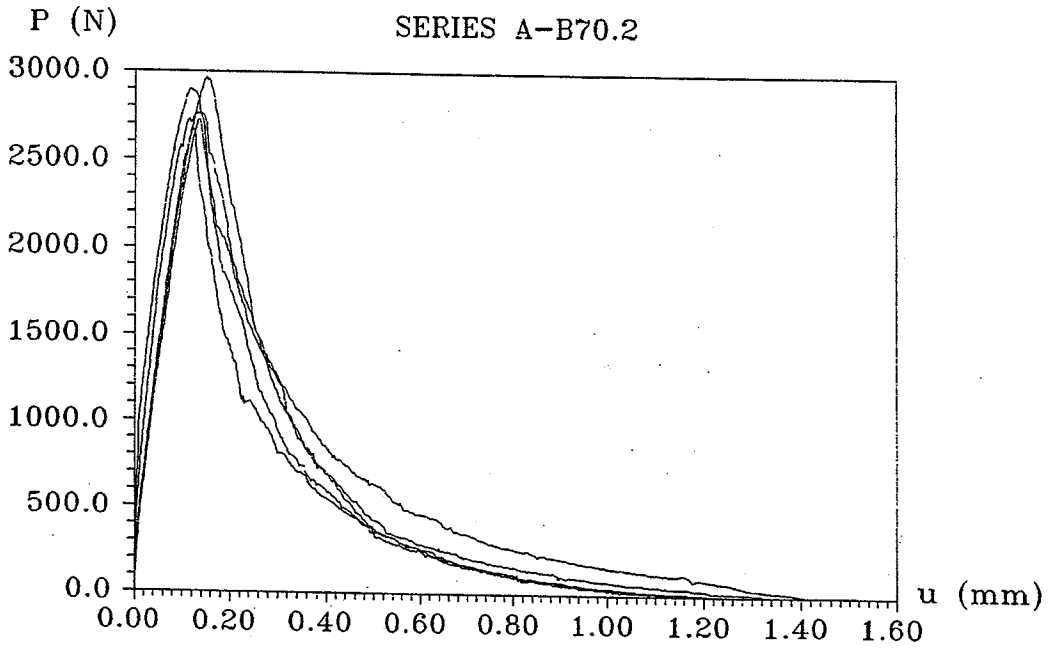

Figure I.20 Load-deflection curves for Series A-B70.2.

Beam no.	a/h	f_c (MPa)	f_{sp} (MPa)	u_0 (mm)	P_{max} (N)	W_e (Nmm)	G_F (N/m)	f_f (MPa)
A-B702-1	0.25	68.08	4.52	1.13	2724.3	734.1	126.1	6.01
A-B702-2				1.21	2672.6	649.7	116.8	5.90
A-B702-3				1.41	2895.6	976.0	165.3	6.38
A-B702-4				1.16	2761.0	735.7	127.0	6.09
A-B702-5				-	-	-	-	-
A-B702-6				1.42	2965.0	825.9	145.3	6.52
Mean	-	-	-	1.27	2803.7	784.3	136.1	6.18

Table I.14 Three point bending test results for Series A-B70.2.

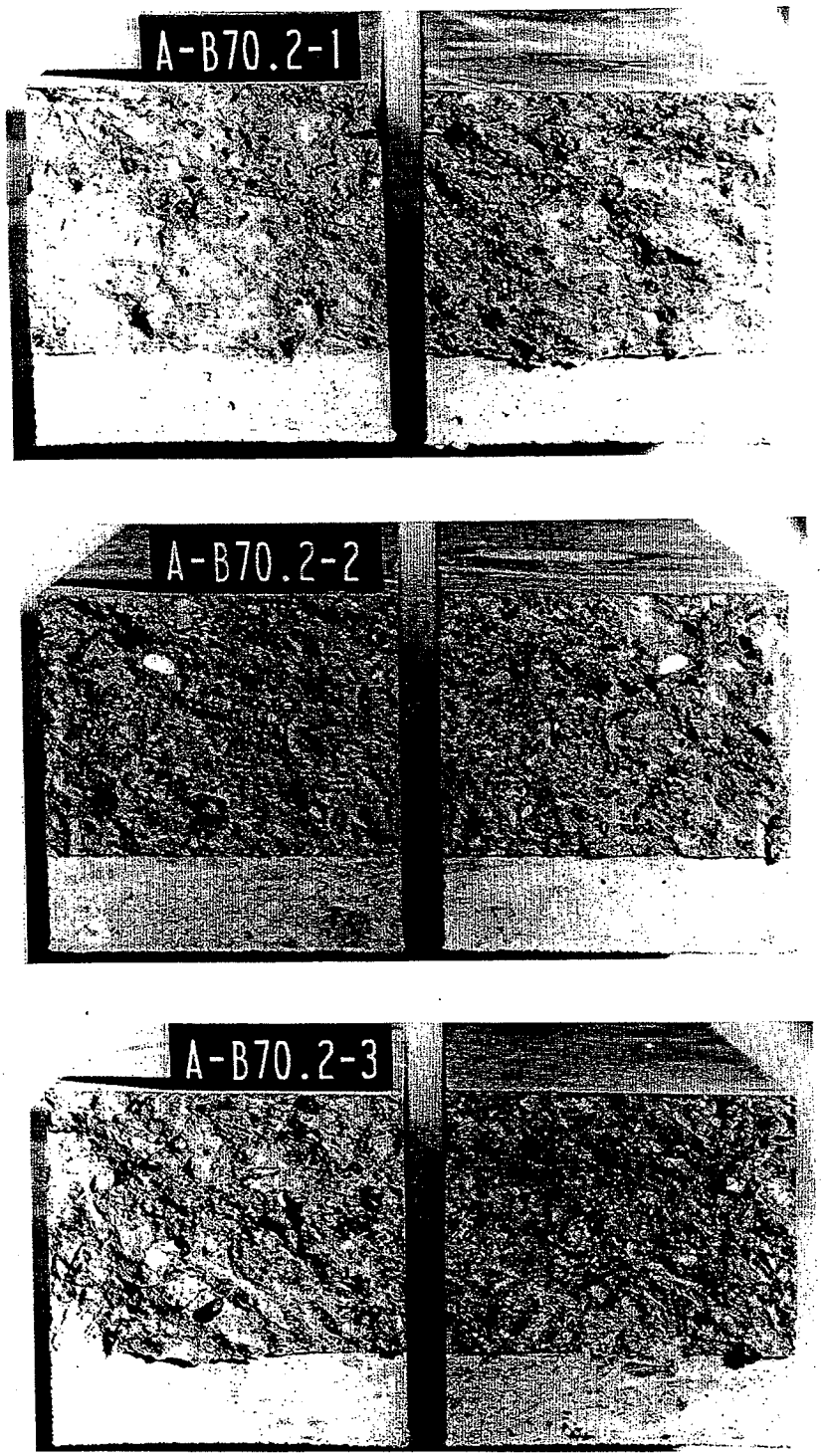

Figure I.21 Fracture area for beams in Series A-B70.2.

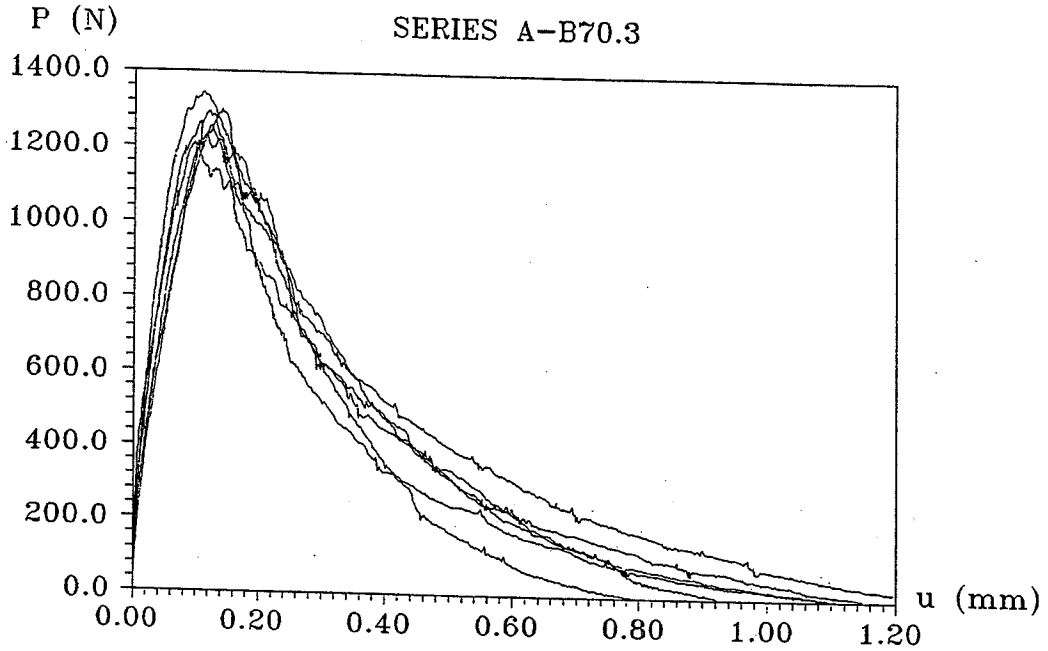

Figure I.22 Load-deflection curves for Series A-B70.3.

Beam no.	a/h	f_c (MPa)	f_{sp} (MPa)	u_0 (mm)	P_{max} (N)	W_e (Nmm)	G_F (N/m)	f_f (MPa)
A-B703-1	0.50	72.03	4.82	1.28	1217.3	495.4	146.8	6.29
A-B703-2				1.11	1292.1	446.9	130.7	6.65
A-B703-3				0.79	1300.2	363.4	102.2	6.69
A-B703-4				1.10	1341.0	400.8	121.1	6.88
A-B703-5				1.15	1255.4	431.4	129.1	6.47
A-B703-6				0.92	1210.5	427.3	119.9	6.26
Mean	-	-	-	1.06	1269.4	427.5	125.0	6.54

Table I.15 Three point bending test results for Series A-B70.3.

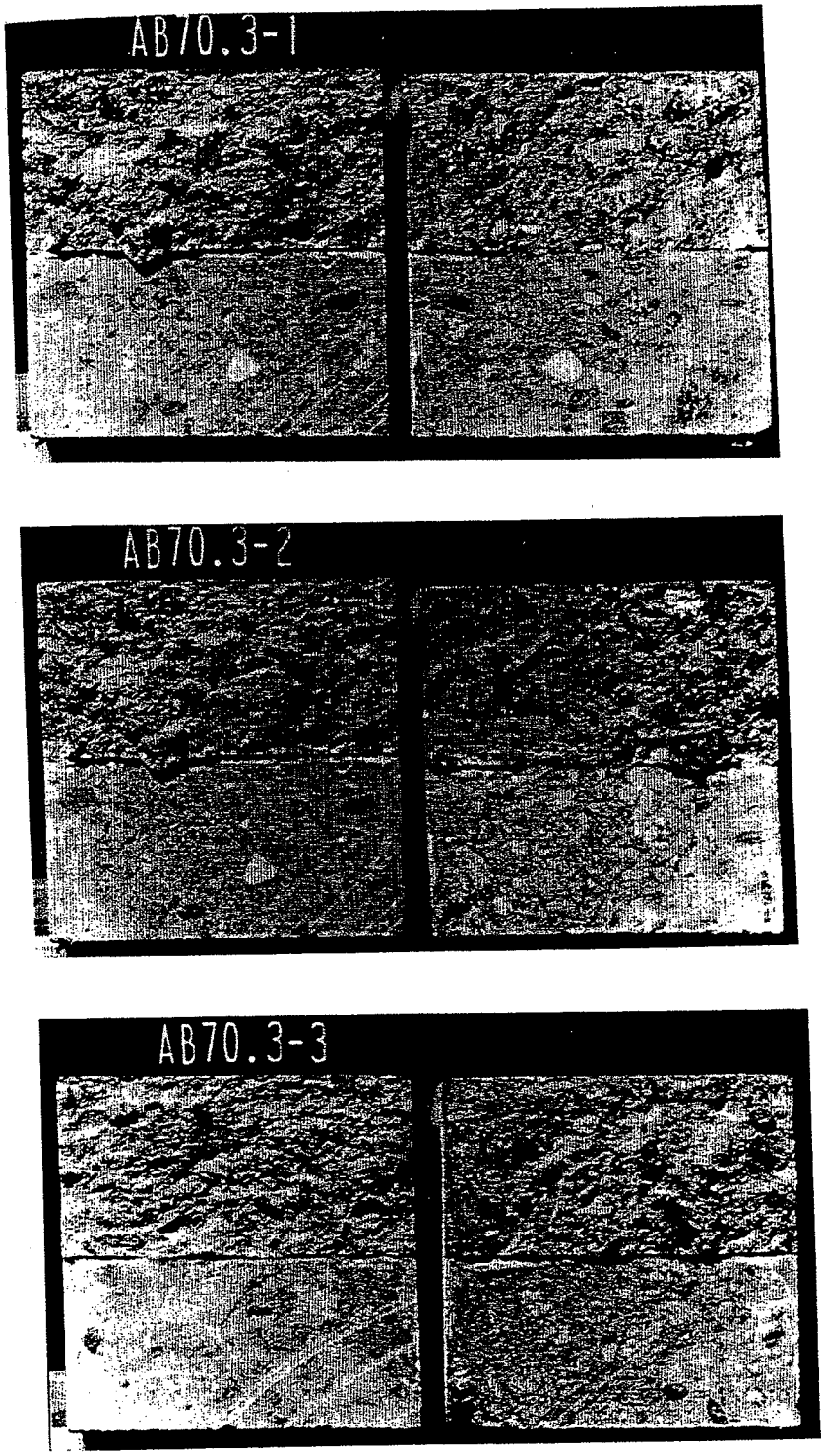

Figure I.23 Fracture area for beams in Series A-B70.3.

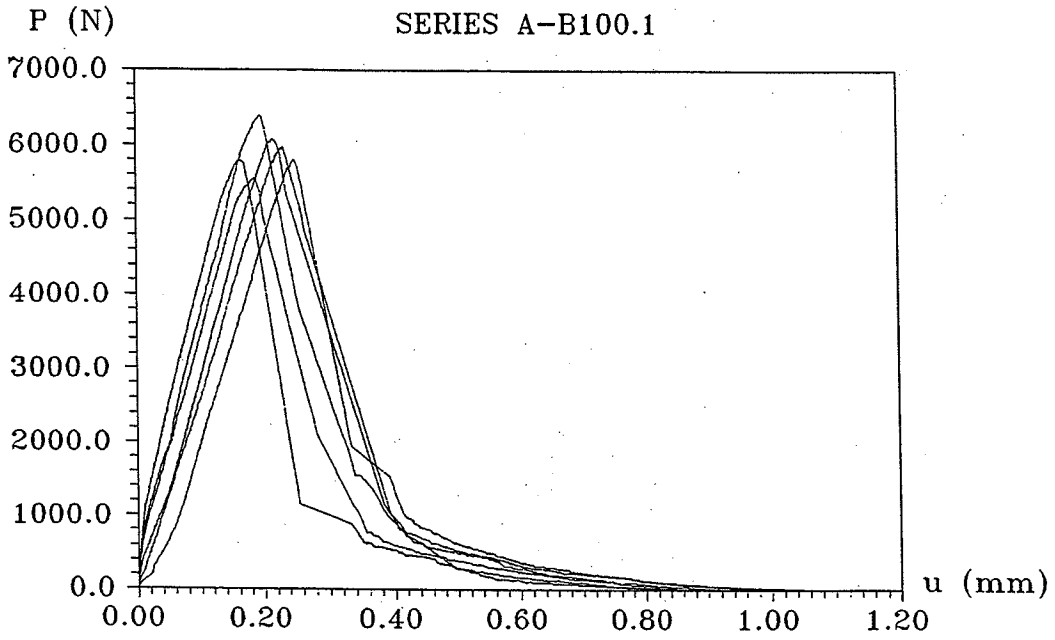

Figure I.24 Load-deflection curves for Series A-B100.1.

Beam no.	a/h	f_c (MPa)	f_{sp} (MPa)	u_0 (mm)	P_{max} (N)	W_e (Nmm)	G_F (N/m)	f_f (MPa)
A-B1001-1	0.10	99.41	5.66	0.90	5784.5	1113.1	142.3	8.71
A-B1001-2				0.95	5550.5	1213.3	154.6	8.36
A-B1001-3				0.94	5968.1	1414.3	176.7	8.98
A-B1001-4				1.05	6079.6	1459.1	183.9	9.14
A-B1001-5				1.02	5787.2	1310.9	166.7	8.71
A-B1001-6				0.85	6389.7	1402.0	173.5	9.60
Mean	-	-	-	0.95	5926.6	1318.8	166.3	8.92

Table I.16 Three point bending test results for Series A-B100.1.

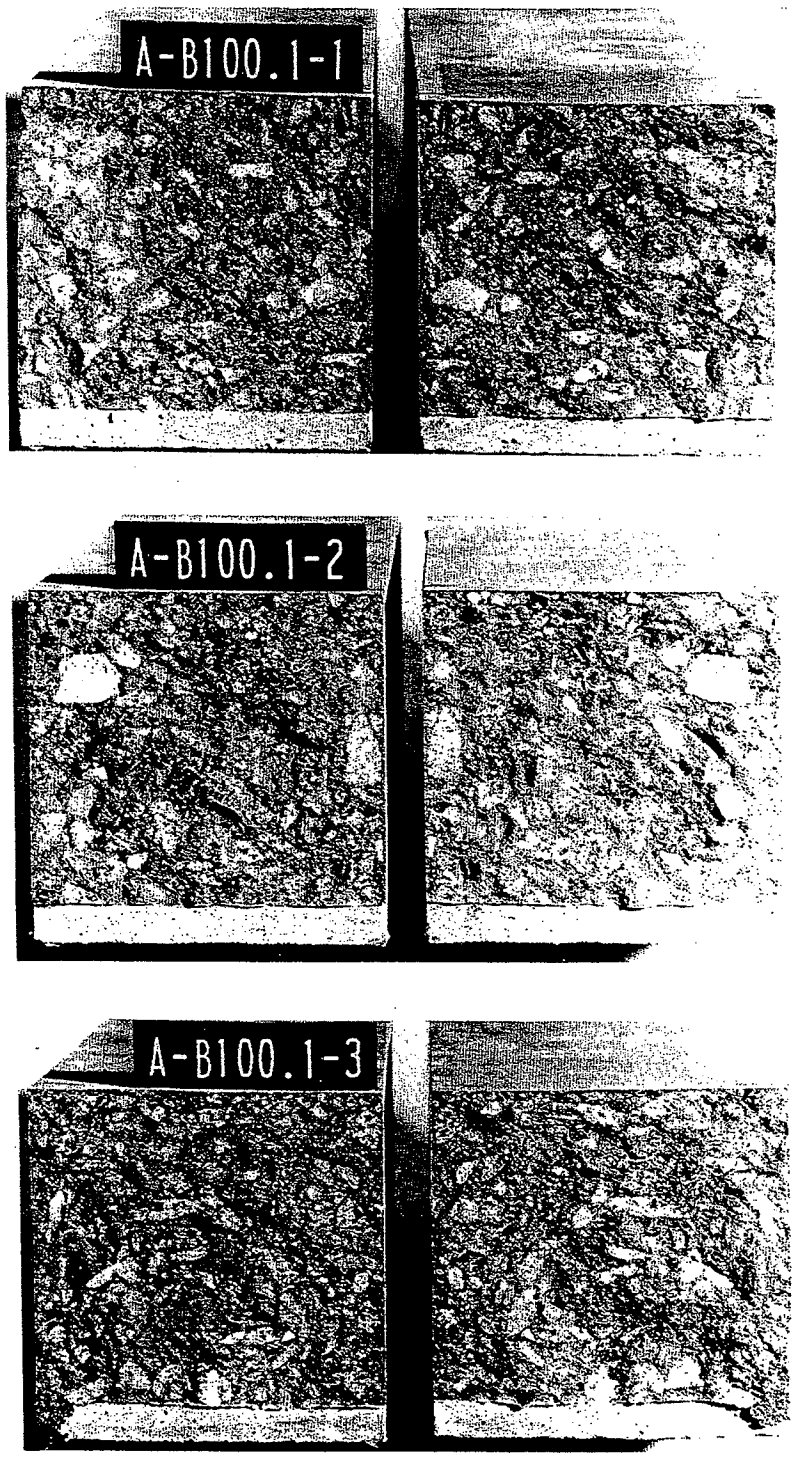

Figure I.25 Fracture area for beams in Series A-B100.1.

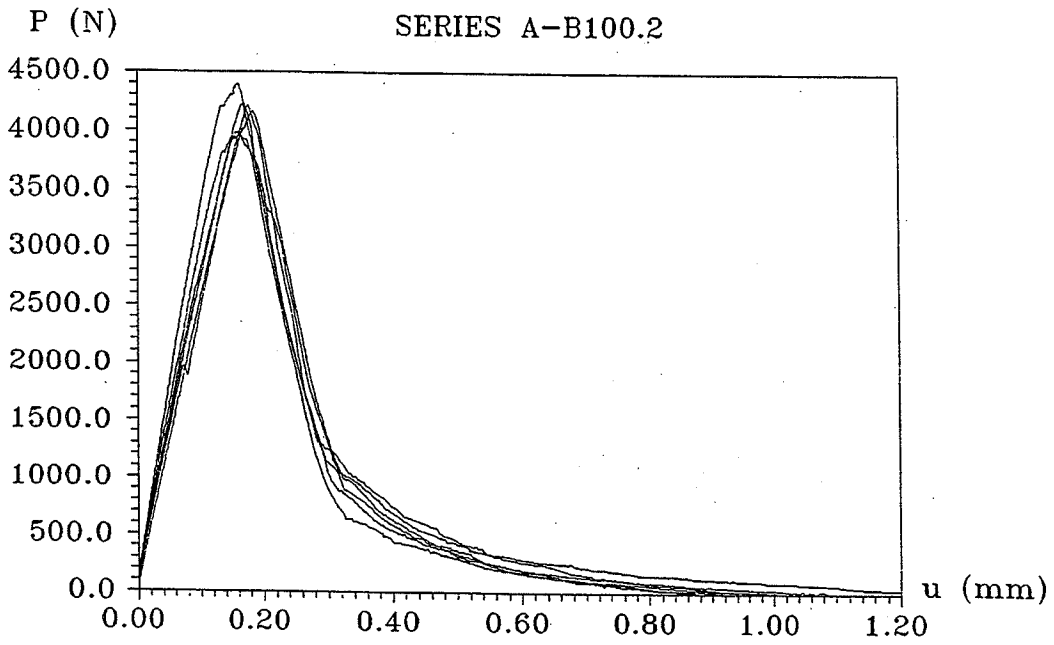

Figure I.26 Load-deflection curves for Series A-B100.2.

Beam no.	a/h	f_c (MPa)	f_{sp} (MPa)	u_0 (mm)	P_{max} (N)	W_e (Nmm)	G_F (N/m)	f_f (MPa)
A-B1002-1	0.25	100.11	5.72	1.02	4210.8	891.4	144.3	9.18
A-B1002-2				0.89	4159.3	923.5	145.2	9.07
A-B1002-3				1.02	3986.4	850.3	138.6	8.70
A-B1002-4				1.10	4393.1	1039.8	165.9	9.57
A-B1002-5				1.35	3956.5	1017.3	169.3	8.64
A-B1002-6				0.93	4238.0	896.8	142.7	9.24
Mean	-	-	-	1.05	4157.4	936.5	151.0	9.07

Table I.17 Three point bending test results for Series A-B100.2.

Figure I.27 Fracture area for beams in Series A-B100.2.

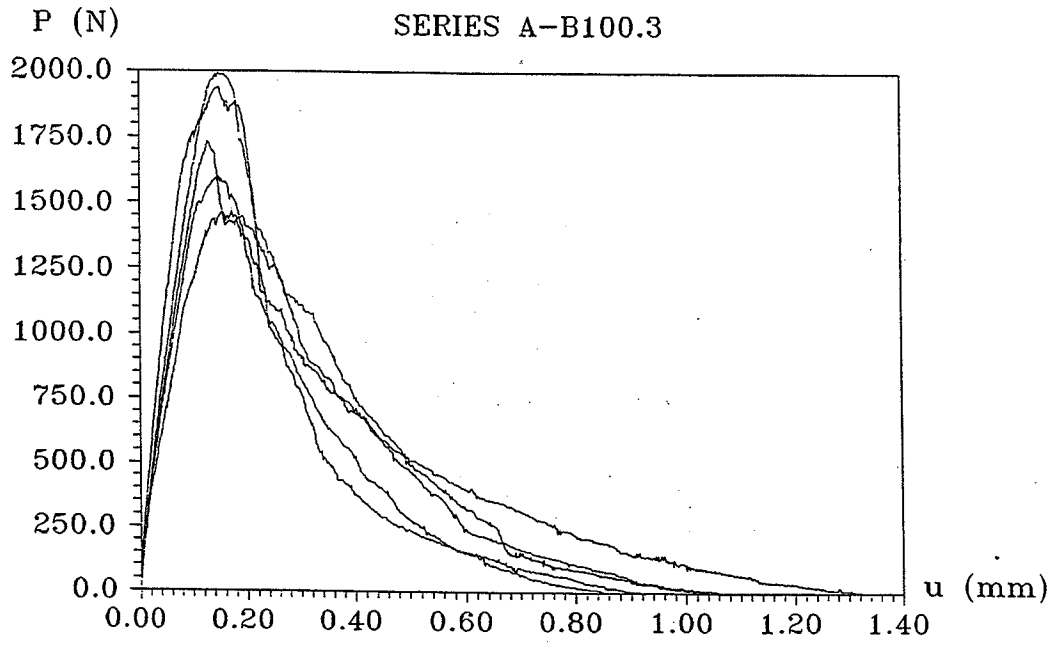

Figure I.28 Load-deflection curves for Series A-B100.3.

Beam no.	a/h	f_c (MPa)	f_{sp} (MPa)	u_0 (mm)	P_{max} (N)	W_e (Nmm)	G_F (N/m)	f_f (MPa)
A-B1003-1	0.50	99.00	5.49	0.92	1598.1	478.9	130.3	8.12
A-B1003-2				1.06	1732.8	602.4	160.1	8.76
A-B1003-3				1.32	1938.1	713.9	192.2	9.75
A-B1003-4				1.05	1468.9	538.1	146.9	7.50
A-B1003-5				0.85	1966.7	499.7	131.6	9.89
A-B1003-6				-	-	-	-	
Mean	-	-	-	1.04	1740.9	566.6	152.2	8.80

Table I.18 Three point bending test results for Series A-B100.3.

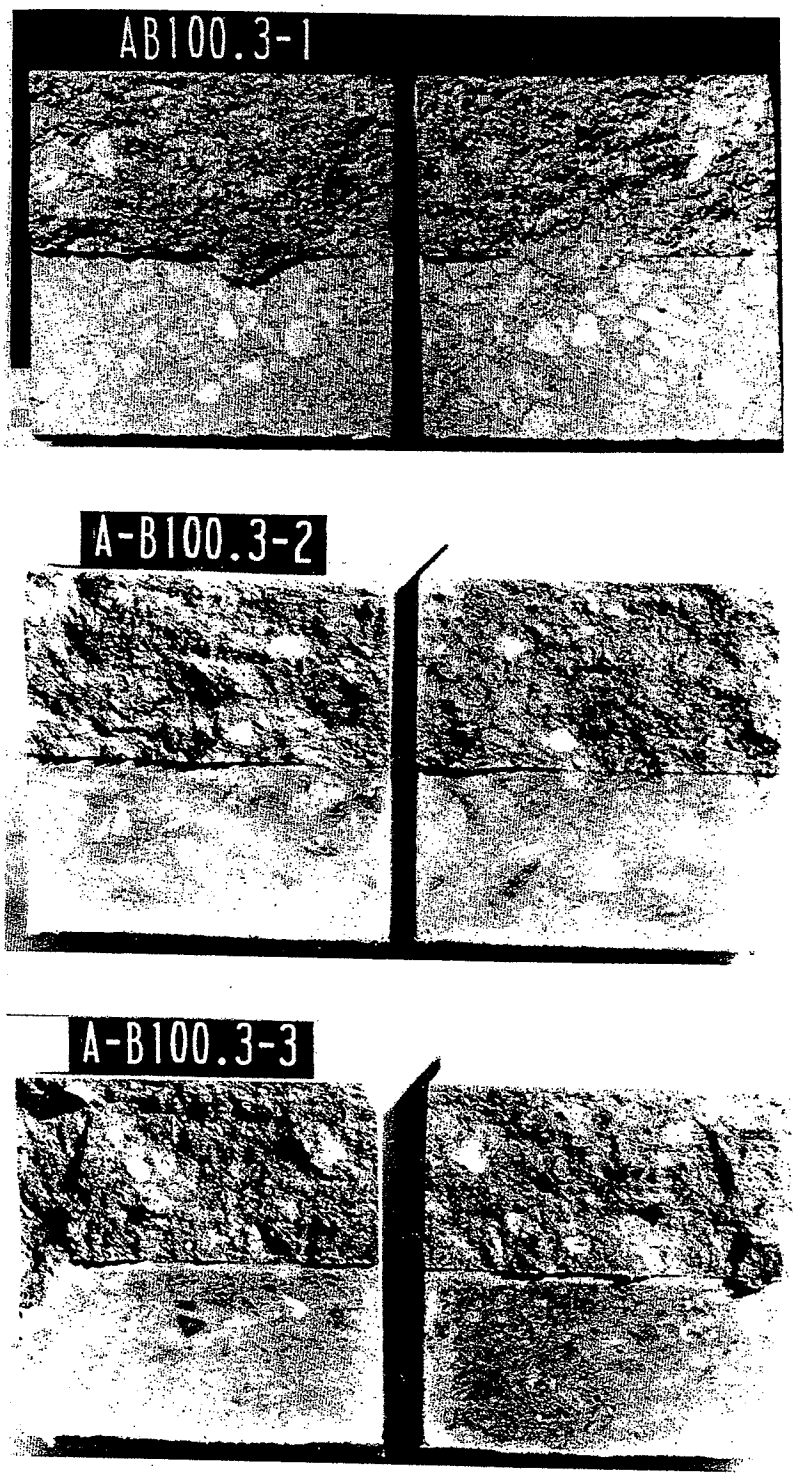

Figure I.29 Fracture area for beams in Series A-B100.3.

SERIES B

Intended Compressive Strength	30 MPa	100 MPa
Materials	kg/m^3	kg/m^3
Portland Rapid Cement	188	390
Fly Ash	80	-
Mikrosilica Fume-Slurry	-	80
Sand 0 - 4 mm	640	521
Natural Gravel 4 - 8 mm	272	247
Crushed Gravel 4 - 16 mm	1089	989
Water	175	61
Plasticizer	-	2.40
Superplasticizer	-	18.04
Water-Cement Ratio	0.84	0.21

Table I.19 Mixing proportions for the concrete in series B.

Batch No	Cur*	Compressive Tests f_c (MPa)		Splitting Tests f_{sp} (MPa)		Modulus of Elasticity E_c (MPa)	
		Mean Value	Standard Deviation	Mean Value	Standard Deviation	Mean Value	Standard Deviation
B-B30.1	1	26.7	1.8	1.95	0.12	24380	834
B-B30.2	2	15.8	0.6	2.02	0.13	15320	1310
B-B30.3	3	34.4	1.4	3.86	0.07	28480	1075
B-B30.4	4	32.4	1.4	3.10	0.12	-	-
B-B100.1	1	83.7	2.6	6.27	0.59	36210	1315
B-B100.2	2	90.6	1.9	4.93	0.51	36900	2066
B-B100.3	3	106.9	5.4	6.47	0.45	41440	203
B-B100.4	4	104.7	3.6	5.48	0.32	-	-

* 1. Specimens were cured outside for 28 days at about 20 °C and 75 % RH.
2. Specimens were cured in a heating chamber for 28 days at 40 °C and 34 % RH.
3. Specimens were cured in water for 14 days (20 °C) and in a heating chamber for 14 days at 40 °C and 34 % RH.
4. Specimens were cured in water for 28 days (20 °C) and in a heating chamber for 161 days at 40 °C and 34 % RH.

Table I.20 Cylinder data for the concrete in Series B.

Batch No	Compressive Strength in MPa.				
	7 Days	14 Days	16 Days	21 Days	28 Days
B-B30.1	16.2	20.4	-	23.8	26.7
B-B30.2	14.6	16.4	-	16.6	15.8
B-B30.3	17.4	20.9	24.1	32.3	34.4
B-B100.1	65.4	76.8	-	83.2	83.7
B-B100.2	92.5	93.7	-	91.1	90.6
B-B100.3	75.0	81.3	99.3	103.4	106.9

Table I.21 Compressive strength developement for cylinders in Series B.

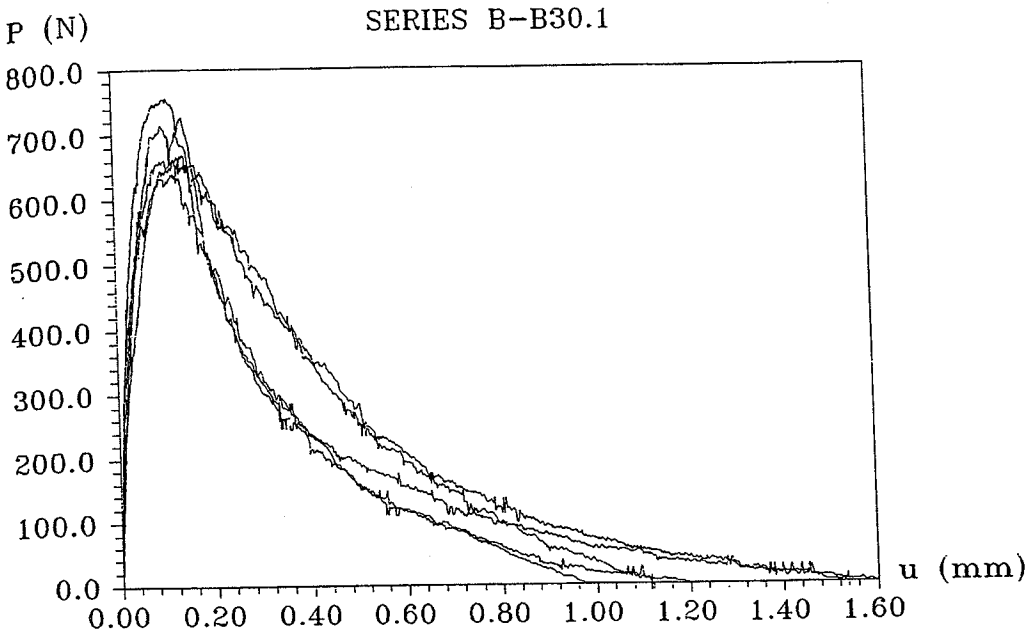

Figure I.30 Load-deflection curves for Series B-B30.1.

Beam no.	Cur.	f_c (MPa)	f_{sp} (MPa)	u_0 (mm)	P_{max} (N)	W_e (Nmm)	G_F (N/m)	f_f (MPa)
B-B301-1	1*	26.7	1.95	1.60	667.8	322.3	124.0	3.65
B-B301-2				1.54	756.2	287.1	114.8	4.08
B-B301-3				1.20	715.4	236.0	92.0	3.88
B-B301-4				1.12	662.4	308.3	103.3	3.63
B-B301-5				1.03	640.6	227.5	83.8	3.52
B-B301-6				-	-	-	-	-
Mean	-	-	-	1.30	688.4	276.2	103.4	3.75

* 1. Specimens were cured outside for 28 days at about 20 °C and 75 % RH.

Table I.22 Three point bending test results for Series B-B30.1.

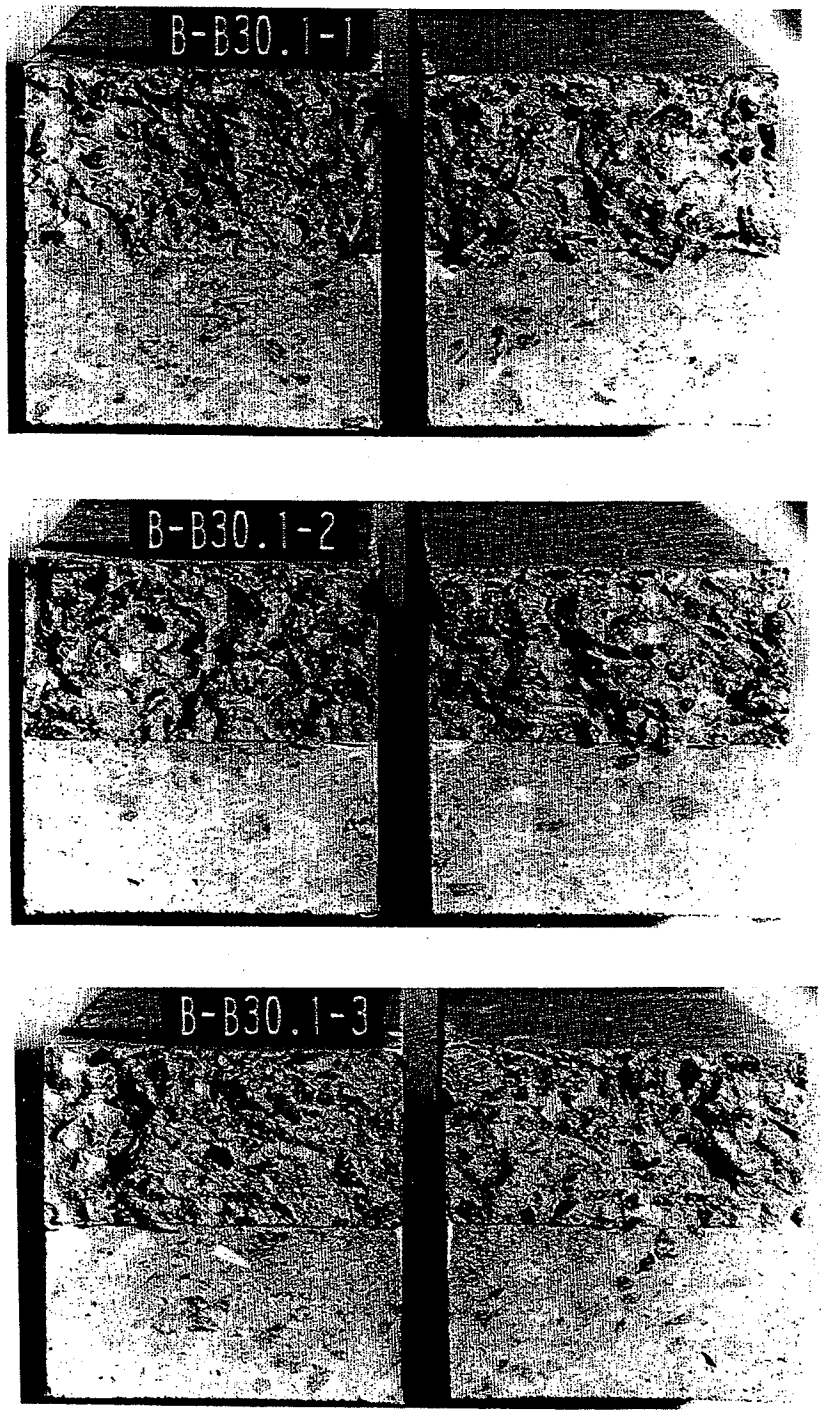

Figure I.31 Fracture area for beams in Series B-B30.1.

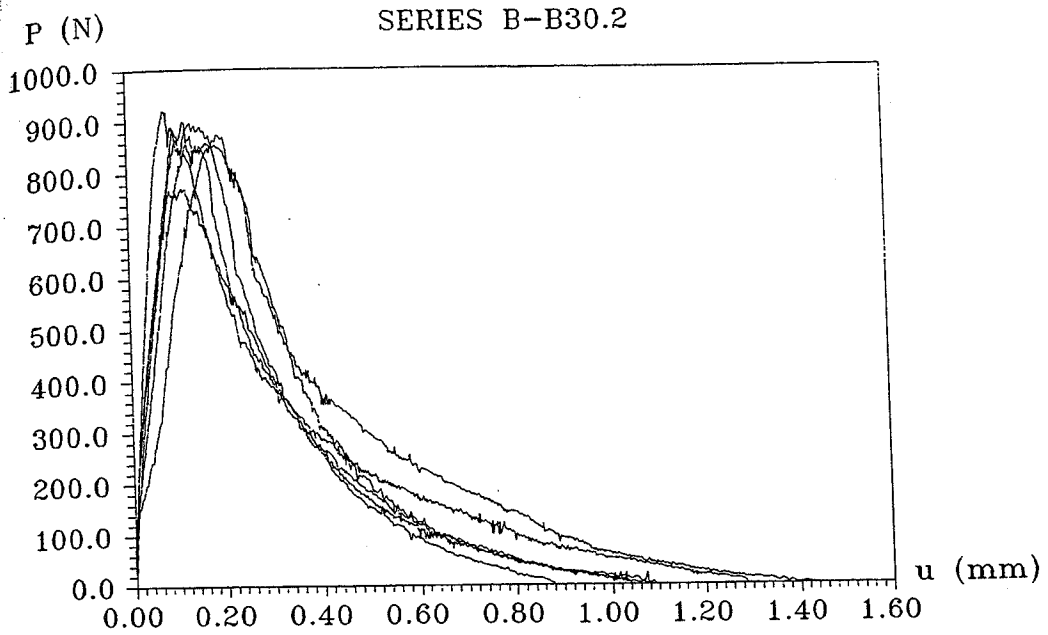

Figure I.32 Load-deflection curves for Series B-B30.2.

Beam no.	Cur.	f_c (MPa)	f_{sp} (MPa)	u_0 (mm)	P_{max} (N)	W_e (Nmm)	G_F (N/m)	f_f (MPa)
B-B302-1	2*	15.8	2.02	1.44	858.2	369.4	127.7	4.57
B-B302-2				1.30	922.1	314.1	111.3	4.87
B-B302-3				1.08	900.4	272.8	94.8	4.77
B-B302-4				0.88	897.7	270.8	87.0	4.76
B-B302-5				1.04	772.5	265.1	91.8	4.16
B-B302-6				1.09	874.5	286.5	98.1	4.64
Mean	-	-	-	1.14	870.9	296.5	101.8	4.63

* 2. Specimens were cured in a heating chamber for 28 days at 40 °C and 34 % RH.

Table I.23 Three point bending test results for Series B-B30.2.

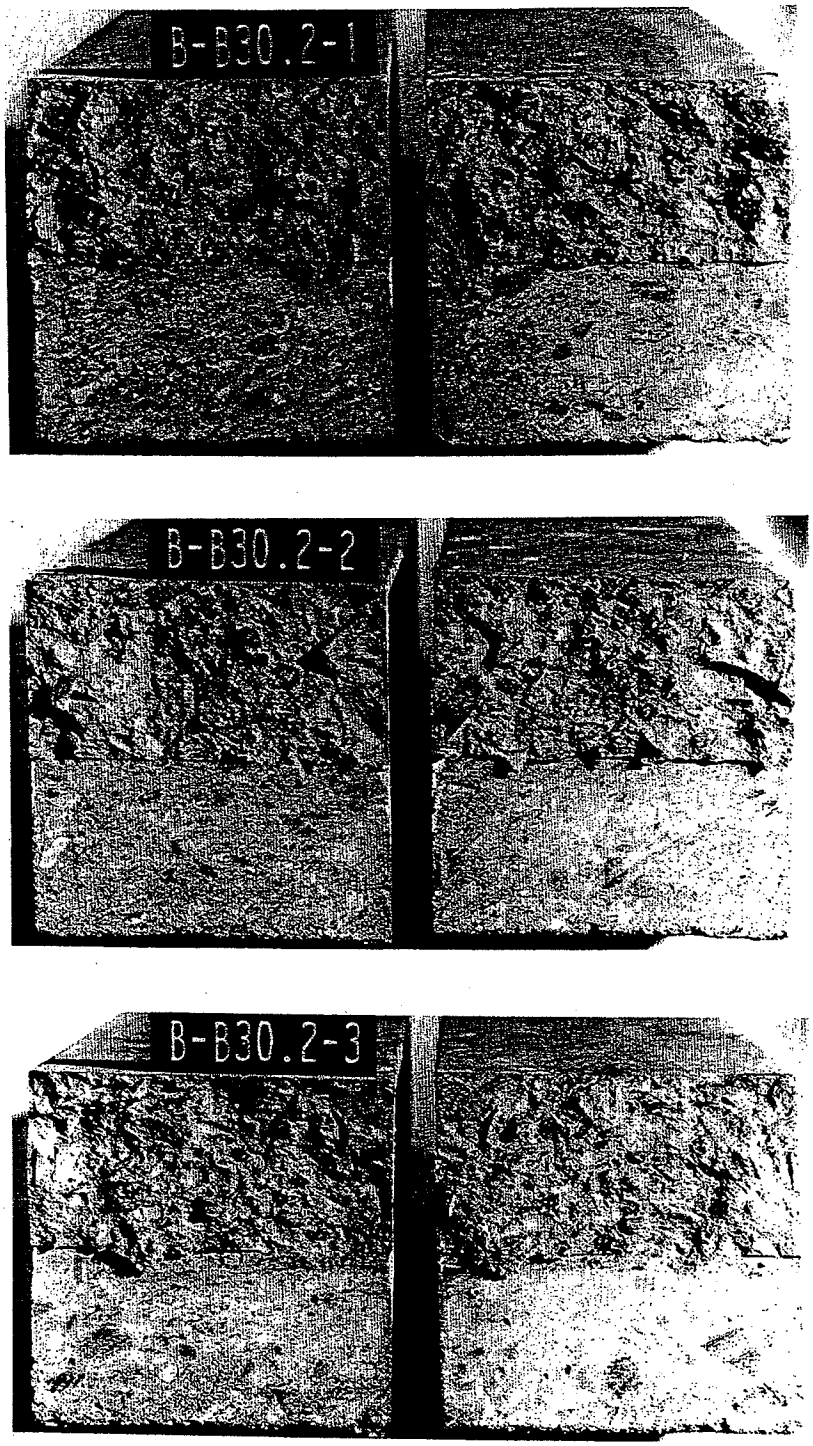

Figure I.33 Fracture area for beams in Series B-B30.2.

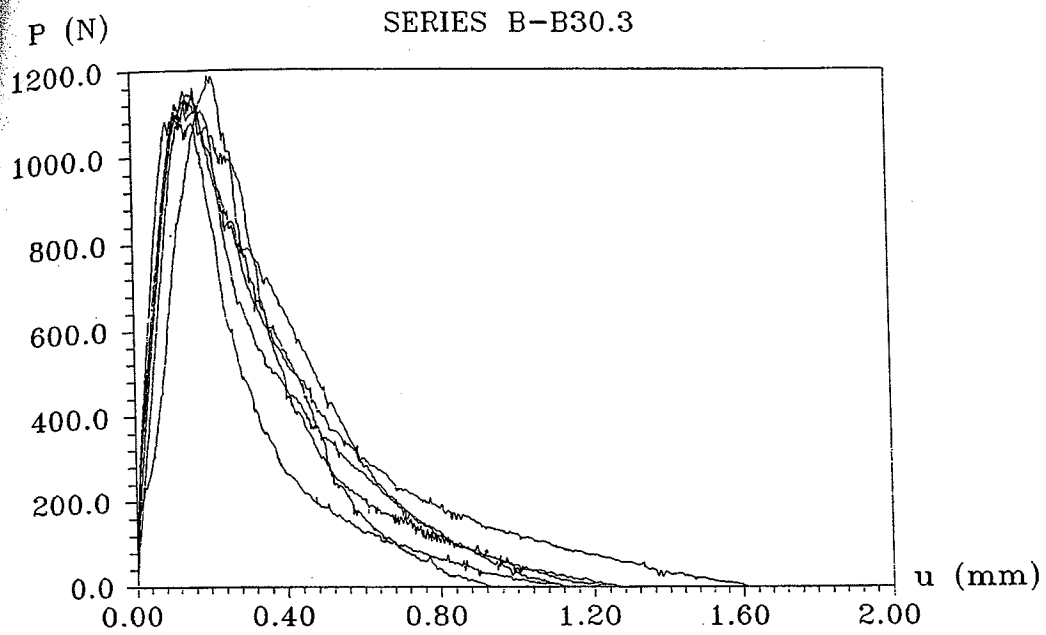

Figure I.34 Load-deflection curves for Series B-B30.3.

Beam no.	Cur.	f_c (MPa)	f_{sp} (MPa)	u_0 (mm)	P_{max} (N)	W_e (Nmm)	G_F (N/m)	f_f (MPa)
B-B303-1	3*	34.4	3.86	1.08	1078.5	328.7	106.1	5.62
B-B303-2				1.61	1128.9	509.8	162.1	5.87
B-B303-3				1.12	1120.7	479.5	137.7	5.83
B-B303-4				1.23	1158.8	479.0	141.8	6.01
B-B303-5				0.93	1186.0	375.8	109.7	6.14
B-B303-6				1.26	1153.4	408.9	129.0	5.98
Mean	-	-	-	1.21	1137.7	430.3	131.1	5.91

* 3. Specimens were cured in water for 14 days (20 °C) and in a heating chamber for 14 days at 40 °C and 34 % RH.

Table I.24 Three point bending test results for Series B-B30.3.

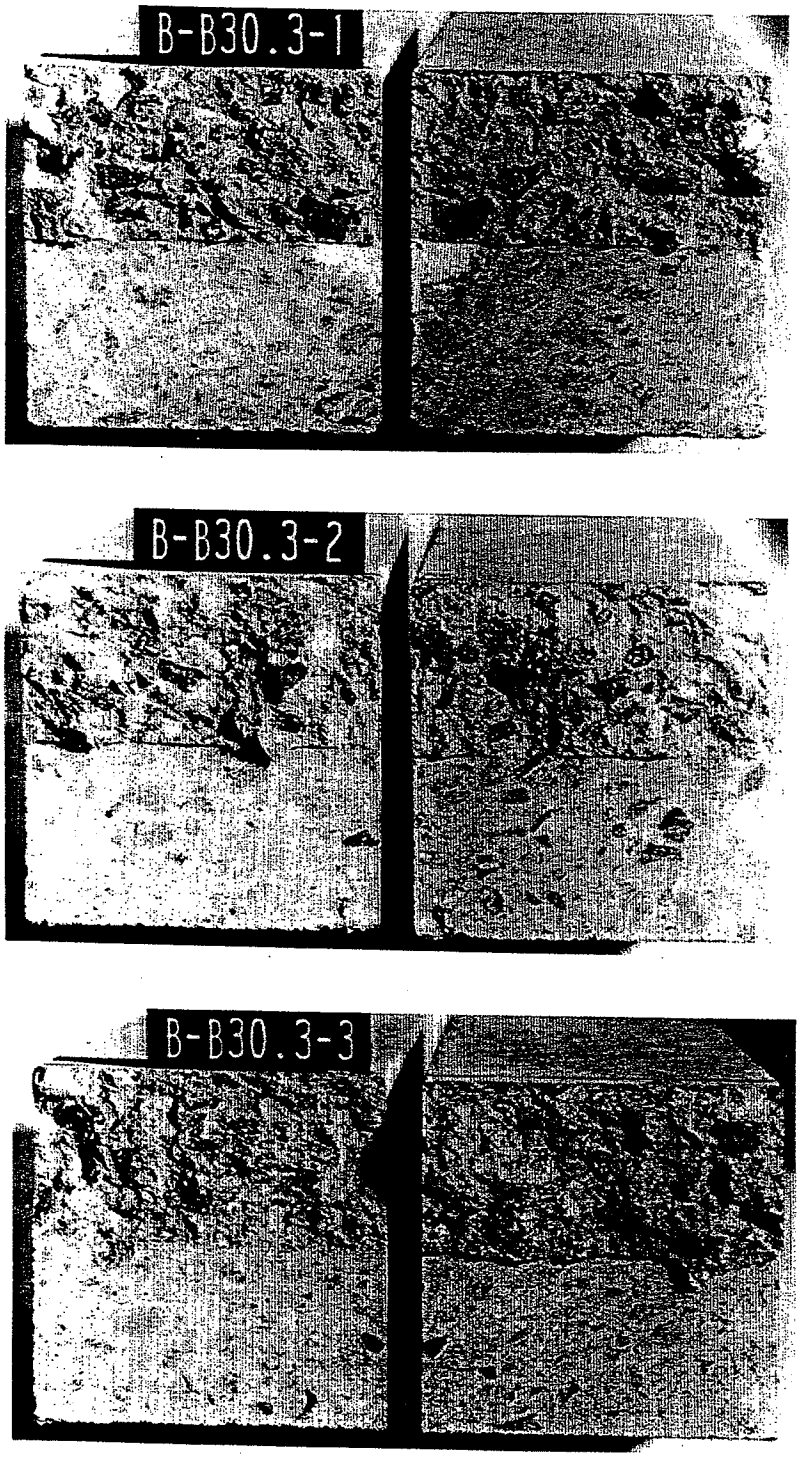

Figure I.35 Fracture area for beams in Series B-B30.3.

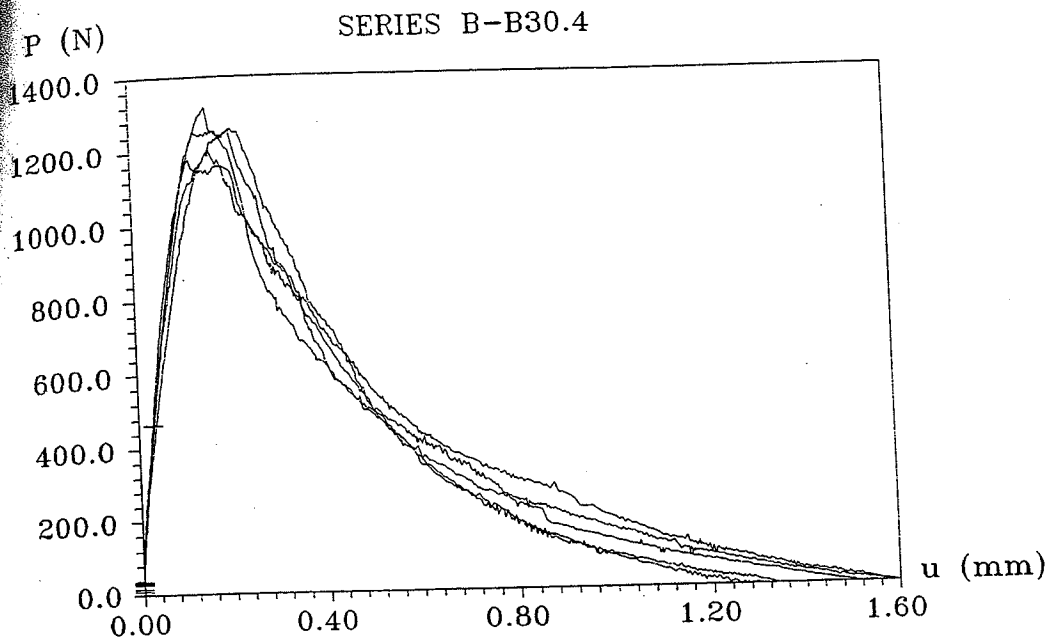

Figure I.36 Load-deflection curves for Series B-B30.4.

Beam no.	Cur.	f_c (MPa)	f_{sp} (MPa)	u_0 (mm)	P_{max} (N)	W_e (Nmm)	G_F (N/m)	f_f (MPa)
B-B304-1	4*	32.4	3.10	1.33	1317.9	588.5	167.4	6.77
B-B304-2				1.51	1176.5	582.8	172.8	6.09
B-B304-3				1.30	1255.4	539.7	156.3	6.47
B-B304-4				1.59	1256.7	620.1	183.4	6.48
B-B304-5				1.56	1203.7	631.8	185.0	6.23
B-B304-6				-	-	-	-	-
Mean	-	-	-	1.46	1242.0	592.6	173.0	6.41

* 4. Specimens were cured in water for 28 days (20 °C) and in a heating chamber for 161 days at 40 °C and 34 % RH.

Table I.25 Three point bending test results for Series B-B30.4.

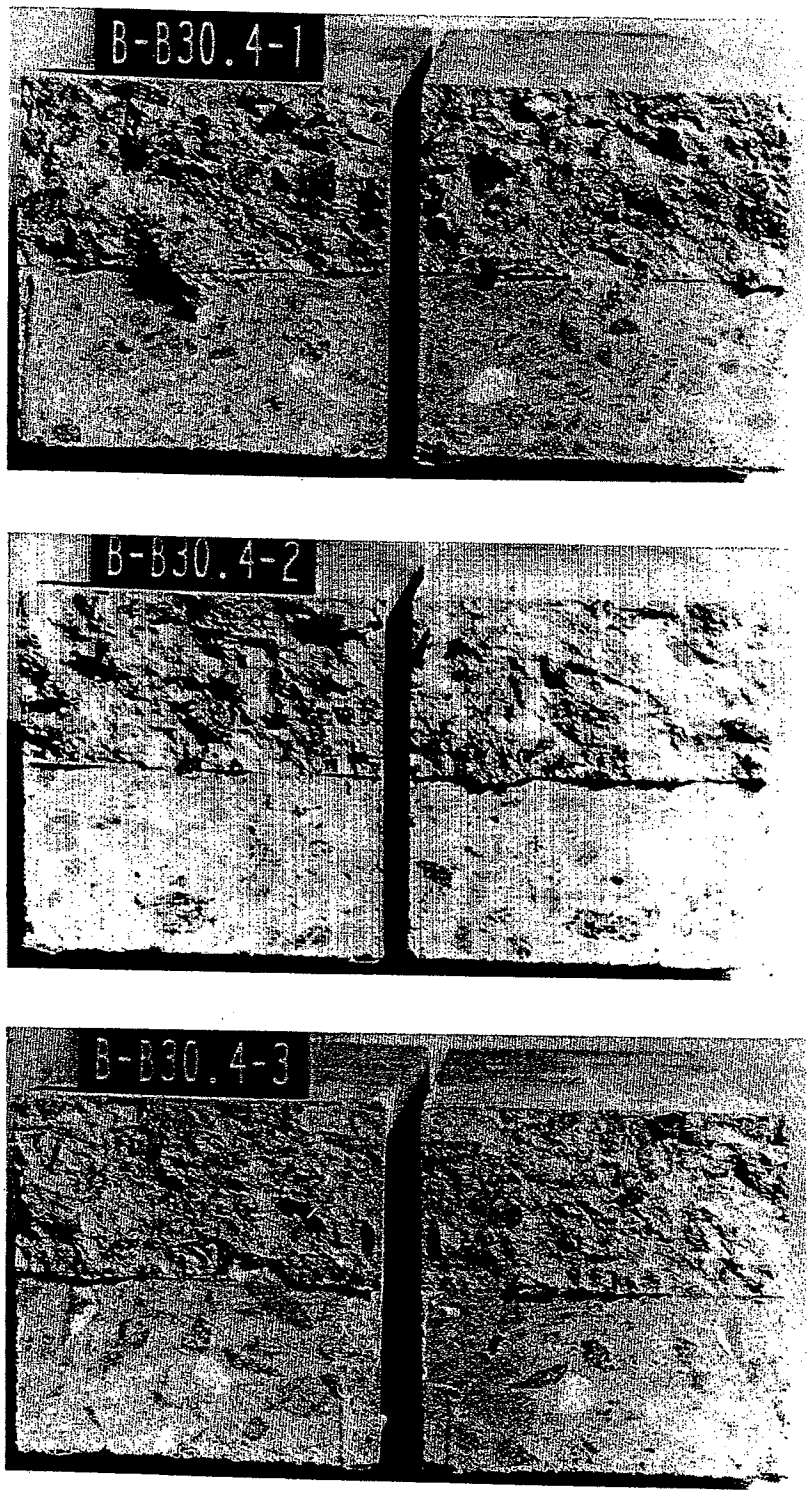

Figure I.37 Fracture area for beams in Series B-B30.4.

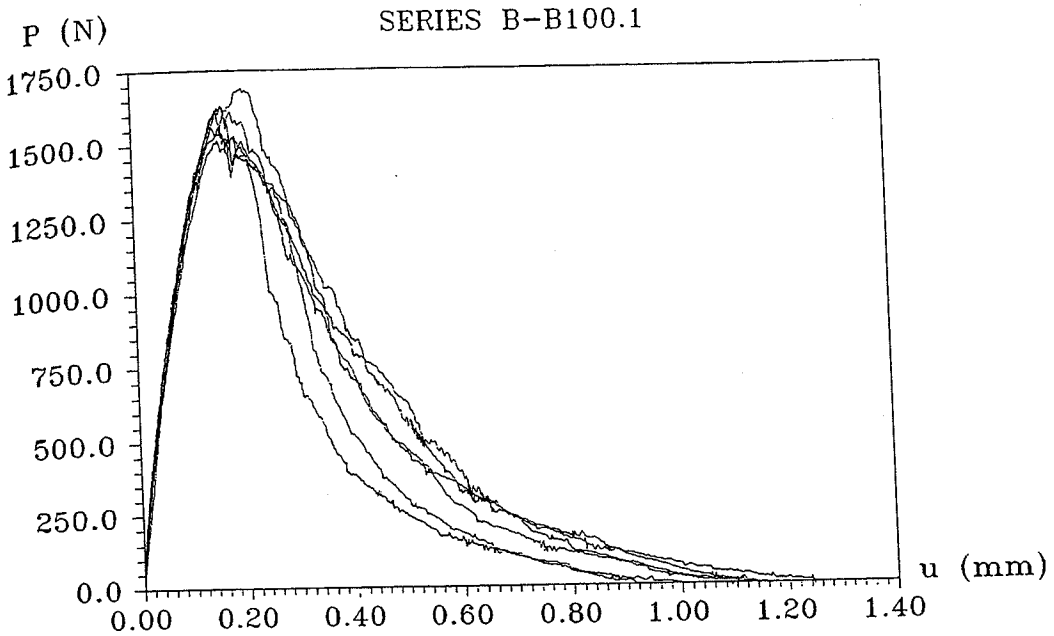

Figure I.38 Load-deflection curves for Series B-B100.1.

Beam no.	Cur.	f_c (MPa)	f_{sp} (MPa)	u_0 (mm)	P_{max} (N)	W_e (Nmm)	G_F (N/m)	f_f (MPa)
B-B1001-1	1*	83.7	6.27	1.15	1513.8	591.7	161.4	7.71
B-B1001-2				1.00	1628.0	457.0	128.7	7.81
B-B1001-3				1.25	1560.0	649.8	176.4	7.49
B-B1001-4				1.14	1690.6	669.1	176.3	8.11
B-B1001-5				0.92	1539.6	512.6	136.7	7.39
B-B1001-6				1.15	1626.7	608.3	164.5	7.81
Mean	-	-	-	1.10	1593.1	581.4	157.3	7.72

* 1. Specimens were cured outside for 28 days at about 20 °C and 75 % RH.

Table I.26 Three point bending test results for Series B-B100.1.

Figure I.39 Fracture area for beams in Series B-B100.1.

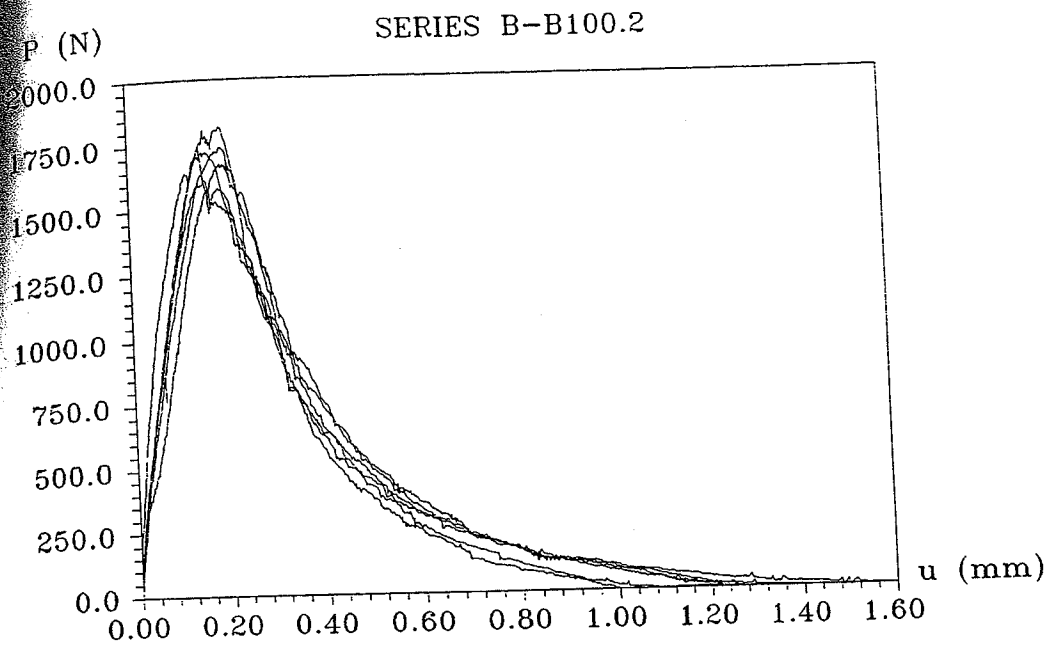

Figure I.40 Load-deflection curves for Series B-B100.2.

Beam no.	Cur.	f_c (MPa)	f_{sp} (MPa)	u_0 (mm)	P_{max} (N)	W_e (Nmm)	G_F (N/m)	f_f (MPa)
B-B1002-1	2*	90.6	4.93	1.29	1671.5	628.2	173.8	8.47
B-B1002-2				1.57	1738.2	624.4	183.4	8.79
B-B1002-3				1.36	1815.7	658.4	182.4	9.16
B-B1002-4				1.40	1611.7	607.8	173.6	8.18
B-B1002-5				1.22	1742.3	549.1	155.4	8.81
B-B1002-6				1.00	1719.2	609.6	159.2	8.70
Mean	-	-	-	1.31	1716.4	612.9	171.3	8.69

* 2. Specimens were cured in a heating chamber for 28 days at 40 °C and 34 % RH.

Table I.27 Three point bending test results for Series B-B100.2.

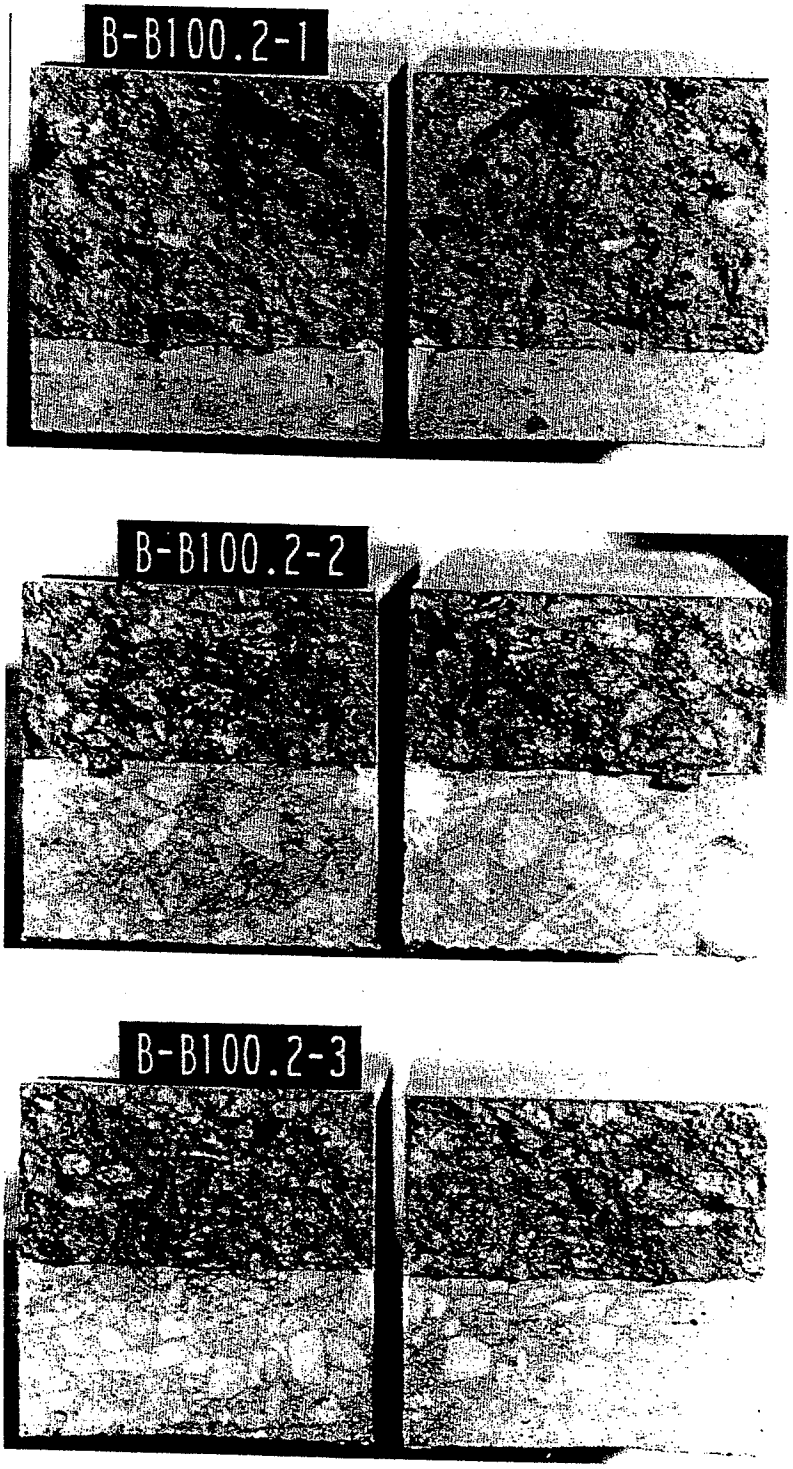

Figure I.41 Fracture area for beams in Series B-B100.2.

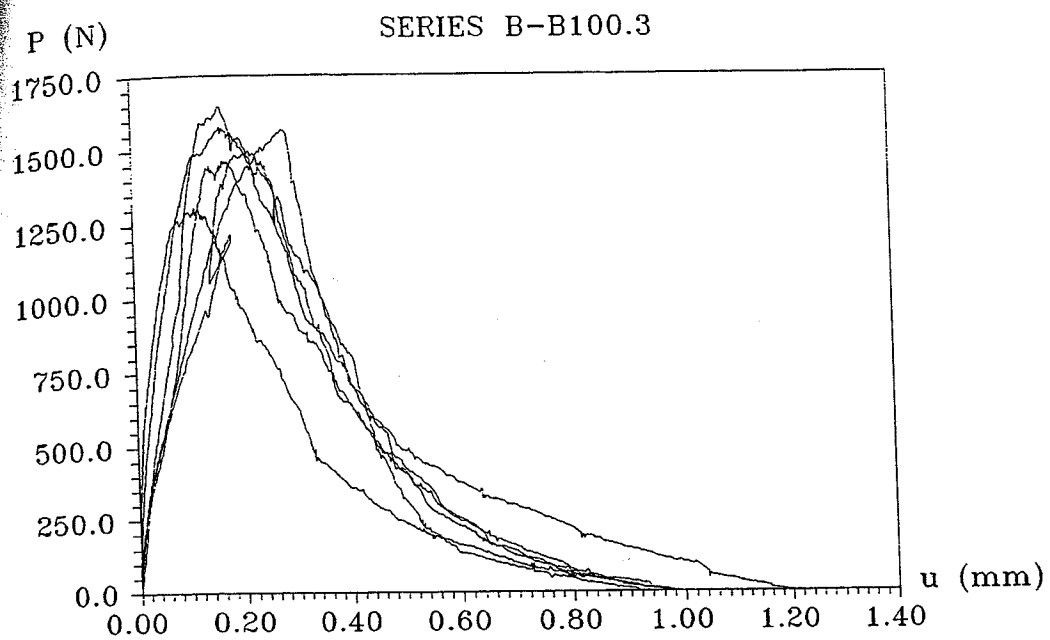

Figure I.42 Load-deflection curves for Series B-B100.3.

Beam no.	Cur.	f_c (MPa)	f_{sp} (MPa)	u_0 (mm)	P_{max} (N)	W_e (Nmm)	G_F (N/m)	f_f (MPa)
B-B1003-1	3*	106.9	6.47	0.99	1645.7	546.1	146.1	8.35
B-B1003-2				0.97	1462.1	502.8	136.9	7.47
B-B1003-3				0.99	1308.4	416.3	120.3	6.73
B-B1003-4				1.21	1579.0	664.1	177.9	8.03
B-B1003-5				0.94	1493.4	494.1	134.0	7.62
B-B1003-6				0.99	1565.5	548.2	146.6	7.96
Mean	-	-	-	1.02	1509.0	528.6	143.6	7.69

* 3. Specimens were cured in water for 14 days (20 °C) and in a heating chamber for 14 days at 40 °C and 34 % RH.

Table I.28 Three point bending test results for Series B-B100.3.

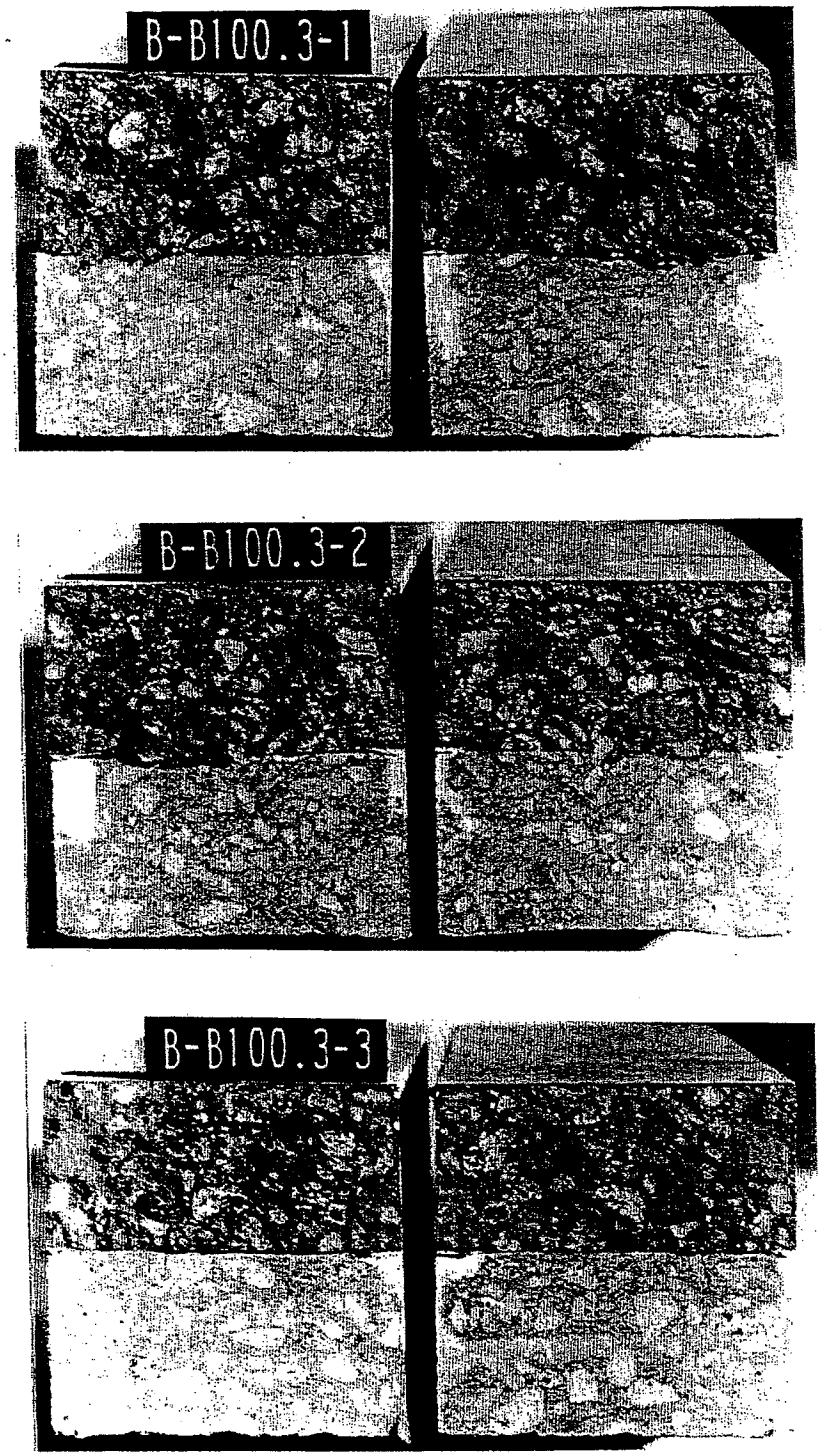

Figure I.43 Fracture area for beams in Series B-B100.3.

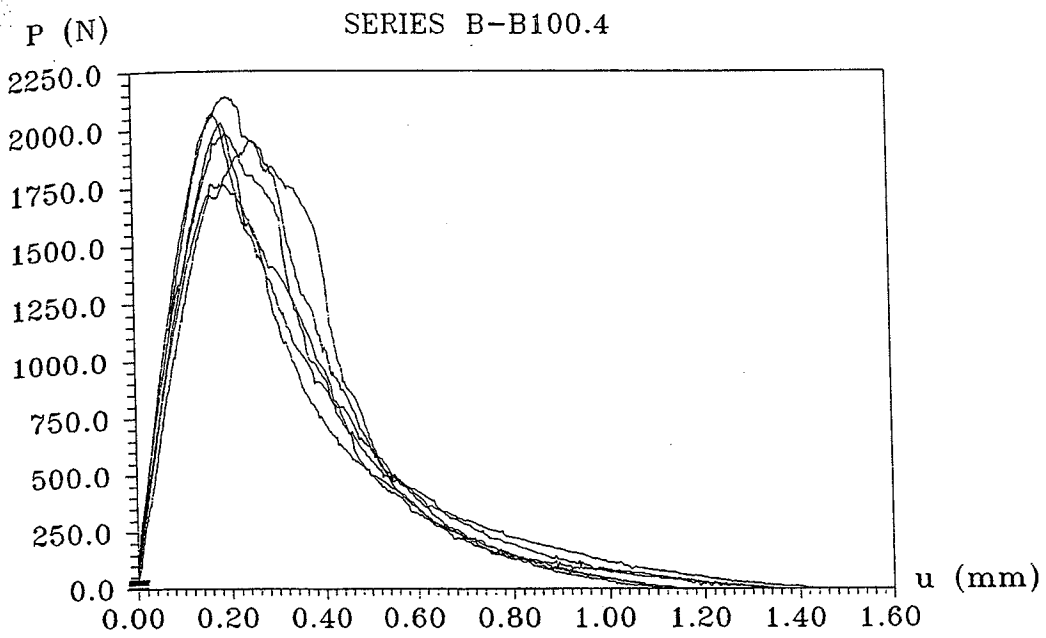

Figure I.44 Load-deflection curves for Series B-B100.4.

Beam no.	Cur.	f_c (MPa)	f_{sp} (MPa)	u_0 (mm)	P_{max} (N)	W_e (Nmm)	G_F (N/m)	f_f (MPa)
B-B1004-1	4*	104.7	5.86	1.44	2068.7	768.9	207.4	10.38
B-B1004-2				1.14	2023.8	669.1	176.3	10.16
B-B1004-3				1.11	2139.4	809.3	203.2	10.72
B-B1004-4				1.33	1949.0	796.4	209.0	9.80
B-B1004-5				1.34	1766.8	734.1	197.0	8.93
B-B1004-6				1.13	1984.4	734.8	189.1	9.97
Mean	-	-	-	1.25	1988.7	752.1	197.0	9.99

* 4. Specimens were cured in water for 28 days (20 °C) and in a heating chamber for 161 days at 40 °C and 34 % RH.

Table I.29 Three point bending test results for Series B-B100.4.

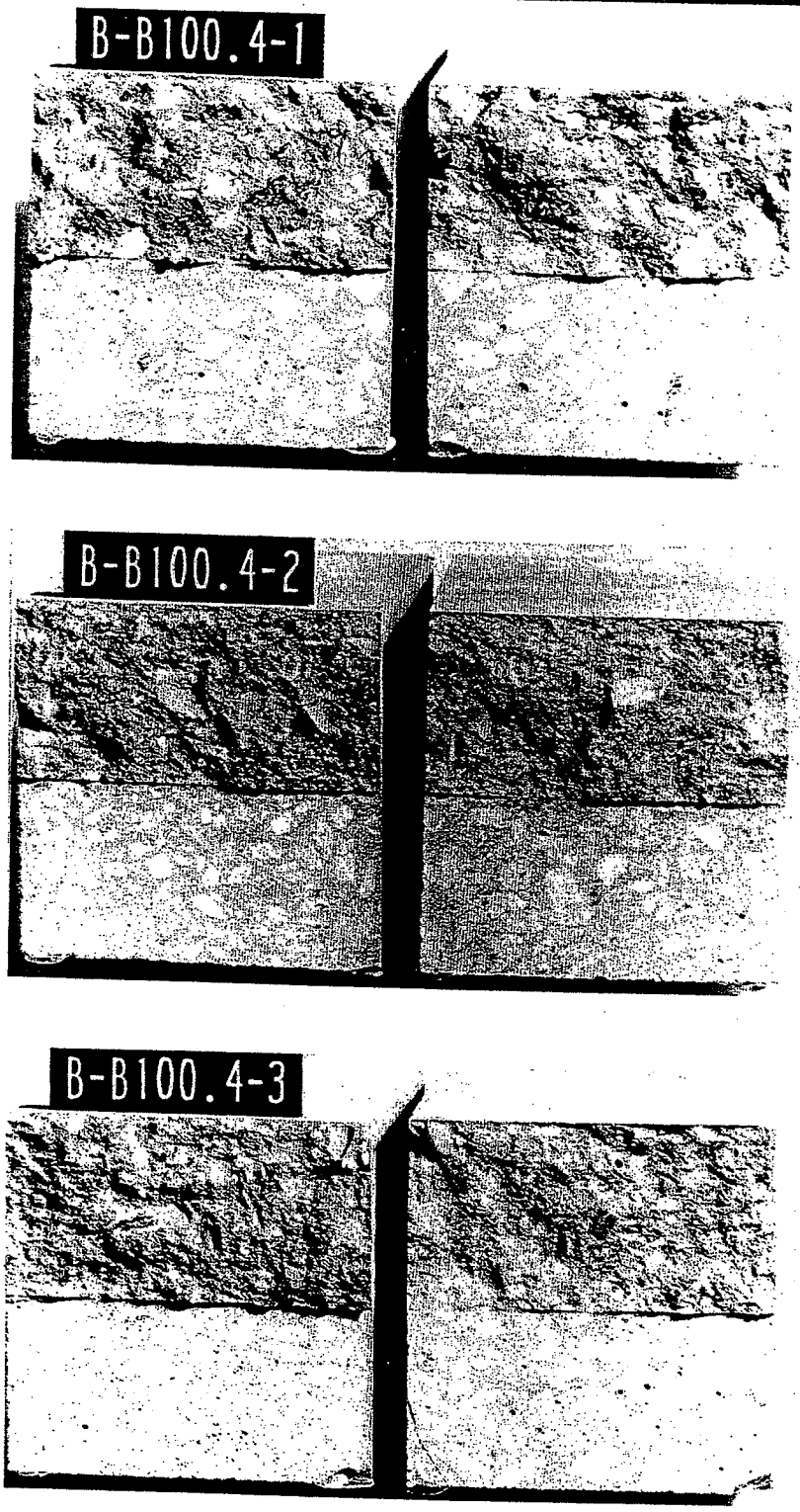

Figure I.45 Fracture area for beams in Series B-B100.4.

SERIES C

Intended Compressive Strength	30 MPa	100 MPa
Materials	kg/m^3	kg/m^3
Portland Rapid Cement	188	390
Fly Ash	80	-
Mikrosilica Fume-Slurry	-	80
Water	175	61
Plasticizer	-	2.0
Superplasticizer	-	15.4
Water-Cement Ratio	0.84	0.21

Table I.30 Mixing proportions for the concrete in series C1. (d_{max} = 0 mm)

Intended Compressive Strength	30 MPa	100 MPa
Materials	kg/m^3	kg/m^3
Portland Rapid Cement	354	390
Fly Ash	80	-
Mikrosilica Fume-Slurry	-	80
Sand 0 - 4 mm	2001	1757
Water	311	61
Plasticizer	-	2.4
Superplasticizer	-	60.0
Water-Cement ratio		

Table I.31 Mixing proportions for the concrete in series C2. (d_{max} = 4 mm)

Intended Compressive Strength	30 MPa	100 MPa
Materials	kg/m^3	kg/m^3
Portland Rapid Cement	206	390
Fly Ash	80	-
Mikrosilica Fume-Slurry	-	80
Sand 0 - 4 mm	640	521
Natural Gravel 4 - 8 mm	1361	1236
Water	190	61
Plasticizer	-	2.4
Superplasticizer	-	18.04
Water-Cement ratio		

Table I.32 Mixing proportions for Series C3. (Natural gravel d_{max} = 8 mm)

	d_{max} (mm)	Compressive Tests f_c (MPa)		Splitting Tests f_{sp} (MPa)		Modulus of Elasticity E_c (MPa)	
Batch No		Mean Value	Standard Deviation	Mean Value	Standard Deviation	Mean Value	Standard Deviation
C-B30.1	0	26.9	1.3	-	-	10450	214
C-B30.2	4	24.4	0.7	2.27	0.28	22120	870
C-B30.3	8	23.3	0.4	2.51	0.21	27460	390
C-B100.1	0	98.9	6.8	4.79	0.54	26370	53
C-B100.2	4	72.5	3.0	4.78	0.29	37230	325
C-B100.3	8	94.8	4.9	5.55	0.16	41470	586

Table I.33 Cylinder data for the concrete in Series C.

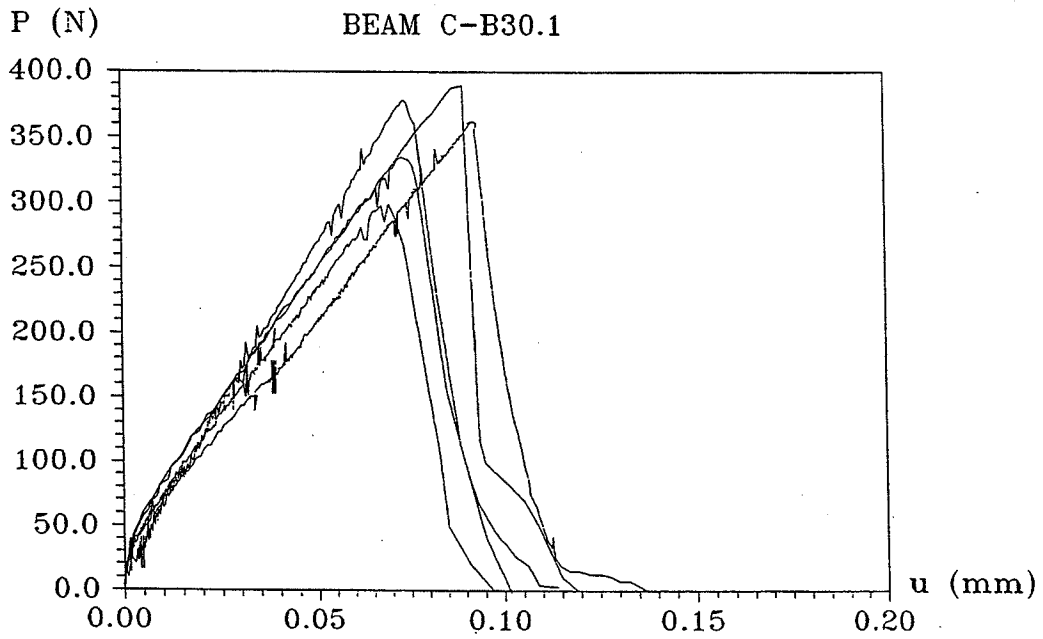

Figure I.46 Load-deflection curves for Series C-B30.1.

Beam no.	d_{max} (mm)	f_c (MPa)	f_{sp} (MPa)	u_0 (mm)	P_{max} (N)	W_e (Nmm)	G_F (N/m)	f_f (MPa)
C-B301-1	0	26.9	-	0.10	389.0	18.3	6.7	2.22
C-B301-2				0.09	334.6	15.8	5.8	1.96
C-B301-3				0.15	390.3	22.7	8.8	2.23
C-B301-4				0.09	378.1	21.2	7.0	2.17
C-B301-5				0.08	299.2	14.8	5.4	1.79
C-B301-6				-	-	-	-	
Mean	-	-	-	0.10	358.2	18.6	6.7	2.07

Table I.34 Three point bending test results for Series C-B30.1.

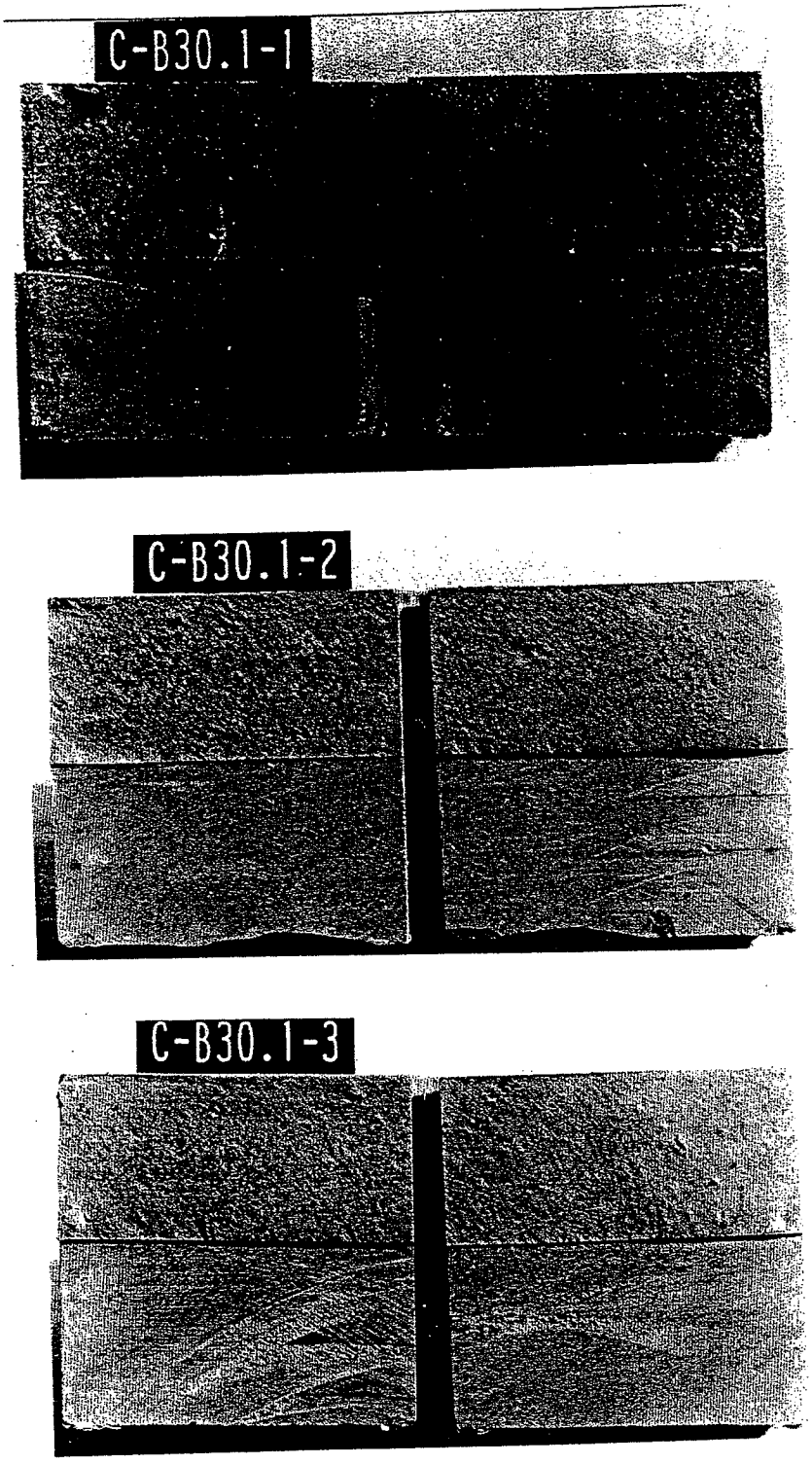

Figure I.47 Fracture area for beams in Series C-B30.1.

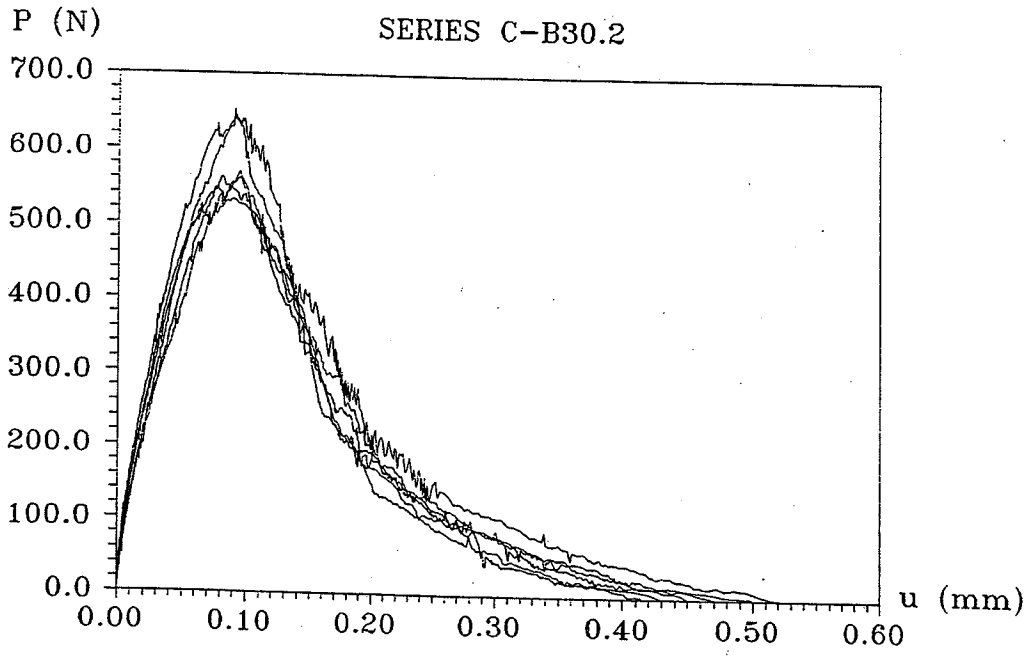

Figure I.48 Load-deflection curves for Series C-B30.2.

Beam no.	d_{max} (mm)	f_c (MPa)	f_{sp} (MPa)	u_0 (mm)	P_{max} (N)	W_e (Nmm)	G_F (N/m)	f_f (MPa)
C-B302-1	4	24.4	2.27	0.46	651.5	87.3	32.1	3.55
C-B302-2				0.47	568.5	89.5	34.6	3.15
C-B302-3				0.50	561.7	92.7	36.2	3.12
C-B302-4				0.52	646.0	109.4	40.3	3.52
C-B302-5				0.45	546.8	89.9	33.9	3.05
C-B302-6				0.43	531.8	86.2	32.4	2.98
Mean	-	-	-	0.47	584.4	92.5	34.9	3.23

Table I.35 Three point bending test results for Series C-B30.2.

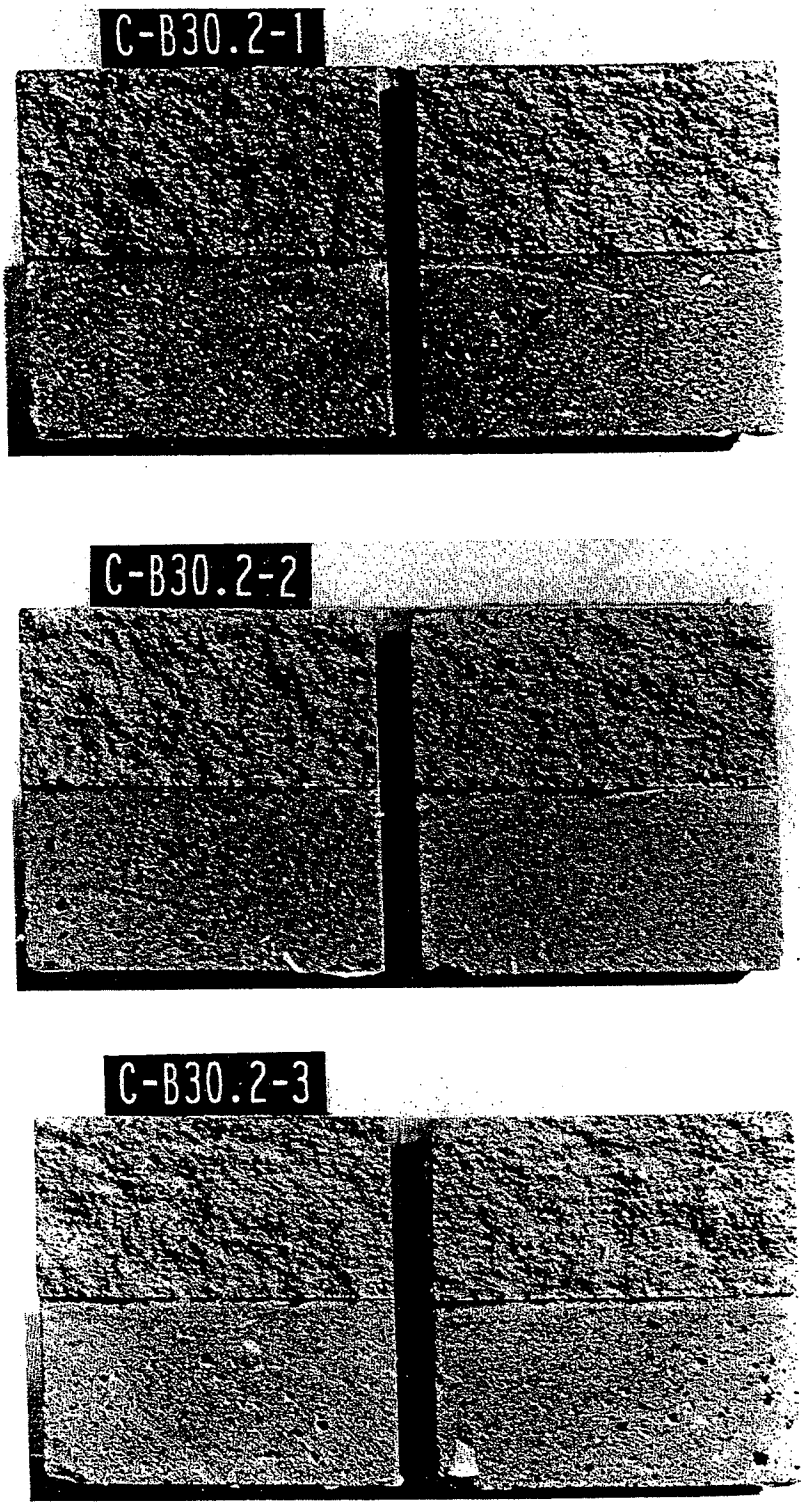

Figure I.49 Fracture area for beams in Series C-B30.2.

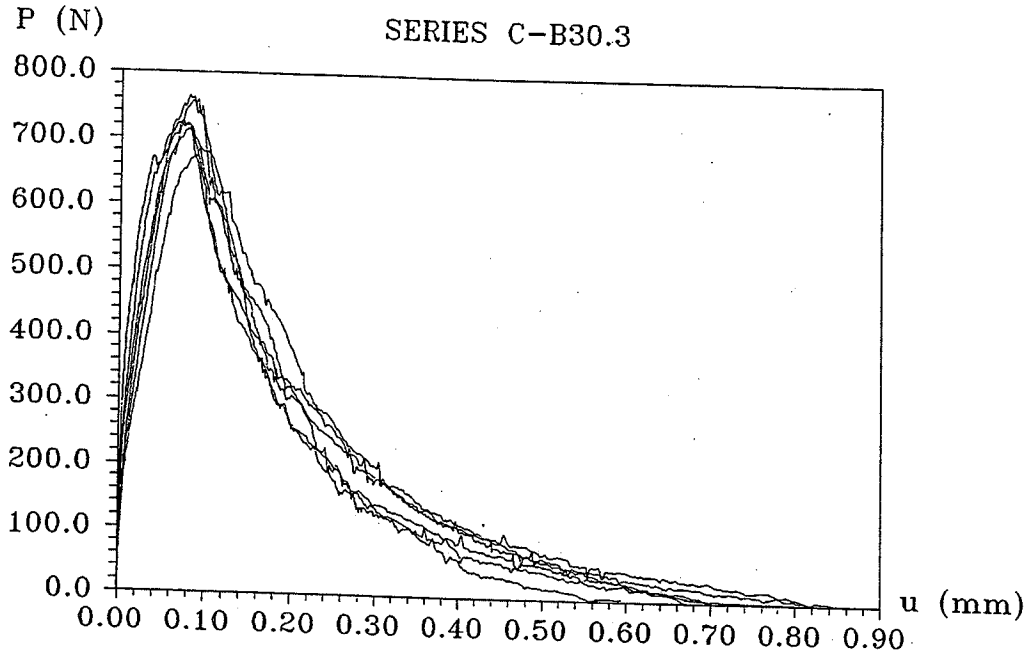

Figure I.50 Load-deflection curves for Series C-B30.3.

Beam no.	d_{max} (mm)	f_c (MPa)	f_{sp} (MPa)	u_0 (mm)	P_{max} (N)	W_e (Nmm)	G_F (N/m)	f_f (MPa)
C-B303-1	8	23.3	2.51	0.70	712.7	138.7	54.0	3.87
C-B303-2				0.83	684.1	162.7	63.4	3.73
C-B303-3				0.85	757.6	157.1	63.2	4.08
C-B303-4				0.59	722.2	140.5	50.3	3.91
C-B303-5				0.67	724.9	154.4	55.8	3.93
C-B303-6				0.80	764.4	138.8	57.6	4.12
Mean				0.74	727.7	148.7	57.4	3.94

Table I.36 Three point bending test results for Series C-B30.3.

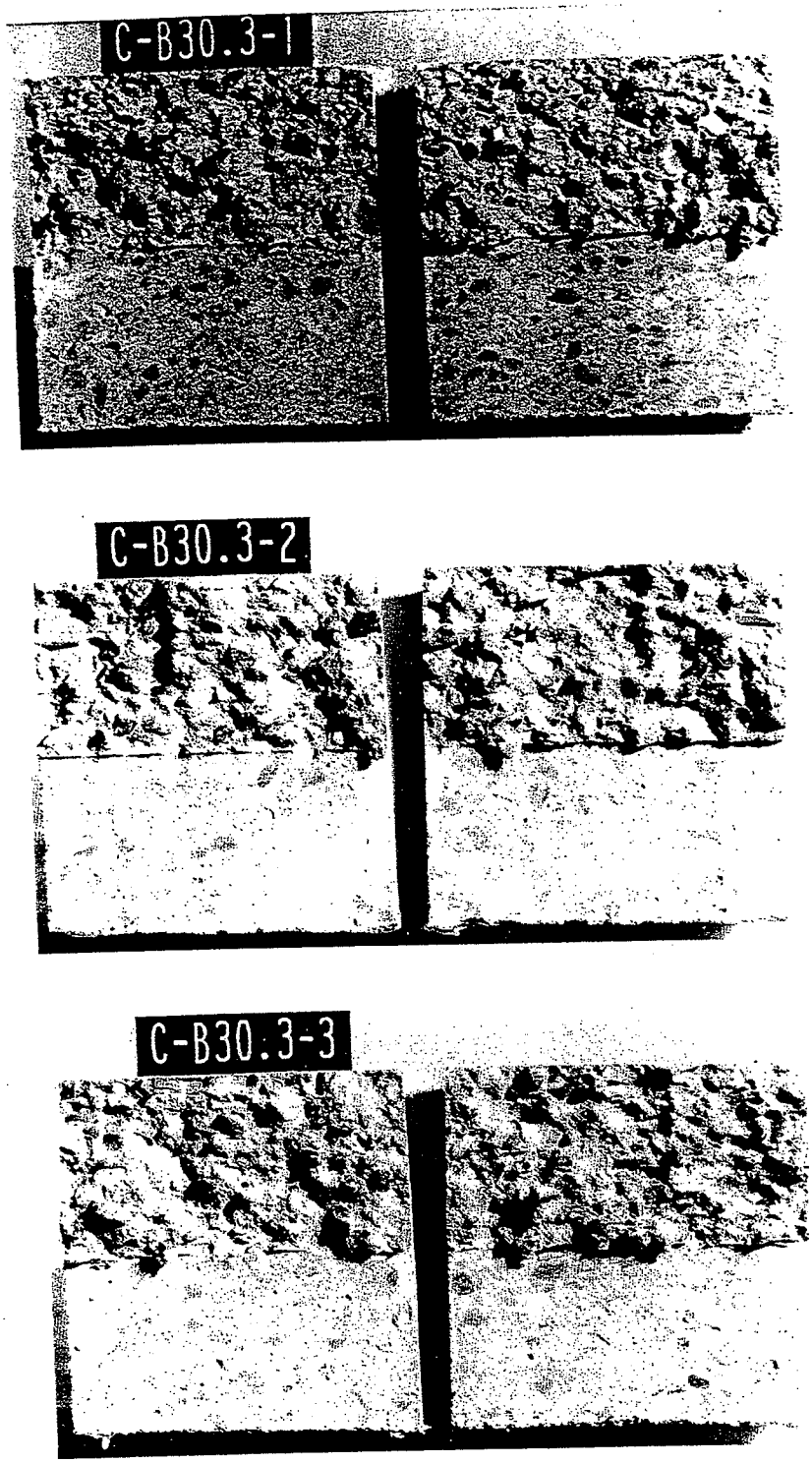

Figure I.51 Fracture area for beams in Series C-B30.3.

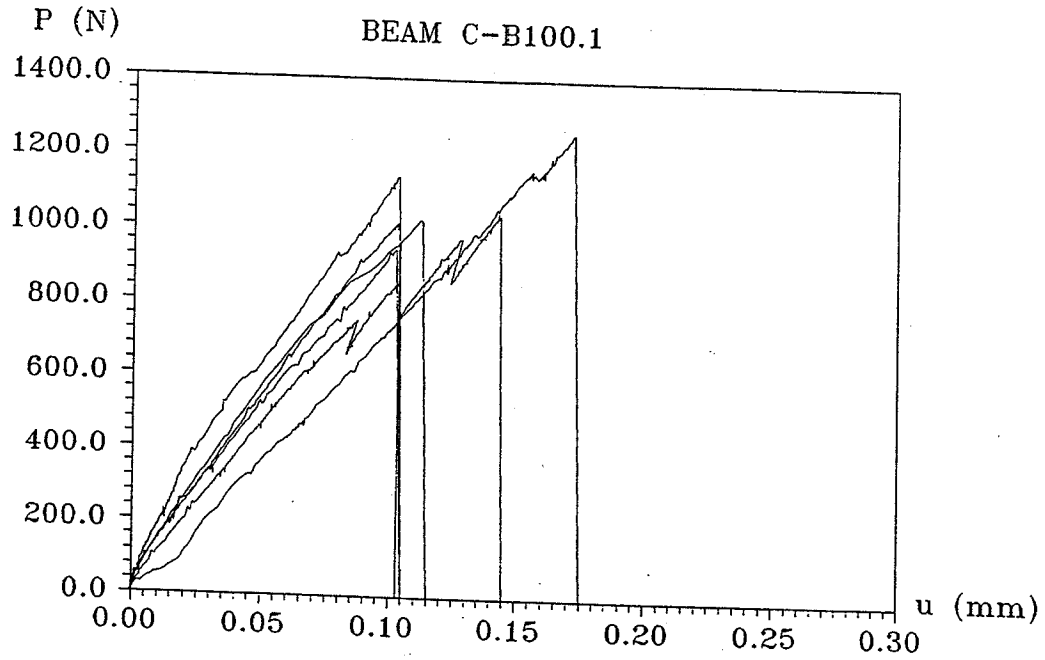

Figure I.52 Load-deflection curves for Series C-B100.1.

Beam no.	d_{max} (mm)	f_c (MPa)	f_{sp} (MPa)	u_0 (mm)	P_{max} (N)	W_e (Nmm)	G_F (N/m)	f_f (MPa)
C-B1001-1	0	98.9	4.79	0.13	1037.7	76.8	20.1	5.40
C-B1001-2				0.10	1017.3	56.5	15.0	5.31
C-B1001-3				0.19	1135.7	103.5	27.3	5.88
C-B1001-4				0.11	1018.7	65.9	17.1	5.31
C-B1001-5				0.17	1259.4	107.1	27.5	6.47
C-B1001-6				0.10	943.9	52.5	14.1	4.95
Mean	-	-	-	0.13	1068.8	77.1	20.2	5.55

Table I.37 Three point bending test results for Series C-B100.1.

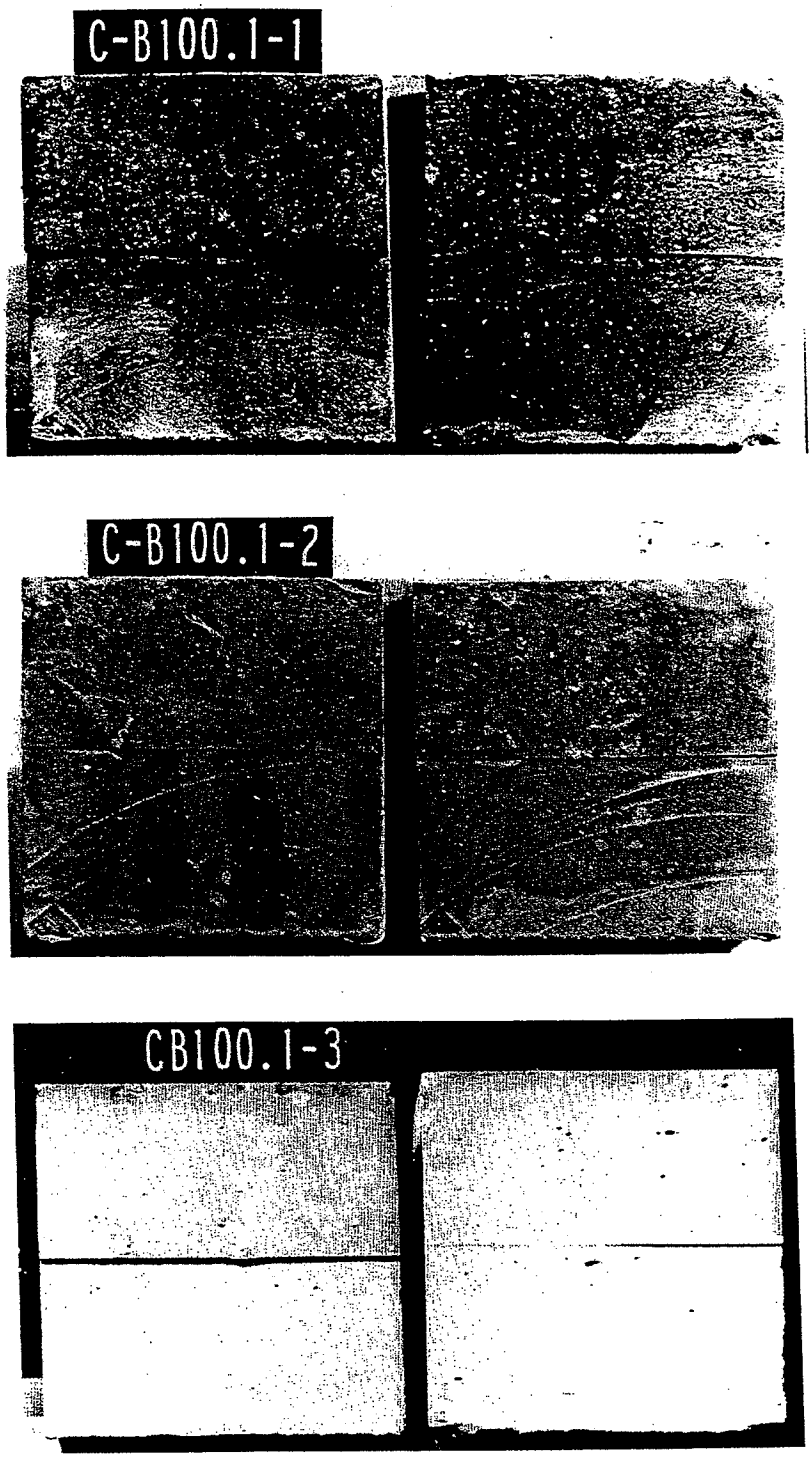

Figure I.53 Fracture area for beams in Series C-B100.1.

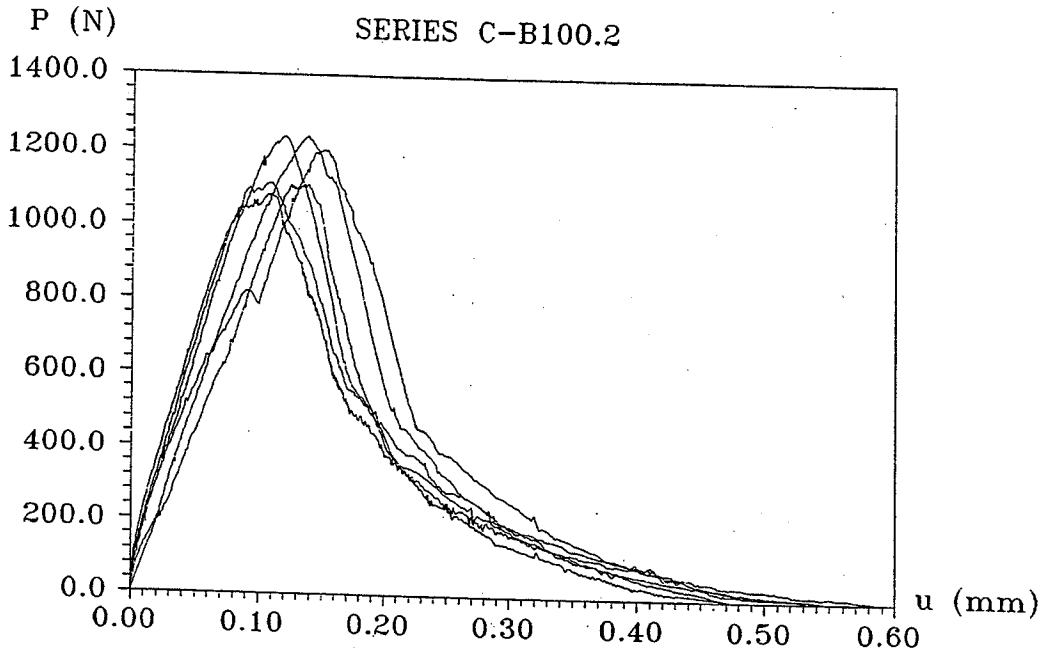

Figure I.54 Load-deflection curves for Series C-B100.2.

Beam no.	d_{max} (mm)	f_c (MPa)	f_{sp} (MPa)	u_0 (mm)	P_{max} (N)	W_e (Nmm)	G_F (N/m)	f_f (MPa)
C-B1002-1	4	72.5	4.78	0.59	1079.1	184.6	58.8	5.63
C-B1002-2				0.51	1199.6	216.6	62.3	6.21
C-B1002-3				0.55	1236.3	199.9	60.3	6.38
C-B1002-4				0.47	1237.7	201.3	57.8	6.39
C-B1002-5				0.47	1107.1	164.1	50.5	5.76
C-B1002-6				0.53	1111.2	186.5	57.1	5.78
Mean	-	-	-	0.52	1161.8	192.2	57.8	6.03

Table I.38 Three point bending test results for Series C-B100.2.

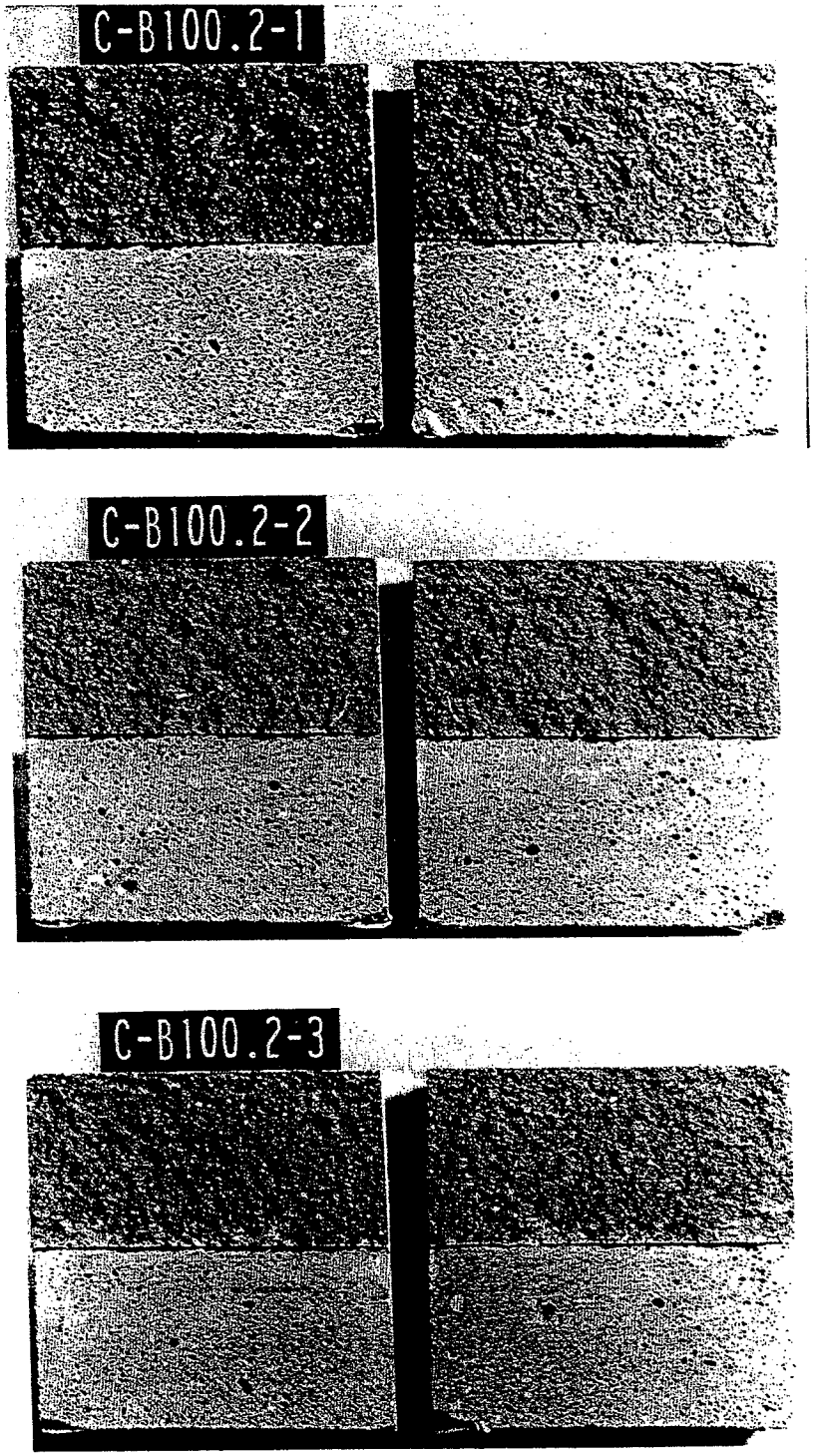

Figure I.55 Fracture area for beams in Series C-B100.2.

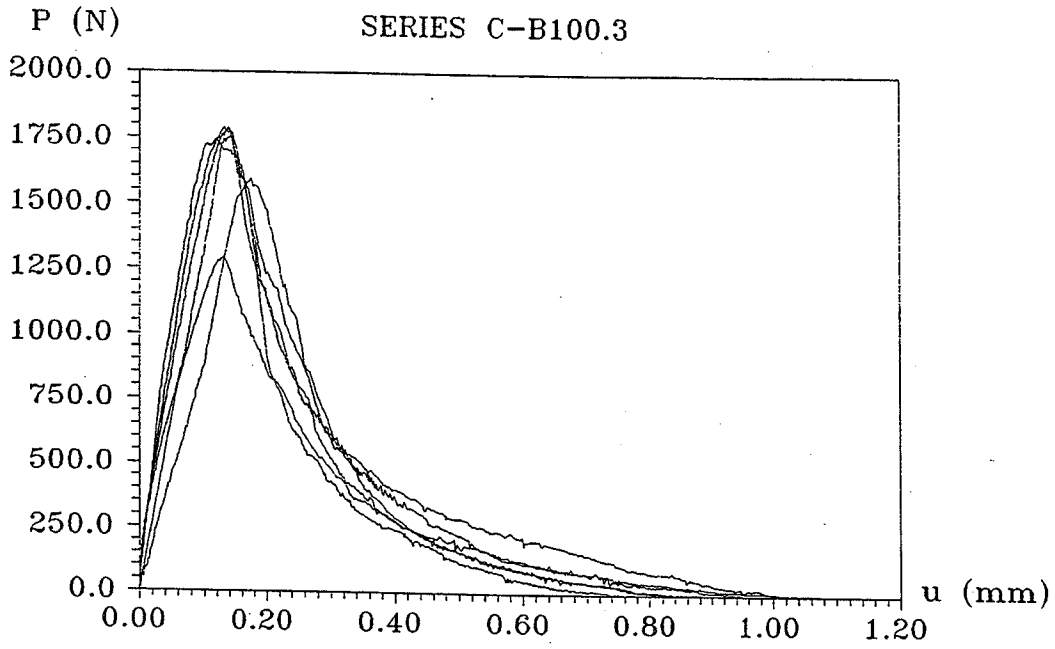

Figure I.56 Load-deflection curves for Series C-B100.3.

Beam no.	d_{max} (mm)	f_c (MPa)	f_{sp} (MPa)	u_0 (mm)	P_{max} (N)	W_e (Nmm)	G_F (N/m)	f_f (MPa)
C-B1003-1	8	94.8	5.55	0.95	1289.4	337.4	102.9	6.64
C-B1003-2				0.81	1592.7	367.9	103.8	8.09
C-B1003-3				0.93	1743.6	463.3	127.3	8.82
C-B1003-4				1.09	1787.2	438.5	128.4	9.03
C-B1003-5				0.75	1784.4	360.9	90.2	9.01
C-B1003-6				1.16	1753.2	525.9	148.3	8.86
Mean	-	-	-	0.95	1658.4	415.7	118.5	8.41

Table I.39 Three point bending test results for Series C-B100.3.

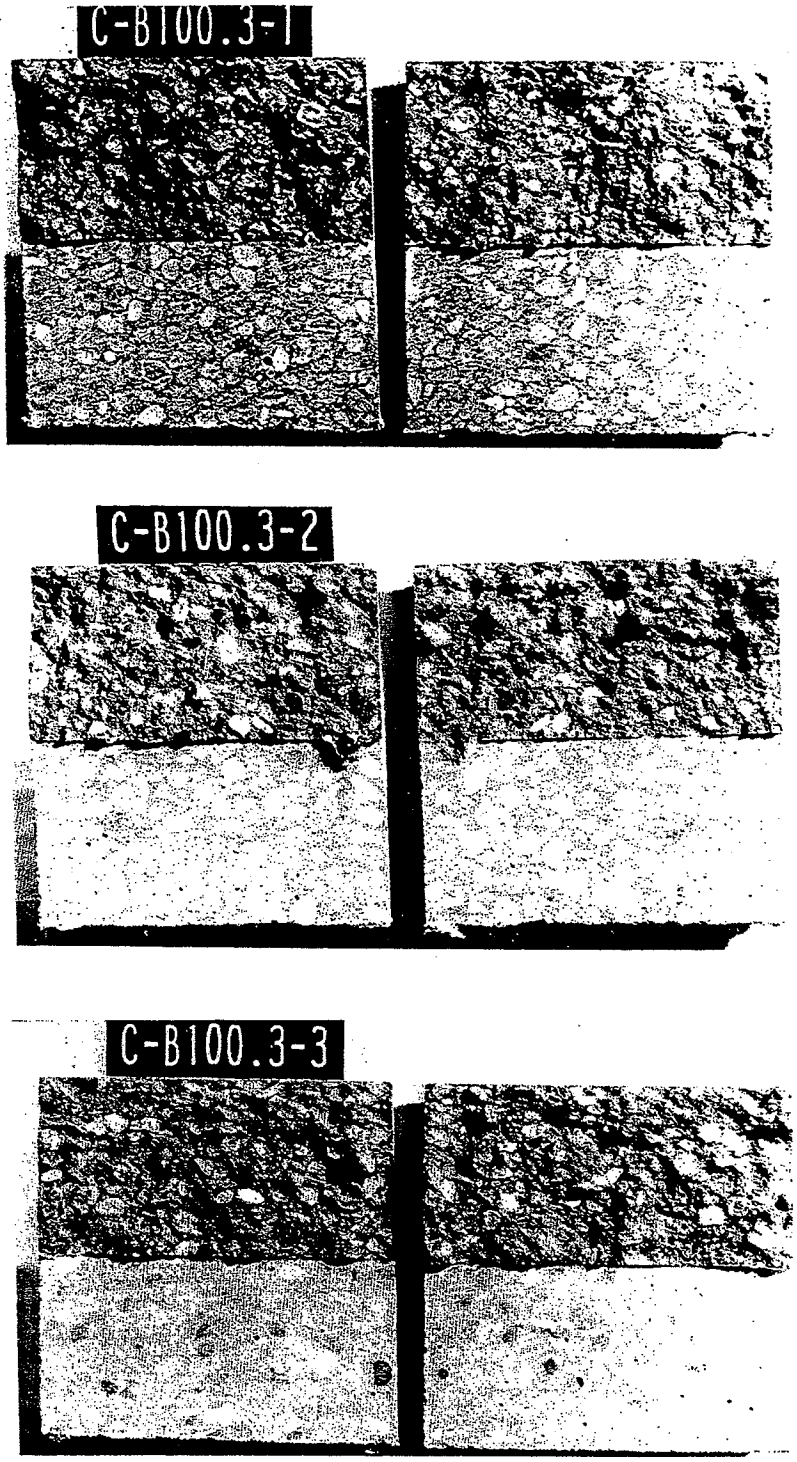

Figure I.57 Fracture area for beams in Series C-B100.3.

SERIES D

Intended Compressive Strength	30 MPa	100 MPa	30 MPa	100 MPa
Intended Air Content	5 %		10 %	
Materials	kg/m^3	kg/m^3	kg/m^3	kg/m^3
Portland Rapid Cement	197	415	265	420
Fly Ash	80	-	40	-
Mikrosilica Fume-Slurry	-	80	36	80
Sand 0 - 4 mm	540	474	508	474
Gravel 4 - 8 mm	297	259	280	259
Gravel 4 - 16 mm	1164	1024	1095	1024
Water	165	61	162	61
Plasticizer	-	2.40	1.33	2.40
Superplasticizer	-	18.04	-	18.04
Air-Entraining Agent	0.393	0.643	0.643	0.993
Water-Cement Ratio				

Table I.40 Mixing proportions for the concrete in Series D.

	Air %	Compressive Tests f_c (MPa)		Splitting Tests f_{sp} (MPa)		Modulus of Elasticity E_c (MPa)	
Batch No		Mean Value	Standard Deviation	Mean Value	Standard Deviation	Mean Value	Standard Deviation
D-B30.1	5.9	27.6	2.1	2.57	0.14	24100	866
D-B30.2	10.0	18.2	0.7	1.86	0.15	14690	93
D-B100.1	3.8	99.3	5.3	6.09	0.12	37870	1407
D-B100.2	9.0	86.6	1.1	5.48	0.10	35390	913

Table I.41 Cylinder data for the concrete in Series D.

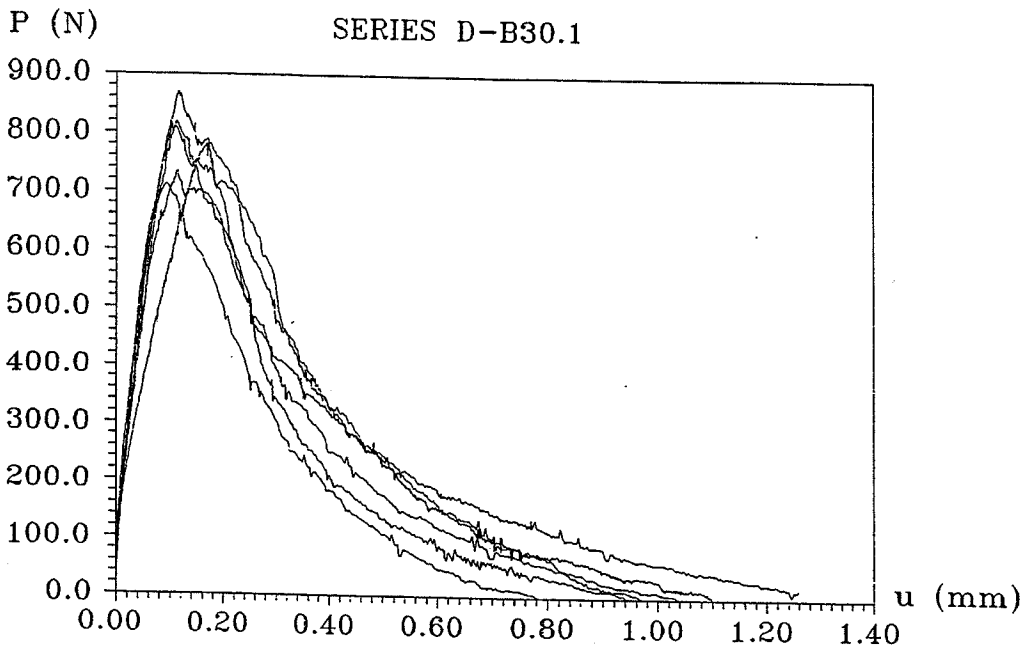

Figure I.58 Load-deflection curves for Series D-B30.1.

Beam no.	Air (%)	f_c (MPa)	f_{sp} (MPa)	u_0 (mm)	P_{max} (N)	W_e (Nmm)	G_F (N/m)	f_f (MPa)
D-B301-1	5.9	27.6	2.57	1.25	733.1	306.8	108.3	3.97
D-B301-2				0.95	783.4	224.6	80.2	4.21
D-B301-3				1.10	870.5	312.5	103.5	4.63
D-B301-4				0.97	809.3	300.7	96.3	4.33
D-B301-5				0.78	711.3	198.3	68.8	3.86
D-B301-6				1.04	818.8	205.6	91.9	4.38
Mean	-	-	-	1.02	787.7	258.1	91.5	4.23

Table I.42 Three point bending test results for Series D-B30.1.

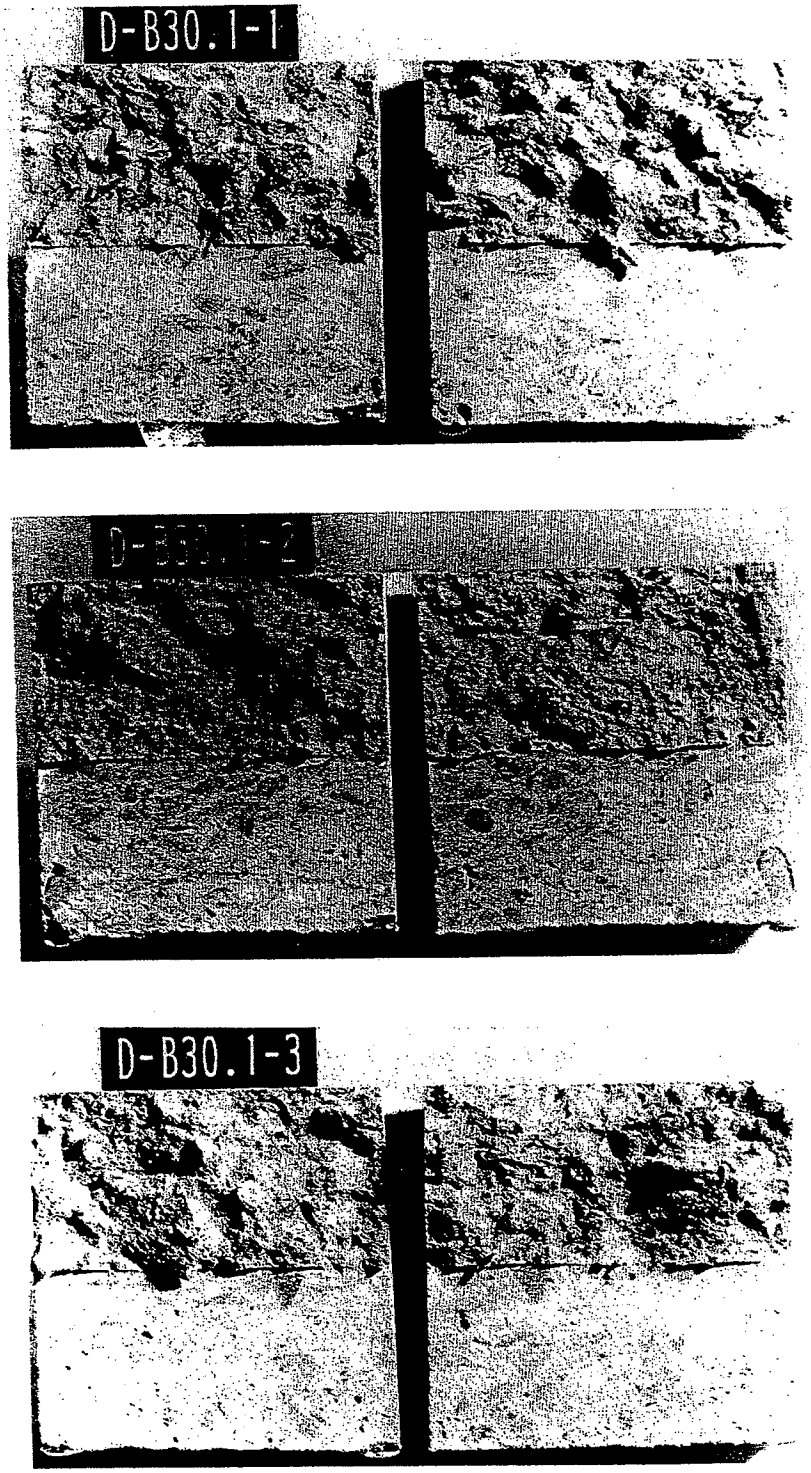

Figure I.59 Fracture area for beams in Series D-B30.1.

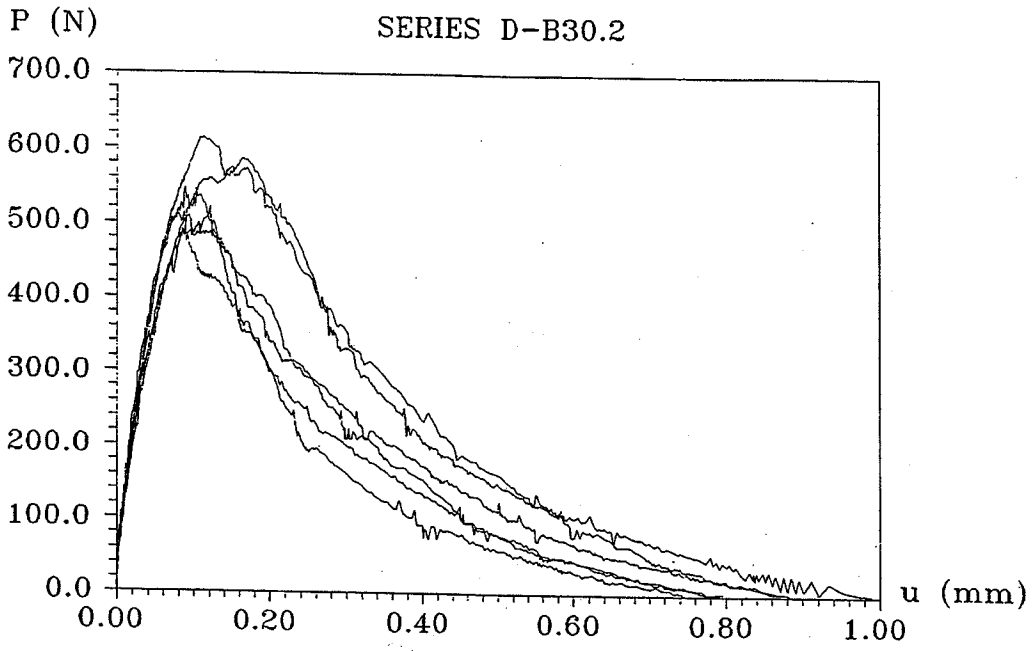

Figure I.60 Load-deflection curves for Series D-B30.2.

Beam no.	Air (%)	f_c (MPa)	f_{sp} (MPa)	u_0 (mm)	P_{max} (N)	W_e (Nmm)	G_F (N/m)	f_f (MPa)
D-B302-1	10.0	18.2	1.86	0.88	546.8	162.7	65.5	3.07
D-B302-2				0.74	520.9	123.2	52.4	2.95
D-B302-3				0.79	488.3	146.0	58.7	2.79
D-B302-4				0.88	584.8	201.5	73.2	3.25
D-B302-5				0.80	512.8	135.8	56.9	2.91
D-B302-6				0.99	614.8	216.9	80.3	3.40
Mean	-	-	-	0.85	544.7	164.4	64.5	3.06

Table I.43 Three point bending test results for Series D-B30.2.

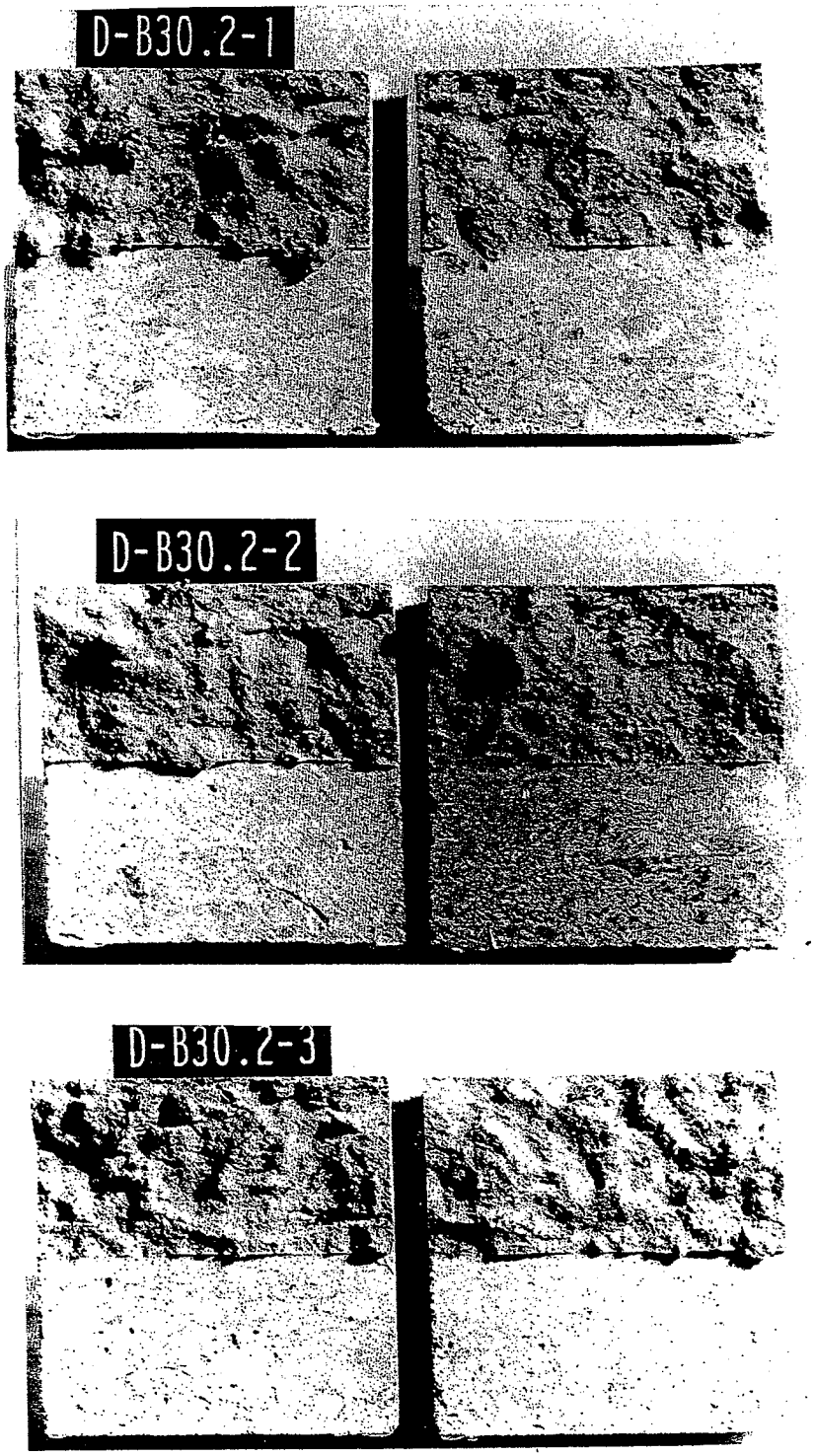

Figure I.61 Fracture area for beams in Series D-B30.2.

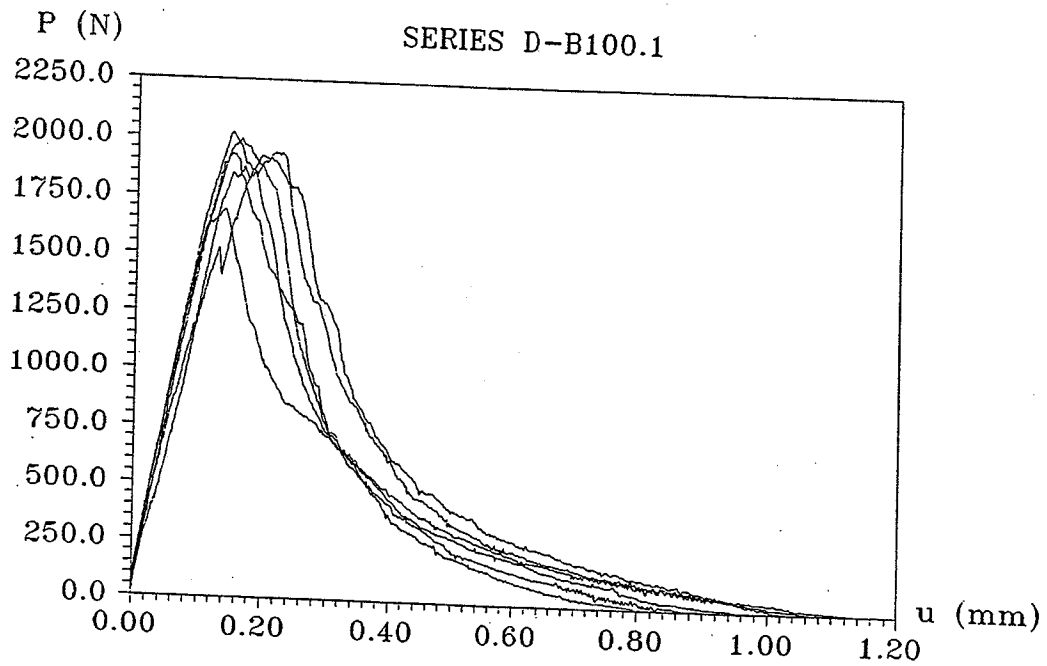

Figure I.62 Load-deflection curves for Series D-B100.1.

Beam no.	Air (%)	f_c (MPa)	f_{sp} (MPa)	u_0 (mm)	P_{max} (N)	W_e (Nmm)	G_F (N/m)	f_f (MPa)
D-B1001-1	3.8	99.3	6.09	1.02	1687.9	478.0	133.7	8.55
D-B1001-2				0.89	1993.9	516.7	136.7	10.02
D-B1001-3				0.95	2022.5	523.1	140.1	10.16
D-B1001-4				1.14	1936.8	599.2	162.3	9.74
D-B1001-5				1.07	1912.3	629.4	165.7	9.63
D-B1001-6				0.79	1931.3	478.3	125.3	9.72
Mean	-	-	-	0.98	1914.1	537.5	144.0	9.64

Table I.44 Three point bending test results for Series D-B100.1.

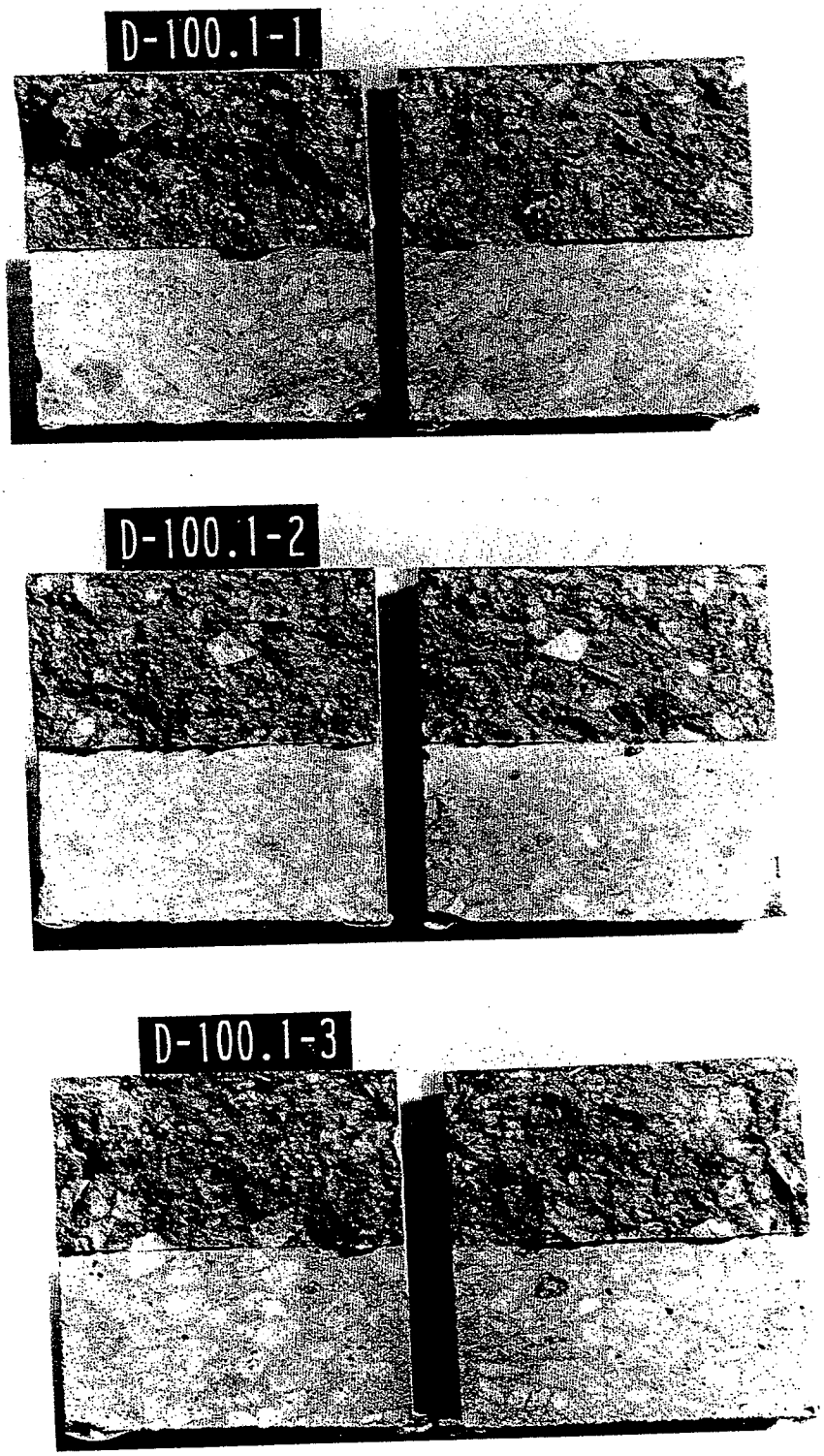

Figure I.63 Fracture area for beams in Series D-B100.1.

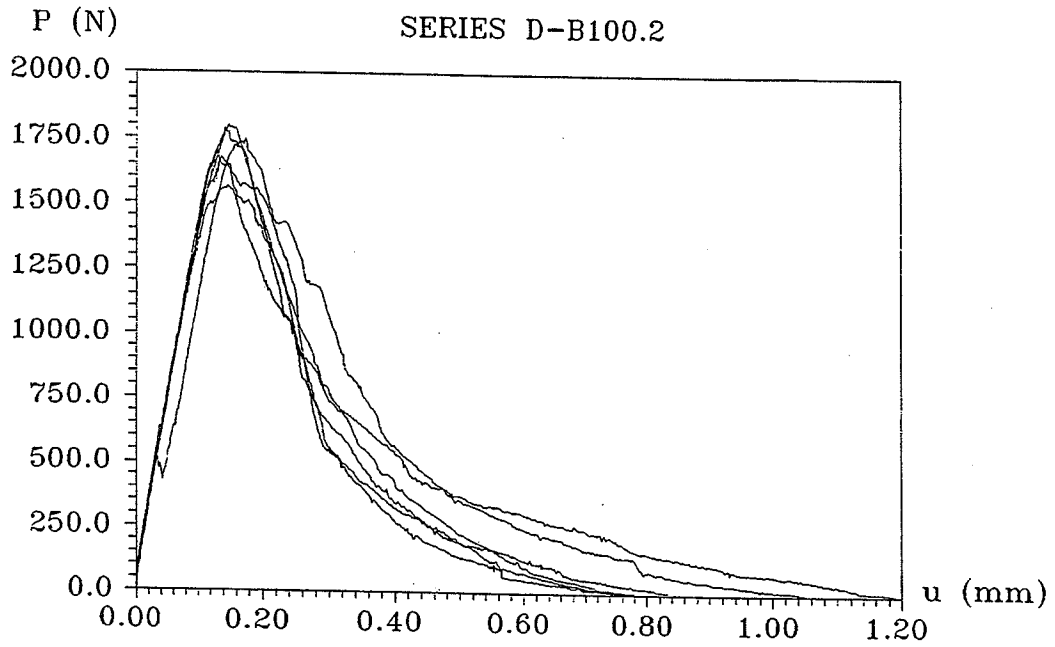

Figure I.64 Load-deflection curves for Series D-B100.2.

Beam no.	Air (%)	f_c (MPa)	f_{sp} (MPa)	u_0 (mm)	P_{max} (N)	W_e (Nmm)	G_F (N/m)	f_f (MPa)
D-B1002-1	9.0	86.6	5.48	0.77	1565.5	385.2	105.9	7.96
D-B1002-2				1.19	1674.3	544.6	153.5	8.48
D-B1002-3				1.05	1776.3	568.6	152.9	8.97
D-B1002-4				0.83	1693.3	438.7	118.8	8.58
D-B1002-5				0.78	1720.5	404.3	109.9	8.71
D-B1002-6				0.77	1795.3	458.2	120.4	9.06
Mean	-	-	-	0.90	1704.2	466.6	126.9	8.63

Table I.45 Three point bending test results for Series D-B100.2.

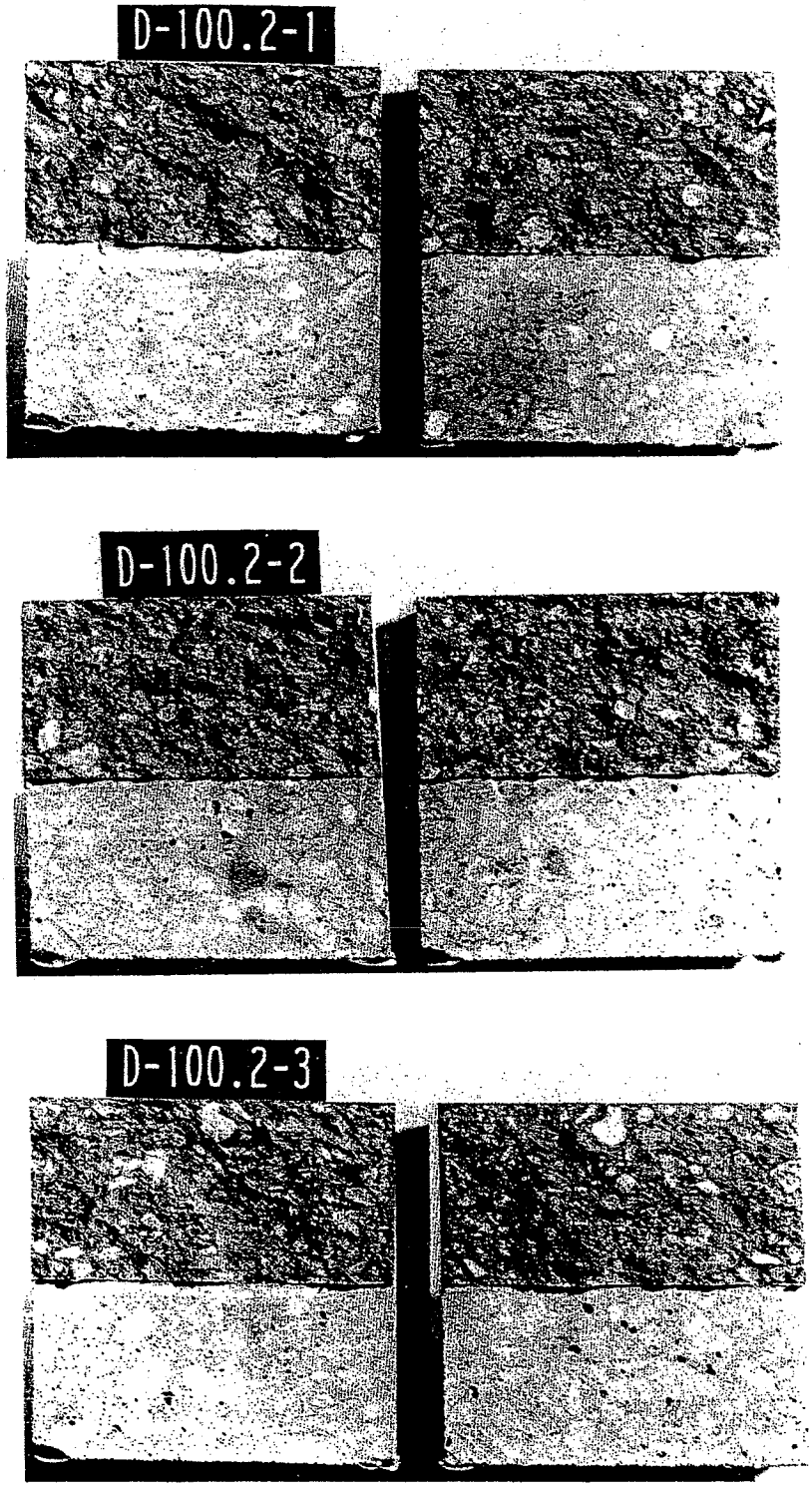

Figure I.65 Fracture area for beams in Series D-B100.2.

SERIES E

Intended Compressive Strength	30 MPa	100 MPa
Materials	kg/m^3	kg/m^3
Portland Rapid Cement	188	390
Fly Ash	80	-
Mikrosilica Fume-Slurry	-	80
Sand 0 - 4 mm	640	521
Natural Gravel 4 - 8 mm	272	247
Crushed Gravel 4 - 16 mm	1089	989
Water	175	61
Plasticizer	-	2.40
Superplasticizer	-	18.04
Water-Cement Ratio	0.84	0.21

Table I.46 Mixing proportions for the concrete in Series E.

	Compressive Tests f_c (MPa)		Splitting Tests f_{sp} (MPa)	
Batch No	Mean Value	Standard Deviation	Mean Value	Standard Deviation
E-B30.1	30.2	1.9	2.82	0.41
E-B30.2	34.0	2.7	2.98	0.21
E-B30.3	31.2	2.3	2.73	0.21
E-B100.1	94.8	2.3	5.83	0.17
E-B100.2	101.7	7.1	6.08	0.14
E-B100.3	102.1	4.0	6.03	0.28

Table I.47 Cylinder data for the concrete in Series E.

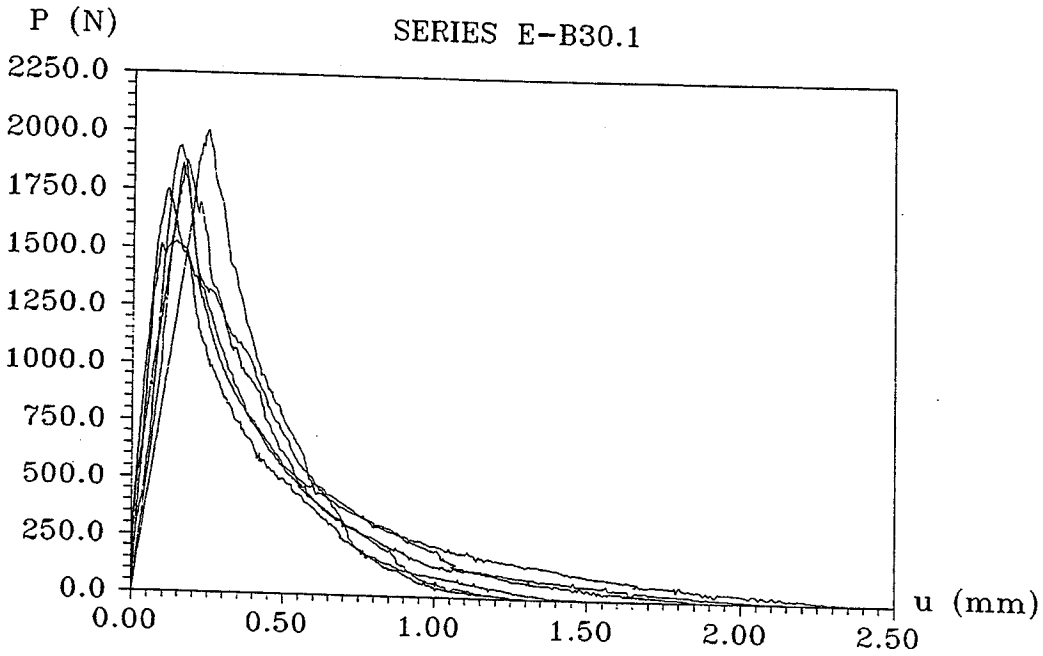

Figure I.66 Load-deflection curves for Series E-B30.1.

Beam no.	L (mm)	f_c (MPa)	f_{sp} (MPa)	u_0 (mm)	P_{max} (N)	W_e (Nmm)	G_F (N/m)	f_f (MPa)
E-B301-1	550	30.2	2.82	2.14	1874.2	780.9	210.9	6.40
E-B301-2				1.53	1512.4	606.2	160.6	5.20
E-B301-3				1.29	2006.1	727.7	178.7	6.83
E-B301-4				2.35	1747.7	822.7	224.8	5.98
E-B301-5				1.86	1934.0	807.4	209.3	6.59
E-B301-6				1.25	1860.6	634.9	159.9	6.35
Mean	-	-	-	1.74	1822.5	730.0	190.7	6.23

Table I.48 Three point bending test results for Series E-B30.1.

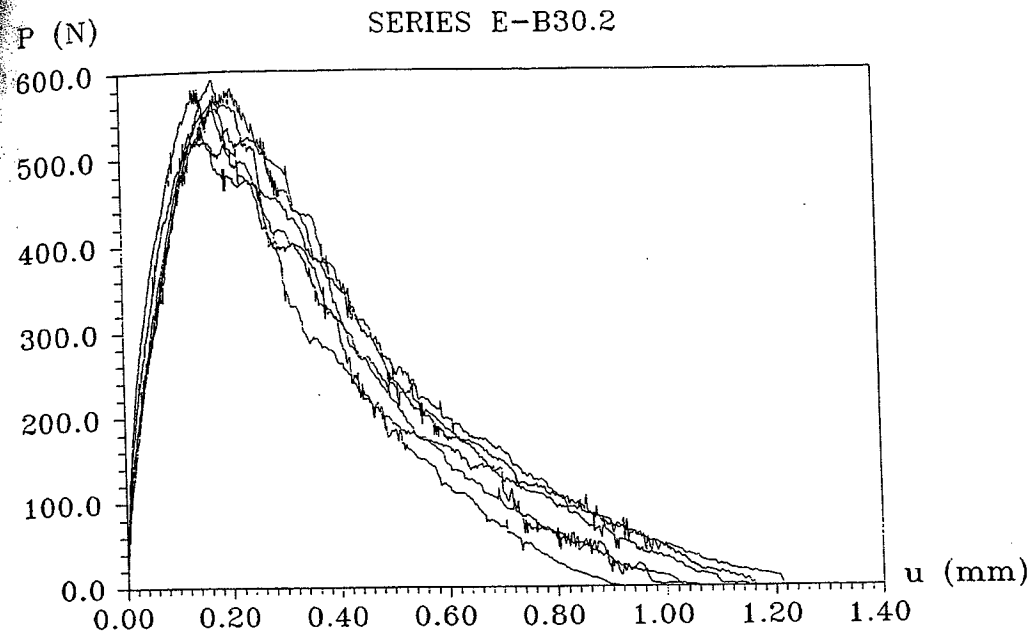

Figure I.67 Load-deflection curves for Series E-B30.2.

Beam no.	L (mm)	f_c (MPa)	f_{sp} (MPa)	u_0 (mm)	P_{max} (N)	W_e (Nmm)	G_F (N/m)	f_f (MPa)
E-B302-1	1200	34.0	2.98	1.06	580.8	254.1	110.2	5.19
E-B302-2				1.02	590.3	241.5	105.6	5.26
E-B302-3				1.21	537.2	238.2	115.5	4.87
E-B302-4				1.16	519.6	264.7	117.9	4.75
E-B302-5				0.94	565.8	217.0	95.8	5.08
E-B302-6				1.15	561.7	273.1	118.9	5.05
Mean	-	-	-	1.09	559.2	248.1	110.7	5.03

Table I.49 Three point bending test results for Series E-B30.2.

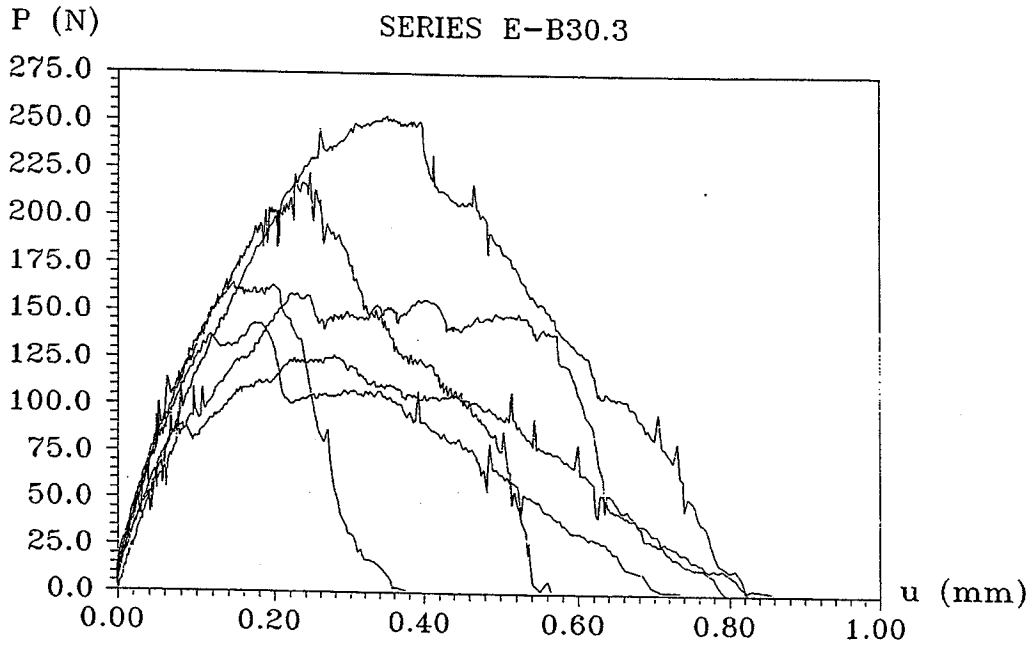

Figure I.68 Load-deflection curves for Series E-B30.3.

Beam no.	L (mm)	f_c (MPa)	f_{sp} (MPa)	u_0 (mm)	P_{max} (N)	W_e (Nmm)	G_F (N/m)	f_f (MPa)
E-B303-1	2000	31.2	2.73	0.86	251.6	1216	104.1	5.82
E-B303-2				0.56	223.1	713	66.8	5.47
E-B303-3				0.37	164.6	349	41.9	4.77
E-B303-4				0.73	142.8	563	79.7	4.51
E-B303-5				0.80	159.1	834	90.8	4.71
E-B303-6				0.82	126.5	645	89.8	4.31
Mean	-	-	-	0.69	178.0	720.0	78.9	4.93

Table I.50 Three point bending test results for Series E-B30.3.

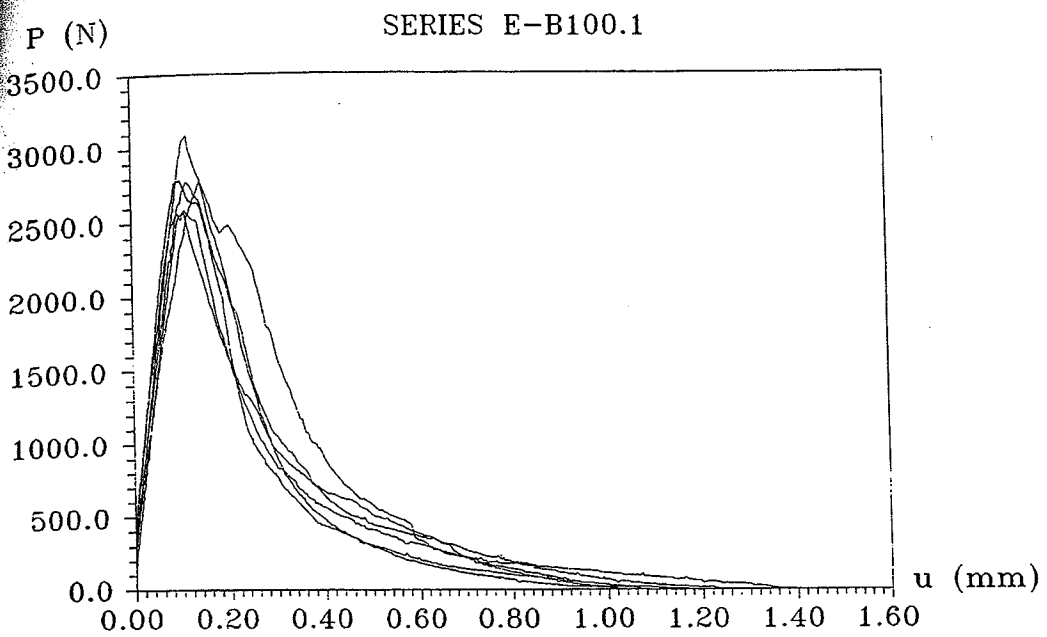

Figure I.69 Load-deflection curves for Series E-B100.1.

Beam no.	L (mm)	f_c (MPa)	f_{sp} (MPa)	u_0 (mm)	P_{max} (N)	W_e (Nmm)	G_F (N/m)	f_f MPa
E-B1001-1	550	94.8	5.83	1.02	2771.9	905.4	208.6	9.37
E-B1001-2				1.26	2588.3	762.0	186.5	8.76
E-B1001-3				1.09	2790.9	811.1	191.6	9.43
E-B1001-4				1.20	2774.6	670.8	166.5	9.38
E-B1001-5				1.40	2562.4	746.2	187.1	8.68
E-B1001-6				1.08	3088.8	728.3	174.9	10.42
Mean	-	-	-	1.18	2762.8	770.6	185.9	9.34

Table I.51 Three point bending test results for Series E-B100.1.

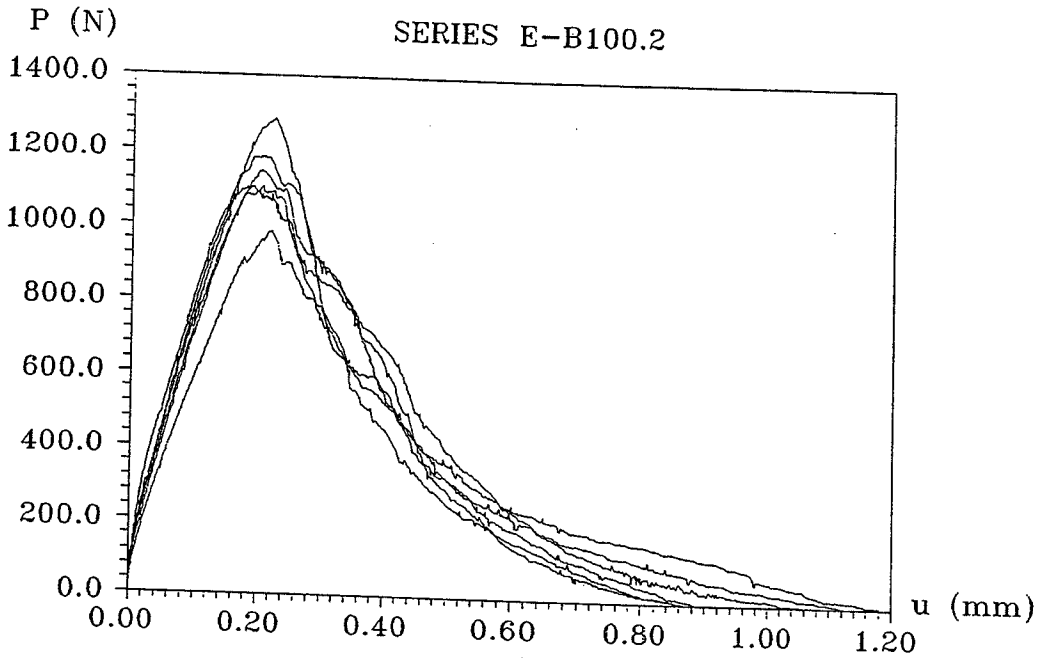

Figure I.70 Load-deflection curves for Series E-B100.2.

Beam no.	L (mm)	f_c (MPa)	f_{sp} (MPa)	u_0 (mm)	P_{max} (N)	W_e (Nmm)	G_F (N/m)	f_f (MPa)
E-B1002-1	1200	101.7	6.08	1.12	983.3	379.8	142.0	8.14
E-B1002-2				0.86	1103.0	376.8	125.9	9.00
E-B1002-3				0.88	1285.3	413.3	134.8	10.31
E-B1002-4				1.07	1104.4	430.1	149.2	9.01
E-B1002-5				0.87	1146.6	398.4	131.0	9.32
E-B1002-6				1.18	1184.6	466.4	162.9	9.59
Mean	-	-	-	1.00	1134.5	410.8	141.0	9.23

Table I.52 Three point bending test results for Series E-B100.2.

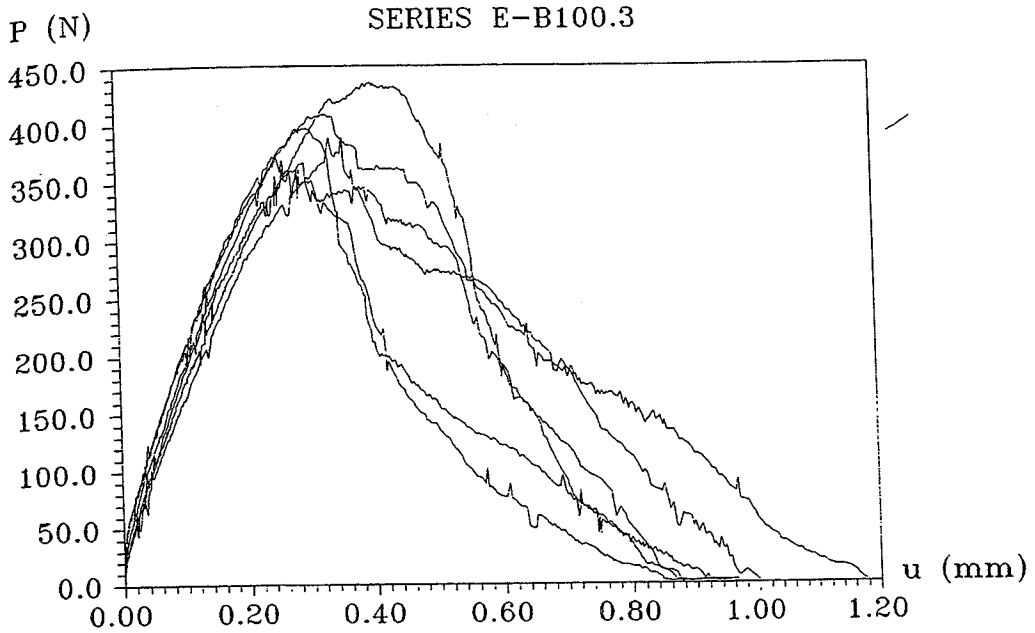

Figure I.71 Load-deflection curves for Series E-B100.3.

Beam no.	L (mm)	f_c (MPa)	f_{sp} (MPa)	u_0 (mm)	P_{max} (N)	W_e (Nmm)	G_F (N/m)	f_f (MPa)
E-B1003-1	2000	102.1	6.03	0.88	435.2	202.2	92.2	8.02
E-B1003-2				1.00	387.6	206.6	100.3	7.45
E-B1003-3				0.96	350.9	131.6	83.6	7.01
E-B1003-4				1.18	408.0	240.7	117.4	7.69
E-B1003-5				0.95	395.8	158.9	87.8	7.55
E-B1003-6				0.88	371.3	191.1	90.2	7.25
Mean	-	-	-	0.98	391.5	188.5	95.3	7.50

Table I.53 Three point bending test results for Series E-B100.3.

INSTITUT FOR BÆRENDE KONSTRUKTIONER OG MATERIALER
DANMARKS TEKNISKE UNIVERSITET

Department of Structural Engineering and Materials
Technical University of Denmark, DK – 2800 Lyngby

SERIE R
(Tidligere: Rapporter)

Abonnement 1.7.1998 – 30.6.1999 kr. 130,–
Subscription rate 1.7.1998 – 30.6.1999 D.Kr. 130.–.